



**University of
Leicester**

Multiwavelength observations of accreting binary systems

Thesis submitted for the degree of

Doctor of Philosophy

at the University of Leicester

by

Kristiina Byckling

X-Ray & Observational Astronomy Group

Department of Physics and Astronomy

University of Leicester

May 28, 2010

©Kristiina Byckling 2010

This thesis is copyright material and no quotation from it may be published without proper acknowledgement.

Declaration

I hereby declare that no part of this thesis has been previously submitted to this, or any other, University as part of the requirement for a higher degree. The work described herein was conducted by the undersigned, except for contributions from colleagues as acknowledged in the text.

Kristiina Byckling

March 2010

Multiwavelength observations of accreting binary systems

Kristiina Byckling

Abstract

CVs are interacting binaries accreting through Roche lobe overflow. The main motivation of this thesis is to enhance our understanding of accretion disc physics, and in particular, the mechanism producing X-rays in these and in other accreting objects.

This thesis comprises four case studies. Two of the studies have focused on individual CVs; a serendipitously discovered polar candidate 2XMM J131223.4 + 173659 (J1312) and a WZ Sge-type dwarf nova (DN), GW Lib, which went into an outburst in 2007. The X-ray analysis of J1312 showed that a soft component, assumed to be a typical spectral characteristic of polars, was not observed in these data. The most likely explanation is that this component probably has too low a temperature to be seen in X-rays. The multiwavelength study of the 2007 outburst of GW Lib represents a unique opportunity for understanding the disc physics of this rare type of outbursting system. A major finding of this study is that the X-rays are not suppressed during the outburst. This is in contrast to the outburst behaviour of WZ Sge, the defining member of this class.

The remainder of this thesis focused on larger source samples. First, I have derived the most accurate 2–10 keV X-ray luminosity function (XLF) of DNe to date with parallax-based distance measurements. The other study consists of a survey of serendipitous X-ray point sources in the direction of the Galactic Plane. The conclusion is that a significant fraction of the source sample could be associated with CVs based on the X-ray spectral characteristics of these sources.

Acknowledgements

I would like to thank several people in the Department and elsewhere for their help and support during my PhD. First, my official research supervisor Julian Osborne and my 'unofficial' supervisors and collaborators Bob Warwick and Koji Mukai to whom I am grateful for guiding me in my PhD research. Koji, you were an excellent host during my visit at the NASA GSFC in 2008! In addition, several other people deserve to be thanked for their help regarding various theory or data analysis questions, in particular Graham Wynn, Andy Beardmore, Kim Page, Valentina Braitto, Mike Goad, Pete Wheatley, Phil Evans, Richard West, Jenny Carter, Steve Sembay, Andy Read and Sean Farrell.

I dedicate this thesis to my parents who have always supported me, and to my wonderful partner Mike. Thank you for always being there when I needed a confidence boost and for putting up with my late nights working in front of my laptop! I would also like to acknowledge the SPARTAN programme for enabling this research and my participation in many conferences and workshops through the Marie Curie Fellowship.

And last but not least, special thanks belong to my friends for giving me encouragement when I needed it and for being there! And of course, how could I forget the Friday night pub crowd!

Publications

Vogel J., Byckling K., Schwobe A., Osborne J. P., Schwarz R., Watson M. G., 2008, **The serendipitous discovery of a short-period eclipsing polar in 2XMMp**, *A&A* , 485, 787

Byckling, K., Osborne J. P., Wheatley P. J., Wynn G. A., Beardmore A., Braitto V., Mukai K., West R., 2009, **Swift observations of GW Lib: a unique insight into a rare outburst**, *MNRAS*, 399, 1576

Byckling K., Mukai K., Thorstensen J., Osborne J. P., 2010, **Deriving an X-ray luminosity function of dwarf novae based on parallax-measurements**, submitted to *MNRAS*

Conference proceedings

Byckling Kristiina, Osborne Julian, Wheatley Peter, 2008, **The Optical, UV and X-ray Lightcurves of GW Lib in Outburst**, A population explosion: The Nature & Evolution of X-ray Binaries in Diverse Environments, AIP Conf. Proc., Vol. 1010, pp.183-185

Byckling Kristiina, Mukai Koji, Thorstensen John, Osborne Julian, 2010, **Deriving an X-ray luminosity function of dwarf novae**, X-ray Astronomy 2009, AIP Conf. Proc., submitted

CONTENTS

1	Introduction	1
1.1	The dominant X-ray processes	2
1.1.1	Blackbody emission	2
1.1.2	Thermal bremsstrahlung	4
1.1.3	Line emission	4
1.1.4	Non-thermal emission processes	5
1.1.5	Absorption and scattering processes	6
1.1.6	Accretion as a source of energy in accreting binaries	7
1.2	Cataclysmic variables	8
1.2.1	The general picture of a cataclysmic variable	9
1.2.2	Sources of X-rays and EUV emission	12

1.2.3	The sources of emission at other wavelengths	13
1.2.4	The motivation for studying CVs	14
1.2.5	The CV family: CV classification	15
1.2.6	CV evolution in a nutshell	16
1.2.7	Polars	19
1.2.8	Dwarf novae	22
1.3	The space-based observatories	26
1.3.1	Charged-Coupled Device	26
1.3.2	XMM-Newton	28
1.3.3	Swift	31
1.3.4	Suzaku	34
1.4	X-ray spectral analysis	36
1.5	The main goals of this thesis	38
2	2XMM J131223.4+173659	40
2.1	Introduction	40
2.2	Observations and data reduction	43
2.2.1	Investigating pile-up	50

2.3	Light curve analysis	51
2.3.1	The folded light curve	54
2.4	Optical Monitor data	57
2.5	Spectral analysis	62
2.5.1	Phase-resolved spectra	67
2.6	Discussion	70
2.6.1	System geometry	70
2.6.2	The missing soft X-ray component	73
2.7	Conclusions	74
3	<i>Swift</i> observations of GW Lib	76
3.1	Introduction	76
3.2	Observations and data reduction	78
3.2.1	X-ray data reduction	81
3.2.2	UV grism data reduction	83
3.2.3	UV filter mode data reduction	89
3.2.4	SuperWASP data reduction	89
3.3	Time series analysis	92

3.3.1	Outburst light curves	92
3.3.2	Search for oscillations in the X-ray data	95
3.4	Spectral analysis	102
3.4.1	Outburst X-ray spectra	102
3.4.2	Fluxes, luminosities and accretion rates	108
3.4.3	Later X-ray observations	108
3.4.4	Outburst UV spectra	110
3.4.5	Later UV observations	113
3.5	Discussion	113
3.5.1	Possible disc models	117
3.6	Conclusions	119
4	Deriving luminosity function	121
4.1	Introduction	121
4.2	The selection criteria and the source sample	125
4.3	Observations and data reduction	129
4.3.1	Suzaku data reduction	129
4.3.2	XMM-Newton data reduction	132

4.3.3	ASCA data reduction	134
4.4	Timing analysis	137
4.5	Spectral analysis	142
4.5.1	Absorption	150
4.5.2	Shock temperatures	150
4.5.3	Abundances	153
4.5.4	Spearman's rank correlation test	154
4.5.5	X-ray fluxes and luminosities	156
4.5.6	The height of the X-ray emission source above the white dwarf surface	159
4.6	Discussion	162
4.6.1	X-ray emissivity	167
4.6.2	Correlations between X-ray luminosity and other parameters	168
4.7	Conclusions	171
5	Galactic Plane	173
5.1	Introduction	173
5.1.1	This work	177
5.2	Screening of the observations and the source sample	178

5.3	Data reduction	185
5.4	Preparing the spectra for spectral analysis	188
5.4.1	Spectral fitting	190
5.4.2	Near-infrared counterparts of the source sample	199
5.5	Discussion	207
5.6	Conclusions	212
6	Summary and future work	214
6.1	2XMM J131223.4+173659	215
6.2	<i>Swift</i> observations of GW Lib	216
6.3	Deriving an X-ray luminosity function	218
6.4	Surveying the Galactic Plane	220

LIST OF FIGURES

1.1	A cataclysmic variable. Credit: A. Beardmore, University of Leicester.	10
1.2	(a) A contour plot illustrating the Roche lobes of M_1 and M_2 connected via L1. CM corresponds to the centre of mass. The figure also shows the locations of the L2 and L3 points. (b) A cross-section of the Roche potential where M_1 and M_2 are located on the x-axis, whereas the y-axis corresponds to the Roche potential Φ_R . The dashed line describes the value of Φ_R at the Lagrangian point L1.	11
1.3	An AM Her type system. Credit: A. Beardmore, University of Leicester.	21
1.4	A simple model of an accretion column above the white dwarf surface.	22
1.5	The effective temperature T_{eff} versus surface density Σ diagram (the "S-curve"). The disc cycles between the lower (lower branch) and upper (upper branch) equilibrium states.	25
1.6	A sketch of <i>XMM-Newton</i> obtained from the <i>XMM-Newton</i> Users Handbook.	28
1.7	The net effective areas of all <i>XMM-Newton</i> X-ray telescopes in linear scale (Source: <i>XMM-Newton</i> Users Handbook).	30

1.8	<i>XMM-Newton</i> OM effective area with the broad band filter passbands (<i>XMM-Newton</i> Users Handbook).	31
1.9	<i>Swift</i> satellite (Gehrels et al., 2004).	32
1.10	A layout of the X-ray telescopes onboard <i>Suzaku</i> obtained from 'The <i>Suzaku</i> Technical Description'.	35
2.1	The EPIC 10–12 keV background lightcurves of the EPIC (a) pn, (b) MOS1, and (c) MOS2 illustrating the background flaring. The unit on the x-axis is the spacecraft time in seconds and on the y-axis the count rate (ct s ⁻¹).	46
2.2	The <i>XMM</i> EPIC pn field of the observation 0200000101. J1312 has been circled in green. The dark columns are caused by exclusion of bad columns from the image. In the image, the scale is logarithmic, and the celestial North is up and East to the left.	47
2.3	A close-up of J1312 (circled in green, where the radius of the circle is 25 arcsec) and the possibly contaminating source (circled in blue).	47
2.4	The point spread function (PSF) of J1312 fitted with a King profile with $r_c = 6.18$ and $\beta = 1.50$	48
2.5	The pn pattern distribution of J1312 taken inside a source radius of 25 arcsec. The upper panel shows the spectral distributions as a function of PI channel for the four event types (see text), and the lower panel the fractions of the four event types relative to the sum. According to the lower panel, these data are not piled-up as the energy dependence follows the standard curves.	49

2.6	The <i>XMM</i> pn (top panel), MOS1 (middle) and MOS2 (bottom) background-subtracted X-ray light curves of J1312 in the energy band 0.2–12 keV. The light curves have been binned into 110 s bins using <i>LCURVE</i>	52
2.7	A close-up of the first short eclipse in the total band (0.2–12 keV) pn X-ray light curve of J1312. The mid-eclipse time is 5702 s. The light curve has been binned into 30 s bins in <i>LCURVE</i>	53
2.8	The soft (0.2–1.5 keV, top panel) and hard (1.5–12.0 keV, middle) <i>XMM</i> pn X-ray light curves of J1312 folded over the orbital period of 91.8 min. The bottom panel shows the hardness ratio of these light curves (hard/soft). The light curves are binned into 80 phase bins.	55
2.9	(a) J1312 (circled in green) in the <i>UVWI</i> filter with a source at $\alpha = 13^h 12^m 23.74^s$, $\delta = +17^\circ 37' 0.103''$ (circled in red) which is probably a marginal detection of the quasar SDSS J131223.75+173701.2 at $z = 2.43$ detected by Vogel et al. (2008), see text for more information. The quasar is not detected in the (b) <i>UVM2</i> and (c) <i>UVW2</i> filters.	59
2.10	(a) <i>GALEX</i> near-ultraviolet (NUV, left) and far-ultraviolet (FUV, right) images of J1312. The NUV bandpass covers 1700–3000 and the FUV 1650–1800 Å. Due to the redshifted Lyman limit (3128 Å), the quasar is not detected within these bandpasses. J1312 has been circled in yellow in these two figures. (b) An <i>SAO DSS</i> image of J1312 (circled in green). The figure also shows the quasar SDSS J131223.75+173701.2 (circled in yellow) at redshift $z = 2.43$. The PSF of the quasar is blended with J1312.	61

2.11	Top panel: pn (green), MOS1 (black) and MOS2 (red) X-ray spectra of J1312 fitted with the best-fit model (photoelectrically absorbed optically thin thermal plasma model). The $\chi^2_\nu = 1.08$ for 361 degrees of freedom (d.o.f). Lower panel shows the residuals.	66
2.12	The 68, 90 and 99 per cent confidence contours of the parameters kT and n_H for the joint spectral fit of the total pn, MOS1 and MOS2 spectra, using the absorbed optically thin thermal plasma model.	66
2.13	Top panel: The five phase-resolved EPIC pn X-ray spectra of the <i>XMM</i> polar candidate J1312 fitted with an absorbed optically thin thermal plasma model (the best-fit model). The hardening of the spectra is clear as the spectral shape changes from phase 1 (black) towards phase 5 (dark blue). Lower panel shows the residuals. The goodness of fit is $\chi^2_\nu/\nu = 1.01/209$	69
2.14	The system geometry of J1312. The horizontal lines (green and red) describe the maximum mass limit (Chandrasekhar mass $1.44 M_\odot$) and the stable accretion mass limit ($M_1 \sim 0.14 M_\odot$) for the white dwarf, the green curve rising from the right hand corner the colatitude δ of the emission region as a function of inclination i , and the three curves rising from $i = 65^\circ$ the best estimate for the white dwarf mass (middle curve) with 90 per cent confidence limits.	73
3.1	A combined PC mode X-ray image of the observations 00030917003–7018. GW Lib has been circled in yellow. The image is shown in logarithmic scale over the energy band 0.3–10 keV.	81
3.2	The XRT PSF of GW Lib over the energy band 0.3–10 keV from the combined observations 00030917003–7018 fitted with a King function with a PSF core radius of $r_c = 5.8$ and a slope $\beta = 1.55$	83

3.3	A <i>Swift</i> UV grism observation (ObsID 00030917023) of GW Lib on the 7th of May, 2007. The image shows the 0th (circled in blue) and 1st (inside the green box) order spectra and the background extraction regions (yellow boxes) for this extension. Since the UVOT grism observations are slitless, all sources in the field of view are dispersed.	84
3.4	The integrated counts of a UV grism spectrum of GW Lib as a function of extraction box width in pixels. A box width of 35 pixels covers ~ 90 per cent of the flux. Narrower box widths reduce the source flux, whereas wider increase the background noise and possible contamination from other sources.	86
3.5	Curvature of a UV grism spectrum of GW Lib measured taking spatial profiles over the spectrum (upper panel), and the corresponding FWHM of each profile centre (lower panel).	87
3.6	Using an extraction box of a width of 35 pixels, no significant loss of flux occurs provided the box is miscentred less than ~ 12 pixels from the centre of the spectrum (cross-dispersion profile).	88
3.7	(a) The field of view of the <i>Swift</i> UVOT <i>UVWI</i> (left) and the <i>V</i> filter (right) in observation 00030917046. GW Lib has been marked with yellow in the centre of the field of view. (b) A close-up of the <i>Swift</i> UVOT <i>UVWI</i> (left) and <i>V</i> (right) filters in observation 00030917046. GW Lib has been circled in yellow and the background regions used in the photometry in magenta. These figures have been plotted in logarithmic scale. The orientation (North up, East to the left) together with an image scale bar are shown in the images. The length of the green scale bar is 3 arcmin.	90

3.8	The <i>WASP</i> images of the field of GW Lib before (left) and after (right) the onset of the outburst. GW Lib is circled in green where the circle radius is 60 arcsec, and the images have been plotted in logarithmic scale. The length of the white scale bar on the left hand side figure is 5 arcmin.	91
3.9	The optical, UV and X-ray outburst light curves of GW Lib. T_0 is JD 2454203.1, which corresponds to the start time of the first data point in the <i>AAVSO</i> light curve. The top panel shows the <i>AAVSO</i> optical light curve (www.aavso.org) in the <i>V</i> band (converted to $\log F$) in black and the <i>WASP</i> light curve in light blue (see text for details). The upper panel insert shows the rapid rise to maximum peaking one day after the onset of the outburst. The middle panel shows the UV in the wavelength range 2200–4000 Å (<i>Swift</i> UV grism), and the bottom panel the X-ray light curve in 0.3–10 keV (<i>Swift</i> XRT). The X-ray data have been binned at 600 s and the other bands are plotted per exposure.	93
3.10	The soft (0.3–1.0 keV, upper panel) light curve, the hard (1.0–10 keV, middle panel) light curve, and the X-ray hardness ratio (hard/soft) of GW Lib. The data have been binned at 700 s.	95
3.11	The average power spectra of (a) the WT mode and (b) the PC mode data of GW Lib. The data have been binned to 1 s for the WT mode and to 5 s time bins for the PC mode.	99

3.12 (a) and (b) upper panels: The (a) WT and (b) PC mode Lomb-Scargle periodograms of the 2007 outburst data of GW Lib, covering frequencies between 0–0.05 Hz. The window functions (red) have been plotted on top of the data (black). Lower panels: close-ups of the WT and PC mode periodograms where frequency has been plotted in logarithmic scale. The dashed lines indicate the 90 (lower) and 99 (upper) per cent detection limits which correspond to the powers of 8.09 and 10.44 (WT), and 10.24 and 12.59 (PC), respectively.	101
3.13 The <i>Swift</i> XRT spectra of GW Lib throughout the outburst.	104
3.14 Upper panel: the best-fit model components of the first outburst spectrum (S1) of GW Lib. The data are fitted with a black body and three optically thin thermal emission components, all absorbed by the same column density. Lower panel shows the residuals.	105
3.15 Upper panel: a spectral fit (a black body and three optically thin thermal emission models with variable abundances (<code>vmekal</code>)) to the first outburst spectrum (S1) with the oxygen abundance fixed to that found in the <i>XMM-Newton</i> quiescent spectrum by Hilton et al. (2007). An oxygen line of this strength (at 0.65 keV) would be detected and the fit is unacceptable with $\chi^2_\nu/\nu = 1.62/221$. The lower panel shows clear residuals between 0.55–0.70 and above 6.5 keV.	107
3.16 Black body parameters derived from the first outburst spectrum (S1) of GW Lib. The 10^{38} (L_{edd}), 10^{37} ($0.1 L_{edd}$) and 10^{36} erg s^{-1} ($0.01 L_{edd}$) bolometric luminosity levels of the black body component are shown as dashed lines. The contours describe the 68, 90 and 99 per cent confidence levels for n_H versus kT_{bb}	109

3.17	The evolution of the background-subtracted <i>Swift</i> UVOT UV grism flux spectra of GW Lib throughout the outburst in descending and chronological order. The top spectrum is an average of three spectra corresponding to days $T_0 + 8$, 13 and 18. The following three spectra correspond to days $T_0 + 23$, 26, and 27 (the spectrum on day $T_0 + 27$ is an average of three spectra during that day). The bottom spectrum shows the background flux level for one of the spectra on day $T_0 + 27$	112
4.1	<i>Suzaku</i> observation of the XIS0 detector of BZ UMa (circled in yellow, the radius of the circle is 260 arcsec = 250 pixels). The bright regions in the corners are the calibration sources. The image has been plotted in the logarithmic scale, and North is up and East to the left.	131
4.2	<i>XMM</i> pn observation of T Leo (circled in green). The image illustrates the out-of-time events (the bright strip across the CCD chip) often associated with bright sources.	133
4.3	The <i>ASCA</i> observation of WZ Sge in SIS (left) and GIS (right).	135
4.4	The Lomb-Scargle periodograms of (a) SS Aur and BZ UMa, (b) VY Aqr and SW UMa, and (c) ASAS J0025. The dashed lines show the 99 (upper) and 90 (lower) per cent detection thresholds. The data, from which linear trends have been removed, is plotted in black (the periodogram), whereas the red curves represent the window functions. The peaks exceeding the 99 per cent detection level at the low frequency end are most likely caused by red noise.	139
4.5	The X-ray light curve of SW UMa folded over the period 7626 s with 100 phase bins.	141

4.6	The X-ray spectra of VY Aqr, SW UMa, BZ UMa, SS Aur and ASAS J0025 fitted with an absorbed cooling flow model with a 6.4 keV Gaussian line. . . .	148
4.7	The two dimensional confidence contours of the normalization (\dot{M}) and the shock temperature kT_{max} for VY Aqr, SW UMa, BZ UMa, SS Aur and ASAS J0025 which have been fitted with an absorbed cooling flow model with a 6.4 keV Gaussian line.	149
4.8	The mass of the white dwarfs, M_{WD} , versus the shock temperature, kT_{max} , of the source sample with errors (90 per cent). The light blue dashed line represents the theoretical shock temperature for a given M_{WD} . The error bar on the right indicates a typical error on the white dwarf mass measurements. .	152
4.9	A histogram showing the X-ray luminosities of the DN source sample in the 2–10 keV energy range.	158
4.10	Geometry of the solid angle $\Omega_{WD}/2\pi$ of the white dwarf which is viewed from the boundary layer. R_{WD} is the white dwarf radius, h the height of the X-ray source measured from the white dwarf surface and A the surface area as measured from a distance of r from the X-ray source.	161
4.11	The cumulative source density distribution (histogram) and the power law fit versus the luminosity in $\log L$ (2–10 keV) when $\alpha = -0.64$. The threshold luminosity at the break between the power law fit and the histogram is $\sim 3 \times 10^{30}$ erg s ⁻¹ . The error bar on the top right represents a typical error on the luminosities.	165

4.12	The cumulative source density distribution (histogram) and the power law fit versus the luminosity in $\log L$ (2–10 keV) when $\alpha = -0.79$. The threshold luminosity at the break between the power law fit and the histogram is $4 \times 10^{30} \text{ erg s}^{-1}$	167
4.13	The figures above show the 2–10 keV X-ray luminosities versus: (a) the orbital periods of the source sample P_{orb} , (b) the maximum shock temperatures kT_{max} , (c) the system inclinations i , and (d) the white dwarf masses M_{WD}	170
5.1	Straylight features (on the right) in the observation 0135960101 which was excluded during the screening. In the image, north is up and east to the left. The image consists of all EPIC (pn and MOS) images and was obtained from the <i>XMM</i> XSA.	179
5.2	(a) The final <i>XMM</i> source sample consisting of 110 sources (red points) and the corresponding observations (0.5×0.5 deg green boxes) along the Galactic Plane. The x-axis corresponds to the Galactic longitude l and the y-axis to the Galactic latitude b . (b) A close-up of the observations and the sources within them (note that due to the small sizes of the source points some of the boxes appear empty as they contain only 1–2 sources which would only be visible if these boxes were zoomed in).	186
5.3	The EPIC pn backgrounds in 10–12 keV of observations (a) 0307170201 and (b) 0112970701. The flaring intervals were cut above 0.4 ct s^{-1} . The figures illustrate the wide range in amplitude of the background flaring.	187
5.4	The broad band (0.5–12 keV) hardness ratio of the 110 sources.	189

5.5	The background-subtracted spectra for source groups (a) H1, H2, H3, and (b) S1, S2 and S3. The y-axis shows Counts/Channel and the x-axis the energy in keV. The vertical dashed lines identify the region of the spectra around 6.7 keV. The green line on the bottom corresponds to zero counts per channel.	191
5.6	The <i>XMM-Newton</i> X-ray spectra of the source groups H1–H3 (panels (a)–(c)), and source groups S1–S3 (panels (d)–(f)). Groups H1–S1 have been fitted with an absorbed powerlaw with an added Gaussian line at 6.7 keV, and groups S2 and S3 with photoelectric absorption and two optically thin thermal plasma models.	197
5.7	The contour plots of (a) the four hardest groups H1, H2, H3, and S1 (from H1 on the right) fitted with an absorbed power law and a Gaussian line at 6.7 keV, and (b) the three softest groups S1, S2 and S3 (from S1 on the right) fitted with an absorbed optically thin thermal plasma model.	198
5.8	The $J - H$ versus $H - K$ colour-colour diagram of this work where the black dots represent the softest sources (groups S1-S3) and the red dots the hardest groups (H1-H2). The arrow with a slope of 1.57 indicates the direction of interstellar reddening and the value of extinction (5 mag) in the V band. . . .	205
5.9	The $J - H$ versus $H - K$ colour-colour diagram of the 2MASS Point Source Catalogue (PSC) from the Galactic Plane. The solid and dashed lines describe the expected evolutionary tracks for dwarfs and giants as given by Koornneef (1983) and Bessell & Brett (1988). The colours indicate the highest source density (red) and the lowest source density (blue).	206

5.10 Upper panel: the EWs of the 6.7 keV lines with error bars from this work.
Middle panel: the EWs of the 6.7 keV lines with error bars of 14 magnetic
CVs (H98, Hellier, Mukai & Osborne, 1998). The long-dashed lines indicate
the straight averages, and the shorter dashed lines the weighted averages of
the 6.7 keV line EWs. For the source groups H1–S1, these values are $167 \pm$
 28 eV (average) and 150 ± 35 eV (weighted), and for the H98 sample, 178
 ± 28 eV (average) and 122 ± 7 eV (weighted). In the upper panel, the x-axis
indicates the source group numbering corresponding to: 1 = H1, 2 = H2, 3
= H3, and 4 = S1, and in the middle panel, the number of the 14 individual
magnetic CVs. The bottom panel shows the 6.7 keV line EW measurements
(~ 300 – 600 eV) from the Galactic Ridge regions between R2 (corresponds
to $x=1$ in the figure) and R8 (corresponds to $x=7$), obtained by Yamauchi et
al. (2009) (Y09), compared with the average 6.7 keV line EWs of the H1–S1
groups and the H98 sample. 209

5.11 The 6.7 keV iron line EW measurements as a function of plasma temperature
 kT assuming an optically thin thermal plasma spectrum as the underlying
spectrum. The black curve illustrates EW measurements for a solar abun-
dance spectrum, and the red curve for a spectrum with $Z = 0.5 Z_0$. The
blue and cyan dashed lines indicate the lowest Galactic Ridge EW measure-
ment (300 eV) by Yamauchi et al. (2009), and the average EW measurement
(167 eV) of groups H1–S1 for the 6.7 keV iron line, respectively. 211

LIST OF TABLES

1.1	The technical characteristics of the X-ray telescopes of <i>XMM-Newton</i> , <i>Swift</i> and <i>Suzaku</i> . The spectral resolution given for each instrument is the resolution at the time of launch. The last three columns give the spectral resolution, the effective area, and the field of view (FOV).	27
2.1	The <i>XMM-Newton</i> observations of J1312 obtained in June 2004.	44
2.2	The observed times t_0 for the mid-eclipses of J1312, the error σ_{t_0} , the calculated mid-eclipse times t_c , <i>O-C</i> values and the cycle numbers E	54
2.3	The <i>XMM</i> OM instrumental magnitudes, corrected source count rates and flux densities with their 1σ errors for J1312 in the <i>UVWI</i> , <i>UVM2</i> and <i>UVW2</i> filters for orbital phase intervals corresponding to phases in Fig. 2.8.	58
2.4	The reduced χ^2 values and degrees of freedom (ν) of the spectral models of J1312 for the total pn and MOS spectra which have been fitted simultaneously. P_0 is the null-hypothesis probability.	65

2.5	The spectral models with their χ^2_ν values and the null hypothesis probabilities P_0 for the five, phase-resolved spectra which have been fitted simultaneously with each model.	68
2.6	The best-fit parameters of the photoelectrically absorbed optically thin thermal plasma model for each phase ϕ_1 – ϕ_5 . Errors refer to $\Delta\chi^2 = 2.71$ (90 per cent confidence for one parameter of interest.)	69
3.1	The <i>Swift</i> XRT and UVOT observations of GW Lib obtained in 2007, 2008 and 2009.	79
3.1	The <i>Swift</i> XRT and UVOT observations of GW Lib obtained in 2007, 2008 and 2009, contd.	80
3.2	The powers, the 99 per cent amplitude upper limits, and the average count rates for the average WT and PC mode power spectra of the GW Lib outburst X-ray data.	99
3.3	The <i>Swift</i> XRT spectra of GW Lib and the corresponding epochs in days since T_0	103
3.4	The results of the spectral fitting using photoelectric absorption, black body and three optically thin thermal plasma components. Not all components are fitted to all spectra. The errors correspond to the 90 per cent confidence limits for one parameter of interest. The measured abundance from the S1 spectrum is $0.02^{+0.01}_{-0.01} Z_\odot$, and the abundances in the other fits have been fixed at this value. The unabsorbed fluxes F_1 , F_2 and F_3 correspond to the three optically thin thermal plasma components in the 0.3–10 keV band.	106

3.5	The fluxes, luminosities and accretion rates in the 0.3–10 keV (fluxes absorbed) and 0.0001–100 keV (bolometric, fluxes unabsorbed) bands of the XRT spectra. The 0.0001–100 keV flux given for S1 is the lower limit, i.e. the blackbody model has been excluded from the calculation.	109
3.6	The spectral fitting parameters with 0.3–10 keV fluxes, luminosities and accretion rates of the 2008 and 2009 (columns 2 and 3) X-ray observations of GW Lib. The fourth column shows the spectral fitting parameters for the combined 2008 and 2009 spectrum.	111
3.7	The observation dates since the onset of the outburst for the <i>Swift</i> UVOT UV grism spectra in Fig. 3.17.	113
3.8	The average magnitudes, fluxes and their 1σ (68.3 per cent confidence level) errors in the UVOT <i>V</i> and <i>UVWI</i> ($\bar{\lambda} = 2600 \text{ \AA}$) filters for the 2008 and 2009 observations of GW Lib. The magnitudes and fluxes are the mean values of different snapshots. Observation time corresponds to the midpoint of each observation in days since T_0 . The exposure times are given in Table 3.1. . . .	114
4.1	The source sample used to derive the X-ray luminosity function (excluding *) with their inclinations, orbital periods, white dwarf masses, distances, and DN types. The types given in the last column are U Gem (UG), SU UMa (SU), WZ Sge (WZ) and Z Cam (ZC). The references are: 1) Thorstensen (2003); 2) Thorstensen, Lépine, & Shara (2008); 3) Harrison et al. (2004); 4) Mason et al. (2001b); 5) Urban & Sion (2006); 6) Friend et al. (1990); 7) Ritter & Kolb (2003); 8) Horne, Wood, & Stiening (1991); 9) Preliminary distance estimate from Thorstensen (in prep.), and 10) Templeton et al. (2006)	128

4.2	Observation times for each source. The exposure times for the <i>Suzaku</i> sources have been obtained from the cleaned event lists. The numbers in brackets for the <i>XMM</i> sources show exposure times after filtering high background flares, and the last column corresponds to the optical state of the source (Q = quiescence, T = transition).	130
4.3	The best-fit parameters of the absorbed optically thin thermal plasma model with a 6.4 keV Gaussian line. The errors are 90 per cent confidence limits on one parameter of interest. n_{H_1} and n_{H_2} are the absorption columns of the photoelectric absorption (<code>wabs</code>) and the partial covering (<code>pcfabs</code>) models, respectively. CFrac is the covering fraction of the partial covering model and Ab the abundance.	145
4.4	The best-fit parameters of the absorbed cooling flow model with a 6.4 keV Gaussian line. The errors are 90 per cent confidence limits on one parameter of interest. n_{H_1} and n_{H_2} are the absorption columns of the photoelectric absorption (<code>wabs</code>) and the partial covering (<code>pcfabs</code>) models, respectively. CFrac is the covering fraction of the partial covering model and Ab the abundance.	146
4.5	The equivalent widths of the Fe 6.4 keV line with their 90 per cent confidence limits derived from the absorbed optically thin thermal plasma (middle column) and cooling flow (right hand column) models.	147
4.6	The fluxes and luminosities in the 2–10 and 0.01–100 keV bands derived by using the cooling flow model. The errors on the 2–10 keV fluxes represent the 90 per cent confidence limits. The errors on the 2–10 keV luminosities have been calculated using the errors on the distances and fluxes.	157

4.7	The significance of the correlations between the X-ray luminosity and the system parameters calculated with Spearman’s rank correlation test. Probability ¹ corresponds to the significance of correlation when GW Lib is included in the sample and Probability ² to the significance when GW Lib is excluded.	171
5.1	The <i>XMM-Newton</i> source sample (110 sources) obtained along the Galactic Plane. In addition to source and observation identification (ID) numbers, the table lists the IAU name of the source, the number of raw (gross) pn counts in the extracted source spectrum (prior to background subtraction), the exposure time of the observations (after flare filtering) as derived from the source spectra, and the RA and DEC (J2000) of the sources (as tabulated in the 2XMM catalogue).	181
5.1	The <i>XMM-Newton</i> source sample (contd.).	182
5.1	The <i>XMM-Newton</i> source sample (contd.).	183
5.1	The <i>XMM-Newton</i> source sample (contd.).	184
5.1	The <i>XMM-Newton</i> source sample (contd.).	185
5.2	The source groups with their broad band hardness ratios and number of sources in each group. The groups have been listed according to the spectral hardness: from the hardest (H1) to the softest one (S3).	190
5.3	The results of the X-ray spectral fitting when using the absorbed powerlaw model with an added Gaussian line at 6.7 keV for groups H1–S1. The table also reports the EWs for the 6.4 keV line for the H1–S1 spectra when it was added to the powerlaw model.	194

5.4	The results of the X-ray spectral fitting when using an absorbed optically thin thermal plasma model. The abundance given is the overall abundance relative to the Sun.	194
5.5	The results of the X-ray spectral fitting for the softer source groups S1, S2 and S3 when using photoelectric absorption with two optically thin thermal plasma models. The abundance given is the overall abundance relative to the Sun.	195
5.6	The 2MASS NIR counterparts for which the probability of identification is > 90 per cent. The last three columns give the 2MASS <i>J</i> (1.24 μm), <i>H</i> (1.66 μm) and <i>K</i> (2.16 μm) magnitudes with errors (the numbers in brackets are the central wavelengths in each band). The Group column gives the group ID where the source belongs to.	201
5.6	The 2MASS NIR counterparts (contd.).	202
5.6	The 2MASS NIR counterparts (contd.).	203
5.6	The 2MASS NIR counterparts (contd.).	204

Chapter 1

Introduction

The development of X-ray astronomy in the 20th century brought a new dimension to the understanding of variable stars. The roots of X-ray astronomy date back to the photon counting experiments onboard a V-2 sounding rocket in 1949 which showed that the Sun was an intense X-ray emitter (Friedman, Lichtman, & Byram, 1951). In 1962, the first X-ray observation of the brightest X-ray source outside the Solar System at the time, *Scorpius X-1*, was made during a rocket flight in 1962 (Giacconi, Gursky, & Paolini, 1962). Some examples of the earliest X-ray satellites dedicated to observing the X-ray sky arrived in the 1970s, such as the first Earth-orbiting X-ray satellite *Uhuru* which scanned the Galactic Plane in the 2–20 keV range discovering 29 discrete X-ray sources (Giacconi et al., 1971) and the first X-ray imaging telescope in space, *Einstein* (Giacconi et al., 1979) which enabled imaging of extended sources, detected faint sources and diffuse emission, and thus changed the view of the X-ray sky. During the 1980s, the *European Space Agency's X-ray Observatory* (EXOSAT) contributed to the understanding of X-ray sources such as cataclysmic variables (CVs), X-ray binaries (XRBs) and Active Galactic Nuclei (AGNs). Subsequently, the *Röntgen Satellite* (ROSAT) operated between 1990 and 1999 with the two main scientific objectives: to carry out the first imaging X-ray and extreme-ultraviolet (EUV) all-sky survey of the entire sky (Voges et al., 1999) and a detailed study of selected X-ray and EUV sources. Currently, 8 X-ray

missions are operating. Of these, it is worth mentioning at least the two large X-ray imaging missions, i.e. the *Chandra* X-ray Observatory with a high resolution and a large effective area which enable observations of very faint X-ray sources, and *XMM-Newton* (Jansen, Lumb & Altieri, 2001) with the largest effective area of all the X-ray satellites and multiwavelength observing capabilities.

The X-ray satellites mentioned above have contributed significantly to the understanding of binary stars, such as CVs which are the main target of research in this thesis. In Section 1.1, I will start by discussing the main processes which are important in the production of X-ray emission in binary systems, and discuss accretion as a source of energy. In Section 1.2, I will discuss CVs and some basic concepts relevant in binary systems. In Section 1.3, I will describe the three space-based X-ray observatories, *XMM-Newton*, *Swift* and *Suzaku* which have enabled the research in this thesis, and in Section 1.4, I will give a brief introduction to X-ray spectral analysis. Finally, the main goals of this research will be discussed in Section 1.5.

1.1 The dominant X-ray processes

In CVs, three dominant astrophysical mechanisms producing emission at X-ray energies exist. These are processes which produce *black body* emission, *thermal*, and *non-thermal* emission. In addition, there are *scattering* and *absorption* processes involved. Since these mechanisms and processes are essential in the production of X-ray emission in CVs, they will be discussed in the following sub-sections.

1.1.1 Blackbody emission

In general, a blackbody is defined as a body which does not reflect any light, but absorbs energy and emits it all at a temperature which is characteristic to the emitting body, independent

of the material of the body. In complete thermodynamic equilibrium, a blackbody does not have temperature differences. The material emitting blackbody emission is *optically thick*, i.e. the optical depth of the material is $\tau_\lambda \gg 1$. The intensity distribution of a blackbody can be calculated according to *Planck's law* expressed per unit wavelength interval

$$I_\lambda = \frac{2hc^2}{\lambda^5} \frac{1}{e^{hc/\lambda kT} - 1}, \quad (1.1)$$

where T is the temperature of the blackbody, h Planck's constant (6.63×10^{-34} Js), c the speed of light (3×10^8 m s⁻¹), k the Boltzmann constant (1.38×10^{-23} J K⁻¹), and λ the wavelength of the photon. The peak of the photon energy E depends only on the blackbody temperature T . If the blackbody temperature increases, the intensity increases and in this case, the location of the peak of the intensity distribution λ_{max} moves to shorter wavelengths. This is called *Wien's displacement law*, i.e.

$$\lambda_{max}T = \text{constant} = 2.898 \times 10^{-3} \text{ m K}. \quad (1.2)$$

In addition, it is important to know the *Stefan-Boltzmann law* which states the total amount of energy L leaving a star per unit surface area per second

$$L = 4\pi R^2 \sigma T_{eff}^4, \quad (1.3)$$

where $\sigma = 5.67 \times 10^{-8}$ J s⁻¹ m⁻² K⁻⁴ is the Stefan-Boltzmann constant and T_{eff} the effective temperature of the star. The effective temperature is the temperature a blackbody would need to have in order to radiate the same amount of energy per cm² as the star.

1.1.2 Thermal bremsstrahlung

Thermal bremsstrahlung, or free-free emission, takes place above the temperature of $T \sim 10^5$ K (Charles & Seward, 1995). In this case, the material is *optically thin*, i.e. $\tau_\lambda \ll 1$. When a gas is ionised, it consists of ions and free electrons. These ions and free electrons interact via collisions, i.e. when a free electron passes close to an ion, the electric force between the two particles causes the electron to change its direction and accelerate. When an electron accelerates, it produces emission, and the energy of the emitted photon corresponds to the change in energy during the collision.

For a gas in thermal equilibrium, the average energy of all the particles in the gas is the same and is determined only by the temperature. In this case, the electrons have a Maxwell-Boltzmann distribution of velocities, i.e., the particles do not constantly interact with each other but they move freely between short collisions, and the emission produced by the collisions of electrons and ions is a bremsstrahlung continuum which has a shape determined only by the temperature. Naturally, the photon energies will be higher with a higher gas temperature and thus faster electrons. The shape of the bremsstrahlung spectrum is characterised by the temperature T , and the spectrum falls off exponentially at high energies.

1.1.3 Line emission

In addition to continuum emission, line emission, i.e. *bound-bound* emission, is also an important radiation source in hot gas. Some heavier elements than hydrogen may not be completely ionised depending on the temperature and thus during a collision of a free electron and an ion, an energy transfer from the electron to the ion causes the bound electrons to move to higher energy levels. These *collisionally excited* ions decay rapidly back to the ground state, radiating photons which have energies corresponding to the spacing of the energy levels passed by the excited electrons. In a *free-bound* process, a free electron is captured by an

atom, and the atom moves to an excited state. This process produces a continuous absorption spectrum. However, as the atom decays back to its ground state, a photon is emitted, and this produces line emission. This is called *radiative recombination*.

1.1.4 Non-thermal emission processes

The third dominant source of X-ray production is non-thermal emission which is produced when electrons are accelerated by some other mechanisms than collisions between the particles. One form of non-thermal emission is *synchrotron radiation* which is produced when a high-energy electron with a relativistic speed moves under the influence of a strong magnetic field which exerts a force perpendicular to the direction of the motion of the electron. Thus, the electron is accelerated due to the changes in its velocity, and emits synchrotron radiation. The observed spectrum depends only on the magnetic field strength B and the energy spectrum of the electrons, for which the assumed spectral form is a power law. If the magnetic field lines are aligned, the emission is strongly polarised. Synchrotron radiation is usually observed at radio wavelengths, but can also extend to X-ray energies. The sources of synchrotron radiation are e.g. supernova remnants.

In this context, it is worth mentioning *cyclotron radiation* which is also produced under the influence of a strong magnetic field, but now the electron energies are not as high as for electrons producing synchrotron radiation (10^4 GeV for electrons producing synchrotron radiation, Charles & Seward, 1995), and they move with a non-relativistic velocity. Similarly to the synchrotron radiation, also cyclotron radiation is strongly polarised and can be seen in the infrared and optical wavelengths. The cyclotron frequency ν , i.e. the Larmor's frequency at which a particle circles a field line is

$$\nu = \frac{qB}{mc}, \quad (1.4)$$

where q is the electric charge of the particle, B the magnetic field strength, m the mass of the particle, and c the speed of light ($3 \times 10^8 \text{ m s}^{-1}$).

1.1.5 Absorption and scattering processes

The dominant absorption process at *low* photon energies is *photoelectric absorption*, or *bound-free* process. At X-ray energies, this form of absorption is most commonly found below ($\lesssim 1 \text{ keV}$, Longair, 1992). In this process, a photon of energy E is absorbed by a bound electron, which gains energy from the photon, and subsequently the electron is emitted. Another process in which a photon loses energy is *Thomson scattering* which operates even at lower energies than photoelectric absorption. In this process, a low-energy photon is scattered from a free charged particle and the wavelength of the scattered photon does not change during the collision. The energy of the incoming photon is much less than the rest mass energy of the electron, i.e. $h\nu \ll m_e c^2$ (Longair, 1992).

At higher energies ($\sim 1\text{--}30 \text{ MeV}$) *Compton scattering* is the dominant physical interaction between photons and charged particles. In Compton scattering, the incoming high-energy photons collide with stationary electrons in which case some of their energy and momentum are transferred to the electrons. Thus, the scattered photons will have less energy and momentum after the collision than before it. The loss of energy corresponds to an increase in the photon's wavelength, because the energy and momentum of the photon are equal to the frequency of the radiation. In *inverse* Compton scattering, which is more relevant for X-ray astronomy, a low-energy photon is scattered by a relativistic electron to higher energies. This form of scattering is seen e.g. in supernovae, AGNs and CVs.

1.1.6 Accretion as a source of energy in accreting binaries

The release of gravitational energy from infalling matter is the principal source of power in several types of close accreting binary systems. It is also believed to power Active Galactic Nuclei (AGNs) and quasars. In general, the released gravitational potential energy ΔE for an accreted mass m to an accretor M with a radius of R_* is

$$\Delta E_{acc} = \frac{GMm}{R_*}, \quad (1.5)$$

where $G = 6.67 \times 10^{-11} \text{ Nm}^2 \text{ kg}^{-2}$ is the gravitational constant, M the mass of the accreting object, and R_* the radius of the accreting object. If accretion is spherically symmetric and steady, we are able to define the *Eddington luminosity*, L_{edd} ,

$$L_{edd} = \frac{4\pi GMm_p c}{\sigma_T} \simeq 1.3 \times 10^{38} \frac{M}{M_\odot} \text{ erg s}^{-1}, \quad (1.6)$$

where m_p is the mass of a proton ($1.67 \times 10^{-27} \text{ kg}$), c the speed of light, and σ_T the Thomson cross-section of an electron ($6.7 \times 10^{-25} \text{ cm}^2$). The Eddington luminosity is the limiting luminosity at which the outward radiation pressure of a star balances the inward gravitational force

$$\frac{GM(m_p + m_e)}{r^2} \sim \frac{GMm_p}{r^2}, \quad (1.7)$$

which affects each proton-electron pair m_p and m_e ($9.11 \times 10^{-31} \text{ kg}$) at a radial distance r from the centre of the star. For objects, which are accretion powered, the Eddington limit implies a maximum limit for the steady accretion rate \dot{M}_{edd} . Assuming that all the kinetic energy of the accreted material is converted into radiation on the surface of the star, then the released accretion luminosity L_{acc} is

$$L_{acc} = \frac{GM\dot{M}}{R_*}, \quad (1.8)$$

where L_{acc} is in units of erg s^{-1} and \dot{M} the accretion rate in units of g s^{-1} . Thus, the efficiency of accretion depends on the compactness M/R_* of the accreting object: for a given M , the accretion is most efficient when the accretor radius R_* is small. If the source radiates as a blackbody, then the source would have the blackbody temperature

$$T_b = \left(\frac{L_{acc}}{4\pi R_*^2 \sigma} \right)^{1/4}. \quad (1.9)$$

If the gravitational potential energy was completely turned into thermal energy, the accreted material would reach the temperature T_{th} according to

$$T_{th} = GMm_p/3kR_*. \quad (1.10)$$

Thus, if the material is optically thick, the emitted radiation temperature $T_{rad} \sim T_b$, whereas in the optically thin case $T_{rad} \sim T_{th}$. Assuming a $1 M_\odot$ accreting white dwarf with a radius of $R_* = 5 \times 10^8$ cm and an accretion luminosity of $L_{acc} \sim 10^{33}$ erg s^{-1} as in Frank, King, & Raine (2002), the photon energies are between $kT_b \sim 6$ eV ($T_b \sim 7 \times 10^4$ K) and $kT_{th} \sim 100$ keV ($T_{th} \sim 1 \times 10^9$ K).

1.2 Cataclysmic variables

In this section, I start by discussing the defining characteristics of CVs, followed by topics, such as how X-ray emission is produced in CVs relating the emission mechanisms introduced in Section 1.1 to this topic, why CVs are important, and CV evolution. I will also present

two CV subclasses relevant to this thesis in more detail. A significant part of the information given in the following sections has been adopted from Warner (1995), Hellier (2001) and Frank, King, & Raine (2002), unless otherwise stated.

1.2.1 The general picture of a cataclysmic variable

Cataclysmic variables (CVs), are close binary systems which consist of a white dwarf (the primary component), a late-type main sequence star (the secondary component) of spectral type K or M, and an accretion disc through which material is transferred from the secondary star to the primary. The white dwarf has a radius of $\sim 10^8\text{--}10^9$ cm (Frank, King, & Raine, 2002), i.e. roughly the radius of the Earth, and a typical white dwarf mass peaks between $\sim 0.6\text{--}0.9 M_{\odot}$ (Sion, 1999). The limiting white dwarf mass, $1.44 M_{\odot}$, is the Chandrasekhar mass limit (Nauenberg, 1972) which defines the maximum mass limit before gravitational collapse takes place. The secondary star usually is less massive than the primary, i.e. between $\sim 0.06\text{--}0.21 M_{\odot}$ (Warner, 1995) with a radius of the order of $\sim 0.15 R_{\odot}$ (Hellier, 2001).

In CVs, the components are close enough to each other so that the gravitational pull from the component closer to the centre of mass of the binary system, i.e. the white dwarf, draws material from the less massive component (the main sequence star), and energy is released through mass accretion to the white dwarf. Fig. 1.1 illustrates a typical CV with an accretion disc, where the larger red component corresponds to the secondary star, and the small blue component to the primary. Material transferred from the secondary component has to lose a significant amount of angular momentum before a disc formation around the white dwarf is possible.

At some point in their evolution, many binaries transfer matter from one companion to the other. Two main routes for mass transfer exist (Frank, King, & Raine, 2002):

- *Roche lobe overflow*: if the mass donating star comes into contact with its Roche lobe,

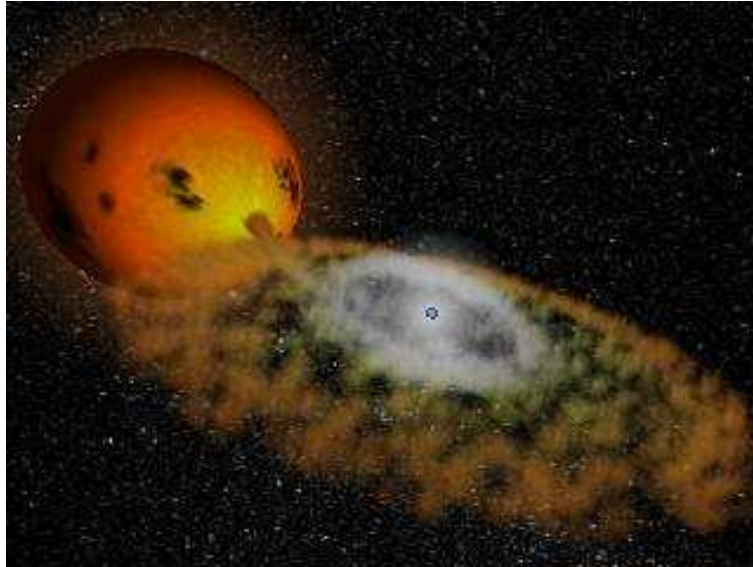


Figure 1.1: A cataclysmic variable. Credit: A. Beardmore, University of Leicester.

mass is transferred via the Lagrangian point L1 (the point which connects the Roche lobes of the primary and secondary stars, see e.g. Paczyński, 1971) to the Roche lobe of the mass accreting companion.

- *Stellar wind accretion*: at some point in its evolution, the other component ejects much of its mass via strong outflowing winds which is then captured by the companion star. This form of mass accretion is more important in binary systems with a massive, early-type secondary star (spectral class O or B), such as high-mass X-ray binaries (Charles & Seward, 1995).

Roche lobes which are equipotential surfaces have been illustrated in Fig. 1.2 (a): the Roche lobes of the binary components M_1 and M_2 are connected via the inner Lagrangian point L1 which is a saddle point for the Roche potential Φ_R . The locations of the Lagrangian points L2 and L3 are also shown in the figure. Fig. 1.2 (b) illustrates a cross-section of the Roche potential through the Lagrangian points L1, L2 and L3 and the component masses M_1 and M_2 . The Lagrangian points are equilibrium points where the gravitational forces of M_1 and M_2 are balanced by the centrifugal force. These points are unstable as a slight displacement of material located on the hilltops of the Lagrangian points will cause the material to accelerate

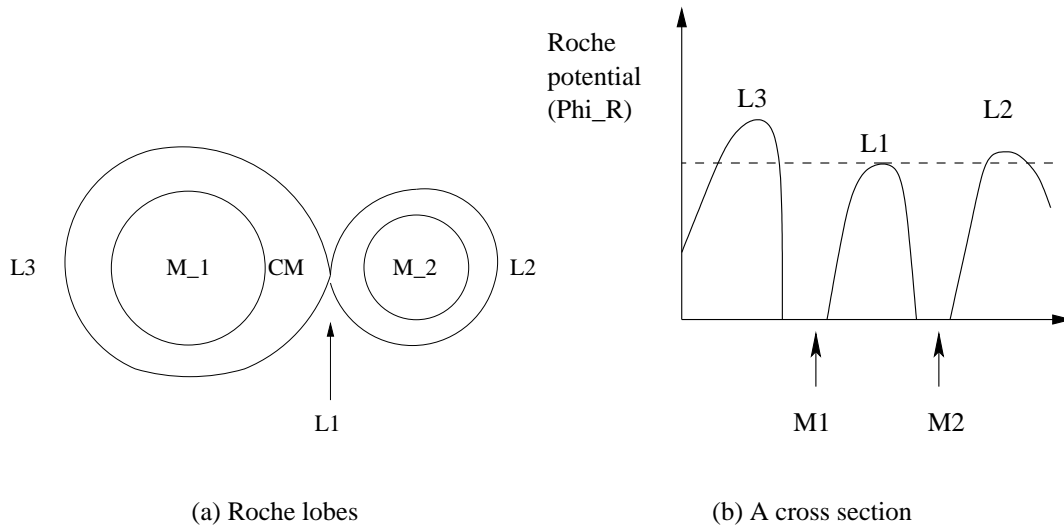


Figure 1.2: (a) A contour plot illustrating the Roche lobes of M_1 and M_2 connected via L1. CM corresponds to the centre of mass. The figure also shows the locations of the L2 and L3 points. (b) A cross-section of the Roche potential where M_1 and M_2 are located on the x-axis, whereas the y-axis corresponds to the Roche potential Φ_R . The dashed line describes the value of Φ_R at the Lagrangian point L1.

downhill away from the equilibrium.

In short period binary systems, such as CVs, accretion takes place via Roche lobe overflow (Frank, King, & Raine, 2002). This is because in short period systems, the secondary comes into contact with its Roche lobe via orbital angular momentum loss, decreasing the binary orbit, and thus shrinking the Roche lobe of the secondary star. In long period systems, mass transfer takes place when the secondary expands and evolves into a giant, and eventually fills its Roche lobe. However, in short period systems the Roche lobe is too small to accommodate such a large star, and thus orbital angular momentum loss via gravitational radiation must operate in order to keep the secondary in contact with its Roche lobe and therefore drive the mass transfer. In short period systems, the mass transfer operates under the stable mass transfer requirement, where the mass ratio $q = M_2/M_1 < 5/6$ (Warner, 1995; Frank, King, & Raine, 2002), where M_2 and M_1 are the secondary and primary masses, respectively.

If the envelope of the secondary, which has filled its Roche lobe, lies close to the L1 point,

any perturbation, such as the pressure of the secondary star's atmosphere, pushes the material over the L1 point to the Roche lobe of the primary component. In the absence of collisions, the mass from the secondary will follow an elliptical orbit. Eventually, the material impacts itself and circularises at a radius called the *circularisation radius*. This is the radius where the material has the same amount of angular momentum as the material at the L1 point. Some unknown physical mechanism (possibly magnetic) redistributes angular momentum within the gas. In order to conserve angular momentum, the material further away from the white dwarf must move outward to larger orbits, and the material closer to the white dwarf must move inward. Thus, the material spreads out into a thin disc. As the material from the secondary flows in, it will eventually be accreted by the white dwarf. An accretion disc has formed. The angular momentum transport mechanism is dissipative and heats the disc material. When the stream of material from the secondary star hits the edge of the accretion disc at supersonic speed, it creates a shock-heated region known as the *bright spot* (or the hot spot) (Warner, 1995).

1.2.2 Sources of X-rays and EUV emission

When the accreting material reaches a region between the white dwarf surface and the inner disc, i.e. the *boundary layer* where the speed of the accreting material is decelerated to the equatorial speed of the white dwarf (Warner, 1995) (which is presumed to be rotating more slowly), the material is accreted by the white dwarf and in this process X-rays are produced. As the gas is accreted, it forms a shock front above the white dwarf photosphere. At the shock front, the wavelength of the radiated luminosity depends on the optical depth of the boundary layer:

- If the boundary layer is optically thick, after thermalising through the boundary layer, the bulk of the radiated luminosity is expected to be emitted in the soft X-ray and extreme-ultraviolet (EUV) regions. According to Charles & Seward (1995), most of

the energy is emitted as ultraviolet lines below 1×10^6 K (< 100 eV), and at 2×10^6 K (~ 200 eV) half of the energy is seen as soft X-rays. This condition applies to high mass accretion rate CVs with $\dot{M} \gtrsim 10^{16}$ g s $^{-1}$ (Patterson & Raymond, 1985).

- If the boundary layer is optically thin, such as for low mass accretion rate CVs ($\dot{M} \lesssim 10^{16}$ g s $^{-1}$, Patterson & Raymond, 1985), the radiation escapes directly from the shock front. The shock front is thought to expand and form a hot diffuse optically thin corona where cooling takes place through free-free (bremsstrahlung) radiation above 1×10^7 K (> 1 keV, where all energy is radiated as X-rays Charles & Seward, 1995).

1.2.3 The sources of emission at other wavelengths

Emission from CVs is also seen at wavelengths other than X-rays. In most CVs, the optical and infrared spectra show characteristic emission lines from low ionization states, such as HI, HeI, FeII and OI with a blend of more ionized species of CIII, OII and NIII at 4640–4660 Å emanating from the accretion disc (Warner, 1995). Although, the emission can almost entirely be dominated by the bright spot (Warner, 1995). Optically thick discs, in particular discs of low inclination, show broad shallow absorption lines of HI, HeI and CaII. The white dwarf, which is a close approximation to a blackbody, is seen as hot and blue in the ultraviolet (~ 900 – 2000 Å) with emission lines (e.g. DN observations of Sion et al., 2004; Urban & Sion, 2006), but also contributes in the optical. The atmosphere of the cooler secondary star is seen in the red and infrared (IR). The IR spectrum of the secondary star is dominated by absorption due to the titanium oxide (TiO) molecule between 6000 and 8000 Å (e.g. the quiescence spectrum of U Gem, Stauffer, Spinrad & Thorstensen, 1979). It is unlikely that the secondary stars in CVs would contribute a detectable amount of X-ray flux (Rucinski, 1984; Eracleous, Halpern, & Patterson, 1991a,b). Also, the cooler outer regions of the disc ($T \sim 5000$ K) are seen in the infrared.

1.2.4 The motivation for studying CVs

CVs provide an excellent nearby laboratory for studying accretion disc physics, or accretion under the influence of magnetic fields (magnetic CVs). Studying accretion disc physics in CVs also helps us to understand the disc physics of other accreting objects in the Galaxy, such as X-ray binaries, accreting young stellar objects (FU Orionis stars), or distant objects, such as AGNs. In addition, CVs are considered as progenitors of Type Ia supernovae which are used as cosmological distance indicators. The Type Ia supernovae are the most commonly observed supernovae (Wheeler, 1991), and are believed to be born as a result of the explosion of a white dwarf whose mass exceeds the Chandrasekhar mass limit $1.44 M_{\odot}$. Recurrent novae, a subtype of CVs (see Section 1.2.5 for a definition), have primary masses close to the Chandrasekhar limit, and thus are considered as strong candidates for Type Ia progenitors (e.g. MacDonald, 1984).

It is also worth mentioning their role in understanding stellar evolution in the presence of another companion. Studying luminous CV phenomena, i.e. outbursts and eruptions of these systems can help us to understand the accretion disc structure and physical conditions leading to eruptions. A comparison between studies of white dwarfs in CVs and isolated white dwarfs can give clues as to the accretion processes in CVs, if differences between the CV white dwarfs and isolated white dwarfs are seen. Studying the CV white dwarf temperatures can yield important information concerning both age and accretion physics (Sion, 1999).

Finally, CVs enable direct measurements of system parameters, such as their component masses. These can be estimated through radial velocity measurements of both binary components and the inclination of the system (see Cropper (1990) and references therein). The radial velocities of the primary and secondary stars can be obtained from spectroscopic observations of these components (Hilditch, 2001). However, the inclination can only be measured reliably in eclipsing binaries (Warner, 1995). Orbital periods can be measured using time-resolved spectroscopy (radial velocity measurements) or photometry (light curve eclipses)

(Gänsicke et al., 2009). Once the orbital period P_{orb} and the component masses are known, the distance a (the semimajor axis) between the components can be calculated using Kepler's third law

$$P_{orb} = \sqrt{\frac{4\pi^2 a^3}{G(m_1 + m_2)}}. \quad (1.11)$$

1.2.5 The CV family: CV classification

According to Warner (1995), CVs have been divided into the following groups: a) *intermediate polars* (IPs), b) *polars*, c) *dwarf novae* (DNe), d) *classical novae* (CNe), e) *recurrent novae* (RNe), and f) *nova-like variables* (NLs). Nova eruptions are believed to take place through thermonuclear runaways where the accreted material deposited on the surface of the white dwarf undergoes an explosive degenerate detonation. When a CN is seen to erupt for a second time, it is classified as a RN. A famous example of a RN is RS Oph, which has had several eruptions in the past, the latest one occurring in 2006 (Sokoloski et al., 2006). DNe are objects with large outburst amplitudes and have been divided into several subclasses based on the outburst behaviour. Their outbursts are due to episodes of increased accretion rate. NLs are pre-novae in which neither nova nor DN eruptions have been observed, and which have optical spectra with emission lines of a typical CV. Finally, in magnetic CVs, i.e. polars and IPs, the magnetic field strength of the white dwarf is strong enough ($B \sim 10\text{--}200$ MG, Ramsay & Cropper, 2004) to disrupt the accreting material from forming a disc (polars) or part of it (IPs).

In this thesis I have studied only two types of CVs: polars and DNe. I will focus on introducing these two groups and their typical characteristics in more detail in Sections 1.2.7 and 1.2.8).

1.2.6 CV evolution in a nutshell

In general, stars are believed to form when a cloud of interstellar gas or dust collapses under its own gravity. The mass of the cloud has to be higher than a limiting mass (known as the Jean's mass) in order for the cloud to collapse under its own gravity. Large, massive clouds form star clusters where individual stars are born close to other individual stars, thus forming binaries, or even more complex systems.

CVs are thought to originate from wide binaries with orbital periods of $\gtrsim 1$ yr (Patterson, 1984). The initial separation of the components is several AUs (Charles & Seward, 1995), where $1 \text{ AU} = 1.5 \times 10^8 \text{ km}$. Due to the angular momentum inherited from the original gas cloud, it is not possible to form a close binary system without first losing a significant amount of angular momentum. Also, the white dwarf progenitor was assumed to be a red giant before the Roche lobe contact, thus requiring larger binary dimensions (Kolb, 2002).

Initially, the binary components are main sequence stars, but usually the other component is more massive, and thus will evolve faster than the lighter component. The more massive star evolves into a red giant, a dynamically unstable mass transfer takes place to the lighter, unevolved secondary, and eventually the whole envelope of the giant is ejected on to the companion star. As this event takes place, the degenerate core of the red giant is exposed. This *common envelope phase* was first suggested by Paczyński (1976), and is believed to be a possible evolutionary channel leading to a close binary system, such as a CV. During this phase, the separation between the binary components shrinks to $\sim 1 R_{\odot}$ in a timescale of 1000 years (Hellier, 2001). Eventually, the envelope is pushed into interstellar space due to energy extracted from the binary orbit, and in this process, a planetary nebula is formed. As a result, a detached white dwarf/red dwarf system is born; this will eventually shrink into Roche lobe contact due to angular momentum loss via gravitational radiation.

As was discussed in Section 1.2.1, a short-period binary has to lose angular momentum in

order to transfer mass between the components (Frank, King, & Raine, 2002). Therefore, the separation between the binary components and thus the Roche lobe of the secondary star, have to decrease. According to the current understanding, two main mechanisms exist to drive angular momentum loss: 1) *gravitational radiation* (Faulkner, 1971, 1976; Paczyński & Sienkiewicz, 1981) and 2) *magnetic braking* via a magnetically constrained stellar wind from the mass donor star (Eggleton, 1976; Verbunt & Zwaan, 1981). Angular momentum loss is thought to be driven by magnetic braking in the early phases of CV evolution corresponding to high mass transfer rates of $\dot{M} \sim 10^{-9} - 10^{-8} M_{\odot} \text{ yr}^{-1}$ and orbital periods of $3.3 \text{ h} < P_{orb} < 1 \text{ day}$, whereas below $P_{orb} \lesssim 3.3 \text{ h}$, the binary evolution to shorter periods is driven by gravitational radiation with low mass transfer rates of $\sim 10^{-11} - 10^{-10} M_{\odot} \text{ yr}^{-1}$ (Patterson, 1984). Patterson (1984) found that in close binary systems, the mass accretion rate strongly correlates with the orbital period: $\dot{M} \propto P_{orb}^{3.2}$.

Between orbital periods of $\sim 2-3 \text{ h}$, a so-called *period gap* exists. In this gap, the number of CVs drops. The lack of CVs in this gap is thought to be caused by disrupted magnetic braking (Pretorius, Knigge, & Kolb (2007) and references therein). As a CV approaches the upper limit of the period gap ($\sim 3 \text{ h}$), the structure of the secondary star changes: a transition from a deep convective envelope to a fully convective state at $\sim 0.3 M_{\odot}$ and at $P_{orb} \sim 2.5 \text{ h}$ takes place (see Spruit & Ritter (1983) and references therein). In this process, the magnetic field structure of the secondary is thought to change, and thus magnetic braking reduces. As a consequence, the mass transfer rate is reduced and the secondary allowed to shrink toward its thermal equilibrium radius, detaching from its Roche lobe. During this period of detachment, the mass transfer rate drops close to zero. In order to resume the mass transfer, the binary orbit has to decrease and thus bring the secondary back in contact with the Roche lobe. This reduction is effected by gravitational radiation, and subsequently at $P_{orb} \sim 2 \text{ h}$, this contact with the Roche lobe takes place and mass transfer recommences (Hellier, 2001).

From now on, gravitational radiation is responsible for continuation of angular momentum loss, mass transfer, and evolution of the binary to shorter periods. As the orbit shrinks,

the mass of the secondary star decreases, and at $P_{orb} \sim 80$ min, the secondary becomes partially degenerate when its mass drops below $0.1 M_{\odot}$ (Hameury et al., 1988a). ~ 80 min is the predicted minimum orbital period in CV evolution (Paczynski & Sienkiewicz, 1981; Rappaport, Joss, & Webbink, 1982). Following the period minimum, a CV starts to evolve back to longer periods, and the mass of the secondary has decreased even further: at $P_{orb} \sim 100$ min, after evolution through the minimum orbital period, the secondary mass is $\sim 0.02 M_{\odot}$ (Hellier, 2001). At this point, the gravitational radiation has decreased and the mass transfer rate has dropped to $\dot{M} \sim 4 \times 10^{-12} M_{\odot} \text{ yr}^{-1}$. Binaries at this evolutionary stage are faint and difficult to detect, and the secondary has shrunk to the size of a planet.

How do observations support the existence of the period minimum at ~ 80 min? CV population models have predicted that as CVs evolve towards shorter periods below 2 h, a period minimum spike, i.e. a significant accumulation of CVs, should be seen at around 78 min representing the period minimum (e.g. Kolb & Baraffe, 1999; Kolb, 2002). In addition, ~ 70 per cent of all Galactic CVs should have reached this period minimum (Kolb, 1993; Howell, Rappaport & Politano, 1997). However, for two decades CV observations did not agree with theoretical predictions since no accumulation, i.e. a spike, of known CVs near the period minimum was seen (e.g. Knigge, 2006). Observations have indicated instead a rather flat distribution with a sharp cut-off at ~ 78 min (King, Schenker & Hameury, 2002). However, recent *Sloan Digital Sky Survey* (SDSS) observations of intrinsically faint CVs by Gänsicke et al. (2009) revealed a significant accumulation of CVs between 80–86 min, which they identified as the period minimum spike predicted by the CV population models. This suggested that the known discrepancy between the CV evolution theory and observations had been resolved.

There does exist a subclass of CVs having orbital periods below even the period minimum (below 1 h, Nelemans et al., 2010). These are known as *AM Canis Venaticorum* (AM CVn) stars and consist of two degenerate components: a white dwarf or a neutron star primary (Nelemans et al. (2010) and references therein) and an evolved degenerate component, such

as a white dwarf, secondary. Only compact and evolved components can fit into such an ultracompact binary system, for which the orbital periods can be as short as ~ 5 min (RX J0806.3+1527, Israel et al., 1999; Beuermann et al., 1999). This is because the mean density of the Roche lobe filling secondary star is proportional to the inverse of the orbital period squared, i.e. $\rho(2) \propto P_{orb}^{-2}$. These ultracompact systems are thought to be strong gravitational radiation emitters. Currently, 26 AM CVn systems are known (Nelemans et al., 2010).

Since the discovery of the first AM CVn, HZ 29 (Greenstein & Matthews, 1957), a typical characteristic in the optical spectra of these objects has been the lack of H lines. However, AM CVns have been observed to be rich in He (Warner, 1995). Three evolutionary models have been suggested for the formation of AM CVns, and all models lead to a degenerate donor star (Nelemans et al. (2010); Roelofs, Nelemans, & Groot (2007) and references therein). For example, in one of the possibilities, the progenitor of the donor star is a non-degenerate He core burning star. Due to angular momentum loss by gravitational radiation, the binary evolves to shorter periods. The mass transfer rate is of the order of a few times $10^{-8} M_{\odot} \text{ yr}^{-1}$, and this stage of evolution lasts between 10^6 and 10^7 years (Nelemans et al., 2010). The orbital period minimum is reached at ~ 10 min and at this point, the secondary has become semi-degenerate. From now on, the binary will evolve back towards longer orbital periods.

1.2.7 Polars

Polars, or *AM Her* type systems (see an extensive review of polars by Cropper, 1990), are recognised by their linearly and circularly polarised optical light due to the presence of a strong magnetic field, and this is from where their name originates. The primary is a white dwarf with a magnetic field strength of $B \sim 10\text{--}200$ MG (Ramsay & Cropper, 2004), whereas the magnetic field strength of the Sun, $B_{\odot} = 1$ G. Another characteristic of polars is a strong soft X-ray emission component below $\lesssim 0.1$ keV. In the past, this has been considered as a

typical signature indicating the polar nature of some newly discovered CVs, but this is not always the case, as will be shown in Chapter 2. In general, polars are found to be both hard and soft X-ray, and EUV emitters.

The strong magnetic fields of polars enforce synchronous rotation, i.e. the spin period of the primary is equal to the orbital period of the system. Intermediate polars are thought to be strong candidates of polar progenitors (e.g. Cropper, 1990; Frank, King, & Raine, 2002). According to Chanmugam & Ray (1984), IPs will have sufficiently strong magnetic fields for the primaries to synchronise as they evolve to shorter periods (Frank, King, & Raine, 2002, the periods of IPs are $> 3\text{--}4$ h). Thus, IPs would become polars. The strong magnetic field in polars prevents the formation of an accretion disc, which is present in non-magnetic CVs, such as in DNe. Instead of a disc, an *accretion column* forms in which the material follows the magnetic field lines of the white dwarf to impact the white dwarf above the magnetic poles. This is illustrated in Fig. 1.3. The supersonically accreted gas forms a shock above the white dwarf photosphere. Below the shock region, the accreted gas cools within an optically thin post-shock region and flows down subsonically on to the white dwarf photosphere. The height of the shock region from the white dwarf surface is determined by the effectiveness of the cooling of the post-shock region. In steady state conditions, the energy deposited in the accretion column at a rate of L_{acc} must be removed at the same rate. If the removal of energy is less than L_{acc} , the gas in the post-shock region expands adiabatically and raises the height at which the shock forms. If the cooling is greater than L_{acc} , the shock region would move in towards the white dwarf surface decreasing the area of the post-shock column.

The photosphere of the white dwarf is irradiated by hard X-rays from the post-shock column. These hard X-rays form near the shock region where photon energies are $kT_{shock} \sim 60$ keV for a white dwarf with a mass of $M_1/M_\odot = 1$ and a radius of $R_9 = R_*/10^9$ cm = 0.5 (Frank, King, & Raine, 2002). The shock and the post-shock regions cool through X-ray (bremsstrahlung and Compton scattering of lower energy photons by energetic, shocked electrons), and strongly polarised optical and infrared cyclotron radiation. A simple model of an accretion column

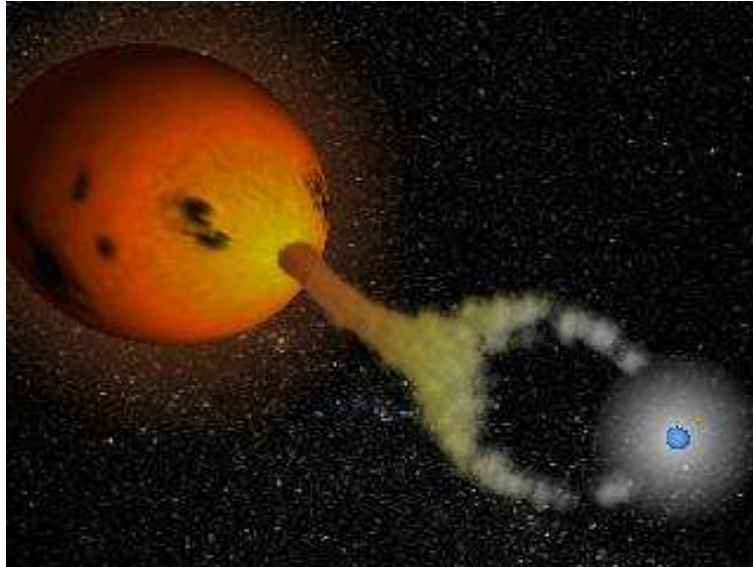


Figure 1.3: An AM Her type system. Credit: A. Beardmore, University of Leicester.

formed above the white dwarf surface with emitted radiation is shown in Fig. 1.4 assuming that the plasma is uniform across the column.

The white dwarf mass determines the shock temperature T_{shock} : the more massive the white dwarf, the higher the shock temperature. Compton cooling is most effective when the electron temperature of the post-shock gas is high and the electron density low. Thus, the best conditions for Compton cooling are closest to the shock region. But, Compton cooling is only significant, if the mass of the white dwarf is large, i.e. $M_1 \sim 1.4 M_{\odot}$. In most cases, bremsstrahlung emission is considered to be the dominant radiative cooling mechanism in the post-shock column. Some fraction of the post-shock column X-rays are absorbed by the white dwarf photosphere and re-emitted as soft X-ray (and EUV) radiation at a temperature of $\lesssim 0.1$ keV. For typical accretion rates of $\dot{M} \lesssim 10^{16} \text{ g s}^{-1}$, the re-emitted luminosity is of the order of $10^{33} \text{ erg s}^{-1}$ (Frank, King, & Raine, 2002).

What fractions of the X-rays are emitted as hard and soft X-rays? The standard model of the shock region by Lamb & Masters (1979) predicts that the energy balance of the emitted blackbody and hard X-ray luminosities is $L_{bb}/L_{shock} \sim 0.56$. However, *EXOSAT* observations of polars in 1983–1986 showed that a number of polars had a large 'soft X-ray excess'. These

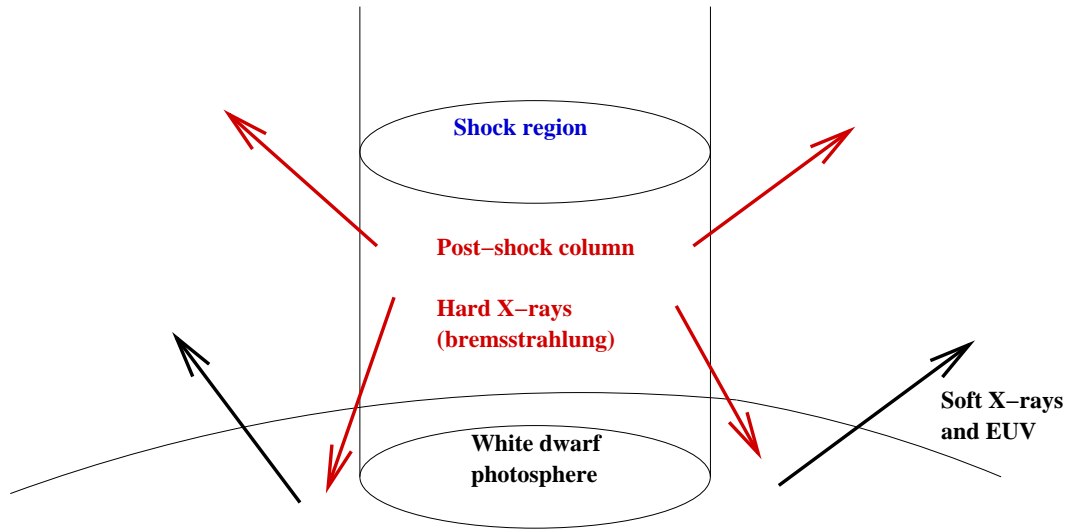


Figure 1.4: A simple model of an accretion column above the white dwarf surface.

results were supported by *ROSAT* observations by Ramsay et al. (1994) and Beuermann & Burwitz (1995). However, more recent *XMM-Newton* observations of 37 polars, in addition to a re-analysis of the *ROSAT* PSPC observations of the polar sample from 1994, showed that the vast majority of the sources had a low soft X-ray excess, consistent with the standard accretion model (Ramsay & Cropper, 2004). In the past, several models have been suggested to account for the soft X-ray excess. The widely accepted model is the so-called 'blobby' accretion model which was first suggested by Kuijpers & Pringle (1982) (see also Frank, King, & Lasota, 1988). In this model, dense blobs of material penetrate deep into the photosphere of the white dwarf, depositing all of their kinetic energy deep in the photosphere. Thus, the accretion energy would be released as X-rays, thermalised in the photosphere, and finally emitted as soft X-rays, giving rise to a soft X-ray excess.

1.2.8 Dwarf novae

Dwarf novae (DNe) consist of a white dwarf primary, a late-type main sequence secondary star and an accretion disc. In a DN, the white dwarf has a weak magnetic field ($B \lesssim 10^6$ G, van Teeseling, Beuermann, & Verbunt, 1996). The known DNe are relatively nearby sources

with distances to known systems varying between $\sim 40\text{--}900$ pc. The orbital periods of DNe are typically between ~ 70 min and 10 h. On timescales of a few weeks to a few months, or even years, the disc in DNe goes into an outburst during which the system brightens by $\sim 2\text{--}9$ magnitudes in the optical wavelength, and this can last from days to several weeks. The main source of optical emission during an outburst is the accretion disc. After this luminous phenomenon, the system returns to quiescence which usually lasts from ~ 10 days to weeks and in a few systems even decades. In quiescence, the optical emission is usually dominated by the bright spot (Mukai, Zietsman, & Still, 2009). Also, the photosphere of the primary contributes substantially at optical wavelengths during quiescence (Warner (1995) and references therein). Quiescent optical spectra of DNe are characterized by a blue continuum with strong Balmer emission lines and weaker HeI lines with some heavier elements. DNe are also sources of hard X-rays which originate from an optically thin boundary layer. In an outburst, the inner region of the disc, i.e. the boundary layer becomes optically thick and a source of soft X-rays and EUV emission (Pringle, 1977; Pringle & Savonije, 1979).

DNe are classified into three sub-groups depending on their outburst behaviour (Warner, 1995). The main DN groups are *SU UMa*, *U Gem*, and *Z Cam* stars. Confirming the type of a DN requires continuous and long-term monitoring in the optical due to irregularities in their outburst behaviour even within one system. For example, *U Gem*-type outbursts occur on timescales of a few weeks to a few months, whereas *SU UMa* stars show normal *U Gem*-type DN outbursts and, in addition, *superoutbursts* with superhumps (variations in the light curves at a period of a few per cent longer than the orbital period) on timescales of several months to years. A defining feature of superoutbursts is a plateau phase in the optical light curve lasting for several days, thus superoutbursts are larger than normal DN outbursts. Superhumps are thought to be caused by a 3:1 resonance in the accretion disc (Whitehurst, 1988): the 3:1 resonance develops in an eccentric disc where the outer disc material orbits three times for every orbital cycle for systems with a mass ratio $q \lesssim 0.33$. The extreme cases of the *SU UMa* class, the *WZ Sge* stars, only have superoutbursts with outburst timescales of decades without normal DN outbursts. The defining characteristic for *Z Cam* stars is standstills, i.e. *Z Cam*

stars may not return to the minimum magnitude after an outburst (unlike U Gem stars) but remain between the minimum and maximum magnitudes for between 10 and 40 days. Observations have shown that the orbital periods of SU UMa stars are mainly below 2 h, whereas for U Gem and Z Cam stars the orbital periods are > 3 h.

The mechanism leading to a DN outburst is thought to be a *disc instability*, first proposed by Hoshi (1979) (for a more detailed discussion see Lasota, 2001). The α *prescription* and the *Balbus-Hawley instability* are helpful concepts in understanding the disc instability. The α prescription was developed by Shakura & Sunyaev (1973) to parameterise viscosity in accretion discs which are too diffuse for molecular viscosity to explain the disc behaviour. According to accretion theory, discs are assumed to be turbulent where blobs of material are exchanged between adjacent disc annuli, and thus angular momentum transfer between the annuli would act as viscosity. Shakura & Sunyaev (1973) suggested that the viscosity ν in a disc can be derived from

$$\nu = \alpha c_s H, \quad (1.12)$$

where c_s is the speed of sound (the speed of a gas molecule), H the scale height of the disc, and α has a value less than 1, and is higher in the hot state (outburst) than in the cold state (quiescence) of a DN. A more physically motivated theory of disc viscosity was made by Balbus & Hawley (1991) who developed a theory of magnetic instabilities. The Balbus-Hawley magnetorotational instability (MRI) is the driving force of the turbulent disc described by Shakura & Sunyaev. According to the MRI theory, a magnetic field is created in a hot and ionised disc. As the magnetic field lines connect two neighbouring disc annuli of material, the field lines are stretched because the inner annulus orbits faster than the outer one. In this process, the inner annulus loses angular momentum, slows down and moves inwards, whereas the outer annulus gains angular momentum, speeds up and moves outwards. This way angular momentum is transported outwards from the disc which is required in order to

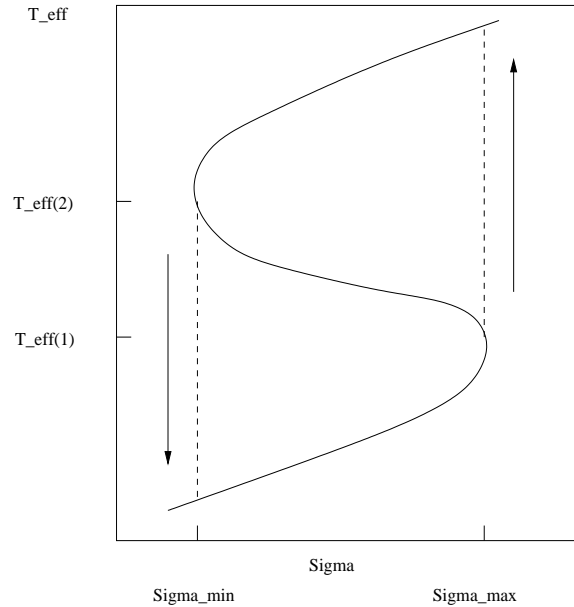


Figure 1.5: The effective temperature T_{eff} versus surface density Σ diagram (the "S-curve"). The disc cycles between the lower (lower branch) and upper (upper branch) equilibrium states.

enable accretion. Stretched magnetic field lines amplify the magnetic field strength and eventually, the result in the disc is a magnetic turbulence, where field lines are stretched, broken and new magnetic loops are created.

In order for a DN outburst to take place, the disc has to be switched from a cold, low viscosity state to a hot, high viscosity state. The hot state is characterised by the partial ionisation of hydrogen which takes place at ~ 6500 K. When the disc contains enough material, the temperature rises and finally at ~ 6500 K, partial ionization of hydrogen takes place. This is when the MRI instability starts to operate; when the material is ionized, the electric field of the free electrons create magnetic fields.

The disc instability (DI) theory, which is the foundation of the outburst theory of DNe, is based on an annulus which moves from a lower temperature and surface density equilibrium state to a higher equilibrium state (Fig. 1.5). When a thermally unstable annulus heats up, it triggers the instability of the surrounding annuli and sends heating pulses inwards and outwards in the disc. This process takes place as a result of the disc filling up with accreted

material from the secondary: the surface density Σ increases, and thus the effective temperature T_{eff} increases. At $T_{eff}(1)$, hydrogen ionises partially, and the surface density stays constant due to the short thermal timescale as the disc moves to the upper equilibrium state with rising T_{eff} . In this process, the viscosity increases. Once the temperature reaches the upper branch in Fig. 1.5, hydrogen is fully ionised and a higher inflow of material in the disc takes place due to higher viscosity. A reverse process starts when the material inflow is much greater than the flow of material from the secondary star: thus the surface density decreases as a function of the disc radius to Σ_{min} with decreasing temperature, and as a result a cooling front propagates through the disc from the outer to the inner disc. At Σ_{min} , hydrogen becomes partially ionised again, temperature drops, viscosity decreases, and the disc returns to quiescence.

1.3 The space-based observatories XMM-Newton, Swift and Suzaku

In the following, I briefly describe the *charged-coupled device*, the instrument commonly used for astronomical observations, and following this, the three major space-based X-ray observatories, *XMM-Newton*, *Swift* and *Suzaku*, which have provided the data for the research in this thesis. Table 1.1 compares some of the technical characteristics of the X-ray telescopes introduced in Sections 1.3.2, 1.3.3, and 1.3.4.

1.3.1 Charged-Coupled Device

A charged-coupled device, i.e., a CCD, is used for various purposes, such as in everyday digital imaging. More importantly, it is used as an astronomical device to carry out imaging, photometry, spectroscopy, or astrometry. In this respect a CCD has advantages over photo-

Table 1.1: The technical characteristics of the X-ray telescopes of *XMM-Newton*, *Swift* and *Suzaku*. The spectral resolution given for each instrument is the resolution at the time of launch. The last three columns give the spectral resolution, the effective area, and the field of view (FOV).

Instrument	Bandpass keV	Spectral res. eV	Eff. area cm ²	FOV arcmin
pn/XMM	0.1–15	~ 150 (@ 6.4 keV)	1227 (@ 1 keV)	30
MOS/XMM	0.1–12	~ 150 (@ 6.4 keV)	922 (@ 1 keV)	30
XRT/Swift	0.2–10	~ 140 (@ 5.9 keV)	110 (@ 1.5 keV)	23.6
XIS/Suzaku	0.2–12 (XIS1)	~ 130 (@ 6 keV)	390 (@ 1.5 keV)	18
	0.4–12 (XIS0,2,3)		340 (@ 1.5 keV)	

graphic plates, as a CCD has a high quantum efficiency (the ratio of the incoming photons over the photons actually detected), a large dynamic range, and linearity of response. A comprehensive introduction to CCDs is given by Howell (2006) which has been used as the main source of information for this sub-section. The basic operating principle of CCDs is based on photoelectric absorption: incident photons are absorbed by a silicon lattice within the CCD pixels, and the silicon releases photoelectrons. These photoelectrons are then held in place by the gate structures located in the pixels until readout. The gate structures can be set to different voltage potentials. Thus, at the end of the exposure, electrons are read out electronically by cycling the voltages associated with the gate structures.

An X-ray CCD differs from an optical CCD in that in an X-ray CCD, silicon releases a fast moving high-energy photoelectron of energy $E - b$, where $E = h\nu$ is the photon energy and b the binding of the electron to the silicon atom. Typically the binding energy is 1780 eV. This high-energy electron produces electron-hole pairs as it moves through the silicon lattice: the higher the energy of the incident photon, the more electron-hole pairs are produced. Thus, the number of photoelectrons produced gives an indication of the energy of the incident photon.

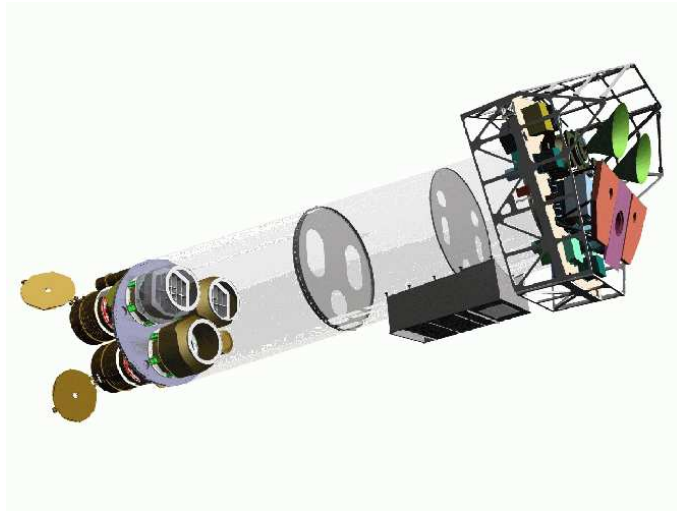


Figure 1.6: A sketch of *XMM-Newton* obtained from the *XMM-Newton* Users Handbook.

1.3.2 XMM-Newton

XMM-Newton (Jansen, Lumb & Altieri, 2001) is the cornerstone mission of the European Space Agency (ESA). *XMM-Newton* has been operating since 1999, and its main scientific objectives have been investigation of the spectra of cosmic X-ray sources at a flux limit of 10^{-15} erg cm $^{-2}$ s $^{-1}$, broad band imaging spectroscopy between 0.1–15 keV, sensitive medium resolution spectroscopy over 0.35–2.5 keV with $R \sim 100$ –700, and simultaneous optical/ultraviolet observations with the co-aligned optical monitor. *XMM-Newton* carries three Wolter-I type X-ray telescopes with the X-ray detectors, the European Photon Imaging Cameras (EPIC pn, Strüder et al. (2001), MOS1 and MOS2, Turner et al. (2001)), in their foci. In addition to the X-ray telescopes, *XMM-Newton* houses the Optical/Ultraviolet Monitor (OM, Mason et al., 2001a) and the Reflection Grating Spectrometer (RGS, den Herder et al., 2001). Fig. 1.6 shows a sketch of *XMM-Newton* where the EPIC instruments have been located on the right hand end of the telescope, and the RGSs on the left. The OM telescope is obscured by the lower mirror module. The X-ray telescopes onboard *XMM-Newton* have the largest effective area of a focusing X-ray telescope ever built: for each telescope, the total mirror effective area at 1.5 keV is ~ 1550 cm 2 , thus giving 4650 cm 2 in total.

EPIC pn and MOS

The EPIC pn and MOS are X-ray imaging detectors which operate in the energy range of 0.15–15 keV (pn) and 0.15–12 keV (MOS). The spectral resolution of the EPIC CCD cameras is moderate with a resolving power of $E/\Delta E \sim 20\text{--}50$. The EPIC CCDs operate in photon counting mode with a fixed frame read-out frequency producing event lists containing the information of the photon events, such as position, arrival time and energy.

Some of the differences between the EPIC pn and MOS instruments are in their geometries and effective areas. Each MOS instrument consists of 7 front-illuminated (FI) CCDs (600x600 pixels each) located in the focal planes of the instruments, whereas the pn consists of 12 CCDs integrated on a single wafer of 400x400 pixel matrix with an area of 36 cm²: this is the largest X-ray CCD detector ever flown. The effective area of the pn is slightly larger than the total effective area of the MOS instruments (see Table 1.1 for the peak effective areas). For both instruments, the effective areas vary slightly below ~ 2 keV depending on the optical blocking filter used (for example, the 'Medium' filter is used to prevent optical contamination from point sources with magnitudes $m_V = 6\text{--}9$). Fig. 1.7 illustrates the on-axis *XMM* effective area for the EPIC and RGS instruments.

The data acquisition of the EPIC cameras can be done in several science modes which determine how the CCDs are read out. The most commonly used mode is the 'full frame' mode where all the pixels of all CCDs are read out, covering the full FOV. The other science modes are extended full frame (only for pn), partial window and timing modes. In the extended full frame mode, the image collection time (the frame time) is longer (199.1 ms) than in the full frame mode (73.4 ms). In the partial window mode, only some of the CCDs are read out. For example, for pn in large window mode (a submode of the partial window mode), only half of the area of all CCDs is read out, whereas for the MOS cameras in the partial window mode, only parts of the central CCDs chips are read out (in large window mode 300x300 pixels and in small window mode 100x100 pixels). The timing mode is for 1-dimensional

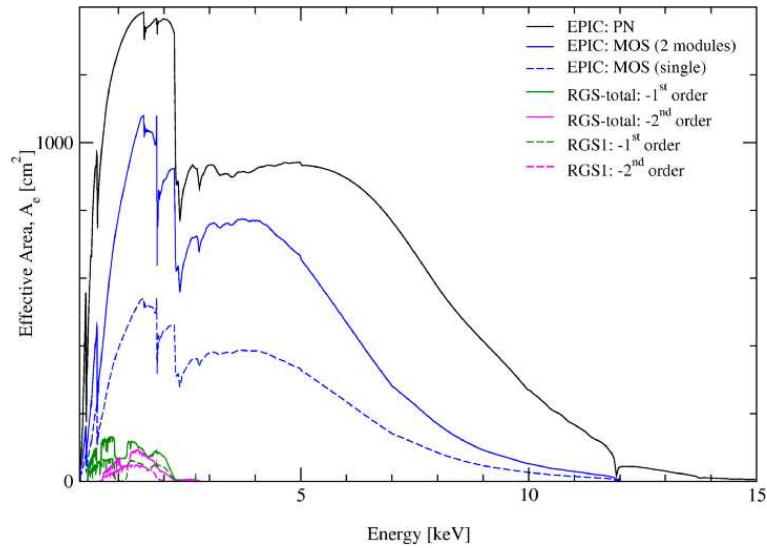


Figure 1.7: The net effective areas of all *XMM-Newton* X-ray telescopes in linear scale (Source: *XMM-Newton* Users Handbook).

imaging. Under this mode, pn can also operate in a so-called burst mode, which has a high time resolution ($7\mu\text{s}$) and is suitable for high-speed photometry of rapidly variable targets. The use of the modes depends on the science to be carried out, for example, for the full frame mode, the maximum defined point source count rate to avoid deteriorated response due to photon pile-up (see Chapter 2 for more discussion on pile-up) is 6 ct s^{-1} ($0.7 \text{ mCrab} = 1.7 \times 10^{-11} \text{ erg cm}^{-2} \text{ s}^{-1}$). In this thesis, most of the *XMM* observations have been obtained in the full frame mode.

The Optical/Ultraviolet Monitor

The *XMM* OM (Mason et al., 2001a) is a 30 cm modified Ritchey-Chrétien telescope, housing a 256×256 pixel CCD detector coupled to a micro-channel plate (MCP) intensifier, with a focal length of 3.8 m. The wavelength coverage is from 170 to 600 nm and the field of view of the telescope is 17×17 arcmin. The incoming photon events are centroided to 1/8th of a CCD pixel to give a sampling element of 2048×2048 centroided pixels on the sky. The limiting sensitivity of the *XMM* OM is 24 magnitudes for a star of spectral type B in white

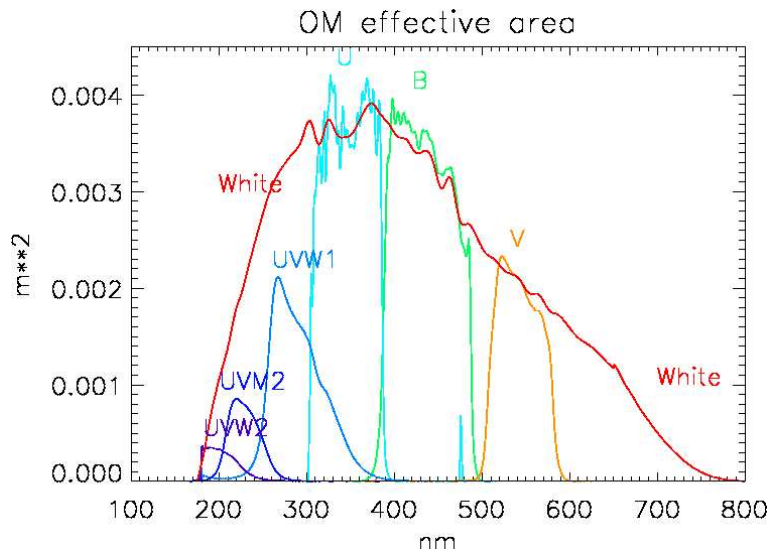


Figure 1.8: *XMM-Newton* OM effective area with the broad band filter passbands (*XMM-Newton* Users Handbook).

light filter.

The OM contains 6 broad band filters UVW2, UVM2, UVW1, U, B, and V, a 'white' light filter, and in addition 2 grisms (UV and V) to provide low resolution spectroscopy in the near ultraviolet and in the visible wavelength. Fig. 1.8 illustrates the OM effective area and the broad band bandpasses.

1.3.3 Swift

The multiwavelength observatory, the *Swift* Gamma-Ray Explorer (Gehrels et al., 2004), was launched on November 20th, 2004, and is a NASA medium-sized explorer mission. It was designed to make prompt multiwavelength observations of Gamma-Ray Bursts (GRBs). The main science goals are to determine the origin of GRBs, the classification of GRBs and the search for new types, to use GRBs to study the early universe, and the interaction of the GRB outflows with the surrounding medium. *Swift* rapidly responds to a detected GRB and disseminates the data on timescales of a few minutes to a few hours.

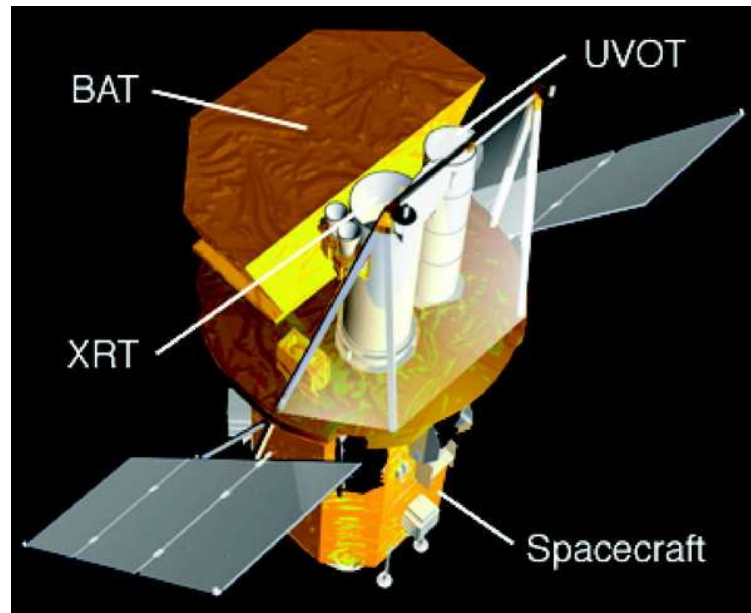


Figure 1.9: *Swift* satellite (Gehrels et al., 2004).

Swift carries three instruments (Fig. 1.9): the X-ray Telescope (XRT, Burrows et al., 2005), the Ultraviolet/Optical Telescope (UVOT, Roming et al., 2005), and the Burst Alert Telescope (BAT, Barthelmy, 2004). The energy range of the BAT and the XRT are 15–150 and 0.2–10 keV, respectively, whereas the UVOT operates in the wavelength range of 170–600 nm. Together, these three co-aligned instruments enable finding of GRB positions rapidly with a few arcsecond accuracy. They are able to measure the spectra and light curves of the GRB prompt emission and its afterglow. In addition to GRBs, *Swift* is also used for observing other high-energy sources, such as CVs.

The X-ray Telescope

The *Swift* XRT, which is an autonomous and sensitive X-ray imaging spectrometer, has been designed to measure fluxes, light curves, and afterglows of GRBs. It also provides accurate positions for GRB bursts with an accuracy better than 5 arcseconds, moderate resolution spectroscopy and light curves with high timing resolution. The XRT telescope uses grazing incidence Wolter-I type telescope which focuses the X-rays onto a detector, which is a cooled

CCD. The focal length of the telescope is 3.5 m, and the total mirror effective area 133.5 cm² at 1 keV.

The *Swift* XRT operates in two states: Auto and Manual; the Manual state is used for commanding a fixed science mode for a given observation and calibration. The Auto state, which is the normal operating state, automatically selects the science mode depending on the source count rate. These science modes are (for both Auto and Manual states): 1. Image Long and Short (IM), 2. Photodiode (PD which is not currently in use), 3. Windowed Timing mode (WT), and 4. Photon Counting mode (PC). The PD mode was designed for high time resolution (0.14 ms) and for very bright sources (0.6–60 Crab), whereas the IM mode is used for obtaining a rapid position of a new GRB. In the WT mode, the image is compressed into 1-dimension and used for fluxes above 2×10^{-14} erg cm⁻² s⁻¹ (1–600 mCrab) with a time resolution of 1.7 ms. Finally, the PC mode is used for fluxes below 1 mCrab (2×10^{-14} erg cm⁻² s⁻¹) with a time resolution of 2.5 s. If the source becomes too bright for the PC mode in the Auto state, the XRT switches into the WT mode in order to avoid pile-up.

The Optical/Ultraviolet Telescope

The Optical/Ultraviolet Telescope (UVOT), which is co-aligned with the XRT, is based on the *XMM-Newton* OM although a few changes were incorporated into the Optical/Ultraviolet Telescope (UVOT), such as straylight elimination outside the field of view and significantly improved sensitivity compared to the OM (for more details see Roming et al., 2005). Thus, see Section 1.3.2 for more information on the technical details which also apply to *Swift* UVOT. The UVOT sensitivity is B = 24 mag in the white light filter in 1000 s. The science goals of the UVOT have been detecting early light of GRBs, and rapid afterglow follow-up and determination of GRB positions. The *Swift* UVOT will be discussed more in Chapter 3, focusing on the *Swift* UV grism.

1.3.4 Suzaku

Suzaku (Mitsuda et al., 2007), originally *Astro-E2*, was launched in 2005 and is Japan's 5th X-ray astronomy mission. Some of the main scientific objectives of *Suzaku* are studies of hot plasmas in various X-ray sources, the structure and evolution of the universe and wide band spectroscopy of black hole candidates and AGNs.

Suzaku carries five light-weight Wolter-I type X-ray Telescopes (XRTs) (Serlemitsos et al., 2007) onboard (Fig. 1.10). Of these telescopes, four are dedicated to the X-ray Imaging Spectrometer (XIS, Koyama et al., 2007) consisting of four sensors XIS0,1,2,3 (XRTI0-I3 in Fig. 1.10), the non-imaging Hard X-ray Detector (HXD, Takahashi et al., 2007), and the X-ray Spectrometer (XRS, Kelley et al., 2007) which has not been used for observations. The focal length of the XRT telescopes is 4.75 m and the total mirror effective area of the four XRT telescopes containing the XIS instruments is 1760 cm² at 1 keV. Together, the XIS and HXD cover the energy range 0.2–600 keV. Since November 9, 2006, the XIS2 unit has not been available for observations.

The XIS

The XIS sensors XIS0,2,3 contain front-illuminated (FI) CCDs and the XIS1 a back-illuminated (BI) CCD. Each sensor has a single MOS type CCD chip where the imaging area is 1024 x 1024 pixels. The sensors have a moderate energy resolution (130 eV @ 5.9 keV) and low background of charged particles. Since the XIS0,2,3 CCDs have a Si and SiO₂ gate structure on the front side of the CCD chip, they are less sensitive to soft X-rays (below 1 keV) than XIS1.

The XIS instruments operate in two clocking modes: the normal and the P-sum modes of which the normal mode produces a 2-dimensional CCD image and is the most frequently used mode for X-ray observations (also used in the *Suzaku* observations in Chapter 4), whereas

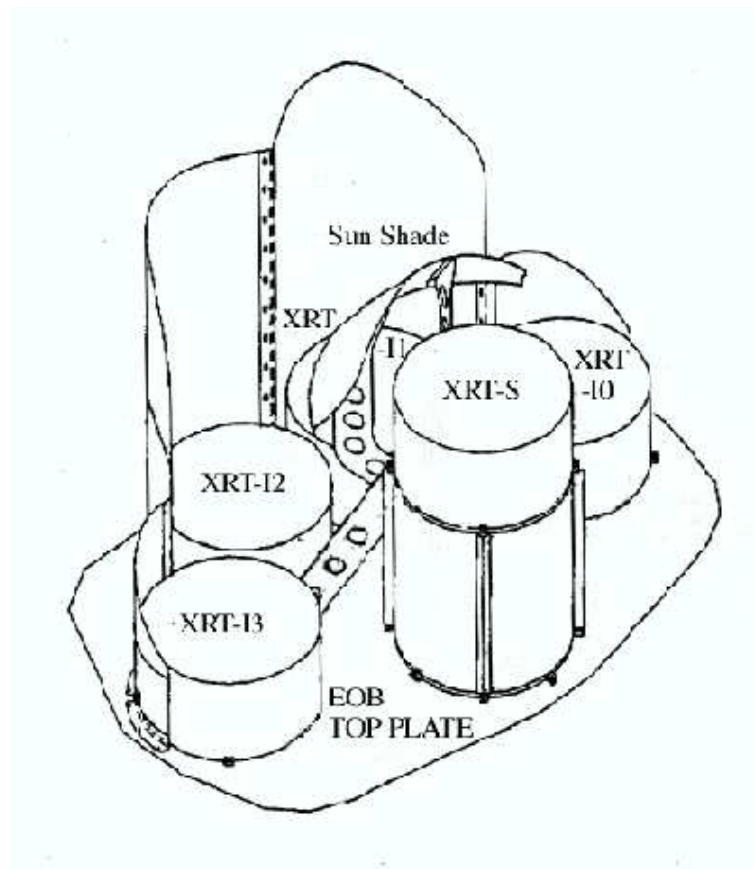


Figure 1.10: A layout of the X-ray telescopes onboard *Suzaku* obtained from 'The *Suzaku* Technical Description'.

the P-sum mode compresses the image into 1-dimension. In general, the clocking modes are used to determine the exposure time, the exposure region and the time resolution of the observation. For example, in the normal mode, the CCD pixels are read out every 8 seconds. In addition to the clocking modes, four editing modes are used for X-ray observations: 5x5, 3x3, 2x2 modes and a timing mode. These editing modes determine the format of the XIS data telemetry and specify how the detected events are edited. The 5x5, 3x3 and 2x2 editing modes are used in combination with the normal clocking mode, whereas the timing mode is used in the P-sum mode. For example, in 5x5 mode, the pulse heights (digitised charge values) of the 25 (5x5) pixels around the event centre pixel are sent to the telemetry together with the (x,y)-coordinates of the event.

1.4 X-ray spectral analysis

This section briefly describes the X-ray spectral fitting procedure. All X-ray spectral analysis in this thesis has been carried out using XSPEC11 (Arnaud, 1996) which is a detector-independent X-ray spectral fitting program. The basic idea behind the spectral fitting process is simple: we create and calculate a model, convolve the model with the detector response and then compare the result with the actual, observed data. If the convolved model does not fit the data, then the model parameters should be changed (or possibly the model which can be wrong), and the model re-calculated (Arnaud, 1996).

A detector (i.e. a spectrometer) does not obtain the actual spectrum but photon counts (C) within specific instrument channels (I). The actual, intrinsic spectrum of the source $f(E)$ at energy E is related to the observed spectrum $C(I)$ according to

$$C(I) = \int_0^{\infty} f(E)R(I, E)dE, \quad (1.13)$$

where $R(I, E)$ is the instrumental response which is proportional to the probability that an incoming photon of energy E is detected in channel I . In general, it is not possible to determine the actual source spectrum $f(E)$ by inverting Eq. 1.13 due to the width of the response function. The alternative is to choose a model spectrum $M(E)$ which is described by a set of parameters and then fit the model to the spectrometer data, as was described above.

In order to test how well the model fits the data, the usual method is to use Pearson's χ^2 test (Pearson, 1900; Cochran, 1952), which calculates a 'goodness-of-fit' according to

$$\chi^2 = \sum_{i=1}^k \left(\frac{C(I) - C_p(I)}{\sigma(I)} \right)^2, \quad (1.14)$$

where $C(I)$ are the observed counts in each spectral channel, $C_p(I)$ the predicted counts for

each model spectrum $M(E)$, and $\sigma(I)$ the errors on the observed counts $C(I)$ in channel I . The χ^2 probability density function (e.g. Wall & Jenkins, 2003) describes the probability Pr that we measure a higher value than the observed χ_{obs}^2 value by chance if the model is correct, i.e.

$$Pr\{\chi^2 > \chi_{obs}^2\} = \int_{\chi_{obs}^2}^{\infty} p(\chi^2|\nu)d\chi^2 = \frac{\chi^{2(\nu/2-1)}}{2^{\nu/2}\Gamma(\nu/2)}e^{-\frac{1}{2}\chi^2}, \quad (1.15)$$

where ν is the number of degrees of freedom and $\Gamma(\nu/2)$ a gamma function. In other words, the null hypothesis probability is a rejection probability giving indication whether a fitted model is a good fit to the data. A general rule is that the fit result is statistically acceptable if the reduced χ^2 (i.e. χ_{ν}^2) is close to 1, where χ_{ν}^2 can be calculated from χ^2/ν . Here ν gives the number of degrees of freedom and is simply the number of data points - the number of varied (or free) model parameters. For an acceptable fit, the null hypothesis probability is $Pr \sim 0.05$ and $\chi^2 \sim \nu$, whereas for a bad fit $\chi^2 \gg \nu$ and $Pr \ll 0.05$. Also, the fit can be too good (e.g. overfitting with too many parameters), and thus $\chi^2 \ll \nu$ and $1-Pr \ll 0.05$. Of course, a statistically acceptable fit does not always guarantee that the model describes the real underlying spectrum of the data.

In order to be able to use the χ^2 statistics, the data in every spectral channel have to follow a Gaussian distribution. The original photon spectrum contains the number of counts which are randomly distributed per spectral channel: in this case the data follow a Poisson distribution. Thus, to make the Poisson distribution to follow the Gaussian distribution and to use the χ^2 statistics, the data have to be binned up so that we have got at least 20 counts per spectral channel. The downside of binning is that it erases some information. Sometimes, the data contain a low number of counts in which case the χ^2 statistics should not be used. Such an example would be a spectrum with a total of 100 net counts. If this is binned by 20 ct bin⁻¹, we would have 5 data points to deal with, which does not provide much spectral information. Thus, the alternative is to leave the data unbinned and use *C statistics* (Cash,

1976, 1979). According to Cash (1979), it becomes important to use the C statistics when the number of data points falls below 10–20 counts in any bin since this is when the χ^2 statistics becomes inaccurate. Cash (1979) showed that when the number of counts is large, the C statistics follows the χ^2 statistics and should be even more efficient than χ^2 . The more relevant statistical method for this thesis is the χ^2 statistics.

1.5 The main goals of this thesis

The main focus of this thesis is multiwavelength studies of cataclysmic variables (CVs), with the emphasis slightly more on X-ray analysis. As was explained in Section 1.2, emission in accreting objects emanates from different parts of the binary system, e.g., the accretion disc and the hot spot emit in the optical, while EUV and soft X-rays are thought to arise from the optically thick boundary layer during dwarf nova outbursts. Therefore, with multiwavelength observations, we will obtain a global picture of the binary system than otherwise obtained by simply focusing on one wavelength region. Ultimately, the goals of this research are to enhance our understanding of accretion disc physics in CVs, and the understanding of X-ray emission mechanisms/production in accreting objects in general.

This thesis has been structured so that first, I will discuss individual objects, and towards the end of the thesis, move on to larger source samples. In Chapter 2, I will present the discovery of a polar candidate, *2XMMp J131223.4+173659*, which was observed serendipitously by *XMM-Newton* in 2004, present the data analysis and the results, and compare them with the results of other known polars. Following this in Chapter 3, I will discuss a WZ Sge type dwarf nova, GW Lib, which went into an outburst in 2007, lasting for ~ 26 days. This second, rare outburst was recorded in X-rays and in ultraviolet by *Swift*, and in the optical by *AAVSO* and *SuperWasp-South*. In addition to the outburst data, I will present the results of the data analysis of the GW Lib observations obtained by *Swift* one and two years following

the outburst.

In Chapter 4, I describe the *Suzaku*, *XMM-Newton* and *ASCA* X-ray analysis of a sample of dwarf novae with the goal of deriving the most accurate X-ray luminosity function (XLF) of dwarf novae to date. By studying XLFs, we aim to understand the source populations in the solar neighbourhood and in the Galaxy. We are also able to estimate how much the studied sources might contribute to the Galactic Ridge X-ray Emission (GRXE), and this way try to understand the origin of the GRXE. In Chapter 5, I will present a study of the serendipitous X-ray source content of the Galactic Plane using archival *XMM-Newton* observations. The general assumption is that the GRXE originates mainly from discrete point sources, such as CVs and X-ray binaries and other accreting objects. This chapter aims to understand the nature of the previously unknown X-ray sources in the direction of the Galactic Plane by studying the X-ray spectral properties of these sources. Ultimately, the goal of this work is to enhance our understanding of the origin of the GRXE. Finally, in Chapter 6, I will summarise the results and conclusions of this thesis and briefly discuss possible future work.

Chapter 2

The XMM-Newton observations of the polar candidate 2XMM J131223.4+173659

2.1 Introduction

As was discussed in Chapter 1, polars, i.e. AM Her stars, contain a strongly magnetic white dwarf which has a magnetic field strength of between 10 and 200 MG (Ramsay & Cropper, 2004). Formation of an accretion disc is prevented due to the strong magnetic field. However, accretion takes place via an accretion column, which forms above the white dwarf surface as the material accreted from the secondary star via Roche lobe overflow follows the magnetic field lines, and is then directed onto the magnetic pole, or poles, of the white dwarf. In this sense, they differ from the usual picture of a disc accreting CV. Since the magnetic field is strong, polars emit strongly polarised optical and infrared radiation (cyclotron radiation). They also emit hard X-rays (bremsstrahlung) from the post-shock column, and soft X-rays and EUV emission from the white dwarf photosphere (see Chapter 1, Polars).

During the last 15–20 years, several all-sky surveys have been carried out in order to gain

a deeper understanding of the source content of the Galaxy. *ROSAT*, which was the first imaging X-ray telescope to perform a soft X-ray/EUV all-sky survey (RASS, Voges et al., 1999), boosted polar discoveries in the 1990s together with subsequent optical follow-up studies (Beuermann & Burwitz, 1995): in 1995, 52 polars and polar candidates had become known compared to the 18 in the pre-*ROSAT* era (Ritter, 1990). These discoveries were enabled by the *ROSAT* Position Sensitive Proportional Counters (PSPC), which were sensitive to soft X-rays in the range of 0.1–2.4 keV, and overlapped with the energy region ($\lesssim 0.1$ keV, Frank, King, & Raine, 2002) where the typical polar characteristic, a soft X-ray component, emerges. In addition to *ROSAT*, the *Extreme Ultraviolet Explorer* (EUVE) (Bowyer & Malina, 1991), which operated between the wavelength range of 70 and 760 Å, and was dedicated to an all-sky survey, also contributed to polar discoveries which are listed in the *EUVE* all-sky survey catalogue (Bowyer et al., 1994).

Since the *ROSAT* and *EUVE* era, no soft X-ray/EUV observatory dedicated to an all-sky survey has been operating: later X-ray missions, such as *ASCA*, focused on observing in harder X-rays, i.e. between energies of 0.2–10 keV with low sensitivity below 0.5 keV. Since the end of the soft X-ray/EUV surveys, the discovery rate of new polars decreased. However, subsequent optical follow-up programmes, such as the *ROSAT* Bright Survey by Schwöpe et al. (2002a) identified 11 X-ray bright CVs observed in the RASS, and among those, 6 were new polars.

More recently, optical sky surveys, such as the *Sloan Digital Sky Survey* (SDSS, York et al., 2000), have increased the number of new polar discoveries. The SDSS is ideal for finding different types of CVs due to the photometry of an area of 10^4 deg² of sky in five different filters with a sensitivity limit greater than 20 magnitudes (Szkody et al., 2002a). In addition to photometry, through the SDSS spectroscopy, strong H Balmer and He emission lines typical for CVs, allow CV identification. Thus, the SDSS has allowed the discovery of intrinsically X-ray faint CV populations, which have not been detected with the traditional observing methods which favoured X-ray bright systems. Examples of such populations are new low-

accretion rate polars with $\dot{M} \lesssim 10^{-13} M_{\odot} \text{ yr}^{-1}$ (Schmidt et al., 2005), and a population of faint CVs (also including 13 new polars), where an accumulation of CVs at the minimum orbital period range of 80–86 min was found (Gänsicke et al., 2009). These studies are important as they further our understanding of the evolution of CVs, and the distribution of different CV types in the Galaxy. Currently, the number of new CVs discovered in SDSS is over 200 (the 6th SDSS data release, Szkody et al., 2009). At the time of writing this chapter, 101 known polars are listed in the Catalogue of Cataclysmic Variables (Ritter & Kolb, 2003).

Although new polar discoveries have not been successful with recent X-ray missions, a few have been made from the 2XMM catalogue (Watson et al., 2009). The 2XMM catalogue was released in 2007, and was the largest X-ray catalogue ever produced, consisting of more than 250,000 X-ray source detections. In addition to the targets in pointed *XMM-Newton* observations, significant numbers of serendipitous X-ray sources have been detected. In 2008, the incremental 2XMM catalogue, 2XMMi, was released consisting of *XMM-Newton* source detections from ~ 4000 observations made between 2000 and 2008, and containing ~ 17 per cent more new detections compared to the 2XMM catalogue. One example of a new polar, discovered serendipitously as a result of screening the light curves in the 2XMMi catalogue for objects showing X-ray variability, was an eclipsing AM Her type system, 2XMMi J225036.9 + 573154 (Ramsay et al., 2009).

A few years earlier, in 2004, *XMM-Newton* made a serendipitous observation of 2XMMp J131223.4 + 173659 (hereafter J1312). This highly variable source was discovered in 2006 during the pre-release screening of the 2XMM catalogue (2XMMp). The variability in the X-ray light curve of J1312 was reminiscent of that seen in the light curve of the prototype polar, AM Her. To seek more evidence for confirming the nature of J1312, I reduced the *XMM* data (Section 2.2) of J1312, and using these data, carried out timing and X-ray spectral analysis which will be discussed in Sections 2.3 and 2.5. I have also performed photometry of the *XMM* Optical Monitor (OM) data of J1312 obtained simultaneously with the X-ray data. This will be discussed in Section 2.4. Finally, I will discuss the constraints derived for the

system geometry of J1312 (Section 2.6). The work presented in this chapter has been carried out by myself (unless otherwise stated by citing Vogel et al. (2008)), but was published in collaboration in Vogel et al. (2008). The results presented in this chapter are consistent with those presented in Vogel et al.

2.2 Observations and data reduction

The *XMM-Newton* observations of J1312 ($\alpha(2000) = 13^h 12^m 23.46^s$, $\delta(2000) = +17^\circ 36' 59.5''$, position error = $0.36''$) were carried out in 2004, starting on June 28th 16:02:36.0 (UTC) and ending on June 29th 00:54:31.0 (UTC). The source position and error were determined by the EPIC pipeline source detection algorithm during the processing of the 2XMMp catalogue. In particular, the source coordinates were determined when the source list was cross-correlated with the USNO B1.0 catalogue (Monet et al., 2003) - see Watson et al. (2009) for more information on the source detection and astrometric correction of the source positions. USNO B1.0 is an all-sky catalogue including positions, proper motions and magnitudes of objects in several optical passbands. The USNO B1.0 is believed to provide all-sky coverage and completeness down to $V = 21$.

The pipeline products containing event lists of the EPIC pn and MOS observations, and the OM data were obtained from the *XMM-Newton Science Archive* (XSA). The target of the observation (ObsID 0200000101), HD 114762, was not detected. J1312 was the brightest object in the field and was uncatalogued. The three EPIC detectors, pn, MOS1 and MOS2, were in operation in full frame imaging mode and the OM in imaging mode during the observations. In the EPIC pn full frame mode, the full field of view (FOV) is in use as all the pixels of the CCDs are read out. Table 2.1 lists the observational information for all the three EPIC cameras and for the OM.

The data reduction was performed using the *XMM-Newton Science Analysis System* (SAS)

Table 2.1: The *XMM-Newton* observations of J1312 obtained in June 2004.

Instrument	ExpID	Mode	Filter	Start time	Stop time	Duration (s)
EPN	U002	PrimeFullWindow	Medium	2004-06-28T16:35:18	2004-06-29T00:46:10	29452
EMOS1	S001	PrimeFullWindow	Medium	2004-06-28T16:03:16	2004-06-29T00:51:07	31671
EMOS2	S002	PrimeFullWindow	Thick	2004-06-28T16:03:16	2004-06-29T00:51:12	31676
OM	S006	Image	U	2004-06-28T16:11:40	2004-06-28T16:24:59	799
OM	S007	Image	UVW1	2004-06-28T17:45:08	2004-06-28T17:58:29	801
OM	S405	Image	UVW1	2004-06-28T18:03:49	2004-06-28T18:17:09	800
OM	S406	Image	UVW1	2004-06-28T18:22:32	2004-06-28T18:35:51	799
OM	S407	Image	UVW1	2004-06-28T18:41:14	2004-06-28T18:54:33	799
OM	S408	Image	UVW1	2004-06-28T19:29:57	2004-06-28T19:43:17	800
OM	S008	Image	UVM2	2004-06-28T19:48:37	2004-06-28T20:10:35	1318
OM	S409	Image	UVM2	2004-06-28T20:45:58	2004-06-28T21:07:58	1320
OM	S410	Image	UVM2	2004-06-28T21:13:20	2004-06-28T21:35:19	1319
OM	S411	Image	UVM2	2004-06-28T21:40:42	2004-06-28T22:02:41	1319
OM	S412	Image	UVM2	2004-06-28T22:08:05	2004-06-28T22:30:05	1320
OM	S009	Image	UVW2	2004-06-28T22:35:25	2004-06-28T22:58:23	1378
OM	S413	Image	UVW2	2004-06-28T23:04:05	2004-06-28T23:27:05	1380
OM	S414	Image	UVW2	2004-06-28T23:32:46	2004-06-28T23:55:45	1379
OM	S415	Image	UVW2	2004-06-29T00:01:27	2004-06-29T00:24:27	1380
OM	S416	Image	UVW2	2004-06-29T00:30:09	2004-06-29T00:53:07	1378

v.7.0.0. Before extracting any data products, the data were reprocessed in order to obtain the most recent calibration and developments in the SAS software. I created a Calibration Index File (CIF) using the SAS task CIFBUILD, and an *observation data file* (ODF) needed in data processing with ODFINGEST. The ODF summary file includes information on instrument housekeeping files and calibration database. And finally, using EPCHAIN and EMCHAIN, which are the default pipeline processing chain tasks for EPIC pn and MOS respectively, I generated the reprocessed event lists. The pn and MOS light curves (binned into 100 s bins) between 10–12 keV were checked for high background flaring caused by soft protons which originate from the Sun and are most likely located around the Earth’s magnetosphere with energies $< \text{few} \times 100 \text{ keV}$. The pn and MOS light curves, which are shown in panels (a), (b) and (c) in Fig. 2.1, show some flaring. For the pn, the background flares were cut above the full field count rate of 0.4 ct s^{-1} and above 0.25 ct s^{-1} for the MOS data. Single and double pixel X-ray events were chosen (PATTERN = 0–4) with FLAG = 0 for the pn, and PATTERN = 0–12 with #XMMEA_EM for the MOS. FLAG = 0 excludes the events close to chip gaps and bad pixels/columns. Due to the filtering, time intervals covering altogether 952 s (pn), 271 s (MOS1) and 76 s (MOS2) were excluded from the time series and spectra. Table 2.1 shows the total duration of the pn and MOS observations before filtering.

Since the field around J1312 is crowded (see Fig. 2.2), the source and background extraction regions had to be chosen carefully in order to avoid contamination from background sources. A point source (circled in blue in Fig. 2.3) possibly affecting J1312, is located 21 arcsec away from J1312 (circled in green in Fig. 2.3). Thus, the point spread function (PSF) of J1312 (Fig. 2.4) was investigated in order to see whether contamination occurs, by fitting the data with a King function¹. The King function is widely used in astrophysics and is defined as

¹See ‘EPIC status of calibration and data analysis’, <http://xmm.vilspa.esa.es/docs/documents/CAL-TN-0018.pdf>

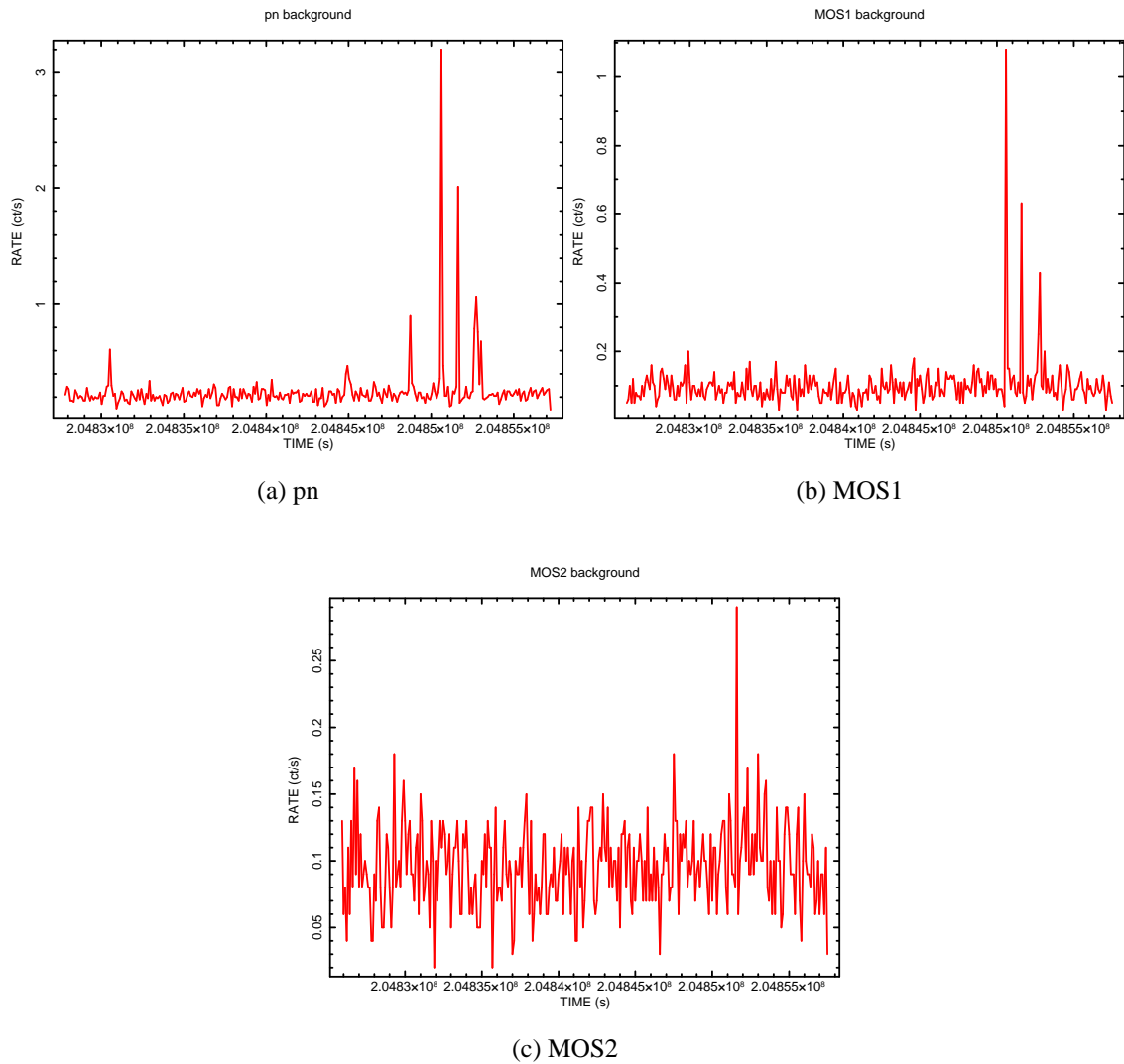


Figure 2.1: The EPIC 10–12 keV background lightcurves of the EPIC (a) pn, (b) MOS1, and (c) MOS2 illustrating the background flaring. The unit on the x-axis is the spacecraft time in seconds and on the y-axis the count rate (ct s^{-1}).

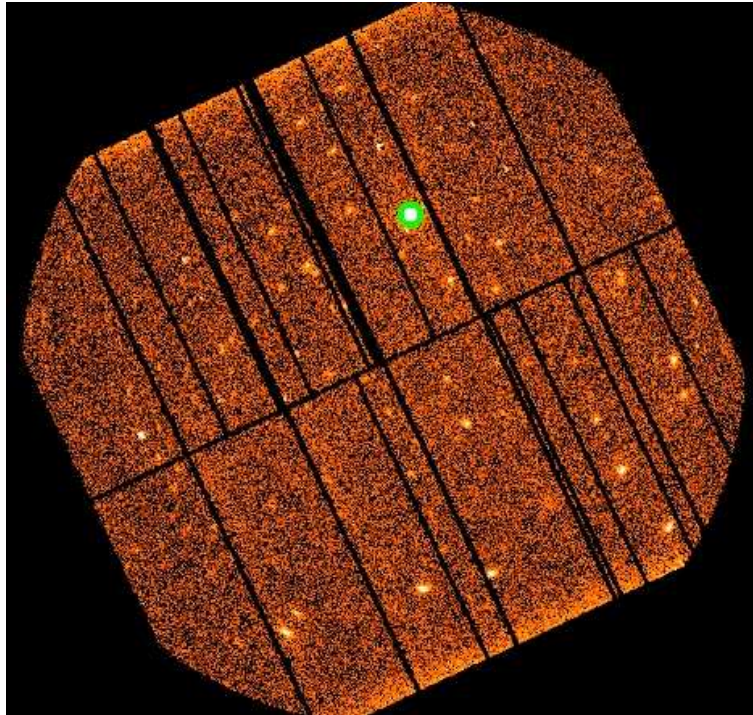


Figure 2.2: The *XMM* EPIC pn field of the observation 0200000101. J1312 has been circled in green. The dark columns are caused by exclusion of bad columns from the image. In the image, the scale is logarithmic, and the celestial North is up and East to the left.

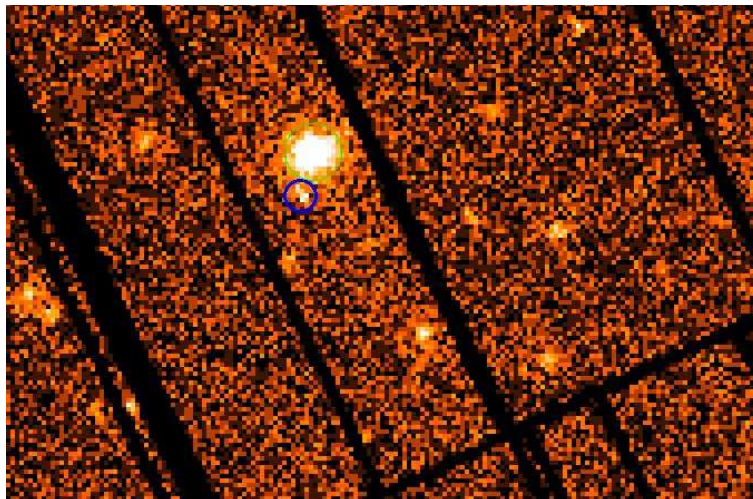


Figure 2.3: A close-up of J1312 (circled in green, where the radius of the circle is 25 arcsec) and the possibly contaminating source (circled in blue).

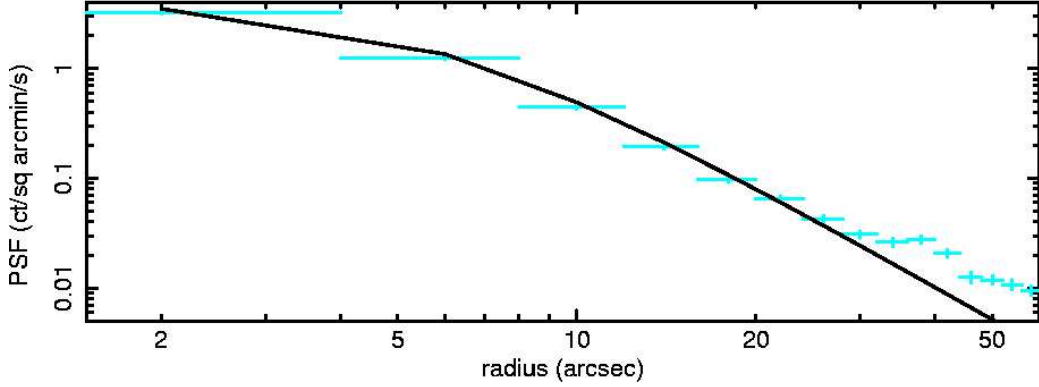


Figure 2.4: The point spread function (PSF) of J1312 fitted with a King profile with $r_c = 6.18$ and $\beta = 1.50$.

$$PSF(r) = \left(1 + \left(\frac{r}{r_c}\right)^2\right)^{-\beta}, \quad (2.1)$$

where r is the radial distance from the centre of the source PSF, r_c the radius of the source PSF core, and β the slope of the King function. The parameters used, $r_c = 6.18$ and $\beta = 1.50$, were obtained from the *XMM* calibration database (CALDB), and they provide a good fit to the data. Fig. 2.4 shows that the King function starts to deviate from the data at radii $r > 25$ arcsec from the centre of the source, however, no deviation is seen at 21 arcsec. Thus, the interpretation is that no contamination by the other point source shown in Fig. 2.3 occurs. Since the PSF profile of J1312 is well-fitted for $r < 25$ arcsec, a circular extraction region with $r = 25$ arcsec, which contains ~ 80 per cent of the flux, was used for extracting the pn and MOS source X-ray spectra and light curves. For the background, a circular extraction region of 120 arcsec was chosen to extract the pn and MOS background spectra and light curves from an adjacent CCD chip to the source chip. The background light curves were subtracted from the source light curves using LCMATH. Since the background extraction area was not equal to the source extraction area, the background area had to be scaled to match the source extraction area before subtraction.

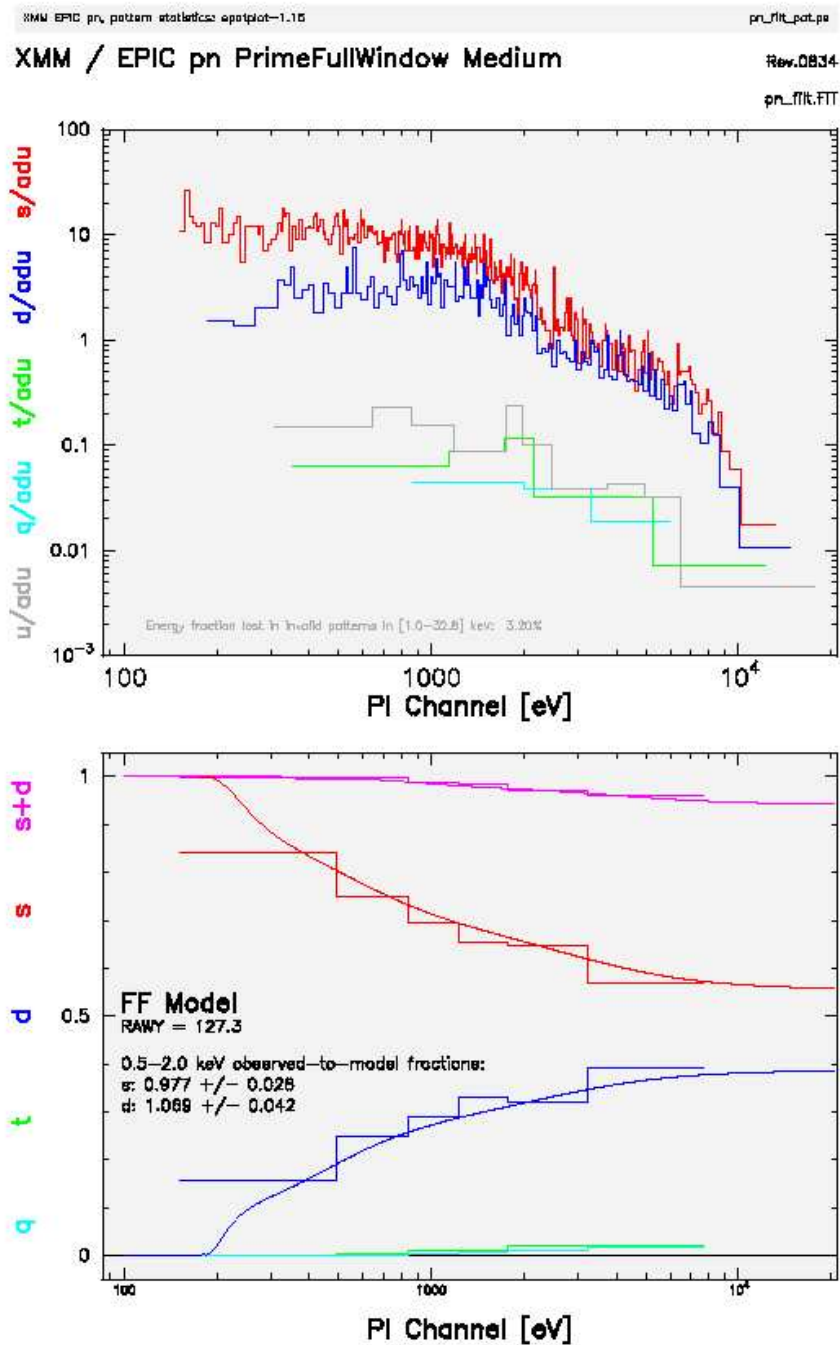


Figure 2.5: The pn pattern distribution of J1312 taken inside a source radius of 25 arcsec. The upper panel shows the spectral distributions as a function of PI channel for the four event types (see text), and the lower panel the fractions of the four event types relative to the sum. According to the lower panel, these data are not piled-up as the energy dependence follows the standard curves.

2.2.1 Investigating pile-up

When carrying out X-ray observations with any X-ray observatory, the observations may suffer from *pile-up*, if the source is too bright for the detector. Pile-up is due to two or more simultaneous X-ray photons hitting the same CCD pixel (or photons hitting very closely located pixels simultaneously, i.e. within a frame accumulation time) and causing overlapping charge distributions in a CCD frame. The overlapping events are read out as one event with a higher energy and this can cause spectral distortion, such as spectral hardening and flux loss. The pile-up 'safety limit' is detector dependent for different X-ray satellites. If a source is badly piled up, this would be seen as a 'hole' in the core of the source point spread function (PSF) in an X-ray image. The importance of pile-up also depends on the spectral shape and can affect very soft spectra even at low count rates.

The pn and MOS data of J1312 were checked in case of pile-up. For full frame exposures, pile-up may be a problem if the count rate exceeds $> 0.7 \text{ ct s}^{-1}$ for the MOS and 6 ct s^{-1} for the pn. Fig. 2.2 and 2.3 do not show evidence of this since no 'hole' is seen in the core of the source. Also, the average net count rates for these data of J1312 are lower than the pile-up limits: $0.200 \pm 0.003 \text{ ct s}^{-1}$ and $0.060 \pm 0.001 \text{ ct s}^{-1}$, and the peak count rates $\sim 0.6 \text{ ct s}^{-1}$ and $\sim 0.20 \text{ ct s}^{-1}$ for the pn and MOS data, respectively.

To investigate possible pile-up in a more formal way, I checked the data of J1312 within a $r = 25$ arcsec source circle with the *XMM* SAS task EPATPLOT which is designed to read and plot pattern event information from the EPIC pn and MOS event files. The upper panel in Fig. 2.5 illustrates the pn spectral distribution as a function of PI channel for single (s), double (d), triple (t), and quadruple (q) events. These are the valid events which can be created by an X-ray photon. The lower panel shows the fractions of the four valid types of events relative to the sum. These fractions are energy-dependent so that higher energy photons produce less single events due to the increasing size of the electron cloud created by the incident photon. The numbers provided in the lower panel in Fig. 2.5 indicate the 0.5–2 keV observed-to-

model singles (s) and doubles (d) pattern fractions. If pile-up is not present, the numbers should be consistent with 1.0 within statistical 1σ errors. As it appears from the lower panel in Fig. 2.5, the single and double ratios are consistent with 1.0 within their errors. Also, the plotted single and double pattern fractions show that there is no pile-up since they do not deviate from the standard model curves (red and blue). A similar analysis for the MOS data also did not indicate evidence of pile-up.

2.3 Light curve analysis

The *XMM* pn (top panel), MOS1 (middle) and MOS2 (bottom) background-subtracted X-ray light curves shown in Fig. 2.6 were created within the timing analysis software package XRONOS v.6.0.5 using LCURVE, which is used for producing binned light curves. The light curves cover the energy band 0.2–12 keV and show a repeating pattern of high and low intensities covering five full cycles. They also show longer and shorter dips leading to zero intensities, i.e. eclipses. The T_0 in the pn light curve corresponds to JD 2453185.169.

The mid-eclipse times of the short eclipses in the EPIC pn X-ray light curve in Fig. 2.6 were used to derive the zero epoch and the orbital period of J1312. In order to study variations in the orbital period of a binary system, astronomers use the *O-C method* (Lombard, 1998). It is a powerful tool for studying period behaviour, motion and evolutionary changes in binary systems (Sterken, 2005). The common method is to calculate *linear ephemeris*

$$C_j = O_0 + E\bar{P}, \quad j = 1, \dots, n, \quad (2.2)$$

where C_j is the calculated time of the minimum (or maximum) light, i.e. the time when minimum (or maximum) could be expected if the period was constant, O_0 the zero epoch of the minimum (or maximum) light, E the number of cycles in the period P elapsed since O_0 ,

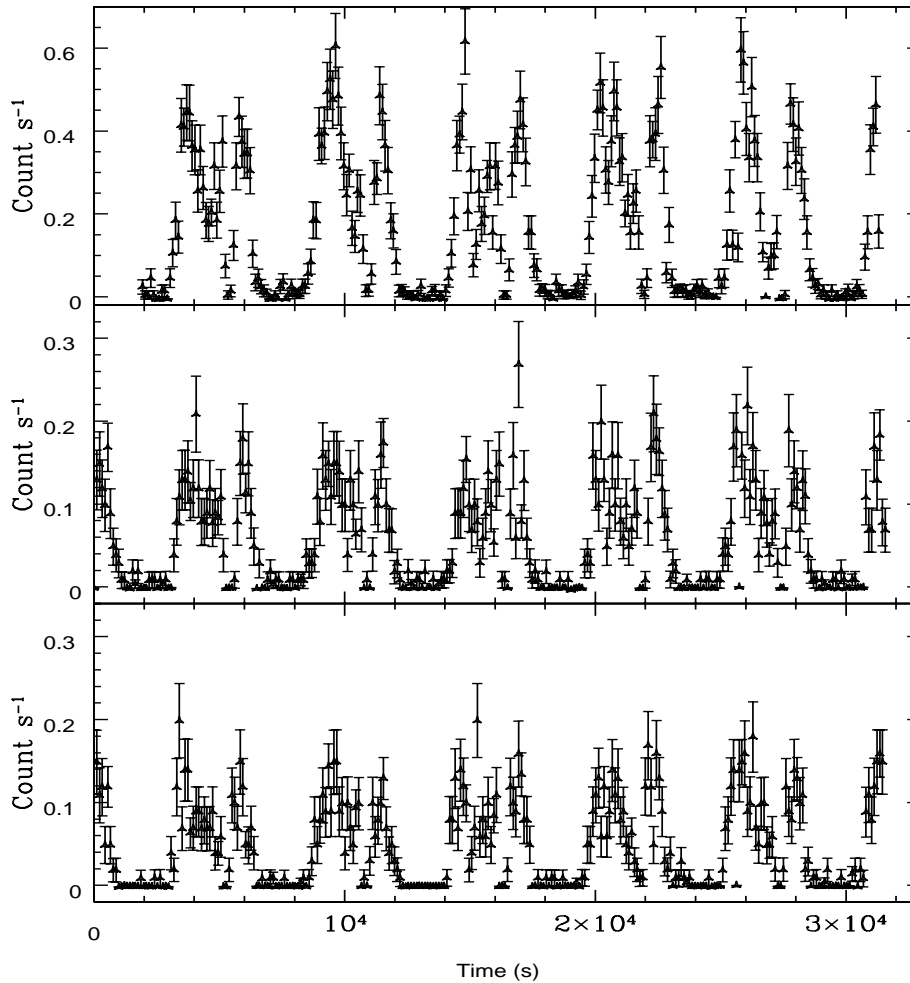


Figure 2.6: The *XMM* pn (top panel), MOS1 (middle) and MOS2 (bottom) background-subtracted X-ray light curves of J1312 in the energy band 0.2–12 keV. The light curves have been binned into 110 s bins using LCURVE.

and \bar{P} the overall mean period $\bar{P} = (O_n - O_0)/n$.

Fig. 2.7 shows a close-up of the first short eclipse from the total band pn light curve in Fig. 2.6. Note that the binning of the light curve in Fig. 2.7 (30 s) is different from the binning used in Fig. 2.6 (110 s). The mid-eclipse times were measured for each short eclipse in a similar manner by measuring the maximum width for each eclipse. The error on the mid-eclipse was estimated from the light curve (30 s) which in this case corresponds to the bin size. As an example, the mid-eclipse time, 5702 s, for the first short eclipse was calculated as an average

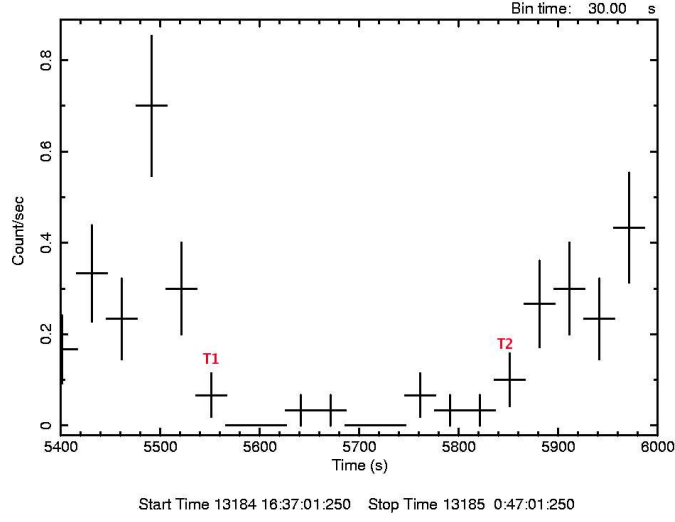


Figure 2.7: A close-up of the first short eclipse in the total band (0.2–12 keV) pn X-ray light curve of J1312. The mid-eclipse time is 5702 s. The light curve has been binned into 30 s bins in LCURVE.

of T1 and T2 as indicated in Fig. 2.7.

The epoch and the orbital period were determined using a least-squares fitting technique where the goodness of fit was measured using the χ^2 statistics, with

$$\chi^2 = \sum \left(\frac{t_0 - t_c}{\sigma_{t_0}} \right)^2, \quad (2.3)$$

where t_0 and σ_{t_0} are the observed mid-eclipse times and their errors, and t_c the time calculated on the basis of the trial period and epoch. Table 2.2 lists the observed mean mid-eclipse times t_0 , the errors on the mid-eclipse times σ_{t_0} , the calculated mid-eclipse times t_c , $O-C$ values and the cycle numbers E . From the observed and calculated mid-eclipse times, we obtain the best-fit linear eclipse ephemeris

$$T_{ecl} = 2453185.38606(4) + 0.063769(23)E, \quad (2.4)$$

in which the epoch is the barycentrically corrected Julian date, and the period is given in days.

Table 2.2: The observed times t_0 for the mid-eclipses of J1312, the error σ_{t_0} , the calculated mid-eclipse times t_c , $O-C$ values and the cycle numbers E .

t_0	σ_{t_0}	t_c	O-C	E
(d)	(d)	(d)	(d)	
0.0660127	0.000347	0.0659868	0.0004	-2
0.1296990	0.000347	0.1297556	-0.0009	-1
0.1934140	0.000347	0.1935243	-0.0017	0
0.2573210	0.000347	0.2572931	0.0004	1
0.3210360	0.000347	0.3210619	-0.0004	2

The barycentric correction is 15 s. The numbers in parentheses are the \pm errors on the last significant digits and correspond to the 68 per cent confidence limits (1σ) for two interesting parameters ($\chi^2_{min} + 2.30$), i.e. the epoch and the period. Thus, when converted to minutes, the period is 91.82736 ± 0.03312 min.

2.3.1 The folded light curve

The folded soft (0.2–1.5 keV) and hard (1.5–12 keV) light curves and their hardness ratio (H/S) are shown in Fig. 2.8. When folding the data over the ephemeris period (91.8 min), a repeatable structure was seen: the light curves show two excursions to zero intensity of which the longer one covers phase interval ~ 0.20 – 0.60 , and the second, much narrower eclipse the phase interval ~ 0.98 – 1.03 . In addition, dip features are seen between ~ 0.70 – 0.97 , in particular in the soft light curve.

These features are reminiscent of the features seen in AM Her stars, such as HU Aqr (Schwope et al., 2001) and UZ For (Osborne et al., 1988). The first similarity is the longer occultation (phase interval 0.20–0.60) which was also seen in HU Aqr and UZ For, and was thought

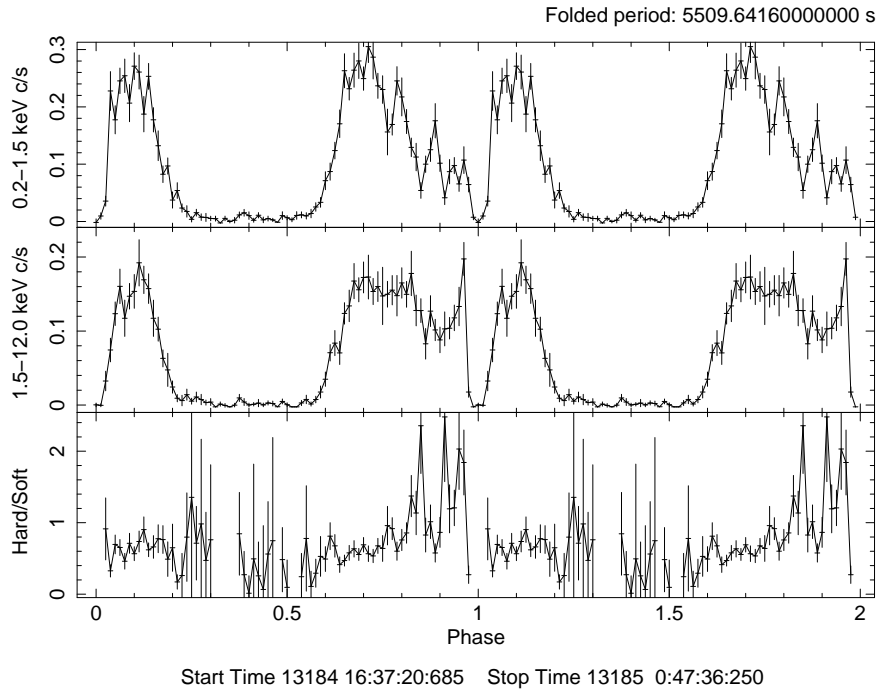


Figure 2.8: The soft (0.2–1.5 keV, top panel) and hard (1.5–12.0 keV, middle) *XMM* pn X-ray light curves of J1312 folded over the orbital period of 91.8 min. The bottom panel shows the hardness ratio of these light curves (hard/soft). The light curves are binned into 80 phase bins.

to be due to the occultation of the emission region by the white dwarf. It was also seen in other previous observations of AM Her type systems, such as in VV Puppis (Patterson et al., 1984) and in E1114+182 (Biermann et al., 1985). Thus, it is very likely that in J1312, the broad minimum at phase interval ~ 0.20 – 0.60 in Fig. 2.8 is caused by the white dwarf self-occultation. The total length of the bright phase in J1312 is nearly equal to the length of the broad minimum in J1312: the duration of the broad minimum is about 40 per cent of the orbital cycle whereas the duration of the total bright phase is about 60 per cent of the cycle. These durations are comparable to those seen, e.g. in E1114+182 (Biermann et al., 1985). The factors affecting the length of the bright phase are the latitude and the vertical and longitudinal extent of the accretion region, and the system inclination (Schwope et al., 2001). The broad minimum being due to the white dwarf self-occultation was explained by e.g. Watson, Mayo, & King (1980) who noted that the accretion column models of King & Lasota (1980) predict that the dimensions of the columns are much smaller than the white dwarf radius. Therefore, the white dwarf is suitable for producing broad dips. Also, Hameury & King.

(1988b) noted that if the accretion column in AM Her systems is not tall (i.e. the height of the shock would be similar to the white dwarf radius), the occultation by the white dwarf only can produce quasisinusoidal X-ray light curves.

The second similarity seen in other AM Her-type systems, such as in UZ For, HU Aqr and E1114+182, is the short and deep eclipse at phase interval ~ 0.97 – 1.03 in the light curve of J1312. In UZ For, HU Aqr and E1114+182, this was thought to be due to the eclipse by the secondary star, and this is probably also the case in J1312. As the secondary passes in front of the white dwarf and passes the line of sight to the observer, the secondary blocks the X-ray emission emanating from the accretion region on the surface of the white dwarf, leading to zero intensity at the mid-eclipse in the light curve (see Fig. 2.8). According to Patterson, Williams, & Hiltner (1981), the white dwarf is the ultimate source of all the energy radiated, and thus an eclipse by the secondary star should produce a deep and sharp eclipse at all wavelengths. See also Allen, Ward & Wright (1981) who refer to the extremely short duration of the narrow eclipse, indicating an eclipse by the secondary star.

Prior to the short eclipse there is a progressive loss of soft X-ray flux, i.e. dips, between phase interval ~ 0.70 – 0.97 (upper panel in Fig. 2.8). The dips in the hard X-ray light curve are clearly not as deep as in the soft X-ray light curve. X-ray dips were also seen in e.g. the soft X-ray light curve of EF Eri by Patterson, Williams, & Hiltner (1981) who suggested that such dips could be due to a 'translucent body', i.e. an absorbing accretion column. The hard X-ray light curve of EF Eri did not show clear dip features. This kind of energy dependence is also seen in the soft and hard X-ray light curves of J1312 (see the dips in the soft light curve versus the lack of dips in the hard light curve in Fig. 2.8). Other examples of eclipsing AM Her systems are VV Puppis (Patterson et al., 1984), UZ For (Osborne et al., 1988) and HU Aqr (Schwope et al., 2001). In all these cases, the dips were thought to be caused by an accretion column crossing through the line of sight, absorbing the low energy photons, and this could also be the case for J1312.

2.4 Optical Monitor data

The Optical Monitor (OM) data of J1312 were obtained with the U ($\lambda_{eff} = 3440 \text{ \AA}$), $UVW1$ ($\lambda_{eff} = 2910 \text{ \AA}$), $UVM2$ ($\lambda_{eff} = 2310 \text{ \AA}$) and $UVW2$ ($\lambda_{eff} = 2120 \text{ \AA}$) filters. There were altogether 16 OM exposures (Table 2.1), and J1312 was visible in only three (ExpID S408, S412 and S416) in $UVW1$, $UVM2$ and $UVW2$ filters. It was not visible in the U filter or in the rest of the $UVW1$, $UVM2$ and $UVW2$ exposures given in Table 2.1 as they did not cover the field around J1312 during the observations. Since the OM data had been fully processed by the SAS pipeline, there was no need to repeat the data processing.

The pipeline end products contain e.g. magnitude and flux information with their errors for J1312. In order to confirm that the results of the pipeline photometry were correct, the *XMM* SAS task OMSOURCE was run to perform photometry on J1312. In general, OMSOURCE allows the user to choose a source in the image, and then carry out interactive photometry. To start the photometry, the source detection algorithm OMDetect was run within the OMSOURCE task. OMDetect automatically runs detection for all of the sources in the field of view, and calculates a background image in order to identify pixels which may be part of a source. Therefore, OMDetect checks if the value within a pixel is higher than the local background value. The algorithm can deal with features, such as strong mod-8 patterns because it examines the order of decreasing pixel brightness. After source detection, OMDetect performs aperture photometry for the detected sources and calculates a count rate for each source with coincidence loss correction. Within OMSOURCE, the source and background region apertures can be adjusted and photometry calculated.

In order to carry out photometry for the detected sources within OMSOURCE, the SAS task OMMAG is used to convert the count rates into instrumental OM magnitudes and to correct the count rates for detector deadtime losses and time sensitivity degradation of the detector. Deadtime losses are caused by the lack of instrumental response during a frame transfer, while the sensitivity degradation is due to ageing of the photo-cathode and micro channel plates

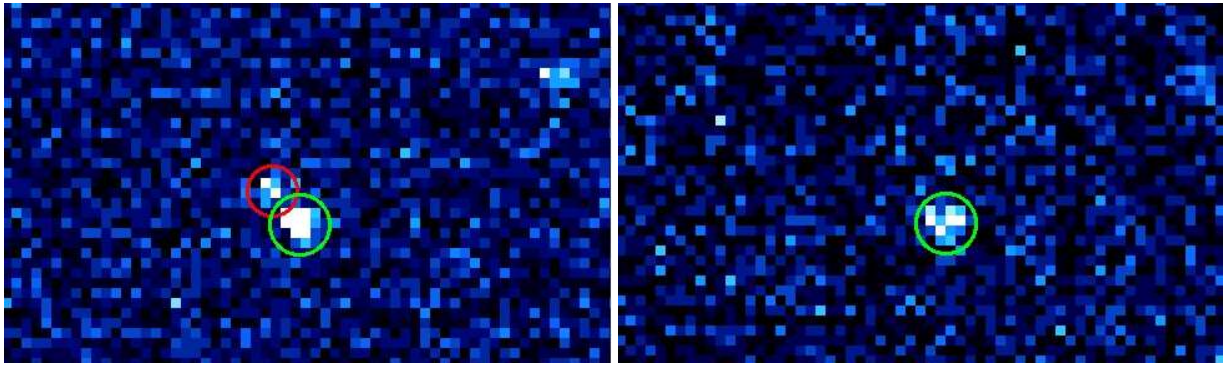
Table 2.3: The *XMM* OM instrumental magnitudes, corrected source count rates and flux densities with their 1σ errors for J1312 in the *UVW1*, *UVM2* and *UVW2* filters for orbital phase intervals corresponding to phases in Fig. 2.8.

Filter	Mag	Corr. ct rate (ct s ⁻¹)	AB Flux $10^{-16} \times \text{erg cm}^{-2} \text{s}^{-1} \text{\AA}^{-1}$	Phase interval
UVW1	18.62 ± 0.18	0.27 ± 0.04	1.30 ± 0.22	0.26–0.41
UVM2	18.35 ± 0.27	0.09 ± 0.02	2.10 ± 0.52	0.99–1.22
UVW2	18.53 ± 0.61	0.04 ± 0.02	1.96 ± 1.09	0.53–0.78

(MCPs) (Talavera, 2009). The shape of the PSF of OM sources is radially symmetric and the net count rate of a source in the UV filters is calculated using a circular aperture of 35 pixels (Talavera, 2009). Thus, if a smaller aperture is used to carry out the interactive photometry, OMMAG extrapolates the PSF of a source to account for a 35 pixel radius aperture.

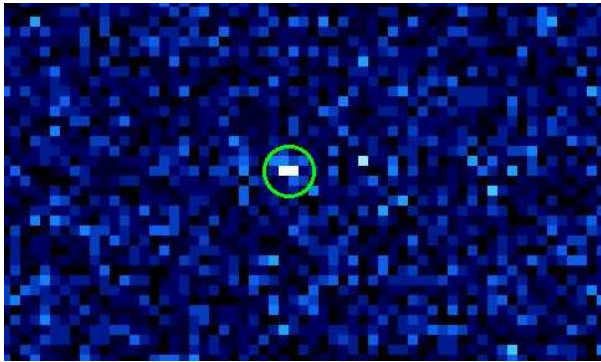
Fig. 2.9 shows OM images of J1312 in the *UVW1* (panel (a)), *UVM2* (panel (b)) and *UVW2* (panel (c)) filters. When carrying out the photometry on J1312, a circular aperture with a radius of $r_{src} = 3$ pixels ≈ 1.43 arcsec was chosen for the source region, and for the background an annulus centred on the source with an inner radius of $r_{inner} = 10$ pixels ≈ 4.77 arcsec and an outer radius of $r_{outer} = 26$ pixels ≈ 12.39 arcsec. The results of the interactive photometry carried out with OMSOURCE for J1312 are given in Table 2.3. It includes the calculated instrumental magnitudes, corrected source count rates (does not include background) and flux densities of the OM data in three ultraviolet (UV) filters. It also lists the orbital phases corresponding to the folded light curve in Fig. 2.8.

J1312 has the highest UV flux in the *UVM2* filter at the phase interval 0.99–1.22. This phase interval corresponds to the eclipse by the secondary star and to the bright phase immediately following the short eclipse in the phase-folded light curve in Fig. 2.8. J1312 does not appear to be bright in the *UVW2* filter (see Fig. 2.9(c)) corresponding to the phase interval 0.53–0.78 after the white dwarf self-occultation although the flux given in Table 2.3 is similar to the flux



(a) UVW1

(b) UVM2



(c) UVW2

Figure 2.9: (a) J1312 (circled in green) in the *UVW1* filter with a source at $\alpha = 13^h 12^m 23.74^s$, $\delta = +17^\circ 37' 0.103''$ (circled in red) which is probably a marginal detection of the quasar SDSS J131223.75+173701.2 at $z = 2.43$ detected by Vogel et al. (2008), see text for more information. The quasar is not detected in the (b) *UVM2* and (c) *UVW2* filters.

measured in the *UVM2* filter. This difference between the measured flux in the *UVW2* filter and the faintness of the object in Fig. 2.9(c) can be explained by a low number of counts and thus a large error on the flux. During the white dwarf occultation at phase interval 0.26–0.41, the UV flux is faintest in the *UVW1* filter. In general, UV emission from CVs is dominated by the white dwarf (Warner, 1995). Vogel et al. (2008) noted that a strong contribution from the accretion stream exists in J1312 in the UV: white dwarf model spectra with temperatures of $T = 20,000$ K and $11,000$ K provide ~ 70 and 60 per cent of the flux in the *UVW1* band, respectively. Thus, the accretion stream has to account for the remaining flux. They also

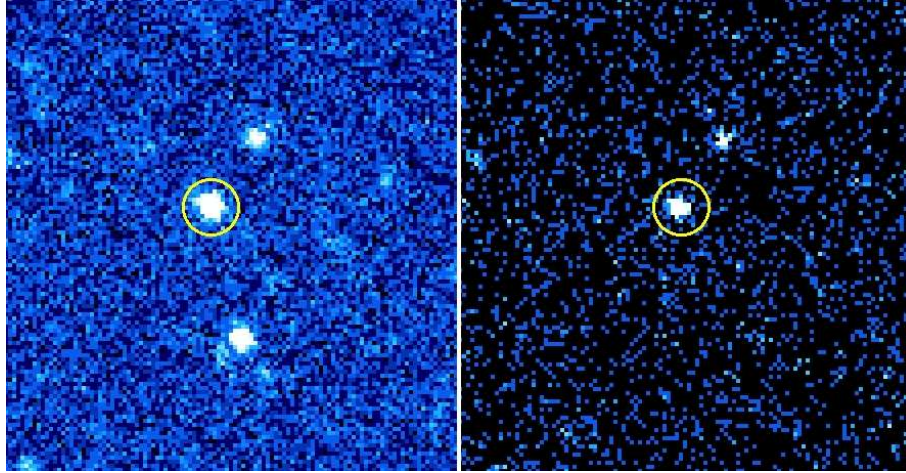
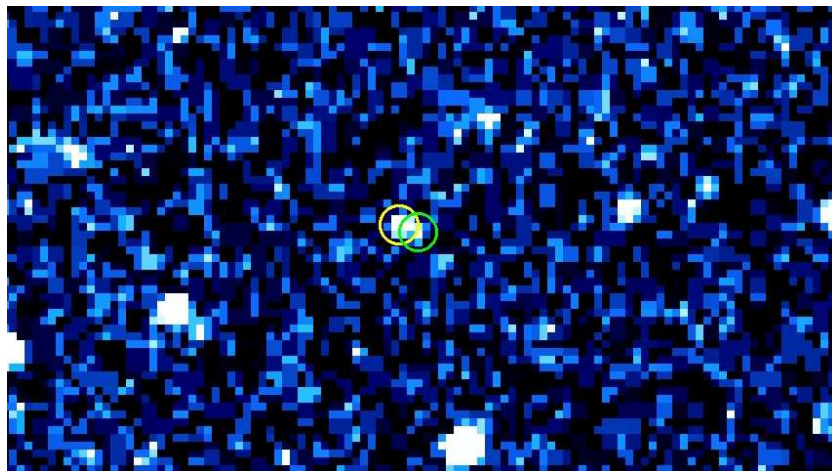
noted that UV photometry could help to constrain the white dwarf temperature.

Fig. 2.9(a) shows a source next to J1312 in the *UVWI* filter circled in red at $\alpha = 13^h 12^m 23.74^s$, $\delta = +17^\circ 37' 0.103''$ (coordinates were determined by the SAS source detection algorithm OMDetect). The distance of this source from J1312 is 4 arcsec. The source has not been detected in the *UVM2* or in the *UVW2* filters. Vogel et al. (2008) reported on a source 4.4 arcsec away from J1312. They identified this source as SDSS J131223.75+173701.2 which, according to the spectroscopic observations of Vogel et al., is a quasar at redshift of $z = 2.43$. At this redshift, the Lyman limit is shifted to 3128 \AA according to

$$\lambda = (1 + z)\lambda_0, \quad (2.5)$$

where $\lambda_0 = 912 \text{ \AA}$ is the Lyman limit, i.e. the limit above which hydrogen becomes ionised, z the redshift and λ the new, redshifted wavelength. This wavelength (3128 \AA) is within the bandpass of the *UVWI* filter (see Chapter 1, Fig. 1.8). Thus, it seems likely that the quasar detected by Vogel et al. (2008) is present in the *UVWI* filter. In this case, it should also be covered by the bandpass of the *U* filter which overlaps with *UVWI*. However, the *U* filter did not cover the field around J1312 and the quasar during the observations.

J1312 has also been observed by the Galaxy Evolution Explorer (*GALEX*) in the near-ultraviolet (NUV) and far-ultraviolet (FUV), and it is visible in the Smithsonian Astrophysical Observatory Digitized Sky Image Survey (*SAO-DSS*). The *GALEX* NUV band covers $\sim 1700\text{--}3000$ and the FUV $\sim 1650\text{--}1800 \text{ \AA}$. The Lyman limit at the redshift of $z = 2.43$ is not within the *GALEX* NUV or FUV bandpasses and thus the quasar is not detected by *GALEX* (Fig. 2.10(a)), but is visible and blended with J1312 in the *SAO-DSS* (Fig. 2.10(b)). The field of view of J1312 obtained by the *DSS* was observed during the Palomar Observatory Sky Survey (*POSS*) with a *POSS-E* red plate thus covering the wavelength range of $5500\text{--}8000 \text{ \AA}$.

(a) *GALEX* NUV (left) and FUV (right)

(b) SAO DSS

Figure 2.10: (a) *GALEX* near-ultraviolet (NUV, left) and far-ultraviolet (FUV, right) images of J1312. The NUV bandpass covers 1700–3000 and the FUV 1650–1800 Å. Due to the redshifted Lyman limit (3128 Å), the quasar is not detected within these bandpasses. J1312 has been circled in yellow in these two figures. (b) An *SAO DSS* image of J1312 (circled in green). The figure also shows the quasar SDSS J131223.75+173701.2 (circled in yellow) at redshift $z = 2.43$. The PSF of the quasar is blended with J1312.

2.5 Spectral analysis

Spectral analysis of the X-ray data aims to understand how well a fitted model describes the underlying source spectrum, and thus tries to reveal the physical processes responsible for the observed emission. The spectral fitting was carried out in XSPEC v.11. In order to investigate the spectral fitting parameters, total EPIC pn and MOS spectra of J1312 covering the whole observation interval were extracted, and to employ Gaussian statistics the data were binned to 20 cts bin⁻¹. The redistribution matrix files (RMF) were created with RMFGEN and the ancillary response files (ARF) with ARFGEN. In general, the ARF files are used in conjunction with the RMF files. The purpose of the ARF is to correct for, e.g. the area of the source region falling outside the field of view or CCD boundaries, or a source area containing bad pixels or columns by reducing the effective area produced in the ARF, and to apply encircled energy correction for a point source (i.e. to correct for the flux falling outside the defined source extraction region). The RMF (which was already discussed in Chapter 1, X-ray spectral analysis) describes the response of the instrument as a function of energy and PI channel. An average RMF is calculated by RMFGEN over the spatial region which was used to extract the source spectrum.

As was explained in Chapter 1, hard X-rays emitted from the post-shock column irradiate the surface of the white dwarf. Some fraction will be absorbed by the surface, and re-emitted as blackbody emission. The cooling gas in the post-shock column is optically thin. In order to model the blackbody emission from the surface of the white dwarf and the optically thin emission spectrum in the post-shock column, the X-ray spectral fitting was performed using a model consisting of a photoelectrically absorbed (`wabs`, Morrison & McCammon, 1983) optically thin thermal plasma model (`mekal`, Mewe, Lemen, & van den Oord, 1986; Liedahl, Osterheld & Goldstein, 1995) with a blackbody component. When fitting CV X-ray spectra, spectral models containing emission lines (such as the optically thin thermal plasma model) are more likely to describe the real underlying CV spectrum than continuum models without

lines, such as bremsstrahlung. This is because line cooling becomes important at 1×10^7 K (~ 1 keV) in X-rays. At this temperature, all the energy is radiated as X-rays, of which half is emitted as lines and half as thermal bremsstrahlung (Charles & Seward, 1995). Thus, in high quality CV X-ray spectra, line emission can be seen, especially below 5 keV, but also between 6–7 keV (iron line complex)

The photoelectric absorption, $A(E)$, is given by

$$A(E) = e^{-n_H \sigma(E)}, \quad (2.6)$$

where n_H is the equivalent hydrogen column density in units of 10^{22} atoms cm^{-2} , and $\sigma(E)$ the photoelectric cross-section in units of cm^2 at a given energy E . The cross section $\sigma(E)$ describes the probability of a photon being absorbed in a photoelectric process (Eisberg & Resnick, 1985). The value of the cross section depends on the energy of a photon and the atomic number: the energy ranges in which photoelectric processes dominate are different for atoms with lower and higher atomic numbers. For example, for lead the photoelectric effect dominates below $h\nu < 5 \times 10^5$ eV, and for aluminium the corresponding value is $h\nu < 5 \times 10^4$ eV, where $h = 4.14 \times 10^{-15}$ eVs (Planck constant) and ν the frequency of the incident photon.

In addition, to take into account other physical conditions in the post-shock region of the accretion column, I also experimented with the spectral models which are described below. Since the cooling gas in the post-shock column is thought to consist of a distribution of temperatures as the gas cools, I tested a multi-temperature model, `cemek1`. The emission measure of this model follows a powerlaw in temperature T , i.e. the emission measure is proportional to $(\frac{T}{T_{max}})^\alpha$, where T_{max} is the maximum shock temperature and α the powerlaw photon index. In general, absorption in the column is not expected to be simple as there will be a range of temperatures and gas densities. The absorption also depends on the viewing angle of the system. If the line of sight coincides with the accretion stream, we are likely to

see more complex absorption because we are looking through layers of accreting gas at different densities. Thus, in order to make the absorption more complex in the spectral model, I tested the partial covering absorption model, `pcfabs`, together with the optically thin thermal plasma model. The partial covering absorption, $M(E)$, is given by

$$M(E) = Ce^{-n_H\sigma(E)} + (1 - C), \quad (2.7)$$

where C is a dimensionless covering fraction. Note that when $C=1$, the model becomes the simple photoelectric absorption model (`wabs`).

The total pn and MOS spectra were fitted simultaneously, and parameters, such as the absorption column n_H , the plasma temperature kT , the normalisations, α and the covering fraction C , were kept tied between the three spectra, rather than allowing them to vary free. When carrying out the spectral fits, the abundance was fixed at the solar value since letting it vary did not improve the fits (free abundance resulted as $1.03_{-0.56}^{+0.65}$). Also, the hydrogen density of the `mekal` group of models, the redshift and the switch parameter controlling the calculation method of the models were kept frozen to their default values and tied between the three spectra.

Fitting with the absorbed optically thin thermal plasma model and a blackbody showed that the blackbody normalisation tended toward 0 (the normalisation of the black body model with errors of 90 per cent confidence on one parameter of interest was $3.45_{-1.76}^{+1.67} \times 10^{-6}$). Thus, the presence of the blackbody component was unnecessary in the spectral fit, and was removed. The absorbed optically thin thermal plasma model without a blackbody provided an equally good description of the data with $\chi^2_\nu = 1.08/361$ and yielded spectral fit parameters of $n_H = (1.77 \pm 0.6) \times 10^{20} \text{ cm}^{-2}$, $kT = 29_{-7.80}^{+11.72} \text{ keV}$, and a mean absorbed flux of $1.37 \times 10^{-12} \text{ erg cm}^{-2} \text{ s}^{-1}$ (0.2–12 keV), all errors 90 per cent confidence on one interesting parameter. Table 2.4 lists the χ^2_ν values for the spectral fits performed for the pn and the MOS data using different models, and shows that the χ^2_ν values are equally good for the absorbed optically

Table 2.4: The reduced χ^2 values and degrees of freedom (ν) of the spectral models of J1312 for the total pn and MOS spectra which have been fitted simultaneously. P_0 is the null-hypothesis probability.

Model	χ^2_ν/ν	P_0
wabs(bb+mekal)	1.07/359	0.172
wabs(mekal)	1.08/361	0.134
pcfabs(mekal)	1.08/360	0.136
wabs*pcfabs(mekal)	1.08/359	0.137
wabs(cemek1)	1.08/361	0.136

thin thermal plasma models with and without the blackbody.

Table 2.4 shows that the spectral fits with more complex absorption models (partial covering) are equally good as with the simpler absorption model (wabs), and thus do not provide evidence of the expected complexity in the post-shock column. Also, the multi-temperature model cemek1 did not improve the fit. The conclusion is that a strong distinction between the different models can not be made. Thus, I choose the least complex model, i.e. the photo-electrically absorbed optically thin thermal plasma model as the best-fit model.

Fig. 2.11 illustrates the total pn and MOS spectra fitted with the best-fit model, i.e. the absorbed optically thin thermal plasma model, and Fig. 2.12 the 68, 90 and 99 per cent confidence contours for the total pn, MOS1 and MOS2 spectra for the plasma temperature kT and the absorption column n_H . These parameters seem to be anti-correlated, but not very strongly (a clear banana-shaped correlation is not seen). In other words, an anti-correlation in this case means that higher plasma temperatures can be obtained by lowering the absorption column and vice versa.

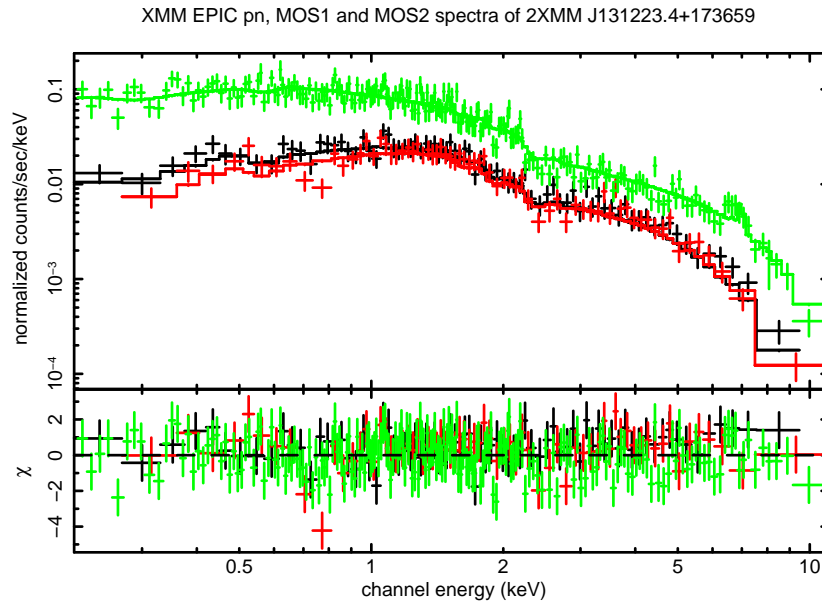


Figure 2.11: Top panel: pn (green), MOS1 (black) and MOS2 (red) X-ray spectra of J1312 fitted with the best-fit model (photoelectrically absorbed optically thin thermal plasma model). The $\chi^2_{\nu} = 1.08$ for 361 degrees of freedom (d.o.f). Lower panel shows the residuals.

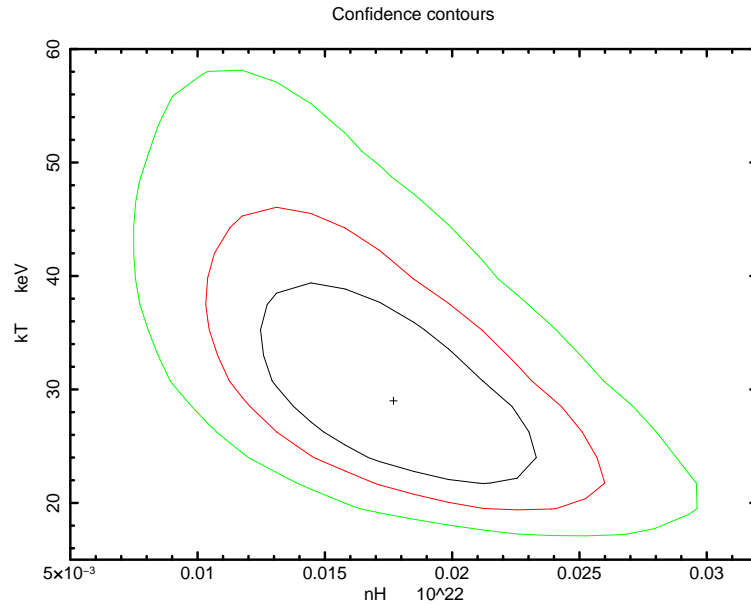


Figure 2.12: The 68, 90 and 99 per cent confidence contours of the parameters kT and n_H for the joint spectral fit of the total pn, MOS1 and MOS2 spectra, using the absorbed optically thin thermal plasma model.

2.5.1 Phase-resolved spectra

Five pn spectra from the bright phases of the binary orbit of J1312 were extracted in order to study the variation (if any) in the phase-resolved spectra. These phase-resolved spectra corresponding to the orbital phase intervals in Fig. 2.8 are $\phi_1 = 0.02\text{--}0.20$, $\phi_2 = 0.60\text{--}0.75$, $\phi_3 = 0.75\text{--}0.84$, $\phi_4 = 0.84\text{--}0.91$ and $\phi_5 = 0.91\text{--}0.99$. Since the combined effective area of the two MOS detectors is nearly equal to the effective area of the pn detector, extracting phase-resolved spectra of the MOS data was not considered necessary as they do not provide significant additional information to the pn spectra.

Similarly to the total X-ray spectra, the same spectral models were employed when fitting the phase-resolved spectra, and the spectra were fitted simultaneously for each model. Since each phase-resolved spectrum represents a different physical part of the binary, viewed at different phases of the orbit as the system revolves, the spectral fitting parameters (n_H , kT , normalisations of the models, C and α) were not tied between the spectra, and they were let to vary free (except the abundance, the hydrogen density of the mekal group of models, the redshift and the switch parameter controlling the calculation method of the model, which were kept frozen to their default values).

The χ^2_ν values of the joint spectral fits of the five phase-resolved spectra are given in Table 2.5. The absorbed optically thin thermal plasma model with a blackbody yielded the best χ^2_ν of all of the models in Table 2.5. However, similarly to the total X-ray spectra, the blackbody normalisation approached 0 for each phase-resolved spectrum, and consequently the blackbody model was removed (for example, the blackbody normalisation with errors of 90 per cent confidence on one parameter of interest was $3.08^{+2.35}_{-2.16} \times 10^{-7}$ for the phase-resolved spectrum in the phase interval $\phi_2 = 0.60\text{--}0.75$). Since the goodness of fit values of all the models were acceptable and there was no significant difference between them, the simplest model, i.e. the absorbed optically thin thermal plasma model was chosen as the best-fit model, as previously used when fitting the total pn and MOS spectra. The best-fit n_H and kT parameters are given

Table 2.5: The spectral models with their χ^2_ν values and the null hypothesis probabilities P_0 for the five, phase-resolved spectra which have been fitted simultaneously with each model.

Model	χ^2_ν/ν	P_0
wabs(bb+mekal)	0.97/199	0.612
wabs(mekal)	1.01/209	0.467
pcfabs(mekal)	1.00/204	0.477
wabs*pcfabs(mekal)	0.99/199	0.510
wabs(cemekl)	1.02/203	0.406

in Table 2.6 for the phase-resolved spectra, and the spectra fitted with the best-fit model are illustrated along with their residuals in Fig. 2.13.

Table 2.6 shows that the absorption n_H increases throughout the different phases towards the eclipse by the secondary star at phase interval $\phi_5 = 0.91\text{--}0.99$ in Fig. 2.8. The change in n_H after phase $\phi_2 = 0.60\text{--}0.75$ (the bright phase in the folded light curve in Fig. 2.8 right after the white dwarf self-occultation), is clearly related to the assumed accretion stream passing through the line of sight absorbing softer photons and causing the dips (discussed in Section 2.3.1) in the soft X-ray light curve in Fig. 2.8.

The plasma temperature kT also increases after phase ϕ_2 , and is not constrained after this phase. Thus, Table 2.6 only quotes the lower 90 per cent limits for the temperatures for phases $\phi_3\text{--}\phi_5$. The increase in n_H and kT is consistent with the rise in the fraction of hard X-rays in Fig. 2.8, and with the spectral hardening seen in Fig. 2.13. The plasma temperature, $kT \approx 8\text{--}14$ keV, as measured from the first two phases ϕ_1 and ϕ_2 (Table 2.6), is consistent with plasma temperatures measured in other magnetic CVs (Ezuka & Ishida, 1999), and probably represents an average plasma temperature in the accretion column of J1312 (the shock temperature would be higher assuming that the white dwarf has a mass of $\sim 0.6\text{--}1.0$

Table 2.6: The best-fit parameters of the photoelectrically absorbed optically thin thermal plasma model for each phase ϕ_1 – ϕ_5 . Errors refer to $\Delta\chi^2 = 2.71$ (90 per cent confidence for one parameter of interest.)

Phase	n_H	kT
	10^{20} cm^{-2}	keV
$\phi_1 = 0.02$ – 0.20	$0.84^{+1.39}_{-0.84}$	$14.61^{+16.09}_{-5.23}$
$\phi_2 = 0.60$ – 0.75	$2.10^{+1.12}_{-0.91}$	$8.23^{+3.27}_{-2.01}$
$\phi_3 = 0.75$ – 0.84	$2.78^{+2.14}_{-1.54}$	> 28.19
$\phi_4 = 0.84$ – 0.91	$5.44^{+4.64}_{-3.20}$	> 14.55
$\phi_5 = 0.91$ – 0.99	$12.70^{+5.65}_{-4.59}$	> 28.28

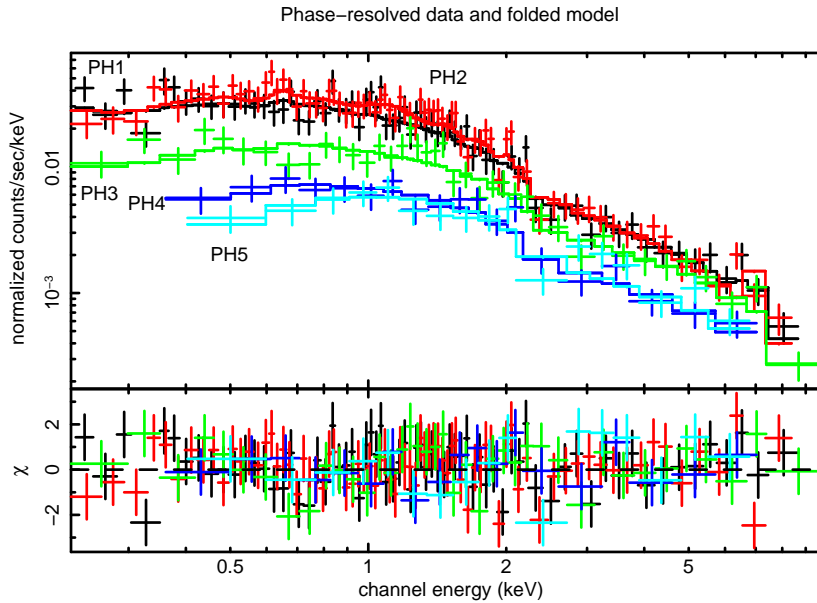


Figure 2.13: Top panel: The five phase-resolved EPIC pn X-ray spectra of the *XMM* polar candidate J1312 fitted with an absorbed optically thin thermal plasma model (the best-fit model). The hardening of the spectra is clear as the spectral shape changes from phase 1 (black) towards phase 5 (dark blue). Lower panel shows the residuals. The goodness of fit is $\chi^2_\nu/\nu = 1.01/209$.

M_{\odot}).

2.6 Discussion

2.6.1 System geometry

The secondary stars of cataclysmic variables generally follow the mass-radius law of empirical Zero Age Main Sequence (ZAMS) stars (Patterson, 1984). For ZAMS stars of mass between $0.1 < \frac{M}{M_{\odot}} \lesssim 0.8$ the following empirical mass-radius relationship applies:

$$\frac{R_2}{R_{\odot}} = \left(\frac{M_2}{M_{\odot}} \right)^{0.88}, \quad (2.8)$$

where R_2 is the volume radius of the Roche lobe of the secondary star, and M_2 the mass of the secondary star. For Roche lobe filling secondary ZAMS stars, M_2 is proportional to the orbital period P according to (Patterson, 1984)

$$\frac{M_2}{M_{\odot}} = 0.380 P_4^{1.22}, \quad (2.9)$$

where P_4 is the orbital period in units of four hours, i.e. $P/(4 \text{ h})$. For J1312, this equation yields a secondary mass of $M_2 = 0.12 M_{\odot}$ for the derived orbital period of $\sim 91.8 \text{ min}$. The secondary mass of J1312 is consistent with the measured secondary masses for other CVs, such as HT Cas ($M_2 = 0.09 \pm 0.02 M_{\odot}$, $P_{orb} = 1.768 \text{ h}$, Horne, Wood, & Stiening, 1991), or OY Car ($M_2 = 0.09 \pm 0.01 M_{\odot}$, $P_{orb} = 1.515 \text{ h}$, Hessman et al., 1989). Using the empirical mass-radius relation in Eq. 2.8, the obtained secondary radius of J1312 is $R_2 = 0.15 R_{\odot}$. According to the Harvard spectral classification system, these values indicate that the secondary of J1312 is a late-type star belonging to the spectral class M and has an

effective temperature of $T_{eff} \leq 3700$ K. Fig. 5 in Beuermann et al. (1998) shows that the spectral type corresponding to the orbital period of ~ 92 min is \sim M5.5-M6.

Next, I derived some constraints for the parameters, such as inclination i , for the system geometry of J1312. In order to see an eclipse at an inclination i , the following condition must be fulfilled (Hilditch, 2001):

$$\sin(90^\circ - i) \leq (R_1 + R_2)/a, \quad (2.10)$$

where a is the distance between the binary components and R_1 and R_2 the radii of the components. Here it is assumed that the radius of the primary component is infinitesimal compared to the radius of the secondary star, and thus not taken into account in the calculations. The duration of the short eclipse by the secondary star, ε , and the duration of the bright phase, $\Delta\phi$, were used to derive constraints for the system geometry of J1312. ε and $\Delta\phi$ were estimated from the folded light curve in Fig. 2.8 ($\varepsilon = 0.04$ and $\Delta\phi = 0.60$ phase units). The eclipse duration ε can be derived geometrically and calculated from

$$(\varepsilon/2)^2 = (\sin^{-1}(R_2/a))^2 - (90^\circ - i)^2, \quad (2.11)$$

The radius of the secondary star, R_2 , is related to the mass ratio q according to Paczyński (1971),

$$\frac{R_2}{a} = 0.462 \left(\frac{q}{1+q} \right)^{1/3} \beta, \quad (2.12)$$

where $q = M_2/M_1$ (M_1 is the mass of the primary), and $\beta = 1$ for $q < 0.52$. Now, when substituting R_2/a in Eq. 2.11 by Eq. 2.12, the white dwarf mass, M_1 , can be derived from

$$M_1 = M_2 \left(\left(\left(\sin \sqrt{(90^\circ - i)^2 + (\varepsilon/2)^2} \right) / 0.462 \right)^{-3} - 1 \right). \quad (2.13)$$

Next we want to know how to derive the colatitude of the emission region on the white dwarf surface. Colatitude is the distance of the emission region from the rotational axis of the white dwarf. For a point-like emission region, the relation (Osborne et al., 1988) between the bright phase $\Delta\phi$, the colatitude δ and the inclination i is

$$\cos(\pi\Delta\phi) = -\cot\delta \cot i. \quad (2.14)$$

Fig. 2.14 illustrates the system parameters which have been derived using Eq. 2.13 and 2.14 above. The white dwarf mass M_1 and the colatitude δ of the emission region are plotted as a function of inclination i . The green curve rising from $i = 90^\circ$ describes the colatitude of the emission region which is constrained by the inclination and the duration of the bright phase $\Delta\phi$ according to Eq. 2.14. The three blue curves starting from $i = 65^\circ$ correspond to the best estimate of the white dwarf mass (the middle curve) and its 90 per cent confidence limits as a function of inclination, derived using Eq. 2.13. The maximum allowed white dwarf mass is shown by the upper green horizontal line which is the Chandrasekhar mass limit $1.44 M_\odot$. The horizontal lower red line corresponds to the minimum white dwarf mass limit, $M_1 \sim 0.14 M_\odot$, below which stable accretion is not possible, corresponding to mass ratio $q < 5/6$ (Frank, King, & Raine, 2002). From Fig. 2.14 we can see that the lower limit for the inclination corresponding to the stable accretion criterion (i.e. to the limit where the blue curves coincide with the lower, horizontal red line) is $i \sim 72^\circ$. The x-axis corresponds to a zero mass white dwarf which sets the minimum boundary, $i \sim 65^\circ$, for the inclination. Since the colatitude depends on the inclination, the colatitude is $\delta < 42^\circ$, which is consistent with $i > 72^\circ$.

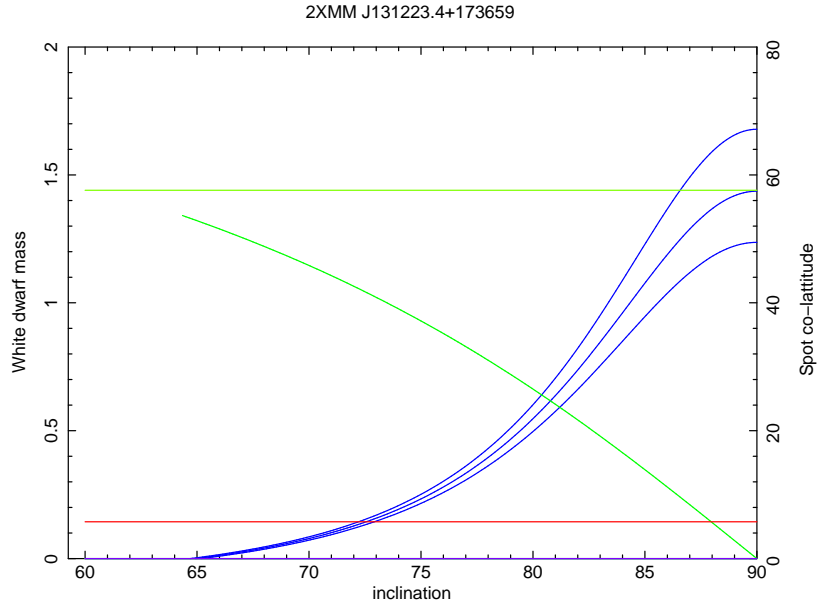


Figure 2.14: The system geometry of J1312. The horizontal lines (green and red) describe the maximum mass limit (Chandrasekhar mass $1.44 M_{\odot}$) and the stable accretion mass limit ($M_1 \sim 0.14 M_{\odot}$) for the white dwarf, the green curve rising from the right hand corner the colatitude δ of the emission region as a function of inclination i , and the three curves rising from $i = 65^{\circ}$ the best estimate for the white dwarf mass (middle curve) with 90 per cent confidence limits.

2.6.2 The missing soft X-ray component

Polars have been known as strong soft X-ray emitters at energies of $\lesssim 0.1$ keV (Frank, King, & Raine, 2002). As was discussed in the introduction of this chapter, *ROSAT* PSPC, due to its sensitivity in soft X-rays, discovered numerous polars. Examples of polars having a soft X-ray component are UZ For (Osborne et al., 1988), QQ Vul (Osborne et al., 1987) and HU Aqr (Schwope et al., 2001). On the contrary to this traditional picture, recent polar observations have shown that the soft component is not always seen, as is the case in J1312. Ramsay & Cropper (2004) studied a sample of 21 polars of which 6 did not show a distinct soft X-ray component. In addition to these 6 systems, the absence of a soft X-ray component has also been seen in the eclipsing polars V2301 Oph (Ramsay & Cropper, 2007), and in 2XMMi J225036.9+573154 (Ramsay et al., 2009). Ramsay et al. (2009) reported that out of 27 polars observed by *XMM-Newton* during their high accretion states ($\dot{M} \sim 10^{-11}$ – $10^{-10} M_{\odot} \text{ yr}^{-1}$, Warner, 1995; Schwope et al., 2002b), 10 sources did not show soft components. Thus, these

observations are changing the general assumption that polars are strong soft X-ray emitters. The reason for the lack of a soft X-ray component in some systems is thought to be due to a large fractional area f over which accretion occurs on the white dwarf surface, or a lower mass accretion rate \dot{M} , (e.g. Ramsay & Cropper, 2004; Ramsay et al., 2009), resulting in a lower blackbody temperature, since the effective temperature $T_{eff} \propto (\dot{M}/f)^{1/4}$ (King & Lasota, 1990). Thus, the soft component would be unobservable in the X-ray band due to the low temperature, and move to the EUV, or the UV region.

2.7 Conclusions

In this chapter, I have analysed the *XMM* data of the polar candidate J1312 in order to find more supporting evidence for its polar-like nature. The shape of the folded X-ray light curve of J1312 ($P_{orb} \approx 91.8$ min) shows similar behaviour to other eclipsing AM Her type stars. The X-ray light curve of J1312 shows two excursions to zero intensities: 1) a longer one which is assumed to be caused by the self-occultation of the white dwarf, and 2) a short and deep eclipse caused by the secondary star. In addition, the X-ray light curve is characterised by a reduction in soft X-rays suggesting the presence of an accretion column crossing our line of sight. The spectral hardening together with a rising absorption column towards the phase where the reduction in soft X-ray flux is seen, support the view of an absorbing accretion stream.

The derived plasma temperature (~ 8 – 14 keV) is consistent with the plasma temperatures measured in other, known magnetic CVs. A soft X-ray component, usually considered as a general characteristic for polars, is not present in these data. The lack of a soft component could be due to the low temperature of this component: if the accretion stream is extended, this leads to a larger and lower temperature accretion region on the white dwarf surface. In this case, the soft component has moved out from the X-ray band to the EUV.

The lower limit for the white dwarf mass, M_1 , corresponding to the stable mass accretion criterion, is $M_1 > 0.14 M_\odot$, and the corresponding system inclination $i > 72^\circ$. The colatitude of the emission region on the white dwarf surface has to be $\delta < 42^\circ$, in order to be consistent with the inclination limit of $i > 72^\circ$.

Chapter 3

SWIFT observations of GW Lib: a unique insight into a rare outburst

3.1 Introduction

GW Librae (hereafter GW Lib), which is a WZ Sge type dwarf nova (DN), was discovered in 1983 when it went into an outburst (Maza & Gonzalez, 1983). It was present in ESO B Survey plates at magnitude 18.5 preceding the 1983 outburst. GW Lib was first classified as a nova due to its brightening by 9 magnitudes during the outburst and then fading back to the quiescent state. Later studies showed that the optical spectrum resembled a dwarf nova in quiescence (narrow H emission lines with broad H absorption lines with some heavier emission elements) (Duerbeck & Seitter, 1987). Also, the quiescence optical *SAAO* spectrum obtained in 1997 was a spectrum typical of that of a cool and low mass-transfer rate CV (van Zyl et al., 2000); the spectrum showed H emission lines sitting on top of broad Balmer absorption lines. Since 1983, no other outbursts of GW Lib had been observed until that of April 12, 2007 (Templeton, 2007). This outburst, which was recorded by the *AAVSO* observers, *WASP-South* and by *Swift*, lasted for 26 days. The brightest optical magnitude was reached at ~ 8

mag in the *V* band. GW Lib has been classified as a WZ Sge type star due to its short period ($P_{orb} = 76.78$ min, Thorstensen et al., 2002) and low accretion rate (van Zyl et al., 2004). Typical characteristics of WZ Sge type stars are short orbital periods, low mass-transfer rates in quiescence ($\lesssim 10^{15}$ g s $^{-1}$), and extremely long recurrence times which can last for decades.

GW Lib was the first observed CV in which the accreting white dwarf showed non-radial pulsations (Warner & van Zyl, 1998). This phenomenon was an unexpected discovery since accreting binaries were considered to be too hot to be located in the DAV instability (evolutionary) strip (van Zyl et al., 2000). Pulsations of white dwarfs are thought to be due to g-mode non-radial gravity waves (Koester & Chanmugam, 1990). DAV describes the spectral type of a white dwarf and means that the white dwarf has a hydrogen-dominated atmosphere (also known as ZZ Ceti stars). The effective temperatures, T_{eff} , of DAV white dwarfs are found to be in a narrow range between 12,500 and 11,100 K (Bergeron et al., 2004). In GW Lib, pulsations are seen near 230, 370 and 650 s in the optical waveband (e.g. *SAAO* data), and also in the *Hubble Space Telescope* (HST) UV data but with ~ 6 times higher amplitudes than in the optical (Szkody et al., 2002b). An *XMM-Newton* observation of GW Lib obtained in 2005 during its quiescent state reveals that these pulsations are also present in the *XMM-Newton* Optical Monitor (OM) data, but not seen in the X-ray data (Hilton et al., 2007). These *XMM-Newton* observations also confirmed that GW Lib has a very low accretion rate during quiescence.

In this chapter, I present the 2007 outburst light curves of GW Lib in the optical (*AAVSO* and *Wasp-South*), UV (*Swift*, UVOT) and X-ray (*Swift*, XRT) bands, and the results of X-ray spectral analysis of the outburst data, and also follow-up *Swift* observations of GW Lib obtained in 2008 and 2009. Based on the data analysis, I aim to clarify the picture of the disc structure in GW Lib. I will also compare the observations of GW Lib with the observations of other SU UMa type systems. Previous multiwavelength observations covering outbursts of SU UMa (and WZ Sge) type systems have been obtained from e.g. VW Hyi (Pringle et al., 1987; Wheatley et al., 1996b), WZ Sge (Kuulkers et al., 2002; Wheatley & Mauche, 2005),

and OY Car (Mauche & Raymond, 2000). Multiwavelength observations of DNe are needed in order to enhance our knowledge of astrophysical systems with discs including CVs, X-ray binaries and AGNs. DN outbursts provide a good opportunity to study the disc physics, and compare the current theory of outbursts with the information obtained from DN observations. The fact that GW Lib does not show any normal outbursts and the recurrence time between the 1983 and the 2007 outbursts was over 20 years, suggests that the inner disc structure could be different from most other DNe. Thus, it is essential to study the outbursts in particular in X-rays, as X-rays provide important clues to the inner region of the accretion disc.

3.2 Observations and data reduction

GW Lib was initially observed by *Swift* between April 13th and May 16th, 2007, over an interval of 30 days. The data were obtained with the Ultraviolet/Optical Telescope (UVOT) and with the X-ray Telescope (XRT) which has an energy resolution of 140 eV at 5.9 keV (at launch) ($R \sim 40$, Capalbi et al., 2005). The XRT was operating in the Window Timing (WT) and Photon-Counting (PC) modes during the observations. The UVOT observations were obtained in the imaging mode with the UV grism in order to provide spectral information and to mitigate against coincidence losses. The resolution of the UV grism is $R \sim 150$ for 11–15 magnitude range stars¹. The details of the 38 observations are listed in Table 3.1. The first two UVOT observations were obtained in imaging mode with the UVM2 filter, but these suffer from severe coincidence loss effects and were thus excluded from the analysis. The optical data were provided by the AAVSO observers and by the *Wide Angle Search for Planets* (WASP) (Pollacco et al., 2006).

In addition to the outburst observations, follow-up *Swift* observations of GW Lib were made in April-May 2008 and February-March 2009. For these observations, the *V* and *UVW1* filters were used in the UVOT instrument. The details of these observations are also given in

¹http://heasarc.gsfc.nasa.gov/docs/swift/analysis/uvot_ugrism.html

Table 3.1: The *Swift* XRT and UVOT observations of GW Lib obtained in 2007, 2008 and 2009.

OBSID	Tstart	Roll angle	UVOT	XRT WT	XRT PC	Ugrism
		deg.	exp. (s)	exp. (s)	exp. (s)	exp. (s)
30917001	2007-04-13T15:19:47	133	4914	2902	1910	0
30917002	2007-04-18T06:22:00	136	4781	4755	0	0
30917003	2007-04-20T17:53:57	141	992	5	990	992
30917004	2007-04-21T03:47:02	142	769	4	772	769
30917005	2007-04-21T14:55:01	142	904	2	910	904
30917006	2007-04-21T22:56:00	142	1442	4	1447	1442
30917008	2007-04-22T23:02:00	142	1264	2	1271	1264
30917009	2007-04-23T11:42:01	142	1050	8	1048	1050
30917010	2007-04-24T00:50:00	142	1352	13	1349	1352
30917011	2007-04-24T13:38:01	142	1288	4	1294	1288
30917012	2007-04-25T02:38:00	142	1635	6	1639	1635
30917013	2007-04-25T12:15:01	142	1632	10	1634	1632
30917014	2007-04-26T02:50:01	142	1393	5	1400	1393
30917015	2007-04-26T20:30:01	142	1344	6	1350	1344
30917016	2007-04-27T02:28:00	155	5868	12	5890	5868
30917017	2007-04-29T01:05:00	155	5643	15	5659	5643
30917018	2007-05-01T01:18:01	168	3150	6	3162	3150
30917019	2007-05-05T09:46:01	168	1597	3	1605	1597
30917020	2007-05-05T22:38:01	168	1596	2	1605	1596
30917022	2007-05-07T00:20:00	151	1589	9	1588	1589
30917023	2007-05-07T11:35:01	151	1358	2	1364	1358
30917024	2007-05-07T22:50:00	151	1595	7	1590	1595
30917025	2007-05-08T10:09:00	156	1294	2	1294	1294
30917026	2007-05-08T21:24:01	156	1247	2	1249	1247
30917027	2007-05-09T08:41:00	156	875	6	872	875

Table 3.1: The *Swift* XRT and UVOT observations of GW Lib obtained in 2007, 2008 and 2009, contd.

OBSID	Tstart	Roll angle deg.	UVOT exp. (s)	XRT WT exp. (s)	XRT PC exp. (s)	Ugrism exp. (s)
30917028	2007-05-09T19:49:01	156	1496	2	1504	1496
30917029	2007-05-10T00:45:01	162	1457	4	1462	1457
30917030	2007-05-10T18:19:00	162	1577	4	1582	1577
30917031	2007-05-11T07:10:01	162	1433	3	1439	1433
30917032	2007-05-11T18:25:01	162	1369	5	1371	1369
30917033	2007-05-12T07:16:00	162	1372	10	1366	1372
30917034	2007-05-12T18:31:00	162	1372	2	1379	1372
30917035	2007-05-13T05:46:01	162	1157	4	1161	1157
30917036	2007-05-13T18:37:00	162	1313	4	1319	1313
30917037	2007-05-14T07:28:01	162	1373	4	1377	1373
30917038	2007-05-14T18:42:01	162	1250	3	1255	1250
30917039	2007-05-15T07:34:01	162	1400	2	1406	1400
30917041	2007-05-16T04:27:01	162	1947	6	1956	1947
30917042	2008-04-24T17:33:01	150	4772	0	4959	0
30917043	2008-05-01T18:25:09	173	83	0	122	0
30917044	2008-05-08T12:38:01	151	1612	0	1627	0
30917045	2009-02-22T02:16:00	111	5939	0	5779	0
30917046	2009-03-02T03:10:01	112	4536	0	4586	0

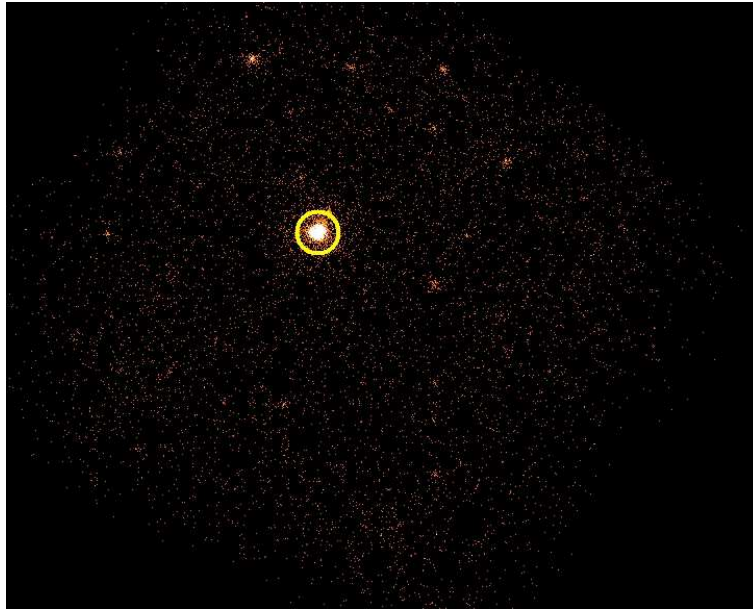


Figure 3.1: A combined PC mode X-ray image of the observations 00030917003–7018. GW Lib has been circled in yellow. The image is shown in logarithmic scale over the energy band 0.3–10 keV.

Table 3.1. The X-ray observation, 7043, did not provide useful information (it was only 83 s long), and so was excluded from the analysis.

3.2.1 X-ray data reduction

The X-ray data reduction was performed with the standard *Swift* pipelines (XRTPIPELINE) retaining grades 0–12 for the PC mode and 0–2 for the WT mode data. These are the standard good grades for the PC and WT mode data. The *Swift* X-ray data cover the energy range 0.3–10 keV, but GW Lib is detected only up to 8.0 keV. The X-ray light curve was extracted automatically from the WT and PC mode data by using the tools described in Evans et al. (2009) which also correct for pile-up.

The X-ray spectra were extracted with the FTOOL XSELECT which is an interactive program used for examining event files and creating data products. For the WT mode data, a 40 pixel (94”) extraction box for the source and an 80 pixel (189”) box for the background region were

used. The normal limit for pile-up in WT mode data is $\sim 100 \text{ ct s}^{-1}$ (Romano et al., 2006). Thus, it was not necessary to correct for pile-up for the WT mode since the count rate was safely below the pile-up limit (the 00030917001 WT mode observation yields a count rate of $\sim 10 \text{ ct s}^{-1}$ for the whole field). The PC mode source data were extracted using a 20 pixel (47") circle which covers 90 per cent of the point spread function (PSF), and the background data within a 60 pixel (141") circular area. Fig. 3.1 shows an image of the field of view of GW Lib (circled in yellow) during the outburst in the PC mode data from the combined observations between the 20th of April and the 1st of May, 2007.

For the first observation, only the WT mode data were used for spectral extraction since the exposure time of the WT mode is longer than for the PC mode data, and the WT data were not piled-up. The second observation does not contain PC mode data, most likely due to too high a count rate for this mode. Although the source count rates of the PC mode data before the background subtraction from the second observation (7002) onwards were low ($\sim 0.4 \text{ ct s}^{-1}$), the PSFs of the PC mode data were checked in case of pile-up by fitting a King function with $r_c = 5.8$, $\beta = 1.55$ (Moretti et al., 2005), and looking for an excess above the nominal profile shape. The definition for the King function was given in Chapter 2. A rough limit for the pile-up of PC mode data² is 0.6 ct s^{-1} . No pile-up was seen, see Fig. 3.2 which shows the source PSF from the combined observations 00030917003–7018 and the fitted King function as an example. Exposure maps were created with XRTEXPOMAP. These are needed in order to correct for possible flux losses if bad columns overlap with the source. Bad columns in the WT and PC modes were caused by a hit of a micrometeorite in 2005. The exposures maps were given as an input to XRTMKARF which creates ancillary response files (ARFs) for the spectra. The ARFs will correct for possible flux losses due to bad columns on the source and loss of flux due to sizes of the extraction regions which do not cover the total source flux.

²<http://www.swift.ac.uk/pileup.shtml>

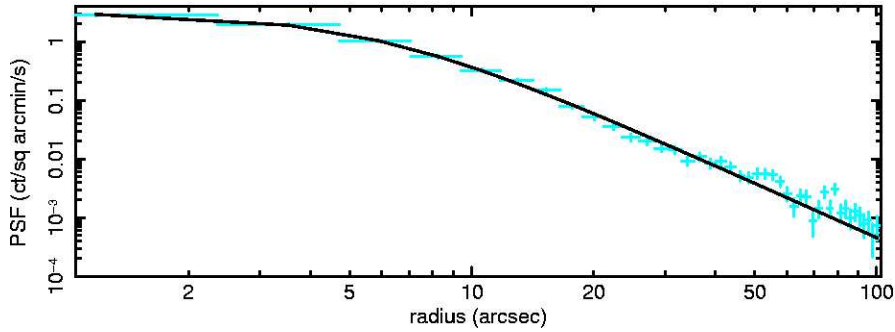


Figure 3.2: The XRT PSF of GW Lib over the energy band 0.3–10 keV from the combined observations 00030917003–7018 fitted with a King function with a PSF core radius of $r_c = 5.8$ and a slope $\beta = 1.55$.

3.2.2 UV grism data reduction

In the UV grism mode, the UVOT provides slitless, medium/low dispersion data ($2.0\text{--}3.5 \text{ \AA pixel}^{-1}$) covering the wavelength range $1700\text{--}2900 \text{ \AA}$. The UV grism spectrum extends far beyond 2900 \AA but beyond 2900 \AA there is contamination by the second order spectrum. The absence of a slit, together with sun-angle observing constraints which prevent us from precisely controlling the spacecraft roll-angle at which the observations were taken, means that the UVOT UV grism data suffer from a number of artifacts. The most important of these is the contamination of the extracted spectrum by other sources in both the source extraction and source background windows. This means that the size, orientation and placement of the source extraction and background extraction slits must be handled with extreme care. In this analysis, these have been chosen on a roll-angle by roll-angle basis.

The UV grism can operate in either *clocked* or *nominal* mode. The clocked mode is useful in crowded fields as it reduces the total background flux, and it has a slightly better sensitivity than the nominal mode. Also, spatial variations in wavelengths and sensitivity are smaller than in the nominal mode. In principle, the clocked mode should reduce contamination of the 1st order spectra by unrelated 0th order images. However, the default UV grism clocking is insufficient to perform this separation between the 1st and 0th order spectra. This can be seen in Fig. 3.3 where the separation between the 1st and 0th order spectra is not large enough,

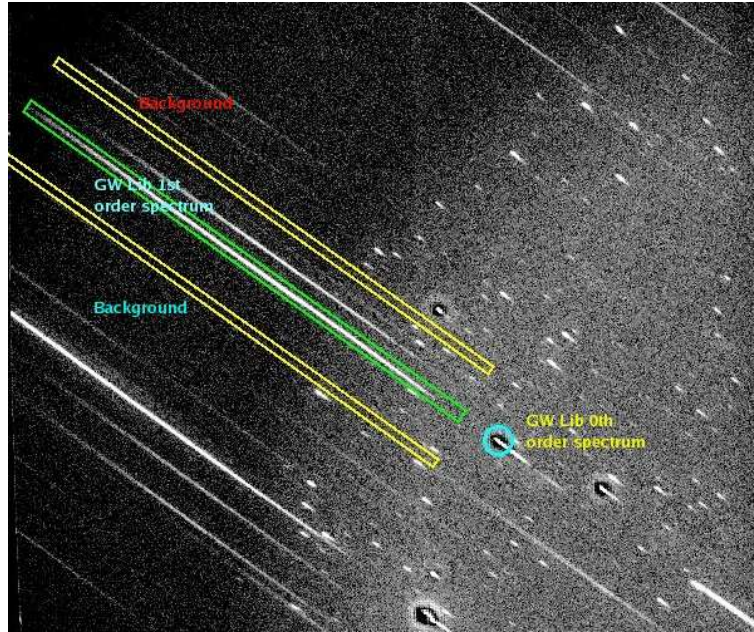


Figure 3.3: A *Swift* UV grism observation (ObsID 00030917023) of GW Lib on the 7th of May, 2007. The image shows the 0th (circled in blue) and 1st (inside the green box) order spectra and the background extraction regions (yellow boxes) for this extension. Since the UVOT grism observations are slitless, all sources in the field of view are dispersed.

thus the 0th order spectra may overlap with the 1st order spectra. For fields which are not crowded, the choice between the nominal and clocked modes is often roll-angle dependent, i.e. which mode gives a better roll angle. The *Swift* UV grism was operating in the clocked mode at the time of the outburst observations.

The UVOT suffers from *coincidence loss effects* (i.e. pile-up) which are not easy to correct for, and currently there is no formal way of correcting for them. Significant coincidence losses start at 10 ct s^{-1} per physical pixel with a readout time of $\sim 11 \text{ ms}$ for the full CCD (Poole et al., 2008). The significance of coincidence losses is determined by averaging over a 3×3 physical pixel array for which the count rate must not exceed $\sim 100 \text{ ct s}^{-1}$. This translates to 100 ct s^{-1} over a 24×24 image pixel array or equivalently 0.17 ct s^{-1} per image pixel. In these UV grism data, the coincidence loss is clearly visible in the early spectra when the source is at its brightest. The effect of coincidence loss appears in the image as darker areas around the 0th and 1st order spectra. The average count rate is $\sim 0.4 \text{ ct s}^{-1}$ per image

pixel which was measured with the GAIA software using the first snapshot of the ObsID 00030917003 when GW Lib was at its brightest.

For the data reduction, I have used an automated pipeline, which is based around the UVOT *Swift* FTOOLS (Immler et al., 2006), for the spectral extraction of the UV grism data. The released version of the *Swift* UVOT analysis software used in this research, HEASOFT v.6.1.2, does not allow grism spectra to be traced, nor extracted optimally, i.e. the signal-to-noise ratio of a spectrum is not maximised. Optimal extraction methods are discussed in Horne et al. (1985). Thus under FTOOLS, the spectral extraction was restricted to using a box of a fixed width for both source and background regions. Box extraction raises a number of important issues. First, the extraction box must be well-centred, aligned in so far as is possible with the dispersion direction and broad enough that slight miscentrings of the box do not preferentially exclude flux from the wings of the extracted spectra at specific wavelengths. To investigate the effects of the width of the extraction box, alignment and miscentring for the GW Lib spectra, I performed a variety of tests which are described below.

First, the loss of flux was determined as a function of extraction box width for a well-centred aperture. This was achieved by taking a spatial cut (i.e. a cut in the cross-dispersion direction), and determining the integrated, background-subtracted source counts as a function of box width for an extraction box which is well-centred, see Fig. 3.4. For a well-centred box, a width of 35 pixels contains ~ 90 per cent of the integrated source counts, and this is the width chosen for the rest of the UV grism analysis. Larger box widths increase the source counts, but can also add in poorly subtracted background counts, and thus will not enhance the signal-to-noise ratio (S/N), and further increases the likelihood of contamination by nearby sources. The width of a background extraction box was chosen to be 25 pixels. The background spectrum under the source extraction region is determined by linearly interpolating between the lower and the upper background extraction regions.

If the 1st order spectrum displays significant curvature, an extraction box which is too narrow,

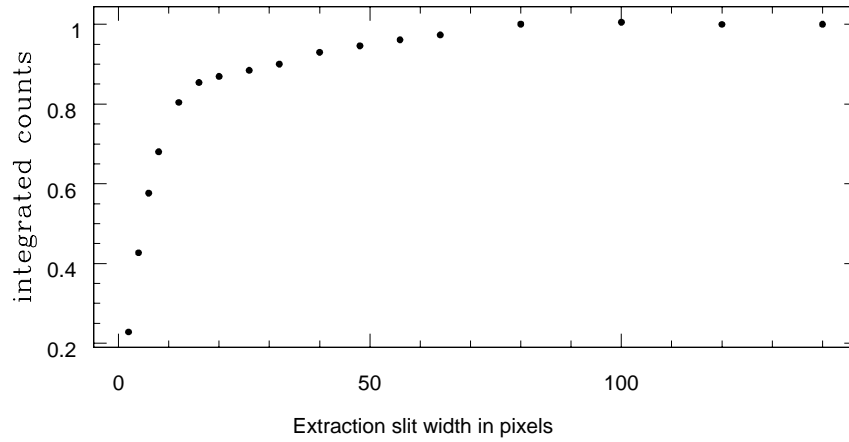


Figure 3.4: The integrated counts of a UV grism spectrum of GW Lib as a function of extraction box width in pixels. A box width of 35 pixels covers ~ 90 per cent of the flux. Narrower box widths reduce the source flux, whereas wider increase the background noise and possible contamination from other sources.

may result in a loss of flux at one end of the spectrum. I measured the deviation of the location of one of the spectra, see the upper panel in Fig. 3.5, relative to the position of the 0th order spectrum (as determined from the RA and DEC of the source), by making spatial cuts at various positions along a single spectrum, fitting them with Gaussians, and measuring their centres. The lower panel shows the full-width at half maximum (FWHM) of the corresponding profiles. The maximum deviation for an extraction box which is aligned with the dispersion direction (as determined from the spacecraft roll-angle), is no larger than ~ 3 image pixels (1 image pixel = 0.009 mm), i.e. flux losses due to curvature of the spectra are negligible. Thus, for a broad extraction box, such as that chosen here, the major source of flux loss from the extraction box is most likely to occur from miscentering the box on the source spectrum.

To estimate the effects of miscentering, a fixed extraction box width of 35 pixels was used, determining the integrated, background-subtracted source counts as a function of offset in pixels from the centre of the cross-dispersion profile, see Fig. 3.6. I estimate that provided the centre of the extraction box is no more than ~ 12 pixels from the centre of the spectrum

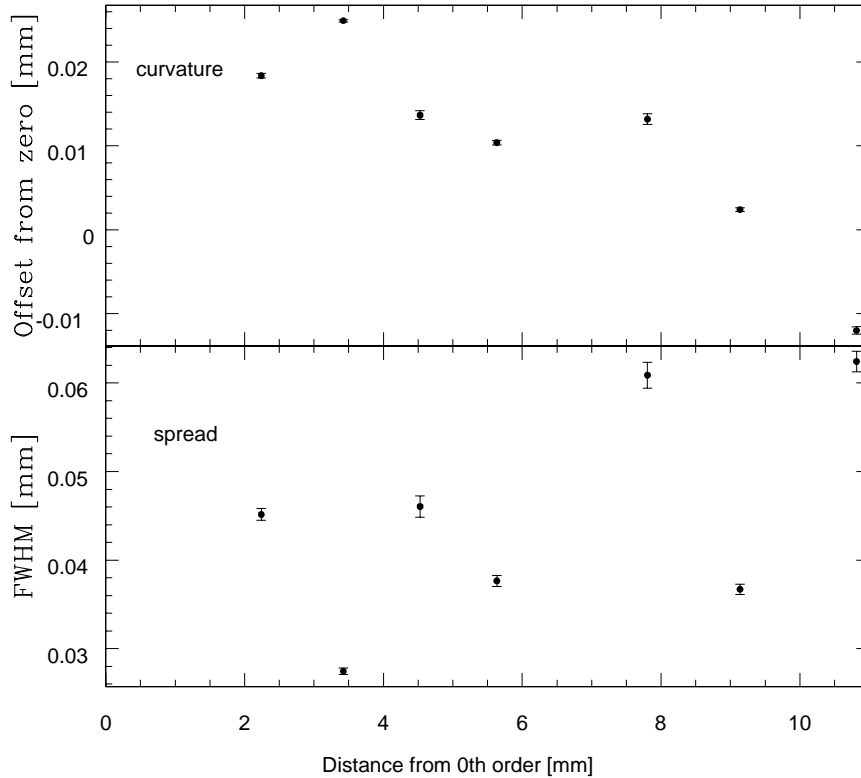


Figure 3.5: Curvature of a UV grism spectrum of GW Lib measured taking spatial profiles over the spectrum (upper panel), and the corresponding FWHM of each profile centre (lower panel).

(i.e. the centre of the cross-dispersion profile), then no significant loss of flux occurs.

After having chosen the extraction box width and background regions for each observation, which are roll-angle dependent, the images were corrected for mod-8 fixed pattern noise, and source and background spectra were extracted automatically using the FTOOL UVO-TIMGRISM. The mod-8 noise is due to centroiding of the photon splash by the onboard algorithm on to an 8×8 pixel grid. Since the sub-pixels (i.e. image pixels) in each physical pixel do not have a uniform effective area, the result is mod-8 noise (mod-8 noise was also mentioned in Chapter 2). Spectral response functions were then created with UVOTRMFGEN. Unfortunately, the last 40 spectra were taken at a roll-angle which placed a nearby source (TYC6766-1570-1, SIMBAD CDS) on a line between GW Lib and in the same direction as the dispersion direction. Thus, the last 40 spectra were severely contaminated by this inter-

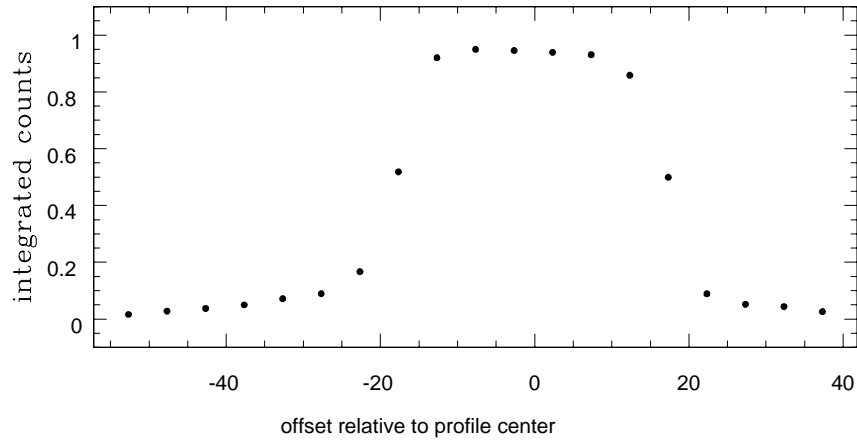


Figure 3.6: Using an extraction box of a width of 35 pixels, no significant loss of flux occurs provided the box is miscentred less than ~ 12 pixels from the centre of the spectrum (cross-dispersion profile).

loper which has proven difficult to remove with any confidence. Therefore, the last 40 spectra were excluded from the analysis.

Due to the lack of a proper calibration of the UV grism wavelength scale, wavelength offsets of between $\sim \pm 20\text{--}30 \text{ \AA}$ ³ are expected in the extracted, wavelength-calibrated spectra. Currently, the UVOT grism data have only been calibrated for on-axis sources. Spatial wavelength scale and sensitivity variations mean that a single wavelength calibration and response are unlikely to be adequate for a series of observations which span a large range of positions on the detector⁴. As a result of the current low quality of the calibration, there might be some flux variations not associated with the source itself that have been inadvertently introduced into the data through the calibration procedure.

³http://heasarc.gsfc.nasa.gov/docs/swift/analysis/uvot_ugrism.html

⁴This can be mitigated to some extent by slew in place but it was not performed for these observations.

3.2.3 UV filter mode data reduction

The 2008 and 2009 UV observations of GW Lib were obtained in filter mode. The magnitudes and fluxes of the *V* and *UVWI* ($\bar{\lambda} = 2600 \text{ \AA}$) filters were derived by using the FTOOL UVOTMAGHIST which calculates instrumental magnitudes and fluxes. The source counts were extracted by using a circular extraction region with a radius of $r_{src} = 5 \text{ arcsec}$ (10 pixels) which is the standard aperture radius and used to derive the photometric zero points for each UVOT filter. An $r_{src} = 5 \text{ arcsec}$ extraction circle contains ~ 86 per cent of the PSF assuming that a 55 pixel aperture radius contains 100 per cent of the PSF (Poole et al., 2008). A circular background extraction region with a radius of $r_{bg} = 10 \text{ arcsec}$ was placed on a source free region in the field of view. Fig. 3.7(a) and (b) show images of the field of view and a close-up of GW Lib and the background regions used in the *UVWI* and *V* filter photometry. The brightest sources in the field of view have suffered from coincidence losses which can be seen as black areas within the sources. Also, the brightest sources in the field of view create ghost images (rings around the sources and in the field of view) as can be seen from Fig. 3.7(a).

3.2.4 SuperWASP data reduction

The *SuperWASP* telescopes observe large areas of the sky in their wide-field imaging instruments (each instrument has a field of view of 482 deg^2). The photometric accuracy of the instruments is better than 1 per cent for objects with *V* magnitude $\sim 7.0\text{--}11.5$. GW Lib falls into a field which was being intensively monitored by the *SuperWASP-South* telescope, fortunately at the time of the outburst, and thus was observed serendipitously. The field of GW Lib (centred on $15^h 02^m, -28^\circ 22''$) was observed between February 16, 2007, and July 19, 2007, with an average of 88 images per night, each with an exposure time of 30 s. Fig. 3.8 shows images 2 days prior to the outburst onset (left), and post-outburst (right) of the field of GW Lib (GW Lib is circled in green).

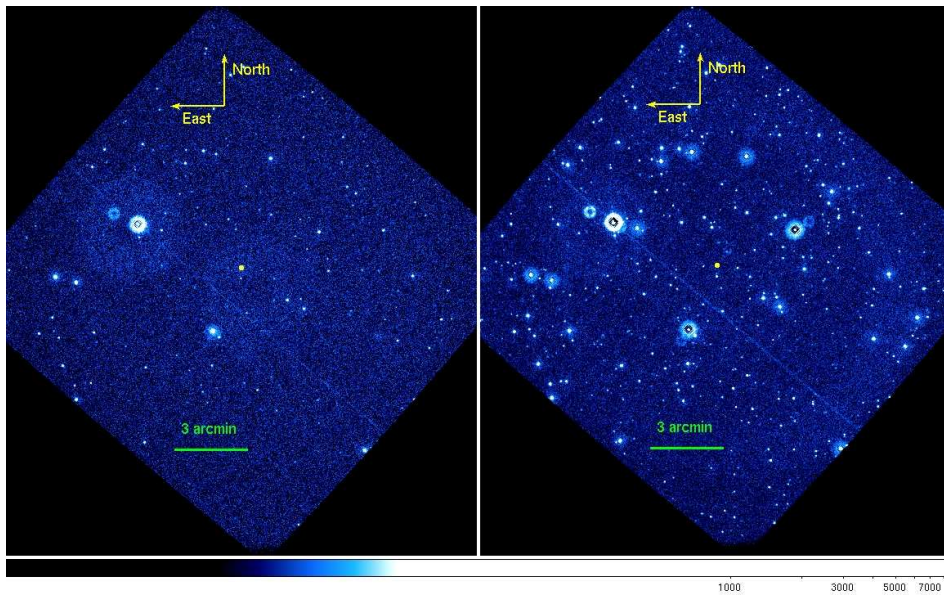
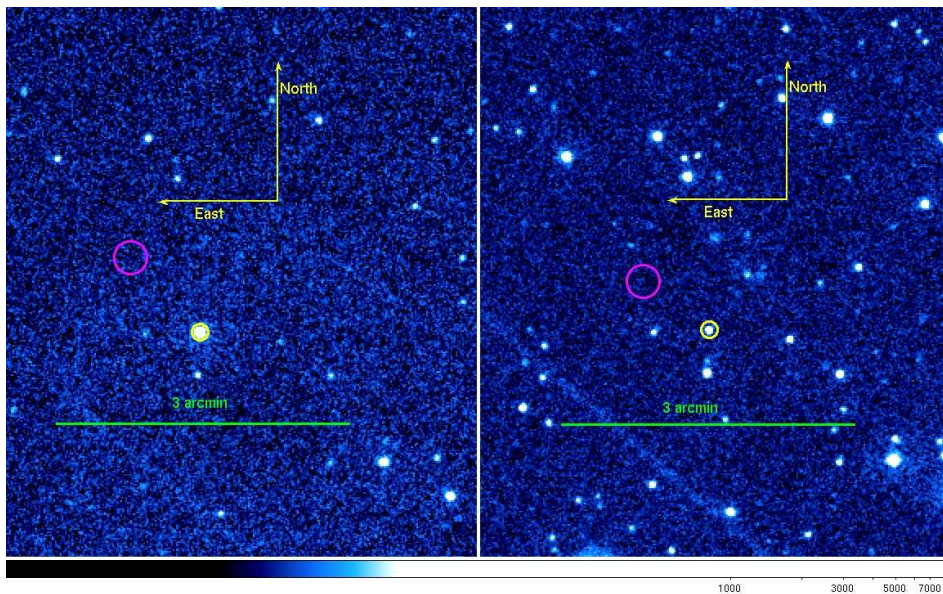
(a) The field of view of GW Lib in *UVW1* and *V* filters(b) A close-up of GW Lib in the *UVW1* and *V* filters

Figure 3.7: (a) The field of view of the *Swift* UVOT *UVW1* (left) and the *V* filter (right) in observation 00030917046. GW Lib has been marked with yellow in the centre of the field of view. (b) A close-up of the *Swift* UVOT *UVW1* (left) and *V* (right) filters in observation 00030917046. GW Lib has been circled in yellow and the background regions used in the photometry in magenta. These figures have been plotted in logarithmic scale. The orientation (North up, East to the left) together with an image scale bar are shown in the images. The length of the green scale bar is 3 arcmin.

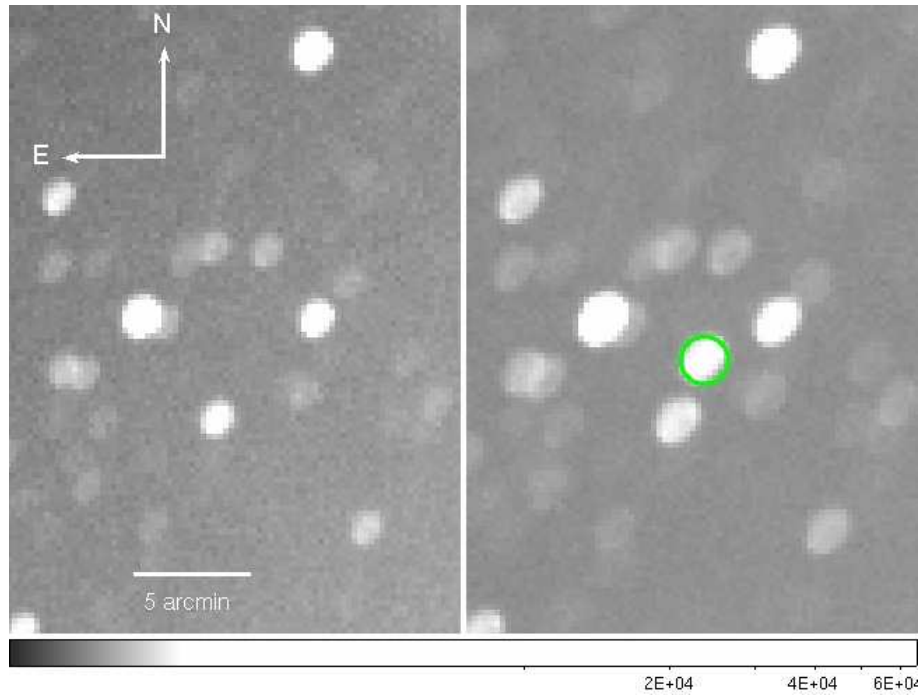


Figure 3.8: The *WASP* images of the field of GW Lib before (left) and after (right) the onset of the outburst. GW Lib is circled in green where the circle radius is 60 arcsec, and the images have been plotted in logarithmic scale. The length of the white scale bar on the left hand side figure is 5 arcmin.

The data were extracted and calibrated in an automated fashion using the standard *Super-WASP* photometric pipeline (Pollacco et al., 2006). In the pipeline, the data frames are bias-subtracted, corrected for thermal dark-current, and finally flat-fielded using exposures of the sky at twilight (outliers, such as cosmic rays or stellar images falling on a pixel, are eliminated). The pipeline performs aperture photometry using three circular apertures with radii 2.5, 3.5 and 4.5 pixels (35", 48" and 62") in order to identify blended sources. The sky background is calculated using an annulus with an inner radius of 13 and an outer radius of 17 pixels. The sky background calculation excludes pixels containing outliers described above. Systematic errors, such as a change in the shape of the PSF, caused by temperature changes in the telescope during night time are removed in the pipeline processing using the Tamuz algorithm (Tamuz, Mazeh, & Zucker, 2005). Full details of the pipeline are given in Pollacco et al. (2006).

3.3 Time series analysis

3.3.1 Outburst light curves

Fig. 3.9 presents the April-May 2007 outburst light curves of GW Lib. The top panel shows the *AAVSO* *V*-band light curve in black and the *WASP* light curve (*V+R* bands) in light blue (scaled to match the *AAVSO* *V* band magnitude). The magnitudes have been converted to $\log F$ in order to make comparison between the optical and UV light curves clearer. The middle and lower panels show the UV and X-ray light curves respectively. The *AAVSO* outburst light curve is already rising from magnitude 13 ($\log F \approx -13.6 \text{ erg cm}^{-2} \text{ s}^{-1} \text{ \AA}^{-1}$) on JD 2454203.1 which is defined as T_0 . It reaches its highest peak one day later at magnitude 7.9 ($\log F \approx -11.7 \text{ erg cm}^{-2} \text{ s}^{-1} \text{ \AA}^{-1}$), and after the peak, declines steadily for 23 days. At 29 days after the beginning of the outburst, the optical brightness declines sharply to magnitude ~ 14 ($\log F \approx -14.2 \text{ erg cm}^{-2} \text{ s}^{-1} \text{ \AA}^{-1}$). Large variations in the *WASP* light curve around day $T_0 + 11$, resulting from poor weather conditions, were excluded.

The rise of the UV emission was not observed for GW Lib, and so it is not possible to quantify any UV delay, i.e. a delay between the optical and UV rise times, such as that previously measured by e.g. Hassall et al. (1983) in VW Hyi. However, the system is already extremely UV bright at the time of the first *Swift* observations, 1 day after the beginning of the outburst, when the *UVM2* filter was used. Unfortunately, these two observations are far too over-exposed to provide useful flux measurements and thus they are not shown in the light curve. The UV light curve (from the UVOT grism data) starts 8 days after the onset of the outburst. It remains almost flat for ~ 6 days and then starts to decline. At 24.5 days after the optical rise the UV light curve shows a steep decline, approximately simultaneously with the sharp optical decline. It reaches a minimum about 2 days later. The UV data after the day $T_0 + 27.5$ have been excluded due to contamination by another source in the field.

The X-ray observations (0.3–10 keV) start 1 day after the rise in the optical, approximately

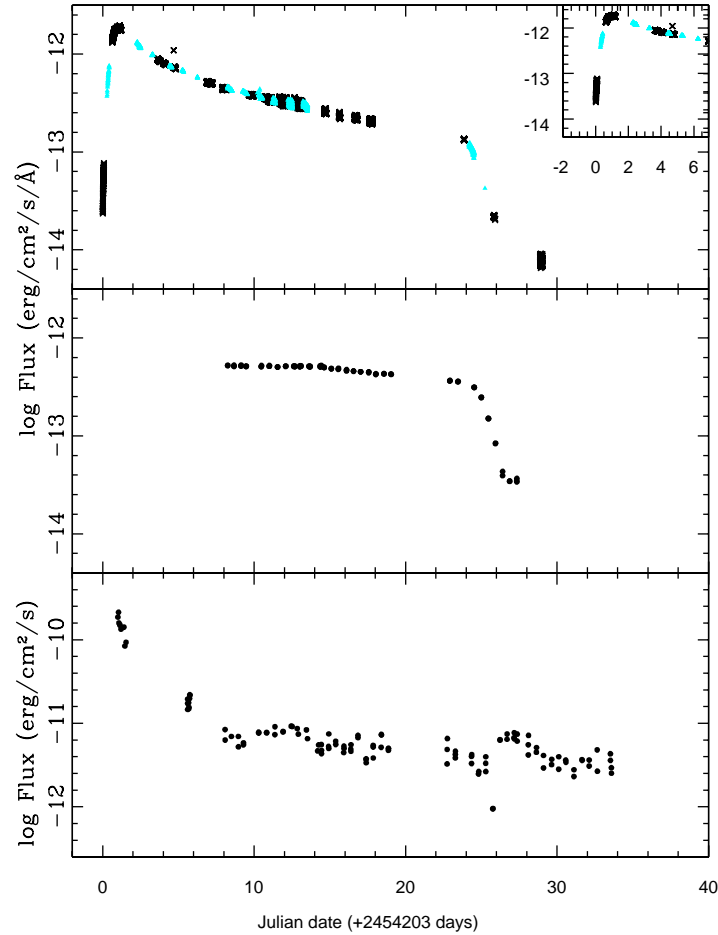


Figure 3.9: The optical, UV and X-ray outburst light curves of GW Lib. T_0 is JD 2454203.1, which corresponds to the start time of the first data point in the AAVSO light curve. The top panel shows the AAVSO optical light curve (www.aavso.org) in the V band (converted to $\log F$) in black and the WASP light curve in light blue (see text for details). The upper panel insert shows the rapid rise to maximum peaking one day after the onset of the outburst. The middle panel shows the UV in the wavelength range 2200–4000 Å (*Swift* UV grism), and the bottom panel the X-ray light curve in 0.3–10 keV (*Swift* XRT). The X-ray data have been binned at 600 s and the other bands are plotted per exposure.

at the time of the optical peak. Because the data do not cover the rise of the X-rays, it is not possible to quantify any delay between the optical and X-ray rise, such as that observed e.g. by Wheatley, Mauche, & Mattei (2003) in SS Cyg. In GW Lib, the X-ray flux is initially ~ 3 orders of magnitude above its pre-outburst quiescent level (Hilton et al., 2007), and it declines rapidly for ~ 10 days before continuing to decline more slowly during the remainder of the optical outburst. Around day $T_0 + 26$, the flux dips sharply from $\log F \approx -11.6 \text{ erg cm}^{-2} \text{ s}^{-1}$ to $\log F \approx -12.0 \text{ erg cm}^{-2} \text{ s}^{-1}$, lasting for less than a day. After having checked the data carefully, it became clear that this is a real dip in the brightness of the source. After the dip, the X-rays rise to the level of $\log F \approx -11.2 \text{ erg cm}^{-2} \text{ s}^{-1}$ and show a bump between days $T_0 + 26$ and $T_0 + 29$, which peaks at approximately the same time that the UV light curve finishes its steep decline. From $T_0 + 29$ days onwards, the X-ray flux remains approximately constant at $\log F \sim -11.5 \text{ erg cm}^{-2} \text{ s}^{-1}$.

During the two follow-up *Swift* observations in 2008, the count rate was consistent on days $T_0 + 378$ and $T_0 + 392$ at $0.03 \pm 0.01 \text{ ct s}^{-1}$. In 2009, 682 and 690 days since T_0 , it was $0.04 \pm 0.01 \text{ ct s}^{-1}$. The count rates and their errors were measured in LCURVE v.1.0. For comparison, Hilton et al. (2007) reported a quiescence count rate of 0.02 ct s^{-1} (0.2–10 keV) in the *XMM-Newton* pn camera on August 25–26, 2005, about two years before the outburst. Assuming a thermal bremsstrahlung model with a plasma temperature of $kT = 4.5 \text{ keV}$ and an absorption column of $N_H = 6.5 \times 10^{20} \text{ cm}^{-2}$ as in Patterson et al. (1998), this corresponds to an XRT count rate of 0.002 ct s^{-1} , where WebPIMMS⁵ was used to make the conversion. Thus the X-ray flux seems to have remained an order of magnitude above the pre-outburst quiescent level for about two years after the outburst.

Fig. 3.10 shows the soft X-ray light curve (upper panel) in the 0.3–1.0 keV band and the hard X-ray light curve (middle panel) in the 1.0–10 keV band from the outburst observations. The lower panel shows the hardness ratio (extracted by using the tools of Evans et al., 2009). The hardness ratio gradually increases during the outburst, and shows a sharp increase at the time

⁵<http://heasarc.gsfc.nasa.gov/Tools/w3pimms.html>

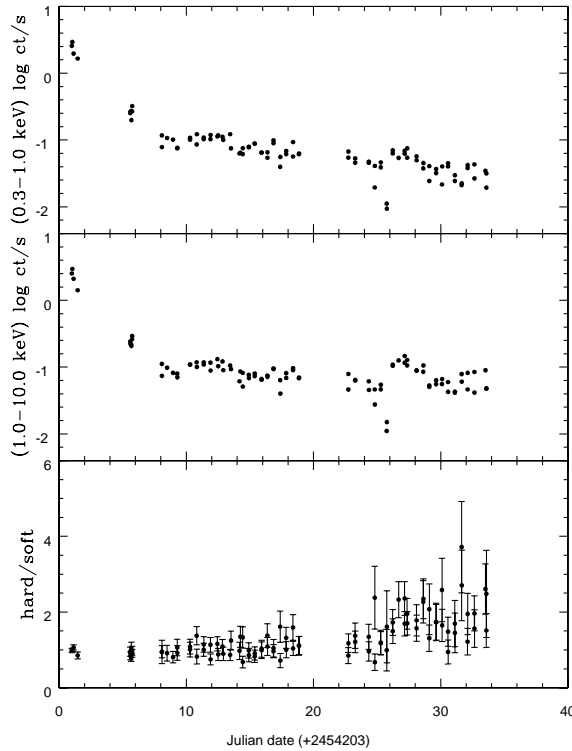


Figure 3.10: The soft (0.3–1.0 keV, upper panel) light curve, the hard (1.0–10 keV, middle panel) light curve, and the X-ray hardness ratio (hard/soft) of GW Lib. The data have been binned at 700 s.

of the bump in the X-ray light curve, which coincides with the steep decline in the optical and UV light curves.

3.3.2 Search for oscillations in the X-ray data

Pulsations were discovered in the quiescent optical emission of GW Lib by Warner & van Zyl (1998). Pulsation periods near 230, 370 and 650 s are seen in the optical and UV wavebands (e.g. van Zyl et al., 2004; Szkody et al., 2002b) and an optical 2.1 h modulation was discovered by Woudt & Warner (2002). van Zyl et al. (2004) reported that the pulsation periods are unstable on timescales of months which is typical behaviour for a cool and large amplitude DA white dwarf. Copperwheat et al. (2009) found that these pulsation periods were sup-

pressed after the 2007 outburst, but that the 2.1 h modulation remained. Copperwheat et al. suggested that since the 2.1 h modulation is quasi-periodic, it is not directly related to the binary orbit or the spin period of the white dwarf, or the precession of the disc. They suggested that the origin of this period is accretion related phenomenon originating from the accretion disc. Hilton et al. (2007) searched for these modulations in the *XMM-Newton* X-ray data taken during quiescence before the outburst, but did not detect any significant periodicities. They measured an upper limit of 0.092 mag for the X-ray pulsations.

The outburst X-ray data of GW Lib were barycentrically corrected and detrended in order to eliminate linear trends in the data. Periodicities were searched by using two methods: 1) *Fast Fourier Transform* (FFT) (Leahy et al., 1983; Lewin, Paradijs & van der Klis, 1988) and 2) *Lomb-Scargle* method (Lomb, 1976; Scargle, 1982). In the following, all equations between Eq. 3.1 and 3.7 have been obtained from Lewin, Paradijs & van der Klis (1988).

When examining shorter timescales (230 and 370 s), the FFT method, which computes the discrete Fourier transform (DFT) more efficiently, was employed (for N data points $O(N \log N)$ compared to the computing time of DFT of $O(N^2)$). Following Leahy et al. (1983) and Lewin, Paradijs & van der Klis (1988), power spectra were taken from near continuous sections of data of length T , dividing these sections into M segments and running FFT for each segment, and applying the normalisation of Leahy et al. (1983) for each segment. The resulting power spectra M were then summed. A power spectrum P_j with the normalisation is calculated according to

$$P_j = 2 | a_j |^2 / N_{ph}, \quad (3.1)$$

where a_j is discrete Fourier transform and N_{ph} the total number of photons per Fourier transform. The normalisation allows the noise powers to be easily characterised so that detection limits can be set. Discrete Fourier transform can be calculated from

$$a_j = \sum_{k=0}^{N-1} x_k \exp(2\pi i j k / N) \quad (j = 0, \frac{1}{2}N), \quad (3.2)$$

where a_j is the complex Fourier amplitude at the Fourier frequency $\nu_j \equiv j/T$, T is the duration of the time series, $i \equiv \sqrt{-1}$, x_k ($k = 0, N - 1$) is the number of photons detected in bin k , and N is the number of consecutive bins of duration T/N . From Lewin, Paradijs & van der Klis (1988) it follows that Eq. 3.1 can be written as

$$P_j = \frac{1}{2} \frac{N^2}{N_{ph}} A^2, \quad (3.3)$$

where A is the amplitude of a sinusoidal signal $x_k = A \sin(2\pi\nu_j t_k)$, which will cause a spike at frequency ν_j in the power spectrum P_j , and where $t_k = kT/N$.

I now consider the detection of a signal in the data. The total power spectrum P_j is the sum of the noise spectrum $P_{j,noise}$ and the signal spectrum $P_{j,signal}$. If P_j exceeds the signal detection level P_{detect} at a particular frequency ν_j , then a signal has been detected with a power

$$P_{j,signal} \geq P_j - P_{detect} \quad (3.4)$$

with a probability $(1 - \epsilon)$. ϵ describes the small probability that P_{detect} is exceeded by at least one of the noise powers $P_{j,noise}$ in the studied frequency range.

If a signal is not detected, we can define an upper limit, P_{UL} , for the signal power $P_{j,signal}$. In a power spectrum, statistical fluctuations can cause the individual noise signals $P_{j,noise}$ to exceed a power level P_{exceed} with a large probability $(1 - \delta)$. Since $P_{j,noise} > P_{exceed}$ with the probability of $(1 - \delta)$, the signal power at the $(1 - \delta)$ confidence level is

$$P_{j,signal} < P_j - P_{exceed}. \quad (3.5)$$

The upper limit P_{UL} for any signal $P_{j,signal}$ which does not exceed P_{detect} at the confidence level $(1 - \delta)$ can finally be derived from

$$P_{UL} = P_{max} - P_{exceed}, \quad (3.6)$$

where P_{max} , which is always less than P_{detect} , is the highest observed power in the power spectrum.

Finally, we want to know the upper limit for the amplitude A . Going back to Eq. 3.3 and replacing P_j by P_{UL} from Eq. 3.6 gives

$$P_{UL} = \frac{1}{2} \frac{N^2}{N_{ph}} A^2, \quad (3.7)$$

from which the upper limit for the amplitude A can be derived.

The FTOOL POWSPEC v.1.0, which calculates the FFT by default, was used when examining the shorter timescales (230 and 370 s). The WT mode data were binned into 1 s time bins and the PC mode data into 5 s time bins, which gave approximately 512 and 256 time bins per Fourier transform from the individual *Swift* orbits, respectively. This gave 13 transforms for the WT mode and 48 transforms for the PC mode data, from which the averaged power spectrum was constructed for each mode. Table 3.2 shows the values for the measured and for the calculated powers which have been derived using the equations given above, the 99 per cent amplitude upper limits corresponding to P_{UL} (Eq. 3.7), and the average count rates of the power spectra.

The average WT and PC mode power spectra are illustrated in Fig. 3.11(a) and (b), respectively. Based on the general appearance of the power spectra, it is clear that there are no significant peaks in the data. The peak seen at the low frequencies of the WT mode data in Fig. 3.11(a) is due to unsuccessful detrending of the data at these frequencies. In addition to

Table 3.2: The powers, the 99 per cent amplitude upper limits, and the average count rates for the average WT and PC mode power spectra of the GW Lib outburst X-ray data.

	P_{detect}	P_{max}	P_{exceed}	P_{UL}	A	Average ct rate
	$\text{ct}^2 \text{s}^{-2}$	$\text{ct}^2 \text{s}^{-2}$	$\text{ct}^2 \text{s}^{-2}$	$\text{ct}^2 \text{s}^{-2}$	ct s^{-1}	ct s^{-1}
WT	4.97	3.96	0.94	3.02	0.220	3.94
PC	3.28	2.71	1.39	1.32	0.018	0.16

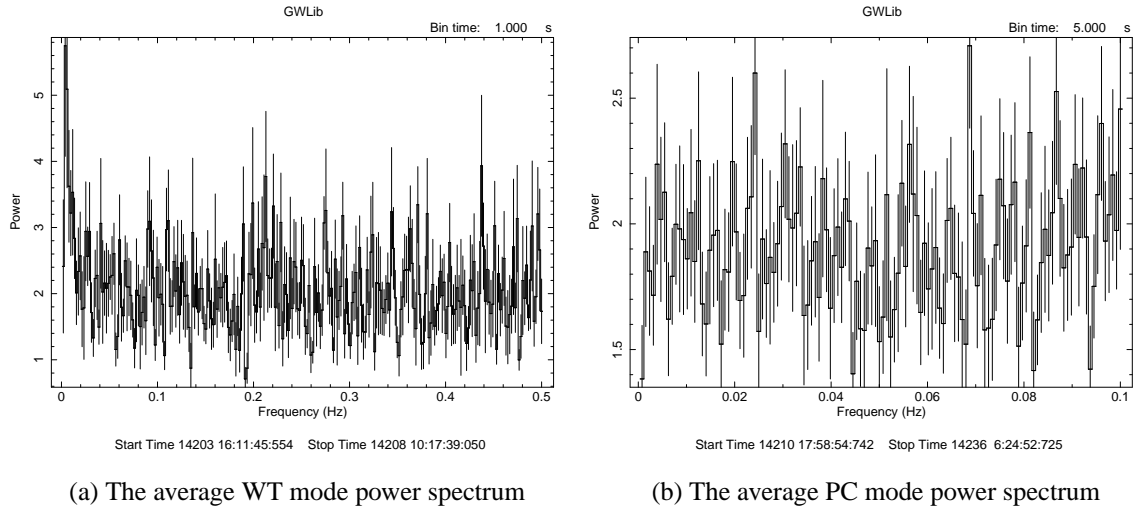


Figure 3.11: The average power spectra of (a) the WT mode and (b) the PC mode data of GW Lib. The data have been binned to 1 s for the WT mode and to 5 s time bins for the PC mode.

the average power spectra, I investigated the individual power spectra for each mode in case averaging the individual power spectra would smooth the peaks and thus would not be seen in the average power spectrum. There were no signs of significant peaks in the individual power spectra. Using the upper limit of the amplitude, we are able to derive the fractional amplitude upper limit which is the ratio of A and the average count rate of the total, average power spectrum. Thus, the 99 per cent fractional amplitude upper limits are ~ 6 per cent over the period range 2–512 s for the WT mode, and 11 per cent over the period range 10–640 s for the PC mode.

When searching for longer timescale modulations, notably at 650 s and at 2.1 h (~ 7560 s), as seen previously by the authors mentioned above, Lomb-Scargle periodograms of the data were calculated. The Lomb-Scargle method uses the discrete Fourier transform, and is better suited for unevenly spaced data than the FFT because it takes into account only those data points which have actually been measured at times t_j , and thus ignores the non-equal spacing of the data.

The Lomb normalised periodogram $P_X(\omega)$ is defined as (Scargle, 1982)

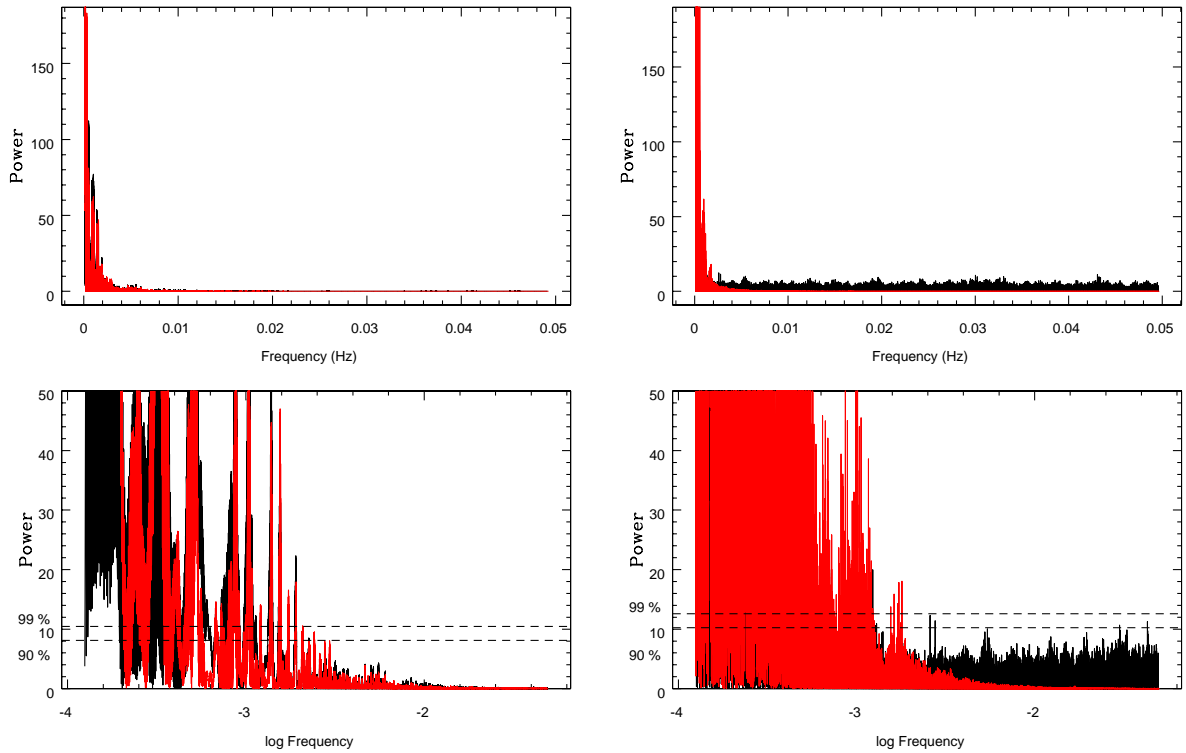
$$P_X(\omega) = \frac{1}{2} \left\{ \frac{\left[\sum_j X_j \cos \omega(t_j - \tau) \right]^2}{\sum_j \cos^2 \omega(t_j - \tau)} + \frac{\left[\sum_j X_j \sin \omega(t_j - \tau) \right]^2}{\sum_j \sin^2 \omega(t_j - \tau)} \right\}$$

where ω is the angular frequency $\omega = 2\pi f > 0$ and t_j a time bin corresponding to the measured signal X_j , where $j = 1, 2, \dots, N_0$. Constant τ , which is an offset making $P_X(\omega)$ completely independent of shifting all the t_j 's by any constant, has been defined as

$$\tan(2\omega\tau) = \frac{\sum_j \sin 2\omega t_j}{\sum_j \cos 2\omega t_j}. \quad (3.8)$$

Unfortunately, the identification of any potentially real modulation in the WT mode data at these timescales was hindered by the window function caused by the light curve sampling. Fig. 3.12(a) and (b) show the WT and PC mode Lomb-Scargle periodograms over the frequency range of 0–0.05 Hz, where 0.05 Hz corresponds to the Nyquist frequency f_c (see Press et al., 1992). The Lomb-Scargle method will be discussed in more detail in Chapter 4 (Timing analysis). The data in Fig. 3.12 have been plotted in black and the window functions in red. The dashed lines show the 90 and 99 per cent detection limits in each case. By folding the PC mode data in QDP at the previously seen longer periods (650 and 7560 s) and at the

orbital period ($P_{orb} = 76.78$ min, Thorstensen et al., 2002), the 99 per cent upper limits to the fractional amplitude of any modulation at 650 s, 76.78 min (~ 4607 s) and 7560 s are 7, 6 and 8 per cent, respectively.



(a) Lomb-Scargle periodogram of WT mode data

(b) Lomb-Scargle periodogram of PC mode data

Figure 3.12: (a) and (b) upper panels: The (a) WT and (b) PC mode Lomb-Scargle periodograms of the 2007 outburst data of GW Lib, covering frequencies between 0–0.05 Hz. The window functions (red) have been plotted on top of the data (black). Lower panels: close-ups of the WT and PC mode periodograms where frequency has been plotted in logarithmic scale. The dashed lines indicate the 90 (lower) and 99 (upper) per cent detection limits which correspond to the powers of 8.09 and 10.44 (WT), and 10.24 and 12.59 (PC), respectively.

The 2008 and 2009 data did not show significant periods. The data were inspected for the shorter and the longer periods with the methods described above. For the 2008 and 2009 PC mode data, the 99 per cent fractional amplitude upper limits were 53 and 39 per cent in the period range 10–640 s, respectively. For the longer periods, the 99 per cent upper limits were

between 30 and 60 per cent. These values for the fractional amplitude indicate that the power spectra were affected by a low number of counts and thus did not provide well constrained upper limits for the searched periods.

3.4 Spectral analysis

3.4.1 Outburst X-ray spectra

Five X-ray spectra were extracted from the outburst observations to investigate the spectral evolution. The first and the second spectra, S1 and S2, consist of single observations (WT mode data) covering days $T_0 + 1-2$ and 6 respectively. The last three spectra, S3, S4 and S5, were extracted by combining observations covering longer time intervals (PC mode data). These intervals are given in Table 3.3. The X-ray spectra were binned at 20 cts bin^{-1} using the FTOOL *grppha*, and the spectral analysis was carried out using XSPEC11. Fig. 3.13 shows the X-ray spectra from the start of the outburst (S1, top) until the end (S5, bottom). The combined spectrum from the 2008 and 2009 follow-up observations is also shown and labelled S6. These outburst spectra show that the increase in hardness apparent in Fig. 3.10 is due to a decrease in the relative strength of emission below about 1 keV. In the first observation (S1), there is an apparent excess of soft X-ray emission below 0.4 keV.

When DNe are in quiescence, the boundary layer is optically thin and assumed to be a source of hard X-rays (Pringle & Savonije, 1979). During an outburst, the boundary layer is optically thick and emits more luminous soft X-ray emission which is usually described as black body emission (Pringle, 1977). The optically thin hard X-ray component is usually somewhat suppressed in outburst as has been observed in other DN outbursts, such as SS Cyg (see e.g. Wheatley, Mauche, & Mattei, 2003).

The *Swift* XRT spectra shown in Fig. 3.13 are clearly dominated by hard X-ray emission,

Table 3.3: The *Swift* XRT spectra of GW Lib and the corresponding epochs in days since T_0 .

Spec	Epoch (d)
S1	1–2
S2	6
S3	8–19
S4	23–28
S5	28–34
S6	2008 and 2009

and so the fitting was started from the first X-ray spectrum (S1) by using an optically thin thermal plasma model (`mekal`, Mewe, Lemen, & van den Oord, 1986; Liedahl, Osterheld & Goldstein, 1995) with photoelectric absorption (`wabs`, Morrison & McCammon, 1983). This fit was not successful ($\chi^2_\nu = 3.35/226$) and a clear excess of soft photons was present below 0.7 keV. To account for this excess, a black body component was added to the fit which improved ($\chi^2_\nu = 2.54/224$). There were still strong residuals between 0.5–0.7 keV suggesting that a second optically thin thermal plasma model was needed. The abundances were allowed to vary but they were tied between the two optically thin emission models. This model (a black body and two optically thin emission components with photoelectric absorption) yielded a statistically acceptable fit to the S1 spectrum ($\chi^2_\nu = 1.11/222$). Adding a third optically thin emission component improved the fit with a slightly better fit statistic of $\chi^2_\nu = 1.08/220$. Using the F-test shows that this model provides a better description of the underlying spectrum with a confidence of 98.5 per cent. These three distinct temperature components are possibly just an approximation to an underlying continuous distribution, such as the cooling flow models used by e.g. Wheatley et al. (1996b) and Mukai et al. (2003). During the fitting process, n_H , kT_{bb} , kT and the normalisation of the optically thin thermal plasma model were untied and let to vary free, apart from the abundance, the switch param-

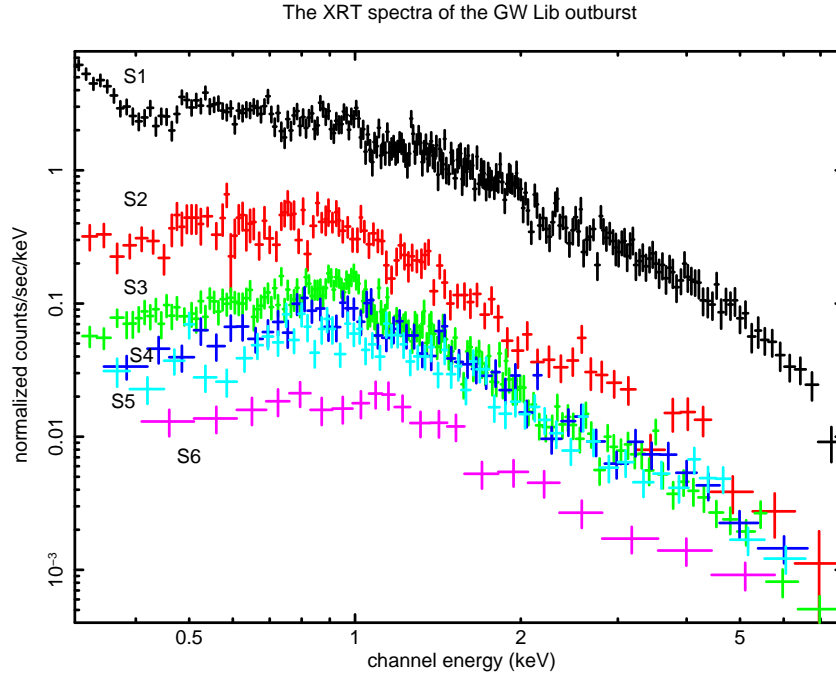


Figure 3.13: The *Swift* XRT spectra of GW Lib throughout the outburst.

eter, the hydrogen density of the thermal plasma model and the redshift which were fixed to their default values.

The F-test is used to test additional free parameters in nested models. The test calculates F-statistic from the measured distribution and compares it to a reference distribution (Fisher-Snedecor distribution). The F-statistic can be calculated from

$$F = \frac{\Delta\chi^2}{\Delta D} \bigg/ \frac{\chi^2}{m_1} = \frac{\chi_0^2 - \chi_1^2}{(D_0 - D_1)(\chi_1^2/D_1)}, \quad (3.9)$$

where D_0 is the degrees of freedom in the original model, and D_1 the degrees of freedom in the new model where new parameters have been included. In general, using the F-test to test for e.g. new model components is not legitimate use of the F-test (Protassov et al., 2002). However, it is legitimate to use it for comparing variances and thus the test is often used to compare χ^2 values. Although, comparing the χ^2 values after adding a third mekal component was not perfectly correct use of the F-test in this study, the test gave some indication on

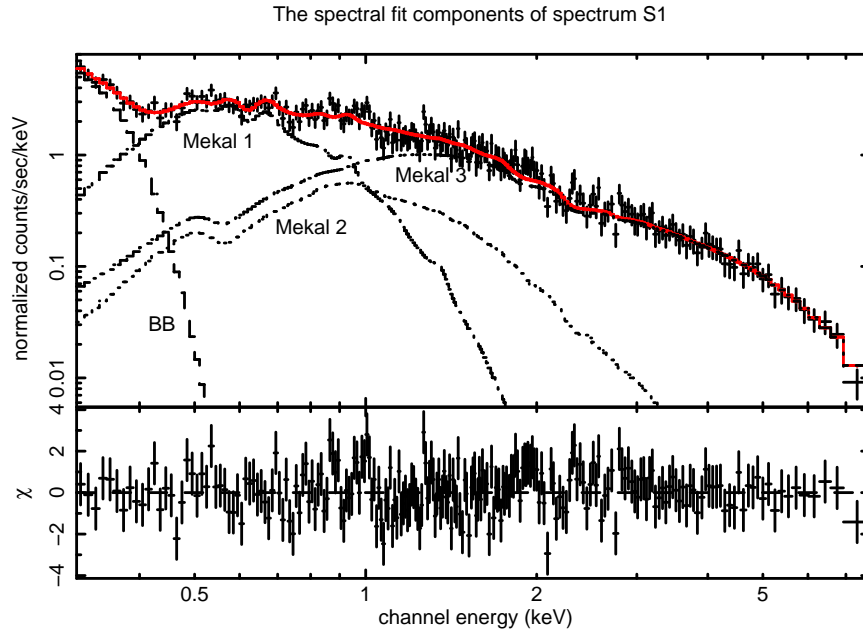


Figure 3.14: Upper panel: the best-fit model components of the first outburst spectrum (S1) of GW Lib. The data are fitted with a black body and three optically thin thermal emission components, all absorbed by the same column density. Lower panel shows the residuals.

how significant adding the third model component was.

The data and the best-fit model components for S1 with residuals are plotted in Fig. 3.14. The full set of fitted parameters is given in Table 3.4. It is worth noting that the fitted abundance is low, only $0.02^{+0.01}_{-0.01} Z_{\odot}$. The low abundance in the fit is driven entirely by the lack of thermal iron lines at around 6.7 keV. Strong line emission is predicted also by the model at ~ 1 keV, but the spectral resolution here is not sufficient to provide strong constraints on abundances. Nevertheless, by fitting with a black body and three optically thin thermal plasma models with variable abundances (`vmekal`), it became obvious that the high oxygen abundance reported by Hilton et al. (2007) in GW Lib in quiescence ($6-8 Z_{\odot}$) can be ruled out for the S1 spectrum. Setting the oxygen abundance to $6 Z_{\odot}$ in the model resulted in an unacceptable best-fit statistic of $\chi^2_{\nu} = 1.62/221$. This fit is plotted in Fig. 3.15.

In order to investigate the evolution of the X-ray spectra of GW Lib during the outburst, the need for multi-temperature optically thin thermal plasma components and for the black body was tested in a similar manner for the second spectrum S2 and the subsequent spectra S3, S4

Table 3.4: The results of the spectral fitting using photoelectric absorption, black body and three optically thin thermal plasma components. Not all components are fitted to all spectra. The errors correspond to the 90 per cent confidence limits for one parameter of interest. The measured abundance from the S1 spectrum is $0.02^{+0.01}_{-0.01} Z_{\odot}$, and the abundances in the other fits have been fixed at this value. The unabsorbed fluxes F_1 , F_2 and F_3 correspond to the three optically thin thermal plasma components in the 0.3–10 keV band.

Spectrum	S1	S2	S3	S4	S5
Model	wa(bb+3me)	wa(3me)	wa(2me)	wa(2me)	wa(2me)
n_H (10^{20} cm^{-2})	$23.83^{+0.05}_{-0.04}$	$8.61^{+5.38}_{-3.99}$	$8.15^{+1.23}_{-1.17}$	$13.25^{+7.28}_{-3.38}$	$14.63^{+6.86}_{-4.36}$
kT_{bb} (keV)	$0.013^{+0.001}_{-0.001}$	–	–	–	–
kT_1 (keV)	$5.46^{+1.26}_{-0.86}$	$4.80^{+6.07}_{-1.66}$	$5.79^{+2.73}_{-1.51}$	$5.19^{+5.13}_{-1.88}$	$4.92^{+3.82}_{-1.36}$
kT_2 (keV)	$0.71^{+0.23}_{-0.13}$	$0.64^{+0.21}_{-0.14}$	$0.66^{+0.06}_{-0.07}$	$0.57^{+0.23}_{-0.24}$	$0.48^{+0.20}_{-0.16}$
kT_3 (keV)	$0.17^{+0.01}_{-0.01}$	$0.17^{+0.10}_{-0.05}$	–	–	–
F_1 ($10^{-12} \text{ erg cm}^{-2} \text{ s}^{-1}$)	120.	6.72	3.05	3.88	3.62
F_2 ($10^{-12} \text{ erg cm}^{-2} \text{ s}^{-1}$)	30.5	8.44	3.94	2.38	1.67
F_3 ($10^{-12} \text{ erg cm}^{-2} \text{ s}^{-1}$)	271.	4.00	–	–	–
χ^2_{ν}/ν	1.08/220	1.25/89	1.13/150	0.94/50	1.19/56

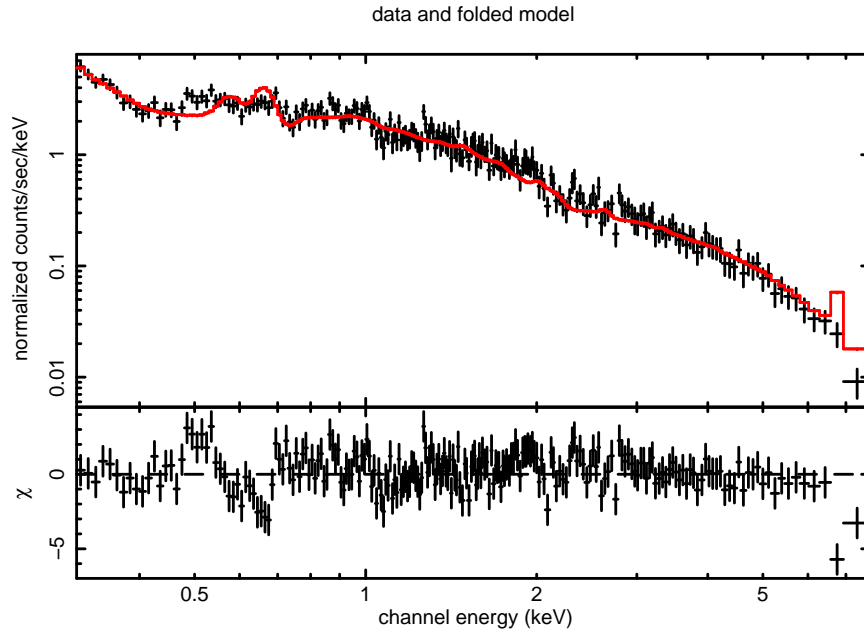


Figure 3.15: Upper panel: a spectral fit (a black body and three optically thin thermal emission models with variable abundances (`vmekal`)) to the first outburst spectrum (S1) with the oxygen abundance fixed to that found in the *XMM-Newton* quiescent spectrum by Hilton et al. (2007). An oxygen line of this strength (at 0.65 keV) would be detected and the fit is unacceptable with $\chi^2_\nu/\nu = 1.62/221$. The lower panel shows clear residuals between 0.55–0.70 and above 6.5 keV.

and S5. Since the abundances of the spectra S2, S3, S4 and S5 were not well-constrained, they were fixed to the best-fit abundance of spectrum S1. There is no evidence for the presence of a black body component in these spectra. Thus, a black body was not employed in the spectral fitting of the subsequent outburst spectra (S2–S5). The best fit for spectrum S2 was found with a photoelectric absorption and three optically thin thermal plasma components which yielded a goodness of fit of $\chi^2_\nu/\nu = 1.25/89$. The rest of the outburst spectra S3, S4 and S5 were fitted successfully with photoelectric absorption and two optically thin thermal plasma components. The best fit values, their 90 per cent confidence limits and the unabsorbed flux for each thermal emission component in the 0.3–10 keV range are given in Table 3.4. It can be seen that the increase in hardness towards the end of the outburst is due to a decrease in the relative quantity of cooler gas as the flux of the cooler temperature component drops in spectra S3–S5.

3.4.2 Fluxes, luminosities and accretion rates

The total fluxes, luminosities and accretion rates in the 0.3–10 keV range are given in Table 3.5. The fluxes given in the 0.3–10 keV range are absorbed fluxes. The distance was taken to be $r = 104$ pc (Thorstensen, 2003) in the luminosity calculation $L = 4\pi r^2 F$. The accretion rates were estimated by using $\dot{M} = 2LR_{WD}/GM_{WD}$, where $M_{WD} = 1 M_{\odot}$ and $R_{WD} = 5.5 \times 10^8$ cm were adopted (Townesley, Arras, & Bildsten, 2004). The first X-ray spectrum gives a luminosity of 2.06×10^{32} erg s⁻¹ which corresponds to $\dot{M} = 1.71 \times 10^{15}$ g s⁻¹ or $2.7 \times 10^{-11} M_{\odot}$ yr⁻¹ in the 0.3–10 keV band. This value is lower compared to the calculated accretion rate of Townesley, Arras, & Bildsten (2004) in quiescence ($\dot{M} \sim 7.3 \times 10^{-11} M_{\odot}$ yr⁻¹) probably because a significant part of the emitted outburst luminosity appears in the EUV. Since a rise in the X-ray intensity was not seen in these observations, it is not clear whether this is the peak luminosity of this outburst. The corresponding parameters for the bolometric luminosity were derived by extrapolating the spectral fit over the energy range 0.0001–100 keV. The bolometric luminosity of the black body component in spectrum S1 is not well-constrained, and the best-fit value exceeds the Eddington limit of 1.3×10^{38} erg s⁻¹ for the assumed mass; Fig. 3.16 shows the 68, 90 and 99 per cent confidence levels of n_H versus kT_{bb} and the corresponding range of bolometric luminosities. It can be seen that fits are allowed with much lower absorption column densities and luminosities. There is no reason to believe that the luminosity would exceed the Eddington limit. Estimating the luminosities of supersoft X-ray sources with black body models is notoriously unreliable (e.g. Krautter et al., 1996). Consequently, the lower limits (blackbody excluded) for the bolometric flux, luminosity and accretion rate are given for S1 in Table 3.5.

3.4.3 Later X-ray observations

The flux and luminosity were determined for the individual integrated spectra of the 2008 and 2009 observations and for the combined 2008+2009 spectrum. The spectra were fitted with

Table 3.5: The fluxes, luminosities and accretion rates in the 0.3–10 keV (fluxes absorbed) and 0.0001–100 keV (bolometric, fluxes unabsorbed) bands of the XRT spectra. The 0.0001–100 keV flux given for S1 is the lower limit, i.e. the blackbody model has been excluded from the calculation.

Spec	F	L	\dot{M}	F	L	\dot{M}
	erg cm ⁻² s ⁻¹	erg s ⁻¹	g s ⁻¹	erg cm ⁻² s ⁻¹	erg s ⁻¹	g s ⁻¹
	(0.3–10 keV)			(0.0001–100 keV)		
S1	1.60×10^{-10}	2.06×10^{32}	1.71×10^{15}	1.98×10^{-9}	2.58×10^{33}	2.14×10^{16}
S2	1.25×10^{-11}	1.63×10^{31}	1.35×10^{14}	5.10×10^{-11}	6.66×10^{31}	5.52×10^{14}
S3	5.18×10^{-12}	6.66×10^{30}	5.52×10^{13}	1.12×10^{-11}	1.44×10^{31}	1.19×10^{14}
S4	4.38×10^{-12}	5.63×10^{30}	4.67×10^{13}	9.53×10^{-12}	1.23×10^{31}	1.02×10^{14}
S5	3.66×10^{-12}	4.71×10^{30}	3.89×10^{13}	8.12×10^{-12}	1.04×10^{31}	8.62×10^{13}

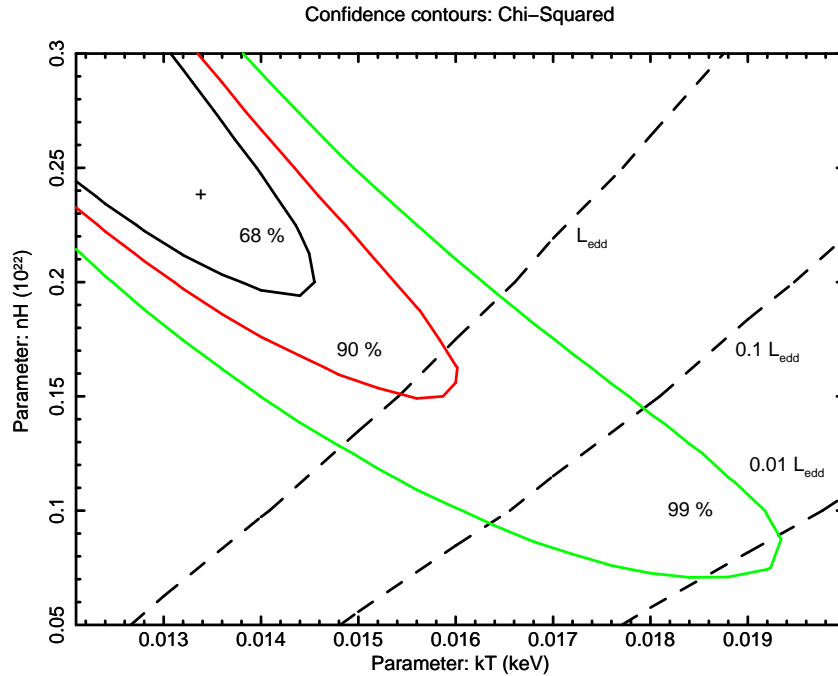


Figure 3.16: Black body parameters derived from the first outburst spectrum (S1) of GW Lib. The 10^{38} (L_{edd}), 10^{37} ($0.1 L_{\text{edd}}$) and 10^{36} erg s⁻¹ ($0.01 L_{\text{edd}}$) bolometric luminosity levels of the black body component are shown as dashed lines. The contours describe the 68, 90 and 99 per cent confidence levels for n_H versus kT_{bb} .

an absorbed single-temperature optically thin thermal plasma emission model. When fitting the individual 2008 and 2009 spectra, Cash statistics was employed due to the low number of counts in the data. The spectral fitting parameters with fluxes and luminosities are given in Table 3.6. The abundance was unconstrained by the data and fixed to the value of $Z = 0.02 Z_{\odot}$ as obtained in outburst. The values in Table 3.6 show that the state of GW Lib did not change significantly between the 2008 and 2009 observations. Compared to the quiescence luminosity obtained by Hilton et al. (2007) \sim two years before the outburst ($L(0.2\text{--}10\text{ keV}) = 9 \times 10^{28}\text{ erg s}^{-1}$), GW Lib was still an order of magnitude brighter in the *Swift* observations \sim two years after the outburst.

3.4.4 Outburst UV spectra

Four background-subtracted UV flux spectra for the source and one background spectrum are shown in Fig. 3.17. The observing dates corresponding to each spectrum are given in Table 3.7. They were chosen to represent the evolution of the UV data with time. The spectra show a blue continuum without strong emission or absorption lines, although weak features would be difficult to identify as the spectra suffer from modulo-8 fixed pattern noise. The top spectrum is an average of three source spectra corresponding to days $T_0 + 8$, 13 and 18 during the initial slow decline of the UV light curve in Fig. 3.9. The two subsequent spectra are from days $T_0 + 23$ (before the steep decline) and $T_0 + 26$ (after the steep decline in the UV light curve). The penultimate spectrum averages three spectra from day $T_0 + 27$ and the bottom spectrum shows the background flux for one of the source spectra on day $T_0 + 27$. It seems the spectra become less blue after the sharp decline in the UV light curve in Fig. 3.9. All of the spectra, including the background spectrum, show a bump around $\sim 2900\text{ \AA}$. This feature is most likely due to the contribution of the second order spectrum (the contribution of the second order spectrum is described in more detail in "Notes for observing with the UVOT UV grism"⁶ where it has been shown that the second-order UV light starts $\sim 2800\text{ \AA}$ for a

⁶http://swift.gsfc.nasa.gov/docs/swift/analysis/uvot_ugrism.html

Table 3.6: The spectral fitting parameters with 0.3–10 keV fluxes, luminosities and accretion rates of the 2008 and 2009 (columns 2 and 3) X-ray observations of GW Lib. The fourth column shows the spectral fitting parameters for the combined 2008 and 2009 spectrum.

Parameter	2008	2009	2008+2009
n_H (10^{20} cm $^{-2}$)	$7.23^{+5.74}_{-5.08}$	$5.63^{+5.09}_{-4.32}$	$0.11^{+4.45}_{-0.11}$
kT (keV)	$1.20^{+0.64}_{-0.33}$	$2.00^{+1.09}_{-0.64}$	$3.51^{+1.46}_{-1.16}$
F(0.3–10 keV) (erg cm $^{-2}$ s $^{-1}$)	7.5×10^{-13}	8.5×10^{-13}	1.1×10^{-12}
L(0.3–10 keV) (erg s $^{-1}$)	9.8×10^{29}	1.1×10^{30}	1.4×10^{30}
\dot{M} (0.3–10 keV) (g s $^{-1}$)	8.2×10^{12}	9.1×10^{12}	1.2×10^{13}
F(0.0001–100 keV) (erg cm $^{-2}$ s $^{-1}$)	1.4×10^{-12}	1.4×10^{-12}	1.3×10^{-12}
L(0.0001–100 keV) (erg s $^{-1}$)	1.8×10^{30}	1.8×10^{30}	1.7×10^{30}
\dot{M} (0.0001–100 keV) (g s $^{-1}$)	1.5×10^{13}	1.5×10^{13}	1.4×10^{13}

calibration white dwarf). In the last two source flux spectra, the background noise features are becoming clearer when the source itself is becoming fainter.

The July 2001 *HST*/Space Telescope Imaging Spectrograph (STIS) outburst spectrum of WZ Sge showed a Mg II absorption line at 2790–2810 Å (Kuulkers et al., 2002). Kuulkers et al. noted that most of it originates from WZ Sge and part of it is due to interstellar absorption. This line is not seen in the UV spectra of GW Lib probably due to the much lower resolution of the *Swift* UV grism: the resolving power of the *HST* STIS E230M grat-

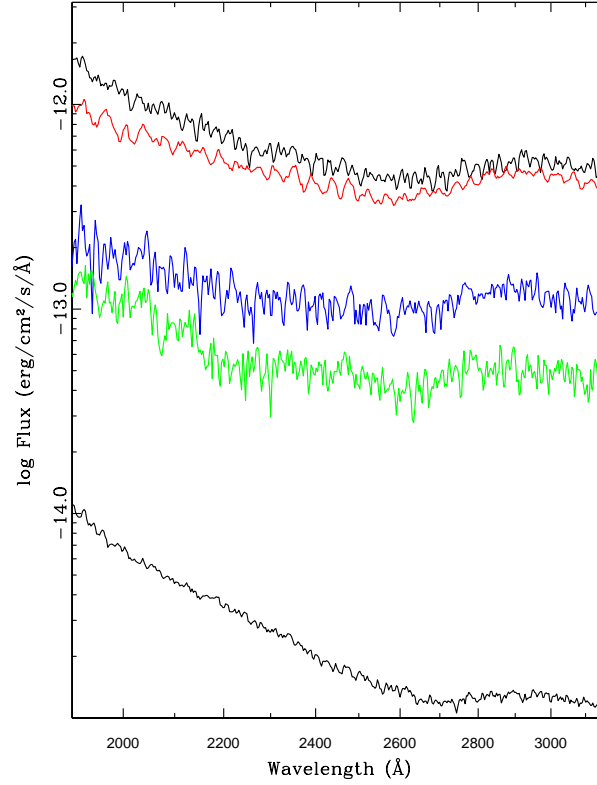


Figure 3.17: The evolution of the background-subtracted *Swift* UVOT UV grism flux spectra of GW Lib throughout the outburst in descending and chronological order. The top spectrum is an average of three spectra corresponding to days $T_0 + 8$, 13 and 18. The following three spectra correspond to days $T_0 + 23$, 26, and 27 (the spectrum on day $T_0 + 27$ is an average of three spectra during that day). The bottom spectrum shows the background flux level for one of the spectra on day $T_0 + 27$.

ing, which was used for the observations of WZ Sge, is $R \sim 23,500$ between 1650–3100 Å, thus $\Delta\lambda \sim 0.1$ Å at 2800 Å, whereas the resolving power of the *Swift* UV grism is $R \sim 150$ and thus the spectral resolution at 2800 Å is $\Delta\lambda \sim 19$ Å.

The calibration of the UV grism is on-going, and consequently absolute flux measurements remain uncertain. Nevertheless, monochromatic fluxes were measured at 2200 Å for the four source flux spectra in Fig. 3.17. The obtained monochromatic fluxes from top to bottom are $\lambda F_{2200} \sim 1.5 \times 10^{-9}$, 1.1×10^{-9} , 2.1×10^{-10} , and 1.2×10^{-10} erg cm $^{-2}$ s $^{-1}$ respectively. For $L = 4\pi r^2 F$ with $r = 104$ pc (Thorstensen, 2003), the fluxes given above correspond to monochromatic luminosities λL_{2200} of $\sim 2 \times 10^{33}$, 1.5×10^{33} , 2.8×10^{32} , and 1.5×10^{32}

Table 3.7: The observation dates since the onset of the outburst for the *Swift* UVOT UV grism spectra in Fig. 3.17.

$T_0 +$	ObsDate
8	2007-04-20
13	2007-04-25
18	2007-04-30
23	2007-05-05
26	2007-05-08
27	2007-05-09

erg s⁻¹.

3.4.5 Later UV observations

The follow-up *Swift* UVOT observations from 2008 and 2009 were obtained in order to study how the UV magnitudes and fluxes have changed since the outburst. The results are given in Table 3.8 which shows that the mean magnitudes and fluxes between different filters have not changed much, but that since the last measurement in the outburst UV light curve (Fig. 3.9), the UV flux has faded by 0.8 in log F.

3.5 Discussion

In this chapter, I have presented the multiwavelength outburst light curves and the UV and X-ray spectra of GW Lib during the rare outburst which took place in spring 2007. I have also shown the results of the *Swift* follow-up X-ray and UV observations which were obtained in 2008 and 2009. The long inter-outburst intervals of GW Lib and other WZ Sge type stars

Table 3.8: The average magnitudes, fluxes and their 1σ (68.3 per cent confidence level) errors in the UVOT *V* and *UVW1* ($\bar{\lambda} = 2600 \text{ \AA}$) filters for the 2008 and 2009 observations of GW Lib. The magnitudes and fluxes are the mean values of different snapshots. Observation time corresponds to the midpoint of each observation in days since T_0 . The exposure times are given in Table 3.1.

ObsID	Obstime	Filter	Magnitude	log Flux
	d		mag	$\text{erg s}^{-1} \text{cm}^{-2} \text{\AA}^{-1}$
7042	378.25	V	16.37 ± 0.01	-14.979 ± 0.005
7042	378.25	UVW1	14.69 ± 0.01	-14.277 ± 0.002
7043	385.21	V	16.40 ± 0.07	-14.987 ± 0.030
7044	392.04	V	16.39 ± 0.02	-14.987 ± 0.009
7044	392.04	UVW1	14.60 ± 0.01	-14.243 ± 0.004
7045	682.08	V	16.54 ± 0.01	-15.042 ± 0.005
7045	682.08	UVW1	14.84 ± 0.01	-14.339 ± 0.002
7046	689.81	V	16.53 ± 0.02	-15.039 ± 0.006
7046	689.81	UVW1	14.84 ± 0.01	-14.338 ± 0.003

mean that the opportunities to study the outbursts of these objects in detail have been very scarce. In this respect, these data represent a rare insight into these intriguing DNe.

In most cases, the hard X-ray emission of DNe is suppressed during an outburst. Previously, the suppression of X-rays has been seen in VW Hyi (Wheatley et al., 1996b), SS Cyg (Ricketts, King, & Raine, 1979; Jones & Watson, 1992; Wheatley, Mauche, & Mattei, 2003), Z Cam (Wheatley et al., 1996a), YZ Cnc (Verbunt, Wheatley, & Mattei, 1999) and WZ Sge (Wheatley & Mauche, 2005). In contrast, the X-rays show different behaviour in GW Lib during its outburst since they peak at two to three orders of magnitude higher than during quiescence in 2005 (Hilton et al., 2007). The only other DN seen to increase its X-ray luminosity during an outburst is U Gem (Swank et al., 1978), and in this case the outburst emission was only about a factor of five above its quiescent level (Mattei, Mauche, & Wheatley, 2000).

The absolute luminosity of the peak X-ray emission of GW Lib is high compared to other DNe, but not extraordinary, see Table 3.5 for outburst fluxes and luminosities. The peak X-ray luminosity of GW Lib is about a factor of two less than the X-ray luminosity of SS Cyg at its optical maximum (Wheatley, Mauche, & Mattei, 2003), only a factor of two more luminous than RU Peg in outburst, and a factor of three brighter than SU UMa in outburst (Baskill, Wheatley, & Osborne, 2005). GW Lib seems to stand out due to its unusually low X-ray luminosity in quiescence, rather than an exceptional X-ray luminosity in outburst. It may be that the relatively high mass of the white dwarf (Townsley, Arras, & Bildsten, 2004) accounts for the high outburst X-ray luminosity, as it may do also in SS Cyg.

Very few systems have good X-ray coverage during an outburst, so it is not clear whether the steep decline in the X-ray luminosity of GW Lib during the first ten days of outburst is typical of other systems. The X-ray flux of WZ Sge itself does decline during the first half of the outburst (Wheatley & Mauche, 2005), but only about a factor of three in ten days, compared with a factor of thirty in GW Lib also over ten days. Although, the first X-ray observation of WZ Sge occurred about 3 days after the optical maximum. SS Cyg also declined after the optical maximum, in this case by about a factor of six over seven days (Wheatley, Mauche, & Mattei, 2003). In contrast, the X-ray flux of VW Hyi was approximately constant during the outburst (Wheatley et al., 1996b).

In most DNe, the dominant high-energy emission during an outburst is optically thick emission from the boundary layer, which emerges in the EUV (Pringle, 1977). This also seems to be the case for GW Lib, with a supersoft component detected in the first *Swift* observation, although the luminosity of this component is poorly constrained by these observations (Fig. 3.16). The supersoft component is detected only in the first outburst X-ray observation, but it is likely to be present also in the later epochs and just too soft to be detected by the *Swift* XRT. Indeed, the EUV components of VW Hyi and WZ Sge were not detected at all with the *ROSAT* PSPC (0.1–2.4 keV) and the *Chandra* ACIS (0.2–10 keV) X-ray detectors respectively (Wheatley et al., 1996b; Wheatley & Mauche, 2005), although they were

detected with the low-energy instruments *EXOSAT* LE (0.05–2 keV) and *Chandra* LETG (0.08–6 keV).

In the few cases where good coverage has been achieved, the EUV emission rises only after the X-ray emission has been suppressed, such as that seen in SS Cyg (e.g. Jones & Watson, 1992; Wheatley et al., 1996a; Wheatley, Mauche, & Mattei, 2003), and it is assumed that this supersoft component takes over as the main source of cooling as the boundary layer becomes optically thick to its own emission. Since the EUV emission is present even in the first *Swift* observation, it is possible that the observed peak in X-ray emission actually represents the suppressed level, and that an even stronger X-ray peak was missed, corresponding to the peak emission of the optically thin boundary layer. In SS Cyg this first X-ray peak is a factor of three brighter than the second, weaker peak corresponding to the optical maximum.

In the later *Swift* observations after the X-ray peak the X-rays decline, then flatten off, and at the end of the disc outburst there is a sharp dip followed by a bump in the X-ray light curve, which coincides with the rapid decline in the optical and UV light curves. The X-ray hardness also increases at this time. These features are shared to some extent with other systems, such as U Gem which shows a dip and a bump in the X-ray light curve (Mattei, Mauche, & Wheatley, 2000) and which is the only other system where X-rays are known to be brighter in outburst than in quiescence. A bump is also seen in SS Cyg where it is thought to correspond to the boundary layer transitioning back to its optically thin state (Wheatley, Mauche, & Mattei, 2003). Another feature similar to GW Lib is the increase in hardness at the end of the outburst in SS Cyg, and indeed, DNe are usually harder in quiescence than in outburst (Baskill, Wheatley, & Osborne, 2005).

When comparing the outburst X-ray emission to quiescence it is important to distinguish between pre- and post-outburst quiescence. GW Lib was unusually faint for a DN in quiescence in the *XMM-Newton* observation made in 2005 (Hilton et al., 2007). The *Swift* XRT outburst observations continued for about six days after the end of the sharp decline in the optical and

UV light curves, which presumably defines the end of the disc outburst. The measured X-ray luminosity after this decline (S5 in Table 3.5) is a factor of fifty higher than the pre-outburst quiescent level (Hilton et al., 2007). The follow-up *Swift* X-ray observations in 2008 and 2009 showed that GW Lib declined by a factor of five after the outburst, but that it remained an order of magnitude brighter than the pre-outburst observations for at least 21 months after the outburst. Another important difference between the *XMM-Newton* and *Swift* observations is that Hilton et al. (2007) found an oxygen abundance enhanced by at least a factor of six above the solar value, whereas the first 2007 outburst spectrum is inconsistent with such a high value and that the iron abundance appears to be significantly sub-solar. It is difficult to understand how observed abundances can change so much between quiescence and outburst.

It has been noted in other systems that the X-ray flux tends to decrease between outbursts. Examples include VW Hyi (van der Woerd & Heise, 1987) and SS Cyg (McGowan, Priedhorsky, & Trudolyubov, 2004). This is in contrast to the usual predictions of the disc instability model (e.g. Lasota, 2001) in which the accretion rate gradually increases during quiescence as the disc refills. The inferred decrease in the quiescent X-ray flux in GW Lib is by a much larger factor than in VW Hyi and SS Cyg, however, the inter-outburst interval is also much larger in GW Lib (decades compared with weeks and months), so there is more time for this decrease to progress.

3.5.1 Possible disc models

To date, the physical cause of the long inter-outburst times of the WZ Sge type DNe has remained elusive. It is not at all clear why the accretion discs in these stars should behave any differently from those in other DNe with very similar system parameters. Yet, while the majority of non-magnetic, short period DNe exhibit outbursts every few weeks or months, the WZ Sge stars outburst every few years or decades. There are two main sets of models which attempt to explain this stark difference in recurrence time. In order to suppress the on-

set of regular outbursts and hence lengthen the inter-outburst interval, either 1) the quiescent viscosity must be much lower than in other systems (Smak, 1993; Howell, Szkody & Cannizzo, 1995) or 2) the inner disc must be somehow truncated (Warner, Livio, & Tout, 1996; Matthews et al., 2007). While the low viscosity models are appealing in that they neatly explain the long recurrence times, they remain unsatisfying in requiring the viscosity in some quiescent discs to be different from others while, at the same time, being very similar during outbursts. Models which appeal to inner disc truncation, suppress regular DN outbursts by removing the inner region of the accretion disc where outbursts are most easily triggered. Often disc truncation is explained by the propeller action of the torque exerted on the accretion disc caused by a magnetic field anchored on a rapidly rotating primary star (Warner, Livio, & Tout, 1996; Matthews et al., 2007) (for WZ Sge, Matthews et al. (2007) assumed a white dwarf magnetic field strength of $B \sim 10^5$ G). In this case, mass would accumulate at large radii leaving a truncated and stabilised, with respect to frequent DN outbursts, outer disc which acts as a large reservoir of mass. If the same physical mechanism was responsible for the long inter-outburst timescales of all of the WZ Sge stars, it may be reasonable to expect their outbursts would look very similar. In this respect, the differences between the observed outburst properties of GW Lib and WZ Sge, as outlined above, are puzzling.

The detailed emission physics of the magnetic propeller models in particular is not well-understood, making theoretical predictions of multiwavelength outburst light curves extremely difficult. However, both the low viscosity and the disc truncation mechanisms tend to reduce the accretion rate during quiescence and may explain the low and decreasing X-ray flux in GW Lib between outbursts. Also, in the case of GW Lib, the X-rays are quenched on a timescale of ~ 10 days. The only plausible timescale close to this value is the *viscous time* of the accretion disc which is the time for accreted material required to diffuse through the accretion disc under viscous torques (Frank, King, & Raine, 2002). Interpreting this as a viscous timescale, $t_{\text{visc}} \sim R^2/\alpha_H c_s H$, yields an associated radius of $R \sim 10^{10}$ cm, where $\alpha_H = 0.1$ as in the hot state of an accretion disc, c_s the sound speed (10 km s^{-1}), and $H = 0.1 R$ the disc scale height. This estimate of R is interesting as it is close to the required values

for disc truncation. Thus, it is conceivable that the quenching of the X-ray flux is associated with the inward progression of the accretion disc toward the white dwarf, and the eventual development of a boundary layer, once the outburst has been triggered.

3.6 Conclusions

The 2007 outburst of the WZ Sge type star GW Lib was observed in the optical, UV and X-rays by *SuperWASP-South*, *AAVSO* and *Swift*. In addition to U Gem, GW Lib stands out as the second known DN where hard X-rays are not suppressed during an outburst. Rather than having a remarkably high outburst X-ray luminosity, GW Lib has a very low quiescence X-ray luminosity compared to other DNe. The outburst X-ray light curve of GW Lib shows some similarities with other DNe, such as a bump seen at the end of the X-ray light curve and hardening of X-rays towards the end of the outburst. These features are also seen in SS Cyg. WZ Sge and GW Lib show some differences in their outburst data: the hard X-rays in WZ Sge are suppressed and the X-rays decline with a much smaller factor in the beginning of the X-ray light curve compared to GW Lib.

A supersoft component, which probably originates from the optically thick boundary layer, is detected in the first outburst spectrum. This component is also seen in other systems, such as in VW Hyi and WZ Sge. Any absorption or emission lines of GW Lib are too weak to be detected by the *Swift* XRT or UVOT.

The outburst X-ray luminosity at the optical maximum was three orders of magnitude higher than during the pre-outburst quiescence level in 2005. GW Lib was still an order of a magnitude brighter at X-ray energies during the 2008 and 2009 post-outburst observations than during the pre-outburst observations.

The structure of the accretion disc in GW Lib could be explained by models which favor very

long recurrence times. The two main categories for these models are: 1) low disc viscosity in quiescence and 2) a truncated inner disc due to a magnetic propeller white dwarf. Assuming that the outbursts of all WZ Sge stars would be driven by a similar physical mechanism, the observed differences in the outburst data of GW Lib and WZ Sge are perplexing.

Chapter 4

Deriving an X-ray luminosity function of dwarf novae based on parallax measurements

4.1 Introduction

The hard X-ray emission above 2 keV, located in the Galactic Plane region, was discovered ~ 40 years ago, and the origin of this emission has been studied since the discovery (e.g. Cooke, Griffiths, & Pounds, 1970; Bleach et al., 1972). In 1982, the *HEAO A2* proportional counter experiment, which was designed to search for large scale features in the unresolved 2–50 keV X-ray background, revealed two components in this emission (Worrall et al., 1982): 1) a large-scale height feature at high Galactic latitudes ($|b| > 10^\circ$), and 2) a narrow X-ray emission ridge along the Galactic Plane. Subsequently, Warwick et al. (1985) used the *European Space Agency's X-ray Observatory (EXOSAT)* to map the distribution of the emission in the Galactic Plane, revealing a continuous ridge of emission extending tens of degrees in longitude along the Galactic Plane, and a few degrees in the Galactic latitude.

The origin of this emission, the Galactic Ridge X-ray Emission (hereafter GRXE), has been debated since the discovery: the two main origins suggested are i) discrete point sources and ii) diffuse emission due to e.g. inverse Compton scattering of the microwave background on cosmic-ray electrons. The spectrum of the GRXE is hard, thermal bremsstrahlung from an optically thin plasma with a temperature between $\sim 5\text{--}10$ keV. The spectrum also has an iron line at 6.7 keV with an equivalent width between 400–700 eV, and the total luminosity of the GRXE is $\sim 10^{38}$ erg s $^{-1}$ (Koyama et al., 1986). If the origin of the GRXE was purely diffuse, the main difficulty would be that the hot, $\sim 5\text{--}10$ keV plasma should be flowing out from the plane (see the discussion and further references in Revnivtsev et al., 2006).

A number of GRXE studies carried out during the last ~ 40 years support the view that the main source of the GRXE is discrete point sources consisting of CVs and other accreting binary systems. E.g., Warwick et al. (1985) concluded that if the GRXE is assumed to be originating from discrete point sources, the bulk of the emission observed must be due to a population of low luminosity X-ray sources ($L_x < 10^{33.5}$ erg s $^{-1}$). Subsequently, Mukai & Shiokawa (1993) suggested that dwarf novae (DNe) could significantly contribute to the GRXE based on their study of an *EXOSAT* Medium Energy (ME) DN sample. According to this study, the space density of DNe is sufficiently high to account for a significant fraction of the GRXE. Also, they found that DNe are spectrally similar to the GRXE, i.e., they have a hard continuum and most of them show a 6.7 keV iron $K\alpha$ line. Later on, Ebisawa et al. (2001) resolved sources down to 3×10^{-15} erg cm $^{-2}$ s $^{-1}$ in their *Chandra* observation of the Galactic Ridge, equivalent to $L_x > 2.3 \times 10^{31}$ erg s $^{-1}$ at 8 kpc, concluding that the number of resolved point sources above this level is insufficient for them to be the major contributor to the GRXE. Since these previous works have not completely resolved the amount of contribution of CVs to the GRXE, further studies in this field are needed. As was noted by Mukai & Shiokawa (1993), unbiased and sensitive surveys with accurate distance measurements of CVs are needed. This way, accurate X-ray luminosity functions (hereafter XLFs) can be obtained, and the contribution to the GRXE estimated more precisely.

XLFs are studied in order to understand the distribution of different types of source populations in the solar neighbourhood and in the Galaxy, and their contribution to the GRXE. When deriving luminosity functions, the key to obtaining accurate luminosity measurements is to have accurate distances to the objects. Accurate distances can be obtained if the distance is based on *parallax* measurements, i.e., measurements of the displacement of a star relative to other stars when it is seen from two different places.

The motivation for this work was mainly given by the inaccuracies in the previous, published XLFs of Galactic CV populations. One example is a study of non-magnetic CVs which was carried out by Baskill, Wheatley, & Osborne (2005) using archival *Advanced Satellite for Cosmology and Astrophysics* (*ASCA*) observations in the 0.1–100 keV range (the energy range was integrated to 100 keV). At the time, *ASCA* had provided long observations of CVs with higher spectral resolution and with a higher effective area across a broader energy range than other previous observations of X-ray satellites, such as the *Röntgen Satellite* (*ROSAT*) (e.g. van Teeseling, Beuermann, & Verbunt, 1996) and *EXOSAT* (see the study by Mukai & Shiokawa, 1993). Thus, observations provided by *ASCA* were suitable for this type of study. Although Baskill, Wheatley, & Osborne (2005) derived their XLF by using only those sources which had parallax measurements, this sample was biased by high X-ray flux sources since *ASCA* was intended to be a spectroscopic mission and the sources in the studied sample were known to be X-ray bright. Also, the *ASCA* study was purely archival without any particular sample selection as Baskill, Wheatley & Osborne chose all non-magnetic CV observations in the *ASCA* archive, they did not filter out sources which were in an outburst state, or restrict the study to one type of object only. The study by Sazonov et al. (2006) focused on building up an XLF in the 2–10 keV range combining the *RXTE* Slew Survey (XSS) and *ROSAT* All-Sky Survey (RASS) observations of active binaries, CVs and young main sequence stars in the luminosity range $10^{30} < L_x < 10^{34}$ erg s⁻¹. However, uncertainties in the luminosities were introduced by inadequate accuracies in the distances, for example, many of the intermediate polars (IPs) in their sample had poorly known distances. Only a few sources had parallax measurements from, e.g., the Hipparcos or Tycho catalogues (astrometric uncertainties ~ 1

mas = milliarcsecond) and ground-based parallax measurements from Thorstensen (2003). In addition, the RASS luminosities had 50 per cent uncertainties in addition to statistical errors after conversion from 0.1–2.4 keV to the 2–10 keV range.

The primary aim of this chapter is to derive the most accurate XLF in 2–10 keV to date by using a carefully selected sample of DNe within 200 pc. The source sample used in this work does not represent a complete sample of DNe within 200 pc: the sample is more of a "fair sample" which was not chosen based on the X-ray properties of the sources, and which represents typical DNe within the solar neighbourhood. Under this "fair sample" assumption, we are able to derive the shape of the XLF, which is the main goal of this work. I aim to minimise the biases seen in other XLFs by using sample selection criteria described in Section 4.2. The motivation for choosing a group of DNe as the focus of this work is based on observations of Galactic CV populations and CV population models. Various authors, such as Howell, Rappaport & Politano (1997), Pretorius, Knigge, & Kolb (2007) and Gänsicke et al. (2009), have pointed out that binaries which are brighter in X-rays and show frequent outbursts, may not represent the true majority of Galactic CV population. The discovery methods of CVs usually favour brighter systems, and thus fainter CVs with low mass accretion rates are likely to be under-represented. However, population models of CVs predict that the majority of CVs are short-period systems ($P_{orb} < 2.5$ h) and X-ray faint (e.g. Kolb, 1993; Howell, Rappaport & Politano, 1997). These models are supported by observational evidence, e.g. Patterson (1984) showed that a sample of CVs with a total space density of 6×10^{-6} pc $^{-3}$ was dominated by low mass accretion rate, and thus short period systems. Finding evidence of the faint CV population requires observing techniques which target faint objects in particular, such as the *Sloan Digital Sky Survey* (SDSS)¹ study of intrinsically faint CVs at the minimum orbital period by Gänsicke et al. (2009). The SDSS has imaged deeper and wider ranges of fluxes than any other optical survey, and these characteristics are the key to finding fainter CVs. The study by Gänsicke et al. (2009) showed that orbital periods of intrinsically faint Galactic CVs accumulated in the 80–86 min range; they found that 20 out of 30 SDSS CVs in this period

¹www.sdss.org

range showed characteristics which implied that they are low mass accretion rate WZ Sge type DNe. As has been shown by these studies, less X-ray luminous objects (such as DNe) dominated the studied volumes, and thus I choose to focus on DNe in this work.

This work has utilised the X-ray observations of the three major X-ray satellites: *XMM-Newton*, *Suzaku* and *ASCA*. The details of the data reduction methods are given in Section 4.3. In order to look for any periodicities, I carried out power spectral analysis (Section 4.4) for 5 *Suzaku* sources which have not been the subjects of previous X-ray imaging observations. I have also carried out X-ray spectral analysis (Section 4.5) for the whole sample and derived an XLF in the 2–10 keV band for 12 of the sources with reliable distance measurements based on those of Thorstensen (2003), Harrison et al. (2004), and Thorstensen, Lépine, & Shara (2008). Finally, Section 4.6 will discuss the obtained XLF and some correlation studies, and Section 4.7 is dedicated to conclusions.

4.2 The selection criteria and the source sample

Since the aim was to obtain accurate luminosities for the sources (and thus an accurate luminosity function), the first step was to avoid selecting sources randomly from the archive (see e.g. Baskill, Wheatley, & Osborne, 2005) or selecting a magnitude limited source sample. As was shown by Pretorius, Knigge, & Kolb (2007), in magnitude limited samples, the period distribution depends strongly on the magnitude limit. At brighter magnitude limits, the ratio of short to long period systems decreases and thus causes a bias towards intrinsically brighter (and longer period) systems. The aim of this work was to have a *distance-limited* sample and thus sources which have accurately measured distances based on parallax measurements within ~ 200 pc from the Sun were chosen. This is a practical limit as ground-based parallax measurements do not give accurate and reliable distance measurements beyond this limit. By using parallax-based distance measurements, errors in distances, and thus in the measured

luminosities, can be minimised.

The distance measurements of the sources chosen for this work are based on trigonometric parallaxes obtained by the *Hubble Space Telescope* (HST) Fine Guidance Sensors (FGSs) (Harrison et al., 2004), by the ground based 2.4 m Hiltner Telescope at the MDM Observatory on Kitt Peak, Arizona (Thorstensen, 2003; Thorstensen, Lépine, & Shara, 2008), and the ongoing work of Thorstensen (in prep.). The first accurate trigonometric parallaxes of DNe (SS Cyg, SS Aur and U Gem) were measured in 1999 using the FGSs which can deliver high-precision parallaxes with submilliarcsecond uncertainties (Harrison et al., 1999). The distance r in units of parsecs to a star can be calculated from

$$r = \frac{1}{p}, \quad (4.1)$$

where p is the parallax angle in units of arcseconds. Harrison et al. (2004) noted that parallaxes are the only confident way to determine distances to CVs. Trigonometric parallaxes derived by ground based observations have uncertainties of ~ 1 mas or less (Thorstensen, 2003; Thorstensen, Lépine, & Shara, 2008) which is almost as good as the uncertainty in the FGS parallax measurements.

The second selection criterion was to restrict the sample to those sources which had been observed by X-ray imaging telescopes with CCDs in the energy range 2–10 keV. Once a list of targets with parallax measurements had been obtained, the next step was to look for archival data of pointed imaging X-ray observations of these targets in the energy range 2–10 keV. If the chosen targets did not have previous X-ray imaging observations, *Suzaku* X-ray observations were requested. The final step was to constrain the sample to those sources which were in their quiescent states during the observations in order to avoid biases in the luminosities, and thus *AAVSO*² light curves of the selected sources were inspected to confirm that the sources were in quiescence during the X-ray observations.

²www.aavso.org

The final source sample consists of 9 SU UMa (including 2 WZ Sge systems), 3 U Gem and 1 Z Cam type DNe. The main characteristic which separates these classes of DNe is the outburst behaviour: U Gem type DNe mainly outburst in timescales of every few weeks to every few months, whereas SU UMa stars show normal DN outbursts and, in addition, superoutbursts with superhumps (variations in the light curves at periods of a few per cent longer than the orbital period) with recurrence times of several months to years. The extreme cases of the SU UMa class, the WZ Sge stars, only have superoutbursts with outburst timescales of decades without normal DN outbursts. The defining characteristic for Z Cam stars is standstills, i.e. they may not return to the minimum magnitude after an outburst (unlike U Gem stars) but remain between the minimum and maximum magnitudes for between ~ 10 and 40 days.

The sources, which were included in the calculation of the XLF and when testing different correlations discussed in Section 4.6, were observed with *Suzaku* (BZ UMa, SW UMa, VY Aqr, SS Cyg, SS Aur, V893 Sco, and ASAS J002511+1217.2), *XMM-Newton* (U Gem, T Leo, HT Cas and GW Lib) and with *ASCA* (WZ Sge). Of the *Suzaku* observations, BZ UMa, SW UMa, VY Aqr, SS Aur, V893 Sco and ASAS J0025 were requested as observations of these objects were not in the archive. Mukai, Zietsman, & Still (2009) discuss the *Suzaku* observations of V893 Sco more closely. Z Cam, which was observed by *ASCA*, was included in the source sample since it has a parallax measurement, but it appeared to be in a transition state during the observations. Thus, only the results of spectral analysis have been reported for Z Cam, but it has been excluded when deriving the XLF and when testing correlations between different parameters. The system parameters for all the 13 sources are given in Table 4.1.

Table 4.1: The source sample used to derive the X-ray luminosity function (excluding *) with their inclinations, orbital periods, white dwarf masses, distances, and DN types. The types given in the last column are U Gem (UG), SU UMa (SU), WZ Sge (WZ) and Z Cam (ZC). The references are: 1) Thorstensen (2003); 2) Thorstensen, Lépine, & Shara (2008); 3) Harrison et al. (2004); 4) Mason et al. (2001b); 5) Urban & Sion (2006); 6) Friend et al. (1990); 7) Ritter & Kolb (2003); 8) Horne, Wood, & Stiening (1991); 9) Preliminary distance estimate from Thorstensen (in prep.), and 10) Templeton et al. (2006)

Source	Inclination deg	P_{orb} h	M_{WD} M_{\odot}	Distance pc	Type
SS Cyg	40 ± 8 ³	6.603 ³	1.19 ⁶	165^{+13}_{-11} ³	UG
V893 Sco	71 ± 5 ¹	1.82 ¹	0.89 ⁴	155^{+58}_{-34} ¹	SU
SW UMa	45 ± 18 ⁷	1.36 ²	0.80 ⁵	164^{+22}_{-19} ²	SU
VY Aqr	63 ± 13 ¹	1.51 ¹	$0.8/0.55$ ⁵	97^{+15}_{-12} ¹	SU
SS Aur	40 ± 7 ³	4.39 ¹	1.03 ⁵	167^{+10}_{-9} ³	UG
BZ UMa	$60-75$ ⁵	1.63 ²	0.55 ⁵	228^{+63}_{-43} ²	SU
U Gem	69 ± 2 ³	4.246 ³	1.03 ⁵	100 ± 4 ³	UG
T Leo	47 ± 19 ¹	1.42 ¹	0.35 ⁵	101^{+13}_{-11} ¹	SU
WZ Sge	76 ± 6 ³	1.36 ¹	0.90 ⁵	43.5 ± 0.3 ³	SU/WZ
HT Cas	81 ± 1 ⁸	1.77 ²	0.8 ⁵	131^{+22}_{-17} ²	SU
GW Lib	11 ± 10 ¹	1.28 ¹	0.8 ⁵	104^{+30}_{-20} ¹	SU/WZ
Z Cam*	65 ± 10 ¹	6.98 ¹	1.21 ⁵	163^{+68}_{-38} ¹	ZC
ASAS J0025	–	1.37 ¹⁰	–	$\sim 175^{+120}_{-40}$ ⁹	SU

4.3 Observations and data reduction

The details of the *Suzaku*, *XMM*, and *ASCA* observations are given in Table 4.2, and the data reduction methods are described in the following sections.

4.3.1 Suzaku data reduction

I reduced and analysed the *Suzaku* X-ray Imaging Spectrometer (XIS) observations. The unfiltered event lists of SS Cyg and V893 Sco were reprocessed with XISPI and screened in XSELECT with XISREPRO since the pipeline version for these observations was older than v. 2.1.6.15. Older pipeline versions do not include corrections for the time- and energy-dependent effects in energy scale calibration, and thus reprocessing of the data is needed. XISPI is used for calculating the Pulse Invariant (PI) values associated with XIS events and also for calculating the grade values for the events according to the pattern in the Pulse Height Amplitude (PHA) column. For the XIS, the relationship between the PI value (0–4095) and the energy is $E(\text{eV}) = 3.65 \times \text{PI}$. The XISREPRO command screens the reprocessed event files by removing flickering pixels and applies event selection with the standard good time interval (GTI) selection in XSELECT. For all the other *Suzaku* observations, the observations had been processed by more recent pipeline versions and thus reprocessing and screening were not necessary. Pile-up was not a problem for the data since the source count rates of all the observations were safely below the pile-up limit, i.e. below 12 ct s^{-1} , which is the safety limit for point sources observed in 'Normal' mode using Full Window³. For example, the count rate of BZ UMa inside a 250 pixel circle was $\sim 0.2 \text{ ct s}^{-1}$ (Fig. 4.1).

The *Suzaku* data reduction described below was carried out in a similar manner for all of the *Suzaku* observations. The cleaned event lists were read into XSELECT in which the X-ray spectra and light curves were extracted for each source. Fig. 4.1 shows an image of the

³http://heasarc.gsfc.nasa.gov/docs/astroe/prop_tools/suzaku_td/

Table 4.2: Observation times for each source. The exposure times for the *Suzaku* sources have been obtained from the cleaned event lists. The numbers in brackets for the *XMM* sources show exposure times after filtering high background flares, and the last column corresponds to the optical state of the source (Q = quiescence, T = transition).

Source	ObsID	Instrument	T_{start}	T_{stop}	T_{exp} ks	State
SS Cyg	400006010	XIS/Suzaku	2005-11-02	2005-11-02	39	Q
V893 Sco	401041010	XIS/Suzaku	2006-08-26	2006-08-27	18	Q
SW UMa	402044010	XIS/Suzaku	2007-11-06	2007-11-06	17	Q
VY Aqr	402043010	XIS/Suzaku	2007-11-10	2007-11-11	25	Q
SS Aur	402045010	XIS/Suzaku	2008-03-04	2008-03-05	19	Q
BZ UMa	402046010	XIS/Suzaku	2008-03-24	2008-03-25	30	Q
ASAS J0025	403039010	XIS/Suzaku	2009-01-10	2009-01-11	33	Q
U Gem	0110070401	MOS/XMM	2002-04-13	2002-04-13	23(22.5)	Q
T Leo	0111970701	PN/XMM	2002-06-01	2002-06-01	13(13)	Q
HT Cas	0111310101	PN/XMM	2003-07-12	2003-07-12	50(6.9)	Q
GW Lib	0303180101	PN/XMM	2005-08-25	2005-08-26	22(6.7)	Q
WZ Sge	34006000	GIS,SIS/ASCA	1996-05-15	1996-05-15	85	Q
Z Cam	35011000	GIS,SIS/ASCA	1997-04-12	1997-04-12	41	T

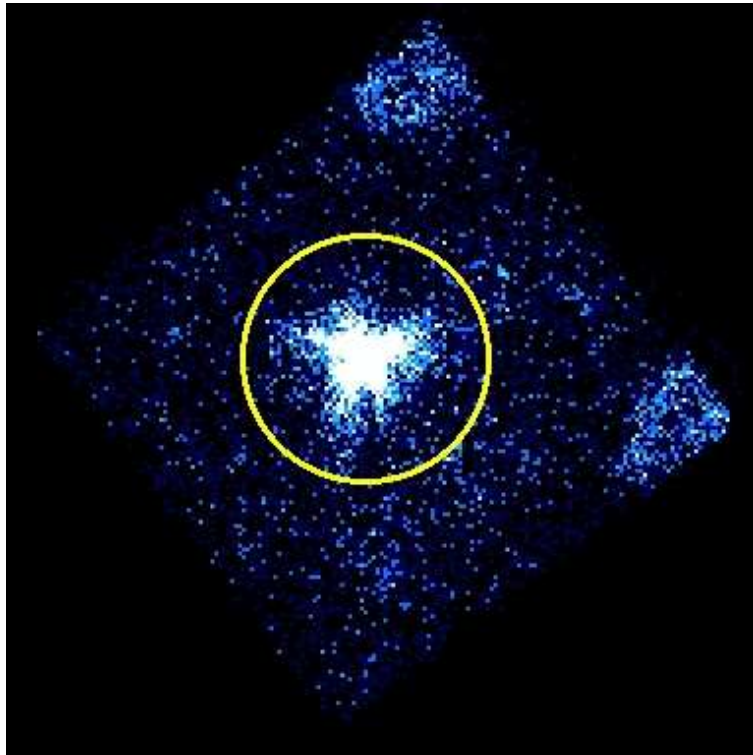


Figure 4.1: *Suzaku* observation of the XIS0 detector of BZ UMa (circled in yellow, the radius of the circle is 260 arcsec = 250 pixels). The bright regions in the corners are the calibration sources. The image has been plotted in the logarithmic scale, and North is up and East to the left.

Suzaku XIS0 observation of BZ UMa which has been circled in yellow. To include 99 per cent of the flux and to obtain the most accurate flux calibration, the spectra and light curves were extracted using a source extraction radius of 260 arcsec (= 250 pixels) (1 pix = 1.04 arcsec). The backgrounds were taken as annuli centering on the source and excluding the source region. The outer radii of the background annuli were determined according to how close the calibration sources were to the target (the calibration sources can be seen in the corners of the field of view in Fig. 4.1). The response matrix files (RMFs) and the ancillary response files (ARFs) were created and combined within XISRESP v. 1.10 to form response files consisting of both ARFs and RMFs for each source. Following this, the individual XIS0,2,3 source and background spectra and the corresponding response files were combined within ADDASCASPEC to form a total XIS0,2,3 source and a background spectrum, and a total XIS0,2,3 response file for each source. Note that only the observations of SS Cyg and V893

SCO contain XIS2 data since these data sets were obtained before the November 9th, 2006, when the XIS2 suffered damage. For the X-ray light curves, the background areas were scaled to match the source areas with a background scaling factor of source area/bg area. The scaled background light curves were subtracted from the source light curves in LCMATH.

4.3.2 XMM-Newton data reduction

The data were obtained from the *XMM-Newton* Science Archive (XSA), and analysed and extracted with the standard manner using the *XMM-Newton* Science Analysis System SAS v. 8.0.0. Each observation was checked for high background flares in the range 10–12 keV using single pixel events (`PATTERN == 0`). The high background flares were cut above 0.35 ct s^{-1} for the MOS data and above 0.40 ct s^{-1} for the pn data.

The source and the background extraction regions were chosen using circular extraction areas. The background regions (with a radius of $r_{bg} = 130$ arcsec) were chosen from the same or an adjacent chip as the source, avoiding any contaminating background sources. The radii of the source extraction regions were calculated by using the SAS task REGION in order to derive source extraction radii of which each includes ~ 90 per cent of the source flux for each source. The REGION task is designed to calculate the source extraction radius depending on how much flux the user wants to include within the extraction region. For most of the observations, only pn observations were analysed. Since the effective area of the *XMM* pn is nearly equal to the total effective area of the two MOS cameras, the MOS spectra would not add any significant information to the pn spectra. The only exception was U Gem pn observation which was obtained in Small Window mode in which only a part of CCD0 at the focal point is used to collect data. Since only a small part of the CCD is used, background information is not available. Instead, the MOS1 and 2 data, which were in Large and Small window modes, respectively, were used. This was convenient as it was possible to select the background regions from the surrounding CCDs. The U Gem MOS1 and MOS2 source and

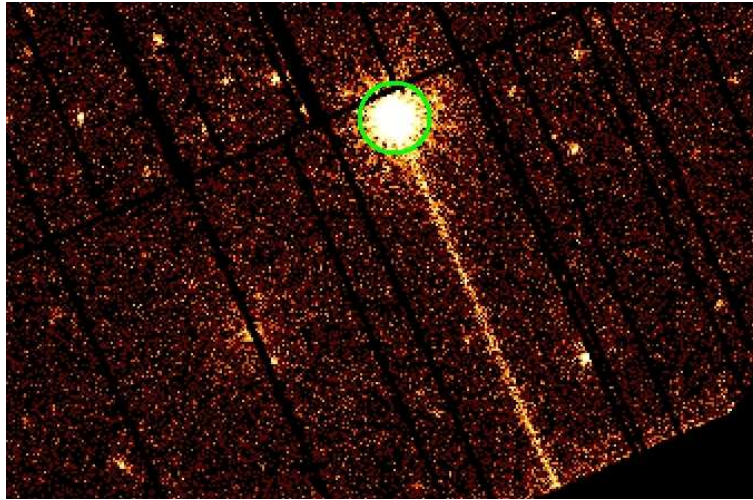


Figure 4.2: *XMM* pn observation of T Leo (circled in green). The image illustrates the out-of-time events (the bright strip across the CCD chip) often associated with bright sources.

background spectral files as well as the RMF and ARF files were combined in ADDASCASPEC to create the total (MOS1+MOS2) source and background spectra and the total ARF and RMF files.

The observations were checked in case of pile-up by using the *XMM* SAS task EPATPLOT (see Chapter 2 for more information on this task). Pile-up did not occur in any of the observations, but the source PSFs of HT Cas and T Leo were contaminated by out-of-time (OoT) events, introduced by these two sources. OoT events can be present in EPIC imaging mode observations and are created when photons are registered also during the readout of the CCD, in addition to the integration interval. They can cause broadening of spectral features, and do not only affect the central source, but also the region between the source and the readout node. Fig. 4.2 illustrates OoT events for the observation of T Leo, where T Leo has been circled in green. These events were removed from the X-ray spectra according to the 'SAS threads'⁴, i.e. the source spectra extracted from the OoT event lists were subtracted from the source spectra extracted from the original event lists. The background regions in the HT Cas and T Leo observations were taken from adjacent chips to the source chips in order to avoid the OoT events in the background regions. When extracting the X-ray spectra, only well-

⁴http://xmm2.esac.esa.int/sas/8.0.0/documentation/threads/EPIC_OoT.html

calibrated X-ray events were selected for all the sources, i.e. for the pn spectra single and double pixel events with $PATTERN \leq 4$ were chosen, and in order to reject bad pixels and events close to CCD gaps, $FLAG == 0$ was used. For the MOS, corresponding values of $PATTERN == 12$ and $\#XMMEA_EM$ were applied.

4.3.3 ASCA data reduction

The *Advanced Satellite for Cosmology and Astrophysics* (ASCA, Tanaka, Inoue, & Holt, 1994) was Japan's fourth cosmic X-ray astronomy mission operating between February 1993 and July 2000 and was the first X-ray observatory which carried CCD cameras. The main science goal of ASCA was X-ray spectroscopy of astrophysical plasmas. It carried four X-ray telescopes with two types of detectors located inside the X-ray telescopes: two CCD cameras, i.e. the Solid-state Imaging Spectrometers (SIS0 and SIS1, spectral resolution 2 per cent at 5.9 keV at launch), and two scintillation proportional counters, i.e. the Gas Imaging Spectrometers (GIS2 and GIS3, spectral resolution 8 per cent at 5.9 keV at launch).

The ASCA data reduction was performed in the standard manner using the standard screening values for the GIS and SIS instruments as described in the NASA ASCA online manual⁵. Fig. 4.3 shows images of WZ Sge in the SIS (left) and GIS (right) detectors during the observation in 1996.

Each SIS camera consisted of four CCD chips. The SIS observations were obtained in 1-CCD mode, i.e. both SIS0 chip 1 and SIS1 chip 3 were active, and for the GIS, both GIS2 and 3 were operating (GIS monitor count house keeping parameters were $G2_L1 > 0.0$ && $G3_L1 > 0.0$). In order to avoid including data which were obtained when the satellite pointing was not stable, the following parameters were applied for both GIS and SIS: $ACS==0$ && $ANG_DIST > 0.0$ && $ANG_DIST < 0.02$. The ACS parameter was set to zero when the

⁵<http://heasarc.gsfc.nasa.gov/docs/asca/abc/abc.html>

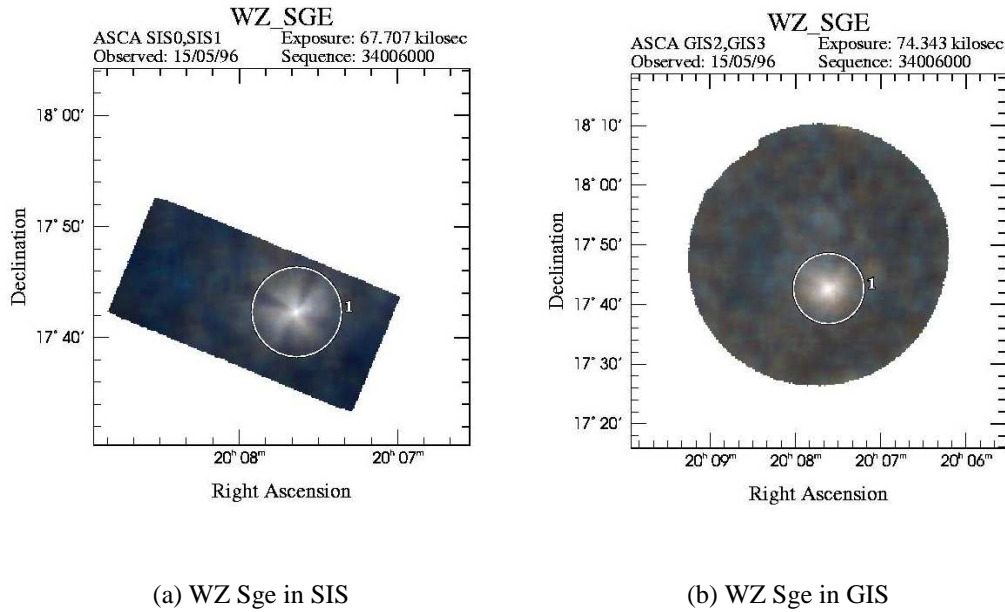


Figure 4.3: The ASCA observation of WZ Sge in SIS (left) and GIS (right).

satellite was in a pointing mode, and the ANG_DIST (in units of degrees) parameter contained the root mean square deviation of the instantaneous pointing from the mean pointing. These parameters ensured that only stable pointing data were selected for the analysis. Also, the elevation angle was set to $ELV > 5$ degrees for both instruments. This is an angle between the Earth's limb and the target. If the angle is too low (below 5 degrees), the target is seen through the Earth's outer atmosphere, in which case absorption and scattering of X-rays would take place, and thus the spectrum would be distorted. For both GIS and SIS, events outside the South Atlantic Anomaly (SAA) were selected ($SAA==0$). The SAA is a region in the low-Earth orbit with an increased flux due to energetic particles (the Earth's inner radiation belt is closest to the Earth's surface in this region).

For the SIS instruments, the bright Earth angle (the angle between the target and the bright limb of the Earth) of $BR_EARTH > 10$ degrees was applied to exclude data contaminated by the illuminated face of the Earth. This criterion was needed as the SIS was also sensitive to ultraviolet and optical radiation scattered within ASCA XRT. To exclude times of measured high background, the Radiation Belt Monitor (RBM) value of $RBM_CONT < 500$ was applied.

The RBM was a small detector attached to the bottom of GIS2 and it was automatically used to reduce high voltage of the GIS sensors during times of high background. To avoid pile-up and telemetry saturation, high background times were also rejected when the PIXL monitor counts for the CCD chips were 3σ above the mean value of the observation. Particle induced events were rejected with the expression $COR > 4$, where COR (cut-off rigidity) describes the strength of the Earth's geomagnetic field to repel cosmic rays in units of GeV c^{-1} . During the passage of the SAA, the high voltage of GIS was turned off, but for the SIS this was not necessary as the high particle flux of the SAA was not a threat to the hardware. However, the data during the SAA passage was useless, and thus was excluded for the SIS by selecting events occurring before the passage of the SAA and at least 32 s after the SAA ($T_SAA < 0 \parallel T_SAA > 32$). Also, events occurring before the first Day-Night observation and at least 32 seconds after the Day-Night transition were included in the SIS data analysis ($T_DY_NT < 0 \parallel T_DY_NT > 32$).

The source and background extraction regions were chosen as described in the following. For the GIS, a ~ 6 arcmin circular source extraction region was used for both Z Cam and WZ Sge, while the SIS source extraction regions were smaller so that they could be fitted safely within the chip. Thus, the source extraction radii for Z Cam were 4.4 arcmin (SIS0) and ~ 3.5 arcmin (SIS1) and for WZ Sge ~ 4 arcmin (SIS0) and ~ 3 arcmin (SIS1). The background extraction region for the GIS was taken centred on the detector excluding a circular region of ~ 8 arcmin centred on the source. The background extraction radii for the GIS2 and GIS3 were 15.7 and 15.5 arcmin (Z Cam), and 15.4 and 13.8 arcmin (WZ Sge). For the SIS background, blank-sky background observations were used for Z Cam due to lack of space for a local background region on the CCDs, whereas for WZ Sge, the total area of the two active CCDs excluding a 5.5 arcmin region around the source was used as the background.

The ancillary response files (ARFs) for the GIS and SIS spectra were created with ASCAARF and the SIS response matrix files (RMFs) with SISRMG. The GIS response matrix was obtained from the calibration data base (CALDB). Finally, the total SIS and GIS X-ray spectra

were created by combining the SIS0 and SIS1, and the GIS2 and GIS3 spectra in ADDAS-CASPEC, respectively.

4.4 Timing analysis

Since VY Aqr, SS Aur, BZ UMa, SW UMa and ASAS J0025 have not been subject to previous, pointed, X-ray imaging observations before the *Suzaku* observations, I carried out power spectral analysis in order to look for periodicities from the *Suzaku* X-ray data of these sources. This was done to ensure that these objects are not intermediate polars (IPs). In general, IP X-ray light curves are known to show stable modulation due to the spin period of the white dwarf or due to a side-band period, a so-called beat period between the spin and the orbital periods (e.g. Ramsay et al., 2008). A good review of IP modulation depths is given by Norton & Watson (1989) who studied all IPs which were observed by *EXOSAT* at the time. They showed that the modulation depth increased with decreasing energy. For example, for V1223 Sgr the modulation depth was 7 per cent in the 6–10 keV band, whereas in the 0.05–2.0 keV band it had increased to 37 per cent. The average modulation depth in the sample was ~ 24 per cent.

The original background-subtracted X-ray light curves were binned at 16 s (2×8 s, where 8 s is the read out time of the XIS CCDs) in the Xronos software *LCURVE*, and linear trends were removed. After this, the periodograms in Fig. 4.4 were calculated by using the Lomb-Scargle periodogram (Scargle, 1982). The Lomb-Scargle method uses the discrete Fourier transform, and is better suited for unevenly spaced data and for data with large gaps, than FFT (see Chapter 3, Search for oscillations in the data). The Lomb normalised periodogram $P_X(\omega)$ (the following equations have been obtained from Scargle (1982) unless otherwise stated), i.e. the spectral power as a function of angular frequency ω , was defined by

$$P_X(\omega) = \frac{1}{2} \left\{ \frac{\left[\sum_j X_j \cos \omega(t_j - \tau) \right]^2}{\sum_j \cos^2 \omega(t_j - \tau)} + \frac{\left[\sum_j X_j \sin \omega(t_j - \tau) \right]^2}{\sum_j \sin^2 \omega(t_j - \tau)} \right\}$$

where ω is angular frequency $\omega = 2\pi f > 0$, t_j a time bin corresponding to the measured signal X_j , and $j = 1, 2, \dots, N_0$.

The Lomb-Scargle periodograms in Fig. 4.4 have been plotted with black and the spectral window (i.e. the window function) in red. The window function $G(\omega)$ describes the response of the data analysis system to a single frequency sine wave (Scargle, 1982) and is defined as

$$G(\omega) = |W(\omega)|^2 = \frac{1}{N_0^2} \left| \sum_{j=1}^{N_0} \exp(i\omega t_j) \right|^2, \quad (4.2)$$

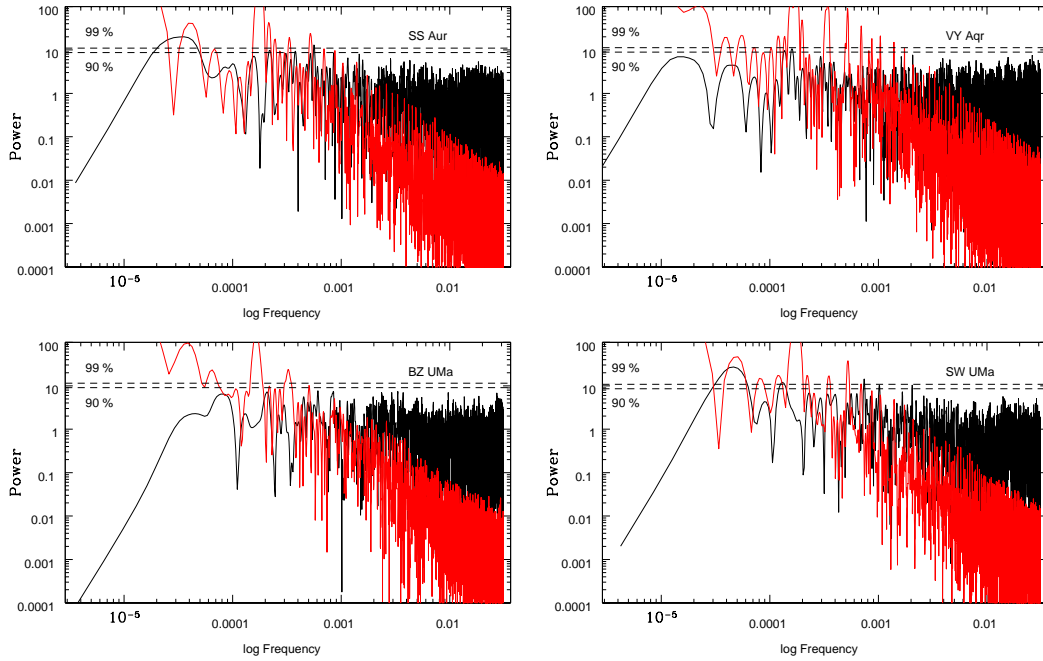
where W is the discrete Fourier transform of the time-domain observing window, N_0 the number of samples, and $i = 1, 2, \dots, N_0$.

Modulation was searched over the frequency range 0.00001–0.03 Hz where 0.03 Hz corresponds to the Nyquist frequency f_c (see Press et al., 1992), i.e. to the critical frequency limit containing information about all the spectral components in signal $f(t)$, and is defined as

$$f_c = \frac{1}{2\Delta}, \quad (4.3)$$

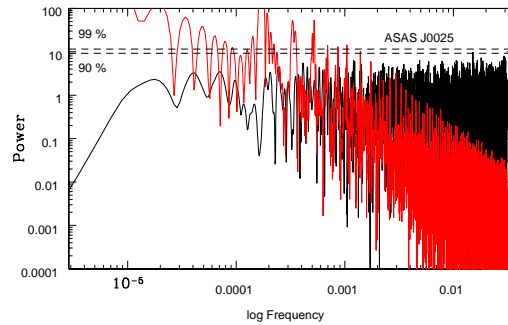
where Δ is the sampling interval of the studied signal. Detection efficiency DE , which is the probability of detecting a signal with power P , was defined by Scargle (1982) according to the equation

$$DE = 1 - p^*(N, P), \quad (4.4)$$



(a) SS Aur and BZ UMa

(b) VY Aqr and SW UMa



(c) ASAS J0025

Figure 4.4: The Lomb-Scargle periodograms of (a) SS Aur and BZ UMa, (b) VY Aqr and SW UMa, and (c) ASAS J0025. The dashed lines show the 99 (upper) and 90 (lower) per cent detection thresholds. The data, from which linear trends have been removed, is plotted in black (the periodogram), whereas the red curves represent the window functions. The peaks exceeding the 99 per cent detection level at the low frequency end are most likely caused by red noise.

where $p^*(N, P)$ describes the probability of missing a signal with power P over a number of frequencies N and is given by

$$p^*(N, P) = 1 - \exp[-(z_0 + P)]\phi(z_0, P). \quad (4.5)$$

Here z_0 is the detection threshold, i.e. signals falling below the threshold will not be detected, and $\phi(z_0, P)$ an integral of a Bessel function which with a series expansion is defined as

$$\phi(x, y) = \sum_{m=0}^{\infty} \sum_{k=0}^m x^k y^k / (k!m!). \quad (4.6)$$

z_0 in Eq. 4.5 is defined with a false alarm probability p_0 according to

$$z_0 = -\ln [1 - (1 - p_0)^{1/N}]. \quad (4.7)$$

But for small p_0 ($p_0 \sim 0.01$)

$$z_0 \approx \ln(N/p_0) = 4.6 + \ln(N). \quad (4.8)$$

A small p_0 value indicates a highly significant periodic signal.

The periodicities exceeding the 99 per cent detection level in Fig. 4.4 are only seen for SW UMa and SS Aur. These periods, with the fractional amplitudes and errors at the 99 per cent significance level for SW UMa are 21492 s (16 ± 3 %), 7626 s (11 ± 5 %) and 1351 s (11 ± 6 %), and for SS Aur 27967 s (13 ± 3 %) and 1781 s (9 ± 4 %). The fractional amplitudes and their errors, which were calculated as the ratio of the amplitude and the mean count rate of the power spectrum, were obtained when folding the data in the Xronos software EFOLD and fitting the data in QDP with a constant and a sinusoidal model components.

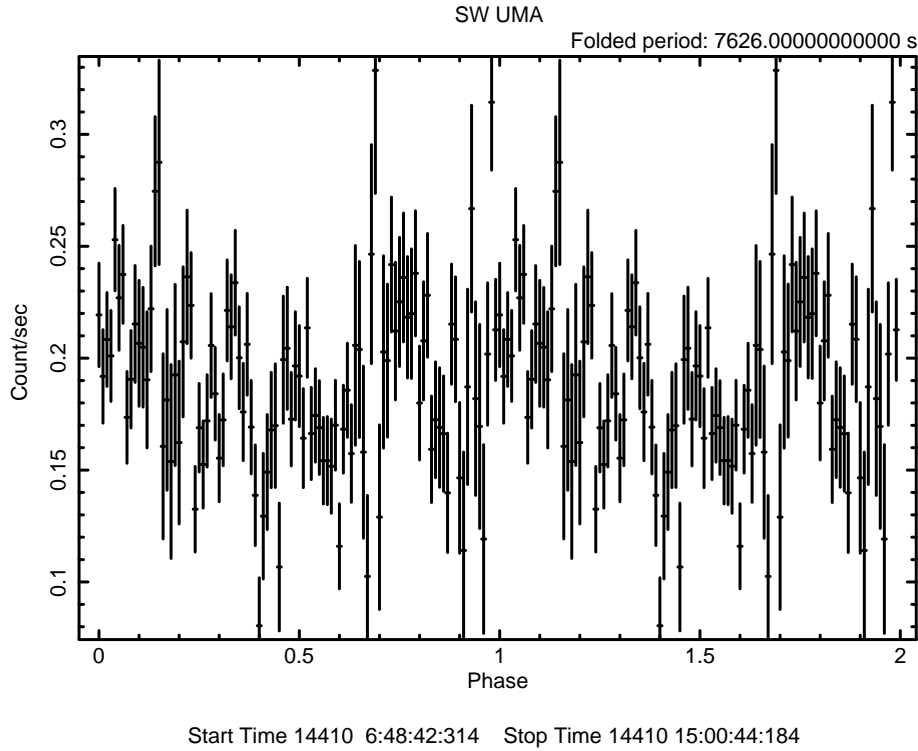


Figure 4.5: The X-ray light curve of SW UMa folded over the period 7626 s with 100 phase bins.

Fig. 4.5 illustrates the folded light curve of SW UMa as an example. This light curve has been folded over the period 7626 s with 100 phase bins in EFOLD. Since the significant signals exceeding the 99 per cent detection level are seen at low frequencies, they are very likely due to red noise which has more energy at low frequencies (see e.g. Baskill, Wheatley, & Osborne, 2005). The significance calculated by the Lomb-Scargle method above is valid only if white noise is present, thus, the presence of red noise invalidates this assumption: peaks exceeding the 99 per cent significance level are not always real when red noise is present. The longest periods (21492 and 27967 s) are most likely related to the total durations of the SW UMa (17 ks) and SS Aur (19 ks) observations.

4.5 Spectral analysis

X-ray spectral analysis was carried out in order to study the underlying spectra of the source sample, and ultimately, in order to calculate the fluxes and luminosities of the sources. To employ Gaussian statistics in χ^2 fitting, the X-ray spectra were binned at 20 ct bin⁻¹ with GRPPHA, and fitted in XSPEC11.

In CVs the power source of X-ray emission is known to be accretion onto the white dwarf. The accreted material is shock-heated to high temperatures ($kT_{max} \sim 10\text{--}50$ keV, Mukai et al., 2003), and this material has to cool before settling onto the white dwarf surface. An isobarically cooling gas flow consists of a range of temperatures which vary from the hot shock temperature kT_{max} to the temperature of the optically thin cooling material which eventually settles on to the surface of the white dwarf (Mukai et al., 1997). Thus, when fitting X-ray spectra of CVs, cooling flow spectral models should represent a more physically correct picture of the cooling plasma flow, compared to single temperature spectral models. Cooling flow models have successfully been applied to CV spectra in previous studies by e.g. Wheatley et al. (1996b) and Mukai et al. (2003). The multi-temperature characteristic is the main motivation for emphasizing the cooling flow model in the rest of this work. As the gas cools from the initial shock temperature of T_{max} to the much lower temperature on the white dwarf surface, the energy radiated by the gas is $5/2 \times kT_{max}$ per particle. Thus, the emitted luminosity from the boundary layer can be derived from (Pandel, Córdova, & Howell, 2003)

$$L_{bl} = \frac{5kT_{max}\dot{M}_{bl}}{2\mu m_p}, \quad (4.9)$$

where m_p is the mass of a proton (1.67×10^{-27} kg), μ the mean molecular weight (~ 0.62), \dot{M}_{bl} the accretion rate from the boundary layer, and k the Boltzmann constant (1.38×10^{-23} J K⁻¹). The mean molecular weight can be calculated from

$$\mu = \frac{1}{2X + 0.75Y + 0.5Z}, \quad (4.10)$$

where X is the fraction of hydrogen ($H = 0.71$), Y is the fraction of helium ($He = 0.27$), and Z is the fraction of heavier elements (0.02).

The X-ray emission source, i.e., the optically thin boundary layer above the white dwarf illuminates the surface of the white dwarf, causing a reflection from the surface. This reflection is then seen as an iron (Fe) $K\alpha$ fluorescence line at 6.4 keV (George & Fabian, 1991). Iron, which is thought to be produced in stellar nucleosynthesis processes, is the most abundant heavy element in the universe (Makishima, 1986). The Fe $K\alpha$ fluorescence line is produced when electron transitions from state $2p$ to $1s$ occur (George & Fabian, 1991). The energy of this line is a slowly increasing function of ionization state: it rises from 6.4 keV in Fe I to 6.45 keV in Fe XVII, but then increases steeply to 6.7 keV in Fe XXV and 6.9 keV in Fe XXVI. According to George & Fabian, an infinite slab reflector subtending a total solid angle of $\Omega = 2\pi$, where the X-ray source is located right above the slab, produces an equivalent width of up to ~ 150 eV for the 6.4 keV Fe $K\alpha$ fluorescence line. The equivalent width of this line depends on the total abundance of the reflector (Done & Osborne, 1997), the inclination angle i between the surface of the reflector and the observer's line of sight, and the photon index of the spectrum of the X-ray emission source (Ishida et al., 2009).

To compare the effects of two different spectral models to the spectral fit parameters, the spectra were fitted with 1) a single temperature optically thin thermal plasma model (`mekal`, Mewe, Lemen, & van den Oord, 1986; Liedahl, Osterheld & Goldstein, 1995) and 2) a cooling flow model (`mkcflow`) which was originally developed to model cooling flows in clusters of galaxies (Mushotzky & Szymkowiak, 1988), adding photoelectric absorption (`wabs`, Morrison & McCammon, 1983) to both models. The spectral fitting parameters with the fit statistics for the models are given in Tables 4.3 and 4.4, respectively. These results show that in general, better χ^2_ν values are achieved with the cooling flow model. For example,

compared to the optically thin thermal plasma model, the improvement in the χ^2_ν value was statistically significant for SW UMa and T Leo when using the cooling flow model. To investigate the equivalent width of the 6.4 keV iron emission line, a Gaussian line was added at 6.4 keV with a line width fixed at $\sigma = 10$ eV. The spectral fits do not necessarily require the 6.4 keV line, e.g. for SS Aur the $\chi^2_\nu = 0.96/629$ when a Gaussian line at 6.4 keV was not included. However, since the line at 6.4 keV is not included in the models mentioned above by default, it has to be added as a separate component to be able to investigate the equivalent width of this line. The measured equivalent widths for the 6.4 keV lines of the sources are given in Table 4.5. The equivalent width of GW Lib is missing from this table as the signal-to-noise at ~ 6 keV is too low to provide a reliable measurement from the GW Lib spectrum.

The *Suzaku* XIS1 and XIS0,2,3 spectra were fitted simultaneously for each source as well as the *ASCA* GIS and SIS spectra of Z Cam and WZ Sge. Some data sets required additional components to improve the fits. Three of the sources, HT Cas, V893 Sco and Z Cam, required the partial covering absorption model, `pcfabs`, to reduce residuals in the low energy end (between ~ 0.6 – 2 keV). The use of the more complex absorption model is consistent with earlier work since absorption has been found to be strong and complex in these objects (HT Cas, Mukai et al. (1997); V893 Sco, Mukai, Zietsman, & Still (2009); Z Cam, Baskill, Wheatley, & Osborne (2001)). With the partial covering model, the low-energy residuals were reduced and the spectral fits gave statistically acceptable χ^2_ν values (Tables 4.3 and 4.4). When fitting the X-ray spectrum of SS Cyg with the optically thin thermal plasma model, residuals existed at ~ 0.80 keV. Thus, to reduce the residuals, I added a Gaussian line at 0.81 keV with a line width of 0.24 keV letting the line energy and the width both to vary free. For the U Gem spectrum, a single absorbed optically thin thermal plasma model yielded a $\chi^2_\nu = 2.23/403$. Since the fit was not statistically satisfactory, I added another optically thin thermal plasma component which improved the fit ($\chi^2_\nu = 1.34/401$).

In the spectral fitting, the parameters of the spectral models (kT , kT_{max} , the normalisations,

Table 4.3: The best-fit parameters of the absorbed optically thin thermal plasma model with a 6.4 keV Gaussian line. The errors are 90 per cent confidence limits on one parameter of interest. n_{H_1} and n_{H_2} are the absorption columns of the photoelectric absorption (wabs) and the partial covering (pcfabs) models, respectively. CFrac is the covering fraction of the partial covering model and Ab the abundance.

Name	n_{H_1} 10^{20} cm^{-2}	n_{H_2} 10^{20} cm^{-2}	CFrac	kT keV	Ab	χ^2_ν/ν	P_{null}
BZ UMa	<0.19	–	–	$4.17^{+0.16}_{-0.17}$	$0.51^{+0.07}_{-0.08}$	1.02/905	0.349
GW Lib	$3.16^{+8.58}_{-3.16}$	–	–	$1.62^{+1.92}_{-0.68}$	$0.20^{+1.23}_{-0.20}$	1.02/8	0.414
HT Cas	–	$15.36^{+2.13}_{-1.08}$	$0.95^{+0.04}_{-0.04}$	$6.43^{+0.60}_{-0.64}$	$0.71^{+0.18}_{-0.17}$	1.07/259	0.207
SS Aur	<0.56	–	–	$6.35^{+0.40}_{-0.40}$	$1.0^{+0.14}_{-0.15}$	1.06/628	0.127
SW UMa	<0.20	–	–	$2.77^{+0.12}_{-0.13}$	$0.20^{+0.07}_{-0.05}$	1.23/470	5.362×10^{-4}
U Gem	$0.89^{+0.19}_{-0.20}$	–	–	$0.78^{+0.03}_{-0.01}$ $6.85^{+0.22}_{-0.23}$	$1.05^{+0.12}_{-0.09}$	1.34/401	5.80×10^{-6}
T Leo	$1.09^{+0.21}_{-0.21}$	–	–	$3.55^{+0.10}_{-0.11}$	$0.50^{+0.06}_{-0.06}$	1.40/631	8.359×10^{-11}
V893 Sco	–	$80.89^{+4.18}_{-3.87}$	$0.86^{+0.01}_{-0.01}$	$7.99^{+0.29}_{-0.27}$	$0.76^{+0.04}_{-0.05}$	1.02/1936	0.245
VY Aqr	<1.64	–	–	$5.06^{+0.43}_{-0.50}$	$0.66^{+0.18}_{-0.17}$	0.90/445	0.942
WZ Sge	$8.97^{+2.41}_{-1.92}$	–	–	$4.88^{+0.55}_{-0.54}$	$0.33^{+0.17}_{-0.19}$	0.84/409	0.993
SS Cyg	$2.98^{+0.14}_{-0.25}$	–	–	$10.44^{+0.16}_{-0.17}$	$0.51^{+0.02}_{-0.01}$	1.24/2881	2.741×10^{-17}
Z Cam	$28.21^{+2.63}_{-2.62}$	$292.41^{+99.42}_{-68.86}$	$0.35^{+0.04}_{-0.05}$	$8.68^{+0.84}_{-0.79}$	1.0	1.10/769	0.03
ASAS	<0.84	–	–	$4.38^{+0.61}_{-0.53}$	$0.56^{+0.29}_{-0.24}$	0.88/366	0.958

the absorption columns n_H of the absorbers and the covering fraction of the partial covering model) were tied between the different instrument spectra and let to vary free, apart from the Gaussian line energy at 6.4 keV, the 6.4 keV line width σ , the switch parameter, the redshift, and the hydrogen density parameter of the emitter, which were kept fixed to their default values. In order to estimate the abundances, the abundance parameter of the models was let to vary free for most data sets (and kept tied between the spectra). For those sources for which the abundance was found to be significantly higher than the solar value, it was fixed at 1.0. In general, CV abundances are found to be lower relative to the solar abundance (e.g. the magnetic CV sample of Ezuka & Ishida, 1999). An example of a source with a super-solar

Table 4.4: The best-fit parameters of the absorbed cooling flow model with a 6.4 keV Gaussian line. The errors are 90 per cent confidence limits on one parameter of interest. n_{H_1} and n_{H_2} are the absorption columns of the photoelectric absorption (wabs) and the partial covering (pcfabs) models, respectively. CFrac is the covering fraction of the partial covering model and Ab the abundance.

Name	n_{H_1} 10^{20}cm^{-2}	n_{H_2} 10^{20}cm^{-2}	CFrac	kT keV	Ab	χ^2_ν/ν	P_{null}
BZ UMa	<0.87	–	–	$13.71^{+1.38}_{-0.81}$	$0.57^{+0.13}_{-0.07}$	0.88/904	0.994
GW Lib	<3.76	–	–	$6.96^{+8.79}_{-3.12}$	1.0	0.60/8	0.782
HT Cas	–	$16.74^{+4.05}_{-2.49}$	$0.92^{+0.05}_{-0.04}$	$23.09^{+4.15}_{-5.33}$	$0.78^{+0.27}_{-0.22}$	0.99/258	0.525
SS Aur	$3.30^{+1.79}_{-1.51}$	–	–	$23.47^{+4.01}_{-3.02}$	1.0	0.95/628	0.832
SW UMa	<0.67	–	–	$8.33^{+0.62}_{-0.99}$	$0.41^{+0.08}_{-0.10}$	0.87/469	0.978
U Gem	$0.76^{+0.28}_{-0.21}$	–	–	$25.82^{+1.98}_{-1.43}$	$1.04^{+0.13}_{-0.11}$	1.23/402	1.1×10^{-3}
T Leo	$0.68^{+0.24}_{-0.21}$	–	–	$10.97^{+0.85}_{-0.67}$	$0.50^{+0.07}_{-0.07}$	1.08/629	7.237×10^{-2}
V893 Sco	–	$103.71^{+3.98}_{-3.07}$	$0.90^{+0.01}_{-0.01}$	$19.32^{+1.29}_{-1.40}$	$0.94^{+0.05}_{-0.05}$	0.94/1934	0.973
VY Aqr	$1.10^{+3.15}_{-1.10}$	–	–	$16.47^{+2.68}_{-2.22}$	$0.69^{+0.25}_{-0.20}$	0.86/444	0.984
WZ Sge	$11.58^{+3.96}_{-3.06}$	–	–	$13.31^{+3.01}_{-3.16}$	$0.23^{+0.16}_{-0.13}$	0.83/408	0.996
SS Cyg	$2.84^{+0.11}_{-0.11}$	–	–	$41.99^{+1.20}_{-0.76}$	$0.61^{+0.03}_{-0.02}$	1.19/2883	4.80×10^{-12}
Z Cam	$31.92^{+4.77}_{-5.00}$	$180.28^{+53.37}_{-35.14}$	$0.47^{+0.07}_{-0.06}$	$25.76^{+5.16}_{-2.39}$	1.0	1.08/768	0.06
ASAS	<2.67	–	–	$14.43^{+4.36}_{-2.69}$	$0.68^{+0.44}_{-0.29}$	0.81/366	0.996

abundance is Z Cam for which the obtained abundance was $1.46^{+0.34}_{-0.19} Z_\odot$ with the absorbed cooling flow model when the abundance was let to vary free.

Fig. 4.6 shows the X-ray spectra of the new *Suzaku* XIS observations, i.e. VY Aqr, SW UMa, BZ UMa, SS Aur, and ASAS J0025, which have been fitted with the absorbed cooling flow model with a 6.4 keV emission line component. The BI spectra (red) correspond to the back-illuminated CCD spectra, i.e. XIS1, and the FI spectra (black) to the front-illuminated spectra, i.e. XIS0 and XIS3. The spectra show that the clearest, discrete emission feature seen is the iron Fe $K\alpha$ complex between 6–7 keV. Iron lines at these energies, especially at 6.7 keV, together with an absorbed hard continuum are typical dominant features for CCD-resolution

Table 4.5: The equivalent widths of the Fe 6.4 keV line with their 90 per cent confidence limits derived from the absorbed optically thin thermal plasma (middle column) and cooling flow (right hand column) models.

Name	EW(mekal) eV	EW(mkcflow) eV
BZ UMa	67^{+42}_{-42}	< 79
HT Cas	< 81	< 91
SS Aur	73^{+37}_{-36}	86^{+52}_{-53}
SW UMa	201^{+124}_{-124}	< 141
U Gem	50^{+25}_{-24}	60^{+33}_{-32}
T Leo	71^{+38}_{-38}	< 73
V893 Sco	46^{+12}_{-11}	45^{+11}_{-12}
VY Aqr	< 156	< 157
WZ Sge	< 140	< 76
SS Cyg	75^{+9}_{-4}	73^{+6}_{-7}
Z Cam	120^{+42}_{-42}	164^{+42}_{-43}
ASAS J0025	< 220	< 200

X-ray spectra of DNe as have been seen in Mukai, Zietsman, & Still (2009), Baskill, Wheatley, & Osborne (2005) and Pandel et al. (2005).

Fig. 4.7 illustrates the two dimensional contour plots corresponding to the spectra in Fig. 4.6. They show the range of allowed values of the normalization parameter (i.e. the mass accretion rate \dot{M} in units of $M_{\odot} \text{ yr}^{-1}$) and the shock temperature kT_{max} of the cooling flow model: it is obvious that there is an anti-correlation between these parameters (see the diagonal banana-shaped contour plots). This anti-correlation exists due to the inverse proportionality $kT_{max} \propto 1/\dot{M}$ in Eq. 4.9, i.e. with decreasing \dot{M} , kT_{max} increases and vice versa.

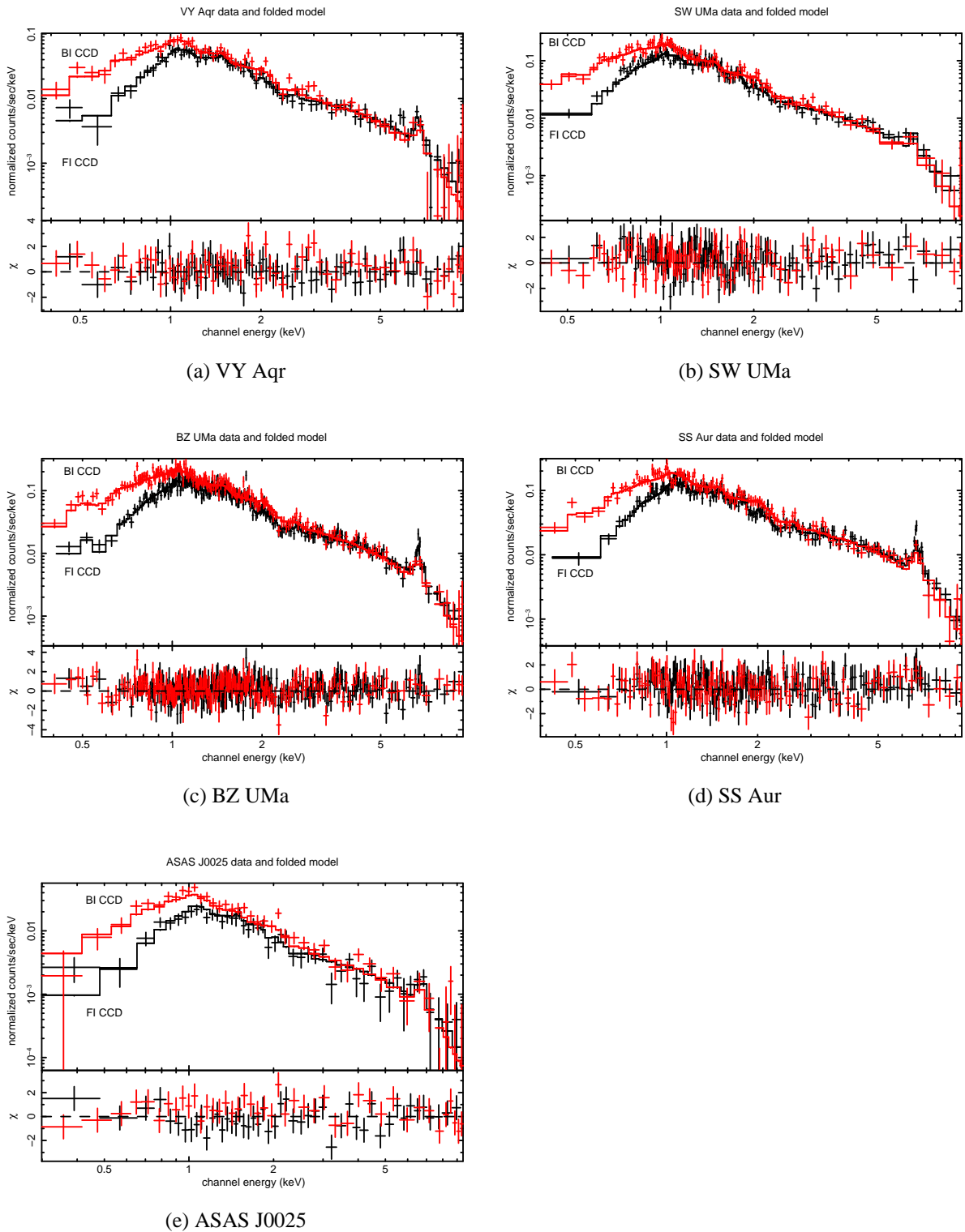
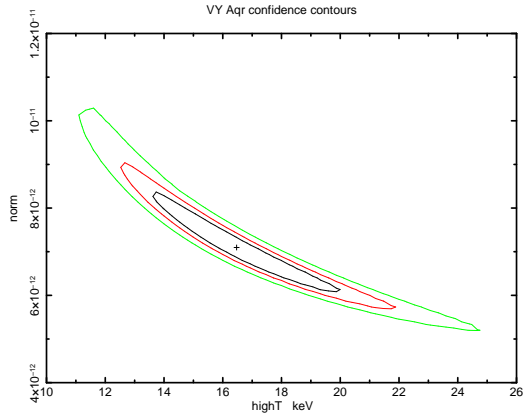
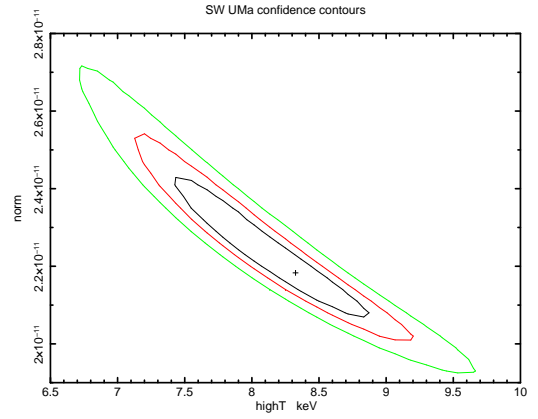


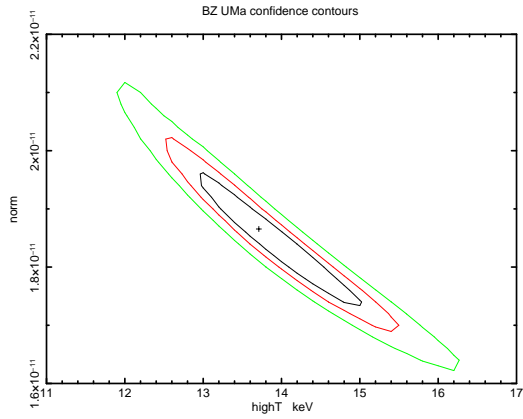
Figure 4.6: The X-ray spectra of VY Aqr, SW UMa, BZ UMa, SS Aur and ASAS J0025 fitted with an absorbed cooling flow model with a 6.4 keV Gaussian line.



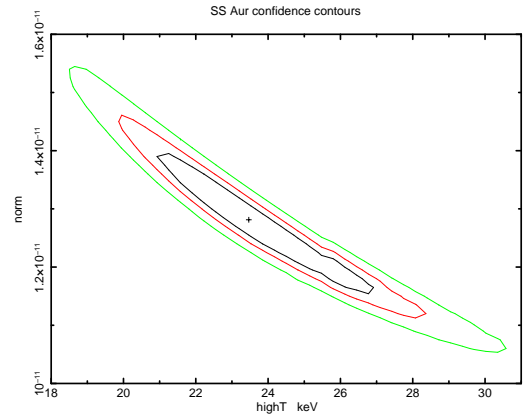
(a) VY Aqr



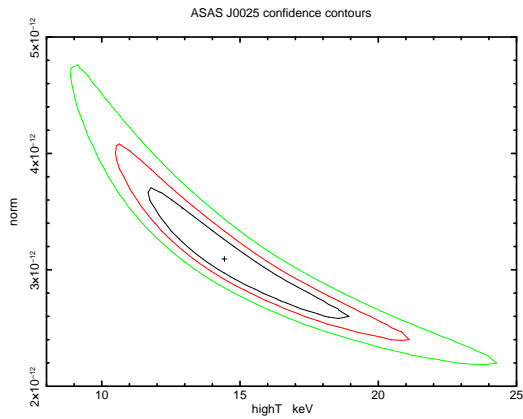
(b) SW UMa



(c) BZ UMa



(d) SS Aur



(e) ASAS J0025

Figure 4.7: The two dimensional confidence contours of the normalization (\dot{M}) and the shock temperature kT_{max} for VY Aqr, SW UMa, BZ UMa, SS Aur and ASAS J0025 which have been fitted with an absorbed cooling flow model with a 6.4 keV Gaussian line.

4.5.1 Absorption

Since the studied sources are all within ~ 200 pc, i.e., within the solar neighbourhood, the effect of interstellar absorption should be negligible. Thus, high measured absorption columns could mainly be due to intrinsic absorption, associated with the sources. For most of the sources, the measured absorption columns were typically of the order of a few $\times 10^{20}$ cm^{-2} , or even lower ($\sim 10^{19}$ cm^{-2}) which indicate low intrinsic and interstellar absorption. However, in some cases the measured absorption column is lower than the Galactic absorption column measured by the HEASARC nh tool. E.g., the Galactic n_H value in the direction of BZ UMa is 4×10^{20} cm^{-2} , but the measured n_{H_1} values are below this ($< 2 \times 10^{19}$ and $< 1 \times 10^{20}$ cm^{-2}). This difference could be explained by the fact that the nh tool also takes into account the absorption column in the space behind the source.

The highest intrinsic absorption columns are found for V893 Sco, Z Cam and HT Cas when compared to the rest of the source sample. All these three sources have partial covering absorbers n_{H_2} with values of the order of 10^{21} – 10^{22} cm^{-2} , depending on the model. In addition to the partial covering absorber, Z Cam also has a simple absorption component with the highest n_{H_1} value, $n_{H_1} \sim 3 \times 10^{21}$ cm^{-2} , within the source sample. Originally, V893 Sco was found to have high intrinsic absorption by Mukai, Zietsman, & Still (2009), and has a partial X-ray eclipse, also discovered by their study. Also, according to the best-fit model of Baskill, Wheatley, & Osborne (2001), Z Cam had large amounts of absorption with $n_H = 9 \times 10^{21}$ cm^{-2} during the transition state. Baskill et al. suggested that this absorption was associated with a clumpy disc wind.

4.5.2 Shock temperatures

The shock temperature of the accreting material depends on the mass of the white dwarf: the more massive the white dwarf, the higher the shock temperature (see Eq. 4.12 below). In

this sample, the measured shock temperatures kT_{max} seem to be correlated with the white dwarf masses M_{WD} (Fig. 4.8) as one would expect. In Fig. 4.8 it has been assumed that the white dwarf mass of VY Aqr is $0.8 M_{\odot}$ (the measured values for the M_{WD} have mainly been obtained from Urban & Sion (2006), Table 4.1). ASAS J0025 is not included in Fig. 4.8 since the mass estimate is currently unknown. Urban & Sion (2006) carried out the white dwarf mass calculations using synthetic spectral analysis of the *International Ultraviolet Explorer* (IUE) archival UV spectra of dwarf novae in or near their quiescence. Their method consisted of synthetic spectral codes for stellar photospheres and optically thick accretion discs, and the best-available distance measurements or estimates. The white dwarf mass for V893 Sco was determined using $H\alpha$ emission line radial velocity measurements together with the secondary star mass function (Mason et al., 2001b), and for SS Cyg using secondary star semi-amplitudes (Friend et al. (1990) and references therein). The uncertainty on the masses obtained by Urban & Sion (2006) is $\pm 0.2 M_{\odot}$, and the mass uncertainties of V893 Sco and SS Cyg are within this value.

The blue dashed line in Fig. 4.8 represents the theoretical shock temperatures for given white dwarf masses. When deriving the theoretical shock temperatures, the radii, R_* , of the given white dwarf masses, M_{WD} , were calculated assuming the mass-radius relation for cold, non-rotating and non-relativistic helium white dwarfs (see Pringle & Webbink, 1975)

$$R_* = 7.7 \times 10^8 x^{0.3767 - 0.00605 \log(x)} \quad (cm), \quad (4.11)$$

where $x = \frac{1.44 M_{\odot}}{M_1} - 1$. Subsequently, the shock temperatures, T_{shock} , for non-magnetic CVs were derived using Eq. 4.12 for optically thin gas (Frank, King, & Raine, 2002)

$$T_{shock} = \frac{3}{16} \frac{GM_{WD}\mu m_H}{kR_*}, \quad (4.12)$$

where m_H is the mass of a hydrogen atom, G the gravitational constant ($6.67 \times 10^{-11} \text{ Nm}^2$

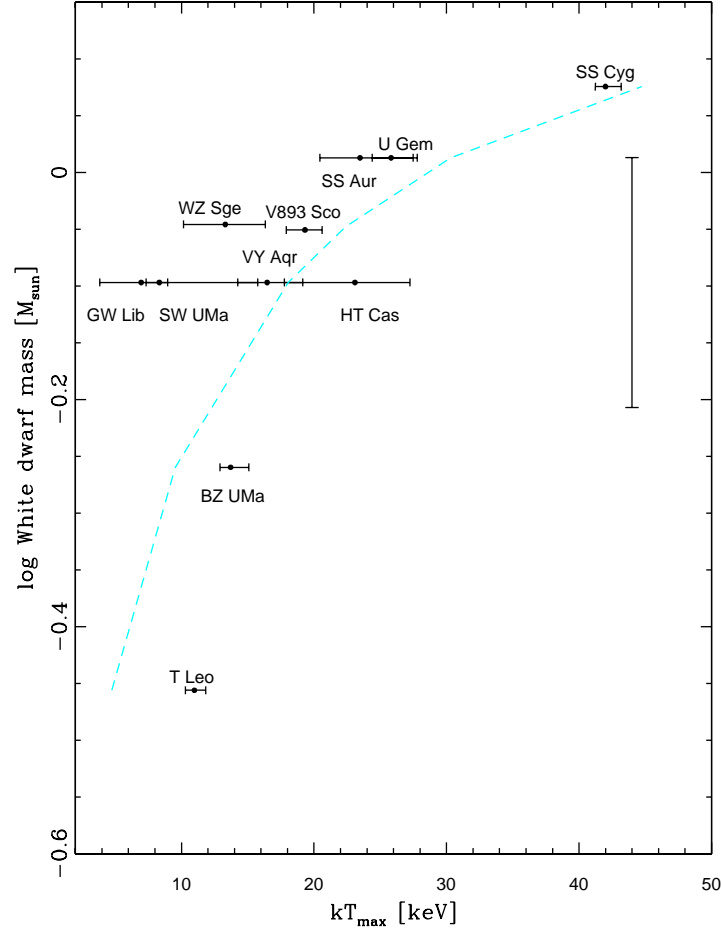


Figure 4.8: The mass of the white dwarfs, M_{WD} , versus the shock temperature, kT_{max} , of the source sample with errors (90 per cent). The light blue dashed line represents the theoretical shock temperature for a given M_{WD} . The error bar on the right indicates a typical error on the white dwarf mass measurements.

kg^{-2} , or in units of $\text{m}^3 \text{kg}^{-1} \text{s}^{-2}$), M_{WD} the given mass of the white dwarf, μ the mean molecular weight, k the Boltzmann constant, and R_* the calculated radius of the white dwarf. Thus, according to Eq. 4.12, the white dwarf mass M_{WD} controls and sets the upper limit for kT_{max} . This equation seems to be holding in practice as, for example, SS Cyg, which is located in the upper right corner in Fig. 4.8, has a high mass white dwarf ($1.19 M_{\odot}$), thus the shock temperature is also high ($\sim 42 \text{ keV}$), whereas BZ UMa with a $0.55 M_{\odot}$ white dwarf has a much lower shock temperature ($\sim 14 \text{ keV}$). The observed kT_{max} temperature of SS Cyg is not far from its theoretical upper limit ($kT_{shock} \sim 45 \text{ keV}$), but the measured kT_{max} of

BZ UMa, and also the kT_{max} of T Leo appear to be higher than the theoretical values. This difference could be explained by white dwarf mass estimates which are too low. The white dwarf mass estimate for T Leo was obtained by Urban & Sion (2006), but Lemm et al. (1993) argue that a low white dwarf mass would not allow superhumps, a defining characteristic for SU UMa stars during superoutbursts and right after, to develop. Also, Patterson et al. (2005) refer to previous superhump studies which have shown that the mass ratio $q = M_2/M_1$ has a key role in producing superhumps where the critical mass ratio would be $q_{crit} \sim 0.3$ (superhumps would be produced with values smaller than this), although this value has not been confirmed by observational evidence.

Next I investigated whether a correlation exists between the M_{WD} and the kT_{max} parameters. To carry out this test, I used the *Spearman's rank correlation test* (this method will be presented in Section 4.5.4), which yields a correlation with a 98.5 per cent significance (2.2σ result, $r_s = 0.71$) between the two parameters. If using $M_{WD} = 0.55 M_\odot$ for VY Aqr, the correlation is only slightly less significant (97.4 per cent, 2.1σ , $r_s = 0.66$).

4.5.3 Abundances

The solar abundance table of Anders & Grevesse (1989), where $[\text{Fe}/\text{H}] = 4.68 \times 10^{-5}$, is the default abundance table built in the XSPEC cooling flow and optically thin thermal plasma models. This abundance table was used in this work. The measured abundances from the sources are the global abundance ratios with respect to the solar abundance. The iron $K\alpha$ complex is the only discrete emission feature seen in the X-ray spectra (Fig. 4.6) which indicates that the total abundance is dominated by iron, whereas emission features of other elements are much weaker. For most of the objects in the sample the abundances were sub-solar with both spectral models. In general, the abundances derived seem to be dependent on the spectral model: abundances are slightly lower when the spectra are fitted with the optically thin thermal plasma model. This is caused by the single temperature characteristic

of this model, in other words, the abundances are lower because the best-fit temperature of this model usually converges close to the peak of the 6.7 keV He-like Fe $K\alpha$ emissivity. But, the cooling flow consists of the temperature at the peak emissivity and, in addition, a range of temperatures outside the peak emissivity. Thus, the abundances will be higher for the cooling flow model to fit the observed data (see the discussion in Mukai, Zietsman, & Still, 2009).

4.5.4 Spearman's rank correlation test

Correlation tests are used to test whether parameters x and y are related. For example, a linear correlation test, also known as *Pearson's* test, is widely used, but interpreting the significance of the correlation coefficient is uncertain. Thus, I used Spearman's rank correlation test (Press et al., 1992) which is also known as a *non-parametric* or *rank correlation* test. Benefits of the Spearman's test compared to the linear correlation test are better robustness and smaller sensitivity to unplanned defects in the data. In practice, if we have N pairs of measurements (x_i, y_i) , Spearman's correlation test replaces the value of each parameter x_i and y_i by a rank which is an integer number. Thus, the final rank list will be a distribution of integers, i.e. 1, 2, ..., N. If ties exist in the data, i.e., if parameters x_i have equal values, or if parameters y_i have equal values, a midrank (the mean of the ranks they would have had if the values had been slightly different) will be calculated for these values. The sum of the ranks in all cases described above will be equal to the sum of integers between 1 and N, i.e., $\frac{1}{2}N(N + 1)$. Finally, a *rank-order correlation coefficient*, r_s , is calculated. The linear correlation coefficient of ranks is calculated according to

$$r_s = \frac{\sum_i (R_i - \bar{R})(S_i - \bar{S})}{\sqrt{\sum_i (R_i - \bar{R})^2} \sqrt{\sum_i (S_i - \bar{S})^2}}, \quad (4.13)$$

where R_i is the rank of parameter x_i among the other x parameters, \bar{R} the mean of R_i 's, S_i the rank of parameter y_i among the other y parameters, and \bar{S} the mean of S_i 's. r_s has a range

between -1 and 1 where a value close to 1 or -1 means a significant correlation, whereas 0 means no correlation. The significance t of a nonzero value of r_s is tested with

$$t = r_s \sqrt{\frac{N-2}{1-r_s^2}}, \quad (4.14)$$

where N is the number of measurements and $(N-2)$ the degrees of freedom. This approximation does not depend on the original distribution of the x and y . r_s is related to a so called *sum squared difference of ranks* D which is defined by

$$D = \sum_{i=1}^N (R_i - S_i)^2. \quad (4.15)$$

When no ties exist in the data, i.e. when the parameters x_i do not have equal values (or the parameters y_i do not have equal values), then D and r_s are related according to

$$r_s = 1 - \frac{6D}{N^3 - N}. \quad (4.16)$$

But, if ties exist in the data, as is the case for some of the data in this work (such as the white dwarf masses M_{WD}), then r_s will be calculated using f_k which is the number of ties in the k th group of ties among R_i 's, and g_m , which is the number of ties in the m th group of ties among S_i 's.

$$r_s = \frac{1 - \frac{6}{N^3 - N} [D + \frac{1}{12} \sum_k (f_k^3 - f_k) + \frac{1}{12} \sum_m (g_m^3 - g_m)]}{\left[1 - \frac{\sum_k (f_k^3 - f_k)}{N^3 - N}\right]^{1/2} \left[1 - \frac{\sum_m (g_m^3 - g_m)}{N^3 - N}\right]^{1/2}}. \quad (4.17)$$

4.5.5 X-ray fluxes and luminosities

The fluxes and luminosities were derived from the cooling flow model in the 2–10 and 0.01–100 keV ranges. These are given in Table 4.6 for each source. These luminosities may be interpreted as the long-term, average quiescent luminosities of these sources, however, it should be noted that the luminosities will vary due to outbursts or possible changes in the mass accretion rate on shorter and longer timescales. The luminosities L were calculated according to

$$L = 4\pi d^2 F, \quad (4.18)$$

where d is the distance to the source in units of parsecs ($1 \text{ pc} = 3.1 \times 10^{18} \text{ cm}$) and F the source flux in units of $\text{erg cm}^{-2} \text{ s}^{-1}$. Note that the number of sources given in Table 4.1 increases with distance as half of the source distances given in Table 4.1 are concentrated around 160 pc. If DNe were uniformly distributed in space, then the number of observed DNe would increase proportional to distance cubed, but eventually drop as the sources become too faint to be detected.

The luminosity errors for the individual sources were derived with

$$L_{lower} = 4\pi d_{lower}^2 F_{lower}, \quad L_{upper} = 4\pi d_{upper}^2 F_{upper}, \quad (4.19)$$

where d_{lower}/d_{upper} are the minimum/maximum distance errors and F_{lower}/F_{upper} the minimum/maximum flux errors. Since the errors are not symmetric, it is not possible to add them in quadrature. The luminosity range of interest is the traditional 2–10 keV band used in X-ray imaging observations, and which is relevant for the GRXE studies. The source luminosities obtained in this range will be used to construct the X-ray luminosity function (Section 4.6). Table 4.6 shows that most of the 2–10 keV X-ray luminosities are concentrated between 10^{30}

Table 4.6: The fluxes and luminosities in the 2–10 and 0.01–100 keV bands derived by using the cooling flow model. The errors on the 2–10 keV fluxes represent the 90 per cent confidence limits. The errors on the 2–10 keV luminosities have been calculated using the errors on the distances and fluxes.

Source	F	L	F	L
	2–10 keV	2–10 keV	0.01–100 keV	0.01–100 keV
	$\times 10^{-12} \text{ erg cm}^{-2} \text{ s}^{-1}$	$\times 10^{30} \text{ erg s}^{-1}$	$\times 10^{-12} \text{ erg cm}^{-2} \text{ s}^{-1}$	$\times 10^{30} \text{ erg s}^{-1}$
BZ UMa	$2.4^{+0.1}_{-0.2}$	$14.9^{+10.8}_{-5.9}$	5.8	36.5
GW Lib	$0.04^{+0.03}_{-0.01}$	$0.05^{+0.10}_{-0.02}$	0.10	0.14
HT Cas	$2.93^{+0.73}_{-0.44}$	$6.07^{+4.23}_{-2.16}$	7.2	14.9
SS Aur	$2.85^{+0.30}_{-0.30}$	$9.59^{+2.31}_{-1.91}$	7.1	23.9
SW UMa	$1.50^{+0.19}_{-0.09}$	$4.87^{+2.19}_{-1.29}$	4.2	13.7
U Gem	$6.88^{+0.27}_{-0.33}$	$8.30^{+1.03}_{-1.01}$	17.1	20.6
T Leo	$5.23^{+0.32}_{-0.33}$	$6.44^{+2.27}_{-1.65}$	13.2	16.3
V893 Sco	$17.3^{+1.1}_{-1.1}$	$50.1^{+51.9}_{-21.4}$	45.7	133.0
VY Aqr	$1.11^{+0.22}_{-0.18}$	$1.26^{+0.75}_{-0.45}$	2.62	2.98
WZ Sge	$3.12^{+1.20}_{-0.50}$	$0.71^{+0.29}_{-0.12}$	7.70	1.76
SS Cyg	$45.7^{+0.5}_{-0.8}$	$150.0^{+29.0}_{-20.0}$	131.7	433.0
Z Cam	$19.2^{+1.9}_{-2.6}$	$61.6^{+74.4}_{-30.3}$	52.3	168.0
ASAS J0025	$0.42^{+0.09}_{-0.08}$	$1.55^{+3.81}_{-0.80}$	1.05	3.88

and $10^{31} \text{ erg s}^{-1}$. This is also seen in Fig. 4.9 which shows a histogram of the X-ray luminosities of the sample. Since the sources are steeply piled up to lower luminosities (between 10^{30} – $10^{31} \text{ erg s}^{-1}$), this could indicate that a population, perhaps a large one, of even lower luminosity sources exists below $10^{30} \text{ erg s}^{-1}$ (but is too faint to be detected with most of the current observing methods). If such a large population was observed and the observations were added to these data, the histogram would continue rising up towards lower luminosity bins. Only one object, GW Lib, stands out with a very low luminosity, $\sim 4 \times 10^{28} \text{ erg s}^{-1}$, which is consistent with the value obtained by Hilton et al. (2007) for GW Lib. Byckling et al. (2009) showed (see Chapter 3), that GW Lib was still an order of a magnitude brighter (L

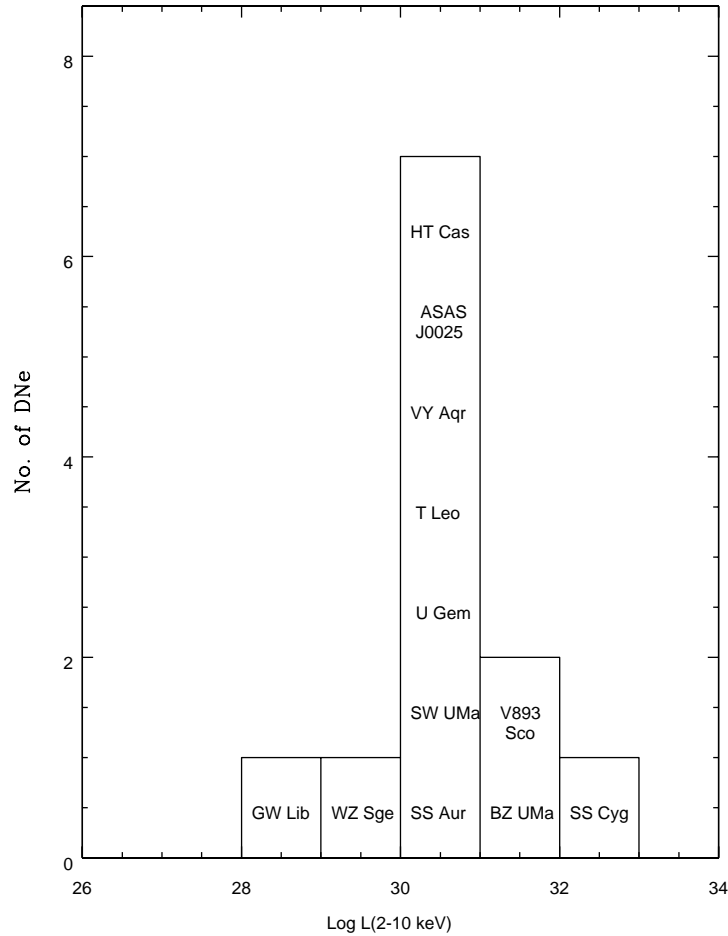


Figure 4.9: A histogram showing the X-ray luminosities of the DN source sample in the 2–10 keV energy range.

$\sim 10^{30}$ erg s $^{-1}$) in X-rays during *Swift* observations two years after the 2007 outburst than in the 2005 measurement by Hilton et al. Since the optical magnitude of GW Lib had not reached the quiescence level ($V \sim 18$) in 2009, the *Swift* 2009 X-ray luminosity should not be considered as the quiescent luminosity. Thus, the higher X-ray luminosity measured in the *Swift* data does not affect the results of this chapter.

One of the sources in the sample, SS Aur, has previously been listed in the *RXTE* All-Sky Slew Survey catalog, where it appears more luminous in X-rays than in the *Suzaku* observation (the *RXTE* flux of SS Aur in 2–10 keV is $\sim 1.1 \times 10^{-11}$ erg cm $^{-2}$ s $^{-1}$). The higher flux in the *RXTE* observation is due to other, bright sources in the field which overestimate the

flux of SS Aur. E.g., the *ROSAT* Bright Source Catalogue lists a cluster of galaxies, Abell 553, which is 53' away from SS Aur and has a WebPIMMS⁶ estimated flux of $\sim 9.3 \times 10^{-12}$ erg cm⁻² s⁻¹ in 2–10 keV (bremsstrahlung kT = 4 keV and Galactic $n_H = 1.56 \times 10^{21}$ cm⁻² as in Ebeling et al., 1996). Thus, the higher *RXTE* flux of SS Aur is very likely biased by the background sources and not reliable.

4.5.6 The height of the X-ray emission source above the white dwarf surface

In this section, I investigate how to constrain the geometry of the boundary layer using a few sources as an example. For that purpose, I will use the measured equivalent widths of the 6.4 keV Fe K α line to calculate the height of the X-ray emission source above the white dwarf (i.e. the height of the boundary layer). The method, which is used below, was applied to the *Suzaku* data of SS Cyg by Ishida et al. (2009).

As was already mentioned in Section 4.5, an equivalent width of up to ~ 150 eV can be expected for the Fe K α fluorescent line at 6.4 keV. I assumed that the reflection originates from the white dwarf surface only, thus any reflection from the accretion disc was not taken into account, i.e. $\Omega_{disc}/2\pi = 0$. The equivalent width of 150 eV occurs under the solar abundance conditions of Morrison & McCammon (1983) where the composition is $[\text{Fe}/\text{H}] = 3.2 \times 10^{-5}$. Anders & Grevesse (1989) abundances, which were employed in this work, were also employed by Ishida et al. who corrected this abundance difference using their measured iron abundance of $0.37 Z_0$. In the following, I take into account the total abundance Z relative to the solar abundance when correcting for the abundance difference between the Anders & Grevesse and Morrison & McCammon abundances. Thus, the observed equivalent width of the 6.4 keV line is

⁶<http://heasarc.gsfc.nasa.gov/Tools/w3pimms.html>

$$\begin{aligned}
EW_{observed} &= 150 \times \frac{4.68 \times 10^{-5}}{3.2 \times 10^{-5}} \left(\frac{\Omega_{WD}}{2\pi} \right) Z \quad (eV) \\
&= 220 \left(\frac{\Omega_{WD}}{2\pi} \right) Z \quad (eV),
\end{aligned} \tag{4.20}$$

where Z is the measured elemental abundance in solar units Z_{\odot} , and Ω_{WD} is the solid angle subtended by the white dwarf viewed from the plasma of the boundary layer. Since the observed equivalent widths are mainly below 150 eV, this means that the boundary layer is located at a height h above the white dwarf surface, compared to the situation $\Omega_{WD}/2\pi = 1$, where the boundary layer is right next to the white dwarf surface. To calculate the height, simple geometry can be used. Fig 4.10 describes the situation when the X-ray source sees the white dwarf surface at a solid angle of $\Omega_{WD}/2\pi$. The solid angle, Ω_{WD} , can be calculated according to

$$\Omega_{WD} = \frac{A}{r^2}, \tag{4.21}$$

where $r = R_{WD} + h$, and A the reflecting surface area as measured from a distance r from the X-ray source. This equation can be written as

$$\Omega_{WD} = \frac{\pi R_{WD}^2}{(R_{WD} + h)^2}, \tag{4.22}$$

and finally

$$\frac{1}{2} \left(\frac{\pi}{\Omega_{WD}} - 1 \right) = \frac{h}{R_{WD}}, \tag{4.23}$$

where Ω_{WD} is obtained from Eq. 4.20.

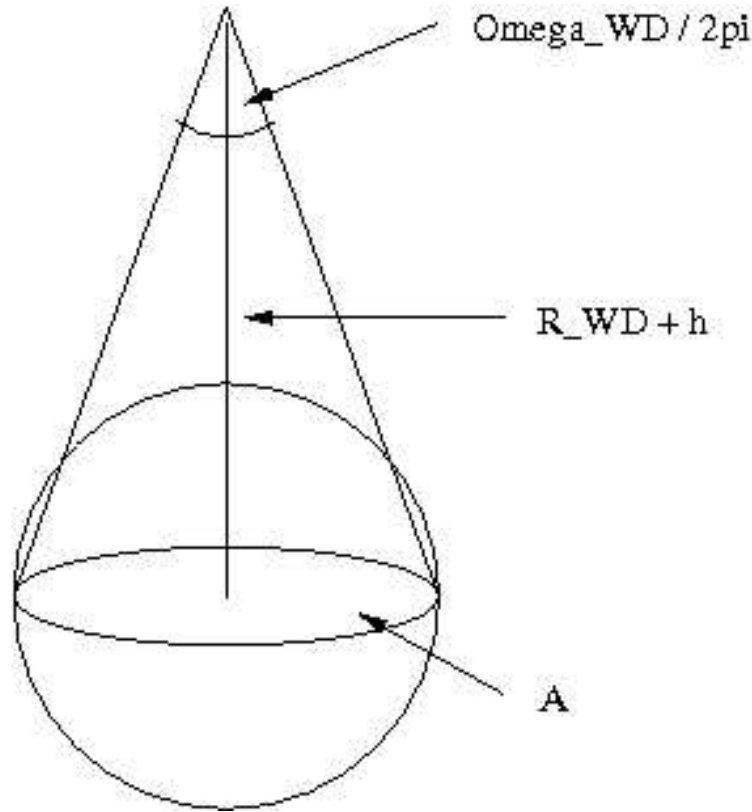


Figure 4.10: Geometry of the solid angle $\Omega_{WD}/2\pi$ of the white dwarf which is viewed from the boundary layer. R_{WD} is the white dwarf radius, h the height of the X-ray source measured from the white dwarf surface and A the surface area as measured from a distance of r from the X-ray source.

The X-ray emission originates from the whole boundary layer (BL), thus we would have to calculate the solid angles for each point in the BL. However, to simplify the calculations, only one point is taken into account and this point describes the typical height h of the whole BL. As an example, the $EW_{observed}$ for SS Aur is 86 eV (Table 4.5), thus Eq. 4.20 gives $\Omega_{WD}/2\pi = 0.39$ (abundance derived from the cooling flow model is $1.0 Z_0$, Table 4.4). If the X-ray source is point-like, the height h of the X-ray source above the white dwarf in SS Aur is $h < 0.14 R_{WD}$ as calculated from Eq. 4.23. As another example, I obtained $\Omega_{WD}/2\pi = 0.22$ and $h < 0.64 R_{WD}$ for V893 Sco ($EW_{observed} = 45$ eV, $Z = 0.94 Z_0$), and $\Omega_{WD}/2\pi = 0.26$ with $h < 0.46 R_{WD}$ ($EW_{observed} = 60$ eV, $Z = 1.04 Z_0$) for U Gem. Thus, as the equivalent width decreases, the height of the boundary layer from the white dwarf surface increases, but of course, the results also depend on the measured source abundances.

4.6 Discussion

I have derived an X-ray luminosity function (XLF) for 12 dwarf novae (excluding Z Cam) using *Suzaku*, *XMM-Newton* and *ASCA* X-ray data. The 2–10 keV luminosities, presented in Table 4.6, range between $\sim 5 \times 10^{28}$ – 1.5×10^{32} erg s⁻¹. A comparison reveals that the measured luminosities in the *ASCA* sample of 10 sources with parallax measurements (Baskill, Wheatley, & Osborne, 2005) appear higher in the range of 10^{31} – 10^{32} erg s⁻¹, whereas most of the source luminosities in the sample presented in this chapter are located within $\sim 10^{30}$ erg s⁻¹ (Fig. 4.9). This difference is most likely due to the fact that I did not select the sample based on X-ray properties of the sources. Also, the objects observed by *ASCA* were known to be X-ray bright, thus the sample of Baskill, Wheatley, & Osborne (2005) is very likely biased by brighter sources.

The integrated XLF, $N(> L)$, was derived for 12 sources (excluding Z Cam) in the sample by using the *maximum likelihood* (ML) method (e.g. Wall & Jenkins, 2003). The likelihood function is defined by

$$L(X_1, X_2, \dots, X_N) = f(X_1, X_2, \dots, X_N | \alpha) \quad (4.24)$$

$$= f(X_1 | \alpha) f(X_2 | \alpha) \dots f(X_N | \alpha) \quad (4.25)$$

$$= \prod_{i=1}^N f(X_i | \alpha), \quad (4.26)$$

where X_1, X_2, \dots, X_N are the data points and α is a parameter characterising the known form of f . To maximise L , we can calculate the *maximum likelihood estimator* (MLE), which is a statistic (depends only on the data and not on any parameters), of α

$$\left. \frac{\partial}{\partial \alpha} \ln L(\alpha) \right|_{\alpha=\hat{\alpha}} = 0. \quad (4.27)$$

In other words, $\hat{\alpha}$ is the maximum likelihood estimator of α , and this is the value of α where L is maximised.

The ML method was used by Jauncey (1967) and Crawford, Jauncey, & Murdoch (1970) to determine the slope of a number-flux-density distribution of astronomical radio sources. The first assumptions in the work of Crawford et al. were that the flux measurements are free of errors and that the flux-density distribution can be approximated with a power law

$$N(> S) = kS^{-\alpha}, \quad (4.28)$$

where $N(> S)$ is the number of sources measured above the flux density S , k a constant, and α the slope. The expression (Wall & Jenkins, 2003) to be maximised by the ML method is

$$\ln L(\alpha) = M \ln \alpha - \alpha \sum_i \ln \frac{S_i}{S_0}, \quad (4.29)$$

where M is the number of sources with flux densities S greater than S_0 . Differentiating Eq. 4.29 with respect to α we obtain

$$\hat{\alpha} = \frac{M}{\sum_i \ln \frac{S_i}{S_0}}. \quad (4.30)$$

In this chapter, these equations were applied to luminosities. The integral form of the luminosity function is

$$N(> L) = k(L/L_t)^{-\alpha}, \quad (4.31)$$

where $N(> L)$ is the number of sources with luminosities greater than the threshold luminosity L_t and k the source density in units of cubic parsec (pc^{-3}).

Fig. 4.11 shows the derived XLF in 2–10 keV: a histogram of the cumulative source density distribution per pc^3 and a power law fit which has been extrapolated below $3 \times 10^{30} \text{ erg s}^{-1}$. The slope α was calculated according to Eq. 4.30 for the higher luminosity end ($> 3 \times 10^{30} \text{ erg s}^{-1}$), giving $\alpha = -0.64$ for the threshold luminosity $L_t = 3 \times 10^{30} \text{ erg s}^{-1}$. The source density k for luminosities L above the threshold luminosity L_t within a spherical volume $V = 4/3 \pi r^3$, where $r = 200 \text{ pc}$ is

$$k = \frac{\frac{4}{3}\pi r^3}{N(L > L_t)} \quad (4.32)$$

where $N(L > L_t)$ is the number of sources above the luminosity L_t . This yielded a normalisation of $k = 2.39 \times 10^{-7} \text{ pc}^{-3}$. The obtained slope α together with the obtained k is a good fit to the histogram, and these values were taken as the best-fit parameters. Also, the Kolmogorov-Smirnov test, which is used to test whether two distributions differ from each other, reveals that the power law is a good fit to the cumulative source density distribution at the higher luminosity end above $3 \times 10^{30} \text{ erg s}^{-1}$ with a significance between ~ 52 and 99 per cent.

At $\sim 3 \times 10^{30} \text{ erg s}^{-1}$, a break is seen between the power law fit and the histogram. This can be due to two possible scenarios: 1) a single α power law describes the luminosity function of DNe, but the sample becomes incomplete at $\sim 3 \times 10^{30} \text{ erg s}^{-1}$, or 2) the shape of the true XLF of DNe is a broken power law with a break at around $3 \times 10^{30} \text{ erg s}^{-1}$. From these two scenarios, the first one is more likely since the sample contains only a few sources below $\sim 10^{30} \text{ erg s}^{-1}$, whereas numerous fainter CVs, such as WZ Sge types, are expected to exist at lower fluxes as was shown by e.g. the study of Gänsicke et al. (2009).

When calculating the total luminosity of the sample, I calculated the total sum of luminosities and the integrated luminosity in order to be able to compare the two values. Note that since the distance of BZ UMa is over 200 pc, it was excluded from the following calculations. The sum L_{tot} of the individual luminosities L_k is simply (e.g. Gilfanov, Grimm, & Sunyaev, 2004)

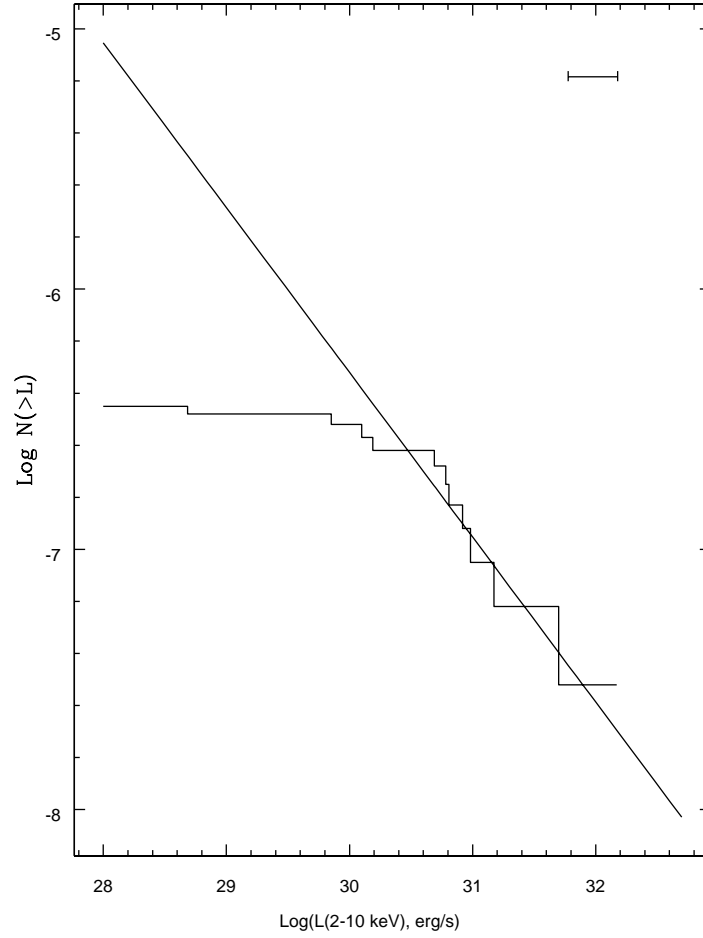


Figure 4.11: The cumulative source density distribution (histogram) and the power law fit versus the luminosity in $\log L$ (2–10 keV) when $\alpha = -0.64$. The threshold luminosity at the break between the power law fit and the histogram is $\sim 3 \times 10^{30} \text{ erg s}^{-1}$. The error bar on the top right represents a typical error on the luminosities.

$$L_{tot} = \sum_{k=1}^N L_k, \quad (4.33)$$

which gives the total luminosity of $2.39 \times 10^{32} \text{ erg s}^{-1}$ for the sample. The differential form of the luminosity function (Eq. 4.31) is

$$\frac{dN}{dL} = k\alpha [L/L_t]^{-\alpha-1}. \quad (4.34)$$

Using Eq. 4.34, the total integrated luminosity can be calculated from

$$\int_{L_1}^{L_2} \frac{dN}{dL} L dL = \frac{k\alpha}{1-\alpha} L_t \left(\left(\frac{L_2}{L_t} \right)^{1-\alpha} - \left(\frac{L_1}{L_t} \right)^{1-\alpha} \right), \quad (4.35)$$

where L_2 is the maximum and L_1 the minimum luminosity.

When calculating the total, integrated luminosity of the sample, I restricted the calculations to the distance of 200 pc, thus excluding BZ UMa. Integrating between the luminosities of 1×10^{28} and the maximum luminosity of the sample ($L_{max} = 1.50 \times 10^{32}$ erg s⁻¹), yields the total integrated luminosity of 1.48×10^{32} erg s⁻¹, whereas the integrated luminosity between the threshold luminosity 3×10^{30} erg s⁻¹ and L_{max} is 1.15×10^{32} erg s⁻¹. These values are \sim a factor of 1.5–2 lower than the total, summed luminosity. The uncertainties in the derived integrated luminosities are most likely introduced by the low number of sources in the sample. In order to obtain a more accurate value for the integrated luminosity, the power law slope ($\alpha = -0.64$) should be better established by adding more DNe to the sample. To give an idea of the uncertainty on the slope, I tested how different threshold luminosities affect the power law slope and the integrated luminosity. For example, raising the threshold luminosity to 4×10^{30} erg s⁻¹ reveals that it is possible to fit a steeper power law which still appears as a good fit to the higher luminosity end above 4×10^{30} erg s⁻¹ (Fig. 4.12) with $\alpha = -0.79$ ($k = 2.09 \times 10^{-7}$ pc⁻³). In this case, the integrated luminosity is higher than obtained with $\alpha = -0.64$: 1.96×10^{32} erg s⁻¹ between 1×10^{28} – 1.5×10^{32} erg s⁻¹, and 1.20×10^{32} erg s⁻¹ between 4×10^{30} – 1.5×10^{32} erg s⁻¹. Thus, a small change in the threshold luminosity notably changes α , and the integrated luminosity in the range 1×10^{28} – 1.5×10^{32} erg s⁻¹.

If the obtained slope ($\alpha = -0.64$) is not far from the true power law slope of DNe in the solar neighbourhood, then the integrated luminosity is dominated by the brighter DNe ($\sim 10^{32}$ erg s⁻¹). Thus, estimating the integrated luminosity more accurately and constraining the higher luminosity end requires more higher luminosity DNe to be included in the sample. Since the

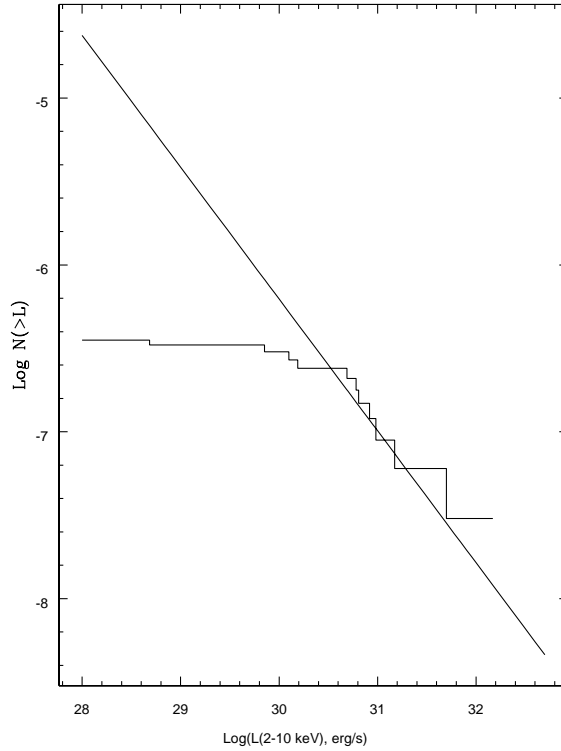


Figure 4.12: The cumulative source density distribution (histogram) and the power law fit versus the luminosity in $\log L$ (2–10 keV) when $\alpha = -0.79$. The threshold luminosity at the break between the power law fit and the histogram is $4 \times 10^{30} \text{ erg s}^{-1}$.

source density at $\sim 10^{32} \text{ erg s}^{-1}$ is $1/3.3 \times 10^7 \text{ pc}^3 \sim 3 \times 10^{-8} \text{ pc}^{-3}$ according to Fig. 4.11, we would need to survey within a volume of $1 \times 10^9 \text{ pc}^3$ to find ~ 30 SS Cyg-type DNe and thus find a statistically significant constraint for the higher luminosities in the sample. This volume would correspond to a distance of $\sim 620 \text{ pc}$ with a flux limit of $\sim 3.2 \times 10^{-12} \text{ erg s}^{-1} \text{ cm}^{-2}$.

4.6.1 X-ray emissivity

How far is the total luminosity of this sample from accounting for the total CV X-ray emissivity? In order to estimate this, I calculated the absolute lower limit for the luminosity per cubic parsec volume (L_x/vol). For a distance of $r = 200 \text{ pc}$, the volume $V = 4/3 \times \pi \times (200$

$\text{pc}^3 = 3.3 \times 10^7 \text{ pc}^3$. When using the total summed luminosity L_x of the sample ($2.39 \times 10^{32} \text{ erg s}^{-1}$), the total absolute lower limit is $L_x/\text{volume} = 7.24 \times 10^{24} \text{ erg s}^{-1} \text{ pc}^{-3}$. Normalising this value to the local stellar mass density of $0.04 M_\odot \text{ pc}^{-3}$ (Jahreiß & Wielen, 1997) yields $1.81 \times 10^{26} \text{ erg s}^{-1} M_\odot^{-1}$ in the 2–10 keV range. For comparison, Sazonov et al. (2006) obtained $(1.1 \pm 0.3) \times 10^{27} \text{ erg s}^{-1} M_\odot^{-1}$ (2–10 keV) for the total CV X-ray emissivity. Thus, my sample would account for ~ 16 per cent of this value.

And finally, how much would my sample account for the GRXE? The Galactic Ridge X-ray emissivity estimated by Revnivtsev et al. (2006) in the 3–20 keV was $L_x/M \sim (3.5 \pm 0.5) \times 10^{27} \text{ erg s}^{-1} M_\odot^{-1}$, meaning that my sample would account for ~ 5 per cent of the Galactic Ridge X-ray emissivity. Assuming that the local space density of DNe within 200 pc is $5 \times 10^{-5} \text{ pc}^{-3}$ (Pretorius, Knigge, & Kolb, 2007) and that DNe are uniformly distributed, then the total number of DNe within 200 pc would be 1700. Also, if a typical DN has an X-ray luminosity corresponding to the mean luminosity ($2 \times 10^{31} \text{ erg s}^{-1}$) of the sample of 11 sources (BZ UMa excluded), then the X-ray emissivity of all DNe in the solar neighbourhood would be $2.6 \times 10^{28} \text{ erg s}^{-1} M_\odot^{-1}$ (2–10 keV). Thus, the X-ray emissivity of all DNe within 200 pc would account for more than 100 per cent of the GRXE emissivity. However, one should remember that the calculated X-ray emissivity of all DNe within 200 pc is probably overestimated by the brighter, known sources in my sample, thus resulting as excess emission. Also, the local space density ($5 \times 10^{-5} \text{ pc}^{-3}$) of Pretorius, Knigge, & Kolb (2007) was calculated for all CVs within 100 pc: the space density of DNe only should be less in order not to produce more apparently diffuse emission than the actual observed GRXE (see also the discussion by Mukai & Shiokawa, 1993).

4.6.2 Correlations between X-ray luminosity and other parameters

To understand whether the X-ray luminosities and the various parameters, P_{orb} , kT_{max} , i , and M_{WD} , are correlated, I carried out a correlation test using Spearman's rank correlation

(Section 4.5.4). The X-ray luminosities have been plotted as a function of these parameters in Fig. 4.13(a), (b), (c) and (d). These plots, in particular Fig. 4.13(c), show that GW Lib seems to appear as an outlier with its low luminosity compared to the rest of the sample. Thus, to see how GW Lib affects the test results, I carried out two test cases: 1) including GW Lib, and 2) excluding GW Lib from the rest of the sample.

These data show a strong correlation at the 99.95 per cent significance level (2.8σ , $r_s = 0.84$) between the X-ray luminosities and orbital periods (Fig. 4.13(a)) when GW Lib is included in the sample. The correlation still holds when GW Lib is excluded (99.67 per cent significance, $r_s = 0.80$). Baskill, Wheatley, & Osborne (2005) noted that there was a weak correlation between the X-ray luminosities and the orbital periods in their *ASCA* sample and they concluded that the X-ray luminosity probably also correlated with long-term mean accretion rate. The X-ray luminosity and the maximum shock temperature kT_{max} show evidence of a correlation at the 2.1σ level when GW Lib is included in the sample (probability is 97.6 per cent, $r_s = 0.64$) in Fig. 4.13(b). As it appears from Fig. 4.13(b), sources with high shock temperatures and low luminosities are not seen. This is sensible since the X-ray luminosity is proportional to kT_{max} (Eq. 4.9), thus we would expect to see high shock temperatures and high luminosities.

The X-ray luminosity and the inclination i are not correlated in either case (Fig. 4.13(c)). The correlation between these parameters was measured when the inclination of BZ UMa was set to 65° (see Table 4.1). Altering the inclination between 60° and 75° did not affect the result of the correlation. This result is in contrast with the discovery of anti-correlation between the emission measure and inclination (van Teeseling, Beuermann, & Verbunt, 1996). It is worth noting that the *ROSAT* bandpass was very narrow, covering only 0.1–2.4 keV where the softer X-ray emission is probably intrinsically absorbed by the sources. An anti-correlation between the X-ray luminosity and inclination in the *ASCA* sample was also seen by Baskill, Wheatley, & Osborne (2005), although, they noted that the inclinations might be uncertain, which can also be the case in this sample.

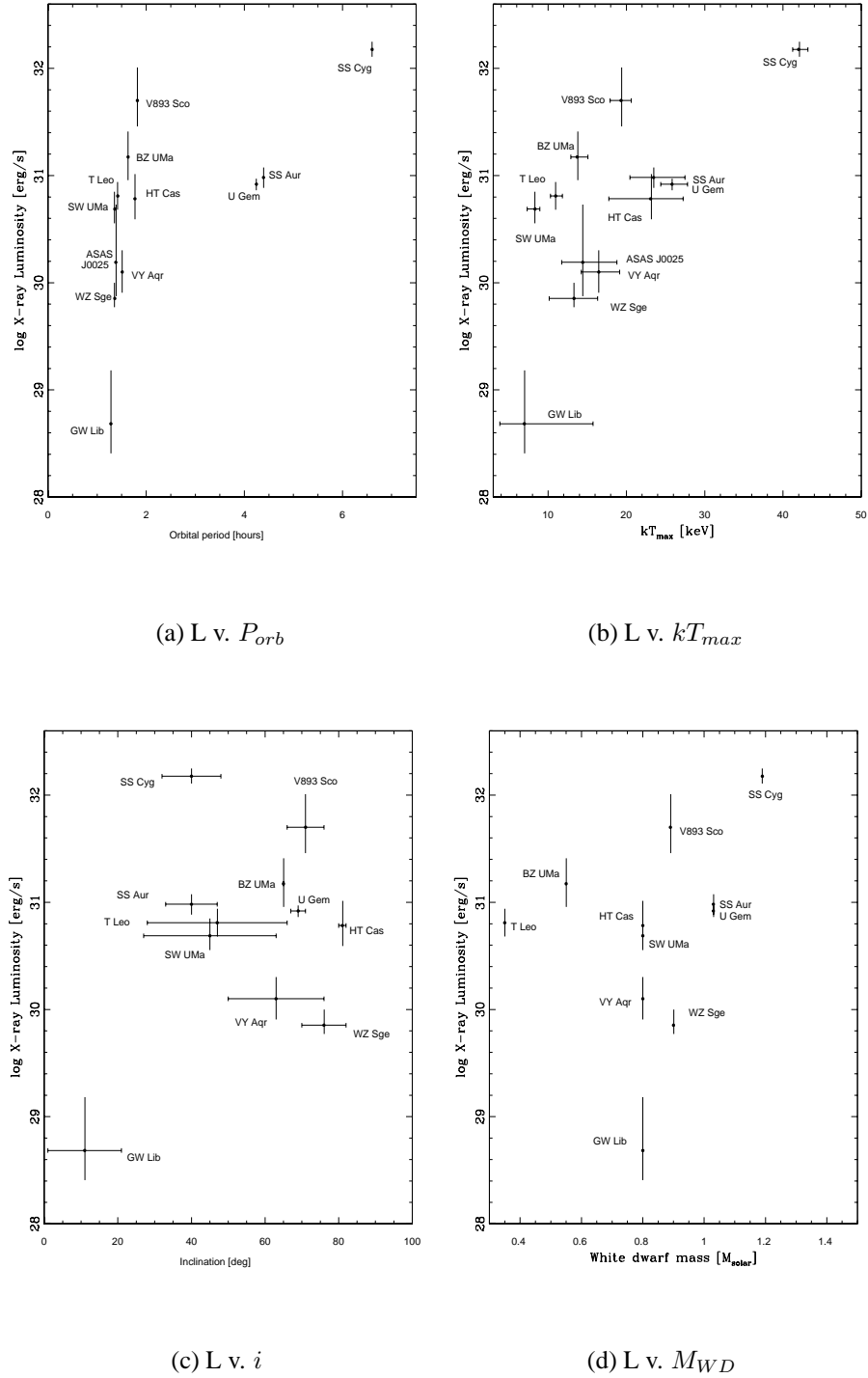


Figure 4.13: The figures above show the 2–10 keV X-ray luminosities versus: (a) the orbital periods of the source sample P_{orb} , (b) the maximum shock temperatures kT_{max} , (c) the system inclinations i , and (d) the white dwarf masses M_{WD} .

Table 4.7: The significance of the correlations between the X-ray luminosity and the system parameters calculated with Spearman’s rank correlation test. Probability¹ corresponds to the significance of correlation when GW Lib is included in the sample and Probability² to the significance when GW Lib is excluded.

	Probability ¹	Probability ²
	%	%
L v. kT_{max}	97.6	91
L v. i	1.1	65
L v. M_{wd}	69	63
L v. P_{orb}	99.95	99.67
M_{wd} v. kT_{max}	98.5	–

Finally, Fig. 4.13(d) shows a plot of the X-ray luminosity versus the white dwarf mass M_{WD} which are not correlated: Spearman’s rank test yields 69 per cent significance ($r_s = 0.34$) when GW Lib is included in the sample, and 63 per cent significance ($r_s = 0.32$) when excluding GW Lib. Changing the white dwarf mass of VY Aqr to $0.55 M_{\odot}$ does not affect the correlation.

The probabilities for each test case (with the mass of VY Aqr $M_{WD} = 0.80$) have been listed in Table 4.7. In order to better explore these potential correlations in DNe, a larger DN sample is needed. Note, that the probability given for M_{WD} versus kT_{max} was calculated in Section 4.5.2.

4.7 Conclusions

In this chapter, I have presented the results of the X-ray data analysis of 13 dwarf novae which have accurate parallax-based distance estimates, and derived an X-ray luminosity function in

the 2–10 keV energy band for 12 of these sources. This sample represents the most accurate X-ray luminosity function in the 2–10 keV band to date due to parallax-based distance measurements.

The derived X-ray luminosities are located between $\sim 10^{28}$ – 10^{32} erg s $^{-1}$, showing a peak at $\sim 10^{30}$ erg s $^{-1}$. The luminosities obtained are lower compared to other previous studies of CV luminosity functions. This result has been achieved due to the fact that an X-ray selected sample was not used in this work. Based on the shape of the X-ray luminosity function, two scenarios are possible: 1) the sample can be described by a single power law but the sample becomes incomplete below $\sim 3 \times 10^{30}$ erg s $^{-1}$, or, 2) the shape of the real X-ray luminosity function of dwarf novae is a broken power law with a break at around 3×10^{30} erg s $^{-1}$. Of these scenarios, the first one is very likely.

The total X-ray emissivity of the sample within a radius of 200 pc is 1.81×10^{26} erg s $^{-1}$ M $_{\odot}^{-1}$ (2–10 keV) between the luminosity range of 1×10^{28} and 1.50×10^{32} erg s $^{-1}$. This accounts for ~ 16 per cent of the total X-ray emissivity of CVs, and ~ 5 per cent of the Galactic Ridge X-ray emissivity. The total integrated luminosity for sources within 200 pc is 1.48×10^{32} erg s $^{-1}$ between the luminosity range of 1×10^{28} and 1.50×10^{32} erg s $^{-1}$. Future X-ray imaging observations of more dwarf novae in the 2–10 keV range with accurate distance measurements are needed to better constrain the integrated luminosity and the slope of the X-ray luminosity function.

The X-ray luminosities and the inclinations of the sample do not show the correlations which have been seen in previous correlation studies, but a strong correlation is seen between the X-ray luminosities and the orbital periods. Also, evidence for a correlation between the white dwarf masses and the shock temperatures exists ($P = 98.5$ per cent). Larger dwarf nova samples are needed in order to confirm these results.

Chapter 5

Surveying the Galactic Plane with *XMM-Newton*

5.1 Introduction

In Chapter 4, I discussed deriving an X-ray luminosity function for dwarf novae (DNe) in the solar neighbourhood, and the contribution of DN emission to the unresolved Galactic Ridge X-ray Emission (GRXE). In this chapter (Chapter 5), I will investigate the origin of the GRXE from a survey point of view using *XMM-Newton* archival observations of serendipitous X-ray sources. In particular, the focus is on the fainter X-ray sources, since the brighter Galactic X-ray sources have mostly been mapped (see below), but many of the properties of the fainter X-ray source population are still not properly known. In general, X-ray surveys are carried out for numerous reasons (see a review of Galactic Plane surveys by Motch, 2006). The reasons for carrying out such studies include furthering our understanding of accretion processes in binary stars, and stellar and Galaxy evolution. In addition, survey studies enhance our information on the evolutionary states of the sources in connection with their distribution and location in the Galaxy (e.g. the evolution of the typical Galactic scale height of stars with

age).

The earliest X-ray observations with collimator experiments carried out in the 1970s with missions, such as *Uhuru*, discovered bright X-ray sources (e.g. Sco X-1 which was the first X-ray source discovered) with luminosities of the order of $\sim 10^{38}$ erg s⁻¹ in the Galactic Plane (Forman et al., 1978). This early work was subsequently followed by *Ariel V* (Warwick et al., 1981) and *HEAO-1* (Wood et al., 1984) observations of the brightest X-ray sources. Thanks to these studies, the first accreting binary stars with neutron star and black hole companions were discovered. Later on with the developing X-ray imaging capabilities of missions, such as *Einstein* and *ROSAT*, Hertz & Grindlay (1984) and Motch et al. (1997) discovered numerous low luminosity sources at low Galactic latitudes. These telescopes operated in the softer bands of 0.5–4.5 keV (*Einstein*) and 0.1–2.4 keV (*ROSAT*). Many of the soft sources so discovered were found to be active stars, although these surveys also revealed the existence of many new accreting white dwarf binary systems. When surveying the Galaxy in the energy bands $\sim < 3$ keV, distant sources, such as background Active Galactic Nuclei (AGNs) are suppressed by absorption in the Galactic interstellar medium (ISM); thus nearby stars typically dominate observations at softer energies. Conversely at higher energies (> 3 keV), hard X-ray emission from background AGNs becomes more important.

In recent years, X-ray imaging capabilities have developed further with enhanced sensitivity and spatial resolution, thus enabling the detection of even a larger number of low luminosity stars. The first hard (2–10 keV) X-ray imaging survey of faint sources focused on the central region of the Galactic Plane ($|l| \lesssim 45^\circ$, $|b| \lesssim 0.^\circ 4$) and was carried out by *ASCA* (Sugizaki et al., 2001). This study was motivated by the fact that the number of faint ($F < 10^{-11}$ erg cm⁻² s⁻¹) discrete sources in the Galaxy and their contribution to the GRXE was unknown. The study by Sugizaki et al. showed that the contribution of the flux of the faint resolved sources to the surface brightness of the GRXE was 11 per cent in the 0.7–2 keV band, and ~ 10 per cent in the hard band (2–10 keV). They suggested that the unresolved GRXE emission below 2 keV was due to local hot bubbles near the solar system (Kaneda et al., 1997), but

above 2 keV the main origin of the GRXE still remained unresolved.

Later, Motch, Herent, & Guillout (2003) carried out an *XMM-Newton* source content survey at low ($b \sim 0^\circ$) and high ($b \sim 50^\circ$) Galactic latitudes with the aim of understanding source properties, relative populations and their contributions to the overall soft and hard X-ray galactic emission. They discovered that at low b , i.e. in the Galactic Plane, there was a luminosity peak between 10^{29} – 10^{30} erg s $^{-1}$, indicating that these X-ray sources were mainly young active stars and binaries, whereas at higher latitudes the X-ray luminosity showed two peaks between 10^{28} – 10^{29} and 10^{30} – 10^{31} erg s $^{-1}$. Of these peaks, the lower luminosity component implied the presence of a relatively old stellar population, but the origin of the higher luminosity peak was not clear. Subsequently, Hands et al. (2004) used *XMM-Newton* to survey the Galactic Plane with 22 pointings between 19° and 22° in Galactic longitude and $\pm 0.6^\circ$ in latitude. They found an excess of hard X-ray emission above the expected extragalactic background, indicating the presence of Galactic hard X-ray sources. They could not identify the faint Galactic population in the flux range of 10^{-13} – 10^{-12} erg cm $^{-2}$ s $^{-1}$, but assumed that sources at these fluxes could mainly be cataclysmic variables (CVs) and RS CVn systems.

Despite several studies, the origin of the diffuse emission in the Galactic Plane has remained unclear, and the ultimate question is whether the unresolved GRXE emission is a superposition of discrete sources or purely diffuse plasma. The latter option is difficult to understand since the plasma pressure would be too high to be stable in the Galactic Plane, and the thermal velocity would exceed the escape velocity of the plane (Koyama et al., 1986). An increasing number of studies of the GRXE support the view that it has a discrete point source origin. For example, Revnivtsev et al. (2006) discovered that the large scale distribution of the GRXE was similar to the Galactic distribution of the intermediate to relatively old stellar populations, such as CVs and active late-type binaries, as inferred from near-infrared (NIR) observations. This correlation between the two distributions suggested that the GRXE is of stellar origin. Later on, an *INTEGRAL* all-sky survey in hard X-rays (17–60 keV) by Revnivtsev et al. (2008) showed that numerous active binaries (such as RS CVns) and faint CVs are expected

to have an important contribution to the cumulative hard X-ray emission of galaxies. And, the most recent survey carried out by using *Chandra* by Revnivtsev et al. (2009) resolved more than 80 per cent of the GRXE into discrete sources between 6–7 keV.

What are the observational facts of the GRXE? The scale height of the ridge emission was found to be ~ 100 pc (Warwick et al., 1985; Yamauchi & Koyama, 1993), and the total luminosity $\sim 10^{38}$ erg s $^{-1}$. As was observed by *Ginga* (Yamasaki et al., 1997) and *Rossi X-ray Timing Explorer* (RXTE) (Valinia & Marshall, 1998), the total X-ray spectrum of the GRXE has a hard power law tail above 10 keV with a slope of ~ 2 , extending all the way to γ -ray region, but below 10 keV, the spectrum is in good agreement with emission from hot plasma with a temperature of $kT \sim 5$ –10 keV with an iron emission line at 6.7 keV. These spectral features indicated the possible presence of both non-thermal and thermal components in the ridge emission (Valinia & Marshall, 1998). Spectrally the GRXE spectrum is similar to CVs and RS CVn stars (Worrall & Marshall, 1983).

The discovery of the iron K-shell line emission from ionised He-like iron at 6.7 keV along the Galactic Ridge was first reported by Koyama et al. (1986). The measured line equivalent width (EW) was between 400–700 eV. The observations were obtained with the Tenma X-ray satellite, and later the 6.7 keV line was also seen by Yamauchi & Koyama (1993) with *Ginga*. Ebisawa et al. (2008) reported for the first time that the iron K-line complex was clearly resolved into three distinct peaks at 6.4 (K α neutral iron line), 6.67 (He-like iron), and 7.0 keV (H-like iron), with line widths less than ~ 50 eV. The likely origin of the He- and H-like K α iron lines is thought to be collisional ionization equilibrium plasma (Ebisawa et al., 2008), and the He-like K α line a blend of resonance, inter-combination and forbidden lines. Ebisawa et al. also noted that if the He-like K α complex could be resolved into individual lines, the density of the plasma and thus the origin of the plasma emission could be constrained. A recent study carried out by Yamauchi et al. (2009) yielded an EW of ~ 300 –980 eV for the 6.7 keV line and < 400 eV for the 6.4 keV line along the Galactic Ridge and the Galactic Centre using *Suzaku*. Yamauchi et al. measured the EWs using X-ray photons from the entire

XIS field of view excluding point sources, and they noted that the 6.7 keV iron line was found in all of their observations along the Galactic Ridge and in the Galactic Centre, indicating the presence of hot, optically thin thermal plasma along the Galactic Plane. Also, the 6.4 keV iron line was present in various regions in their observations in the Galactic Plane ($b \sim 0^\circ$), being particularly conspicuous close to the Galactic Centre. The presence of this line was puzzling, as this line originates from near neutral material. Yamauchi et al. suggested that, if the GRXE has a point source origin, the presence of the 6.4 keV iron line together with the 6.7 and 6.97 keV iron lines implies that CVs, which show these features in their X-ray spectra, are the major contributor to the GRXE emission.

5.1.1 This work

In this work, I have studied *XMM-Newton* archival observations of serendipitous point sources in a 'narrow strip' extending over $|l| < 45$ degrees of the Galactic longitude and $|b| < 2.5$ degrees of the Galactic latitude. Motivated by the previous published X-ray surveys, the main goal of the work presented in this chapter is to obtain a further insight into the properties of serendipitous X-ray point sources in the Galactic Plane. Ultimately, the goals are to understand whether a significant proportion of these sources might be CVs, and how much they might contribute to the GRXE, but these questions are beyond the scope of the present chapter and will be the subject of future work. Hence, the focus will be in understanding the broad properties of the population of point sources at faint/intermediate X-ray fluxes ($< 10^{-11}$ – 10^{-12} erg cm $^{-2}$ s $^{-1}$). Since the main interest will be in studying the spectral characteristics of these sources, a requirement is that they have to have sufficient counts to allow meaningful spectral analysis.

Currently, there are no published *XMM-Newton* surveys which would cover the whole plane, although closely related work exists, such as the studies by Motch, Herent, & Guillout (2003), and Hands et al. (2004). *XMM-Newton* with its large effective area (~ 1500 cm 2 at 1 keV

for each X-ray telescope), excellent sensitivity (flux limit $\sim 10^{-14}$ erg cm $^{-2}$ s $^{-1}$ for EPIC pn and MOS in the energy range 0.15–15 keV), and a wide field of view (30 arcmin in diameter) is well-suited for surveys looking for faint X-ray sources in the Galaxy. For the purpose of defining a sample of sources at faint/intermediate fluxes in the Galactic Plane, I have employed the *2XMM* catalogue (Watson et al., 2009) which is the largest X-ray source catalogue ever produced and contains nearly 250,000 X-ray source detections. In addition to the target in pointed *XMM-Newton* observations, significant numbers of serendipitous X-ray sources have been detected. Thus, the *2XMM* is a catalogue dominated by serendipitous sources. Due to its large size and well-defined selection criteria, the *2XMM* catalogue is an excellent resource for the study of the X-ray source content of the Galaxy.

The outline of this chapter is following: In Section 5.2, I will outline the screening criteria used to derive the source sample, and in Sections 5.3 and 5.4 the data reduction methods and spectral analysis, respectively. Sub-section 5.4.2 discusses the results of cross-matching the *2XMM* sample with the *Two Micron All Sky Survey* (2MASS). Finally, Sections 5.5 and 5.6 will be dedicated to the discussion and conclusions sections of this chapter.

5.2 Screening of the observations and the source sample

The X-ray observations were obtained from the *XMM-Newton* Science Archive (XSA)¹. The data reduction was performed in the standard manner as described in the *XMM-Newton Science Analysis System User Guide*². All observations were obtained in full frame mode. The original list of *XMM-Newton* observations included 249 archival *XMM-Newton* pn and MOS observations which had been obtained along the Galactic Plane covering (+45,-45) degrees of Galactic longitude l , and (+2.5,-2.5) degrees of Galactic latitude b . The initial screening involved checking each *XMM-Newton* image by eye and excluding those observations which

¹<http://xmm.esac.esa.int/xsa/>

²http://xmm.esac.esa.int/external/xmm_user_support/documentation/sas.usg/USG/

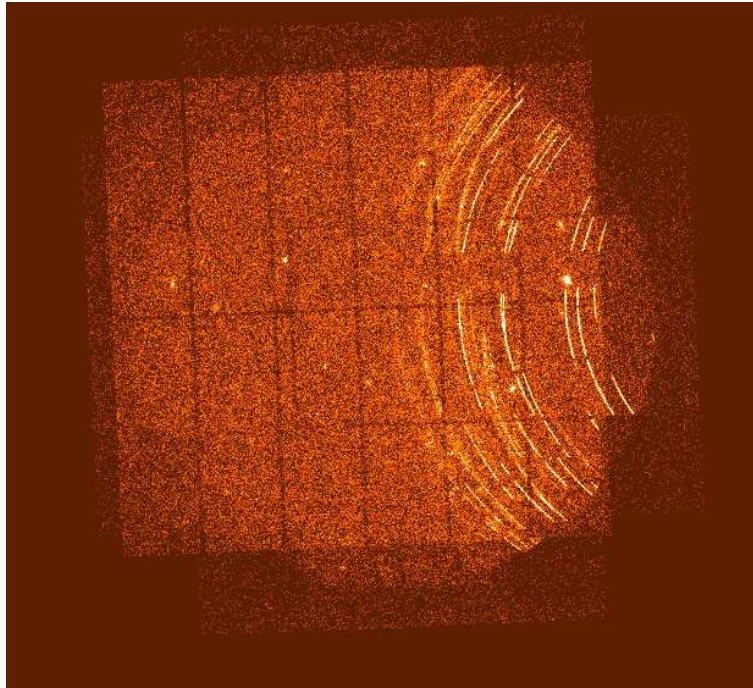


Figure 5.1: Straylight features (on the right) in the observation 0135960101 which was excluded during the screening. In the image, north is up and east to the left. The image consists of all EPIC (pn and MOS) images and was obtained from the *XMM* XSA.

had unwanted and contaminating artifacts and features, such as X-ray straylight features, or large supernova remnants covering the whole or most of the FOV, in which case point sources were contaminated. Straylight features are caused by X-ray sources which are located outside the field of view, and X-rays from these sources are singly reflected by the mirrors onto the active focal plane area. The resulting arc-shaped features are illustrated in Fig. 5.1.

Once the observation fields had been screened by eyeballing, the number of sources regarded as acceptable for further investigation was ~ 1600 consisting of both pn and MOS sources. Next, the focus was to select a suitable sample of point sources with sufficient counts for spectral analysis. Only pn sources were studied in this work, and I chose only those source observations which were obtained with the Medium filter (useful for preventing optical contamination from point sources as bright as $m_V = 6-9$). To obtain a statistically meaningful source signal, the minimum pn gross count limit was set to 100. In case of multiple observations of the same source, the longer exposure time and/or better quality observation was

chosen. Some of the individual sources in the observations were not suitable to be included in the analysis due to confusion with another source, or due to being too close or partly on chip gaps or bad columns, or on the edge of the field of view. After applying these screening criteria, the number of sources reduced significantly: from 1600 to 116 pn sources. Of these, 7 sources were suspiciously bright having more than 1000 pn gross counts. Subsequently, these sources were inspected using SIMBAD Astronomical Database³, which is widely used for finding information on individual astronomical objects. Identifications were found for 6 out of the 7 bright sources and these were subsequently excluded from the sample since they were known objects (e.g. one of the bright sources was a cluster of galaxies, Nevalainen et al., 2001). However, one source with gross pn counts of 1083 (source number 158936, Table 5.1) was included since no identification was found for it in SIMBAD and after background subtraction, the number of net pn counts was less than 1000 (800). The final *XMM-Newton* source sample listed in Table 5.1, comprises 110 point sources detected in 45 different observations. These sources and observations have been plotted in Fig. 5.2 (a) and cover a region between 43° and 327° in longitude and between -2.16° and $+2.44^\circ$ in latitude with a sky coverage of $\sim 10 \text{ deg}^2$. Fig. 5.2 (b) shows a close-up of the observations. The sizes of the green boxes correspond to the size of the field of view of EPIC pn (0.5×0.5 degree).

³<http://simbad.u-strasbg.fr/simbad/>

Table 5.1: The *XMM-Newton* source sample (110 sources) obtained along the Galactic Plane. In addition to source and observation identification (ID) numbers, the table lists the IAU name of the source, the number of raw (gross) pn counts in the extracted source spectrum (prior to background subtraction), the exposure time of the observations (after flare filtering) as derived from the source spectra, and the RA and DEC (J2000) of the sources (as tabulated in the 2XMM catalogue).

Source	ObsID	IAU name 2XMM	pn counts	T_{exp} s	R.A.(J2000.0) deg	DEC(J2000.0) deg
142052	0203910101	J154951.7-541630	760	3401	237.465658	-54.2750444
142126	0203910101	J155037.5-540722	170	2910	237.656316	-54.1227998
148350	0307170201	J163737.0-472951	529	38169	249.404259	-47.4975634
148374	0307170201	J163748.3-472220	537	43853	249.451563	-47.3722512
148388	0307170201	J163756.4-471949	792	36199	249.485311	-47.3304365
148402	0307170201	J163802.7-471357	551	22285	249.511278	-47.2325863
148411	0307170201	J163808.5-472607	633	53515	249.535738	-47.4354710
148493	0307170201	J163835.9-472145	774	38197	249.649899	-47.3625027
148497	0303100101	J163837.7-464725	427	15426	249.657553	-46.7905177
148502	0303100101	J163839.2-470618	556	19400	249.663486	-47.1052154
148509	0307170201	J163840.9-471952	482	31991	249.670763	-47.3313047
148513	0307170201	J163842.3-473008	611	36339	249.676618	-47.5023776
148559	0303100101	J163855.1-470146	859	29651	249.729939	-47.0295199
148620	0303100101	J163914.5-470020	672	29403	249.810491	-47.0057364
148624	0307170201	J163915.1-472310	432	22748	249.813242	-47.3861357
148707	0307170201	J163937.8-471951	460	16375	249.907890	-47.3311098
148790	0303100101	J164004.1-470419	651	13713	250.017432	-47.0721000
150181	0112460201	J165340.2-395709	179	13194	253.417520	-39.9526689
150188	0112460201	J165341.1-395735	146	12071	253.421601	-39.9598987
150845	0112460201	J165443.1-394804	317	10044	253.679689	-39.8011146
150957	0112460201	J165515.6-394544	393	5810	253.815356	-39.7622544
151081	0200900101	J165739.8-425715	667	13926	254.416036	-42.9543592

Table 5.1: The *XMM-Newton* source sample (contd.).

Source	ObsID	IAU name 2XMM	pn counts	T_{exp} s	R.A.(J2000.0) deg	DEC(J2000.0) deg
151278	0200900101	J165906.6-424210	430	6662	254.777526	-42.7028169
152200	0144080101	J170713.1-405414	317	9653	256.804773	-40.9039008
152262	0144080101	J170819.6-404606	210	3449	257.081810	-40.7684999
155792	0112971901	J174351.2-284638	196	1788	265.964078	-28.7771176
155865	0112970701	J174423.3-291743	700	14074	266.097100	-29.2953294
156080	0103261301	J174508.0-303906	146	1932	266.283579	-30.6516822
157004	0112970201	J174645.2-281547	342	5961	266.688484	-28.2631686
157045	0112970201	J174654.6-281658	304	6419	266.727791	-28.2827113
157148	0205240101	J174716.1-281047	584	4437	266.817344	-28.1799679
157193	0205240101	J174722.8-280905	493	5063	266.845612	-28.1518676
157247	0205240101	J174730.8-281347	257	5253	266.878799	-28.2301412
157393	0205240101	J174804.1-281446	259	7901	267.017633	-28.2461563
157432	0205240101	J174814.0-281621	185	7490	267.058645	-28.2727040
157439	0205240101	J174816.9-280750	251	13112	267.070596	-28.1307254
157532	0112970101	J174841.1-280136	134	9078	267.172494	-28.0274295
157544	0112970101	J174848.0-281240	541	7211	267.200171	-28.2110904
157571	0112970101	J174858.3-281422	284	5792	267.243276	-28.2394799
158008	0206990101	J175035.2-311825	268	5795	267.646990	-31.3070195
158050	0206990101	J175046.8-311629	335	6924	267.695166	-31.2748370
158318	0307110101	J175137.1-295522	493	6088	267.904688	-29.9228717
158373	0307110101	J175155.9-295113	794	9280	267.983322	-29.8536568
158409	0307110101	J175233.1-293944	359	5339	268.138201	-29.6623991
158631	0302570101	J175446.3-285659	529	11116	268.693471	-28.9500546
158719	0206590201	J175516.6-293655	498	4718	268.819520	-29.6154075

Table 5.1: The *XMM-Newton* source sample (contd.).

Source	ObsID	IAU name 2XMM	pn counts	T_{exp} s	RA(J2000) deg	DEC(J2000) deg
158755	0302570101	J175528.8-290002	945	22101	268.870267	-29.0006910
158765	0302570101	J175533.4-290148	818	23524	268.889748	-29.0301473
158770	0302570101	J175534.1-291136	820	12482	268.892750	-29.1935731
158784	0302570101	J175539.0-285637	830	18406	268.912842	-28.9439729
158786	0302570101	J175540.7-290641	385	18625	268.920074	-29.1116151
158847	0302570101	J175607.6-290752	582	12393	269.032228	-29.1312861
158874	0302570101	J175624.0-290924	529	7527	269.100312	-29.1567159
158926	0099760201	J175656.5-214833	191	16751	269.235557	-21.8092493
158936	0099760201	J175659.8-214350	1083	23978	269.249456	-21.7306871
158945	0099760201	J175701.8-213336	503	19949	269.257872	-21.5601146
159002	0099760201	J175722.3-213729	549	29775	269.343328	-21.6249229
159099	0099760201	J175741.1-214309	729	25967	269.421421	-21.7191735
159225	0099760201	J175800.6-213856	831	18030	269.502797	-21.6491029
160502	0135742801	J180154.4-224647	300	3989	270.476754	-22.7798893
162701	0024940201	J180706.8-192559	457	7791	271.778454	-19.4331379
162842	0024940201	J180736.4-192658	504	13526	271.901787	-19.4494564
162991	0024940201	J180802.0-191505	530	12375	272.008692	-19.2515124
163107	0024940201	J180822.4-191813	385	13564	272.093537	-19.3038061
163285	0152832901	J180859.3-200504	250	3025	272.246936	-20.0845222
163722	0152835701	J181024.8-183712	352	4864	272.603540	-18.6202497
165111	0152834901	J181848.0-152753	456	4343	274.700226	-15.4648934
165128	0152834501	J181851.2-155920	405	3474	274.713590	-15.9890124
165294	0152834501	J181913.4-160118	365	3351	274.806080	-16.0219059
165845	0040140201	J182258.0-135322	401	4558	275.741926	-13.8895434

Table 5.1: The *XMM-Newton* source sample (contd.).

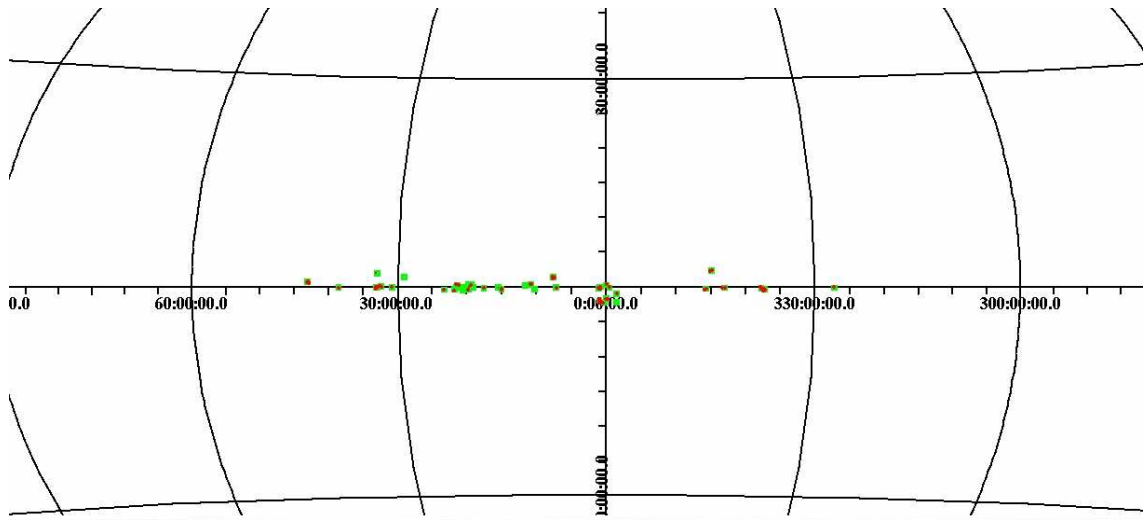
Source	ObsID	IAU name 2XMM	pn counts	T_{exp} s	RA(J2000) deg	DEC(J2000) deg
165849	0040140201	J182304.3-135036	414	6194	275.768137	-13.8434457
165864	0040140201	J182319.7-134009	525	10105	275.832197	-13.6692289
165865	0040140201	J182321.2-134643	555	9288	275.838532	-13.7788005
165873	0040140201	J182342.7-134947	703	6307	275.928304	-13.8299195
165933	0051940101	J182524.5-114525	325	3071	276.352429	-11.7569984
165958	0104460701	J182533.6-121452	241	3956	276.390195	-12.2478079
166079	0051940301	J182626.7-112854	303	3729	276.611412	-11.4817562
166111	0135745401	J182639.6-114216	313	5397	276.665378	-11.7044734
166331	0104460401	J182756.7-110448	236	3855	276.986660	-11.0800277
166437	0051940401	J182830.8-114514	316	4478	277.128638	-11.7540997
166459	0104460401	J182845.5-111710	613	1962	277.190100	-11.2859481
166461	0135745701	J182847.6-101337	592	2974	277.198352	-10.226928
166477	0135745701	J182855.9-095414	368	2307	277.232783	-9.90395787
166494	0104460901	J182905.6-104635	305	9972	277.273721	-10.7764318
166583	0135745801	J182948.6-110604	331	9721	277.452519	-11.1012463
166713	0135746301	J183038.2-100246	252	3515	277.659340	-10.0462562
166900	0135741601	J183251.4-100106	175	2183	278.214516	-10.0183448
167248	0302560301	J183514.6-083740	283	5812	278.811114	-8.62802097
167514	0301880901	J183939.8-024935	341	6450	279.915880	-2.8264969
167528	0301880901	J183947.4-024504	331	5979	279.947866	-2.75130141
168039	0017740601	J184447.7+011131	409	4946	281.198764	1.19210825
168124	0203850101	J184720.6-015248	353	14234	281.835951	-1.88007375
168249	0136030101	J184953.6-003007	489	13078	282.473627	-0.502027855
168254	0136030101	J184958.7-002018	303	11945	282.494768	-0.338458017

Table 5.1: The *XMM-Newton* source sample (contd.).

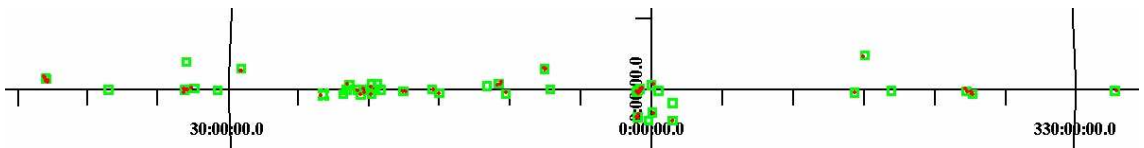
Source	ObsID	IAU name 2XMM	pn counts	T_{exp} s	RA(J2000) deg	DEC(J2000) deg
168272	0136030101	J185020.0-001313	616	5849	282.583392	-0.220432317
168300	0017740401	J185114.3-000004	331	11180	282.810021	-1.405767523E-03
168311	0017740401	J185125.1+000742	446	19833	282.854495	0.128359508
168323	0017740401	J185139.1+001635	547	13984	282.912794	0.276320641
168324	0017740401	J185139.9+001308	390	18751	282.916253	0.218768541
168428	0017740401	J185233.2+000638	418	9004	283.138536	0.110526059
169142	0136030201	J190109.0+045751	427	7805	285.287529	4.96427966
169247	0136030201	J190144.5+045915	419	11696	285.435614	4.98753562
169433	0305580101	J190653.7+092051	482	15538	286.724208	9.34727636
169434	0305580101	J190655.9+093240	282	7114	286.733306	9.54491116
169450	0305580201	J190704.0+092532	282	11833	286.766625	9.42565572
169470	0305580101	J190712.7+091109	454	13122	286.803325	9.18589301
169482	0305580101	J190717.7+092421	445	15480	286.824453	9.40605826
169532	0305580101	J190742.0+090713	421	7211	286.925895	9.12062364
169538	0410580101	J190746.3+092420	285	8156	286.942694	9.40573028
169547	0410580101	J190756.0+091736	322	7403	286.983657	9.29345445

5.3 Data reduction

After the sample selection, I carried out data reduction using the *XMM-Newton* Science Analysis System (SAS) v.8.0.0. Before extracting any data products, the data were reprocessed in a similar manner as described in Chapter 2 data reduction section. After the reprocessing, the observations were screened for high background flares by applying a cut in the 10–12 keV band above a full field count rate of 0.4 ct s^{-1} , which is the normal recommendation for pn



(a) A view of the source sample along the Galactic Plane.



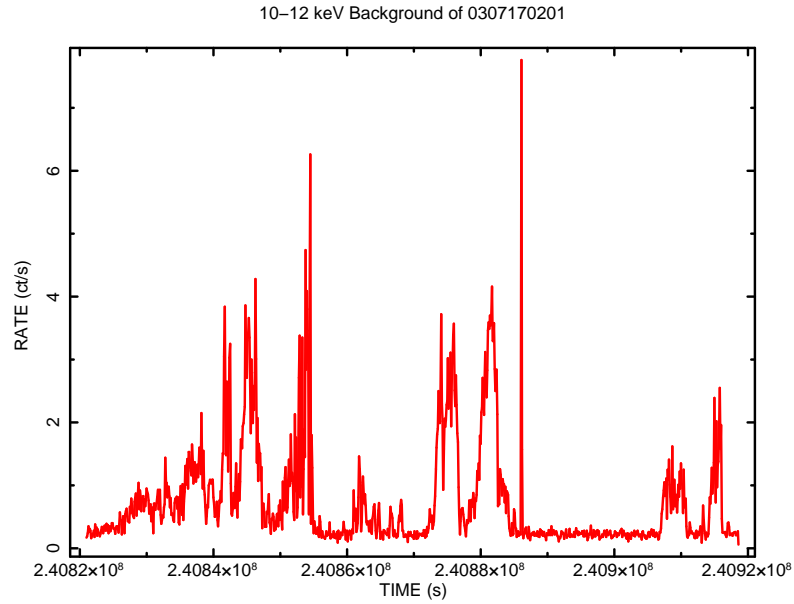
(b) A close-up of the observations.

Figure 5.2: (a) The final *XMM* source sample consisting of 110 sources (red points) and the corresponding observations (0.5×0.5 deg green boxes) along the Galactic Plane. The x-axis corresponds to the Galactic longitude l and the y-axis to the Galactic latitude b . (b) A close-up of the observations and the sources within them (note that due to the small sizes of the source points some of the boxes appear empty as they contain only 1–2 sources which would only be visible if these boxes were zoomed in).

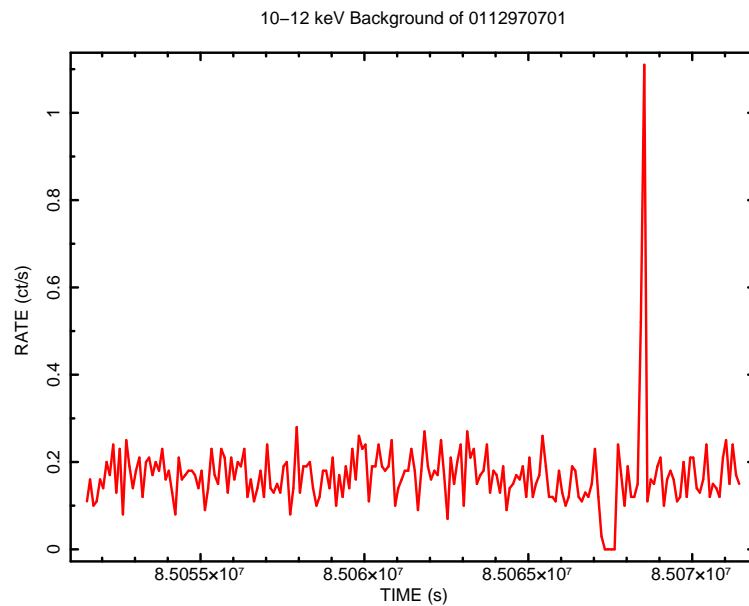
data given in the SAS manual⁴. Single and double X-ray events were chosen (`PATTERN = 0–4`) with `FLAG = 0` for the pn. In Fig. 5.3, panels (a) and (b) illustrate typical backgrounds in the 10–12 keV band ranging from an observation badly affected by flaring to one in which the background is relatively quiescent.

For most of the sources, a fixed source extraction region was used with a radius of $35''$ (= 700 pixels) which includes ~ 85 – 90 per cent of the point spread function (PSF). However,

⁴http://xmm.esac.esa.int/external/xmm_user_support/documentation/sas_usg/USG/



(a) 0307170201



(b) 0112970701

Figure 5.3: The EPIC pn backgrounds in 10–12 keV of observations (a) 0307170201 and (b) 0112970701. The flaring intervals were cut above 0.4 ct s^{-1} . The figures illustrate the wide range in amplitude of the background flaring.

for 13 individual sources there was a contaminating source close to the studied source, and thus the radius of the source extraction region was calculated by the SAS task REGION. It calculates the radius of a source extraction region according to the desired percentage of the PSF, and can shrink (a user-dependent option) the extraction radius if there are any nearby sources which might cause confusion. Sources, which are located on the edge of the field of view suffer from *vignetting*, i.e. a decline in the effective area of the mirrors with increasing off-axis angle. Source count rates quoted in the 2XMM catalogue have been corrected for this effect (whereas in spectral analysis the ancillary response file (ARF) provides the necessary calibration).

A background region with a circular extraction radius of 120'' (= 2600 pixels), was chosen from the same chip of the CCD as the source, or in the case of very crowded fields, from an adjacent chip. Finally, the redistribution matrix files (RMFs) and the ancillary response files (ARFs) were created within RMFGEN and ARFGEN for each individual source spectrum.

5.4 Preparing the spectra for spectral analysis

After obtaining the final source list and carrying out the data reduction, the hardness ratios of the sources were inspected more carefully, with the aim of dividing the sources into groups. The reason for doing this was that, individually, the source spectra did not provide enough counts to distinguish any detailed features in their spectra. Thus, the sources were divided into 6 groups based on their spectral hardness (Fig. 5.4) with the aim of creating a "stacked" spectrum for each group. The broad band hardness ratio for each source was calculated using the spectral channel information in the extracted spectral files according to

$$HR = \frac{H - S}{H + S}, \quad (5.1)$$

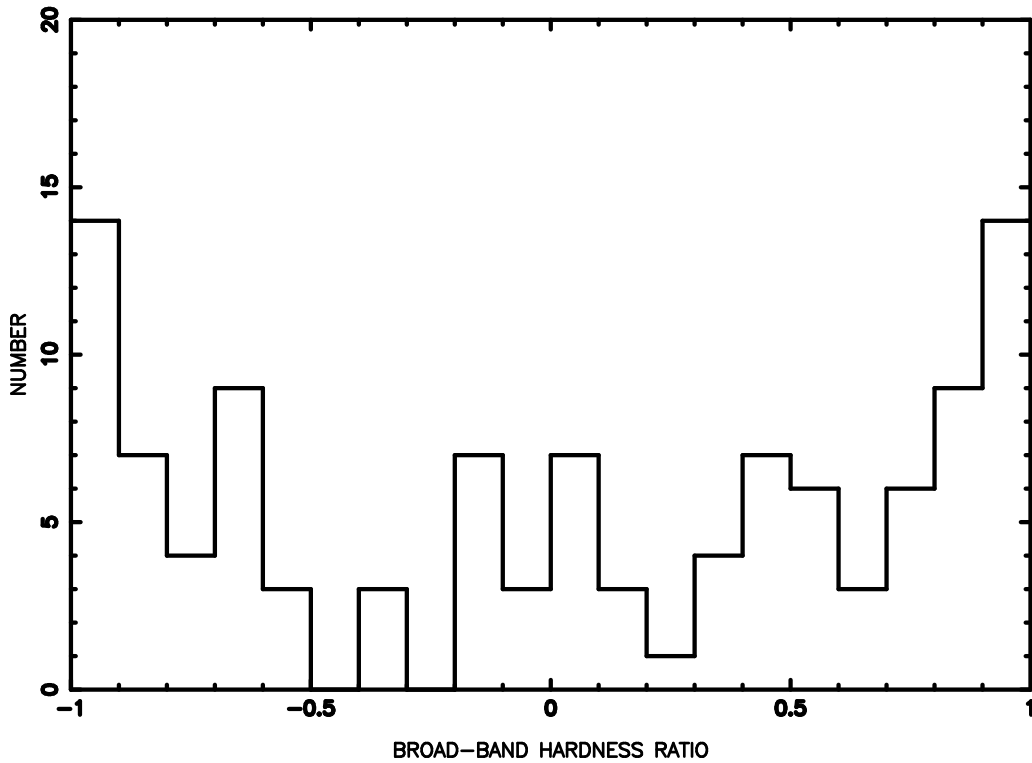


Figure 5.4: The broad band (0.5–12 keV) hardness ratio of the 110 sources.

where H contains the spectral channel information between the 2–12 keV and S between the 0.5–2 keV energy ranges. The division into 6 groups was done so that each group contained approximately a similar number of sources. The group names with their 0.5–12 keV hardness ratio limits and number of sources per group are given in Table 5.2. Note, that a similar procedure was used by Sugizaki et al. (2001) to classify their *ASCA* sources.

To create the "stacked" spectra for all the 6 groups, the individual source spectra within each group were summed, and correspondingly, the background spectrum for each group was created by summing the appropriate background spectra. Since the areas of the background and source extraction regions were not equal, the individual background spectra had to be scaled to match the source extraction regions before background subtraction.

The background-subtracted source spectra for the six groups are illustrated in Fig. 5.5. The spectra show the trend from the harder groups H1–H3 in panel (a) to softer groups S1–S3 in panel (b). This trend is expected on the basis of the hardness ratio selection. Evidence

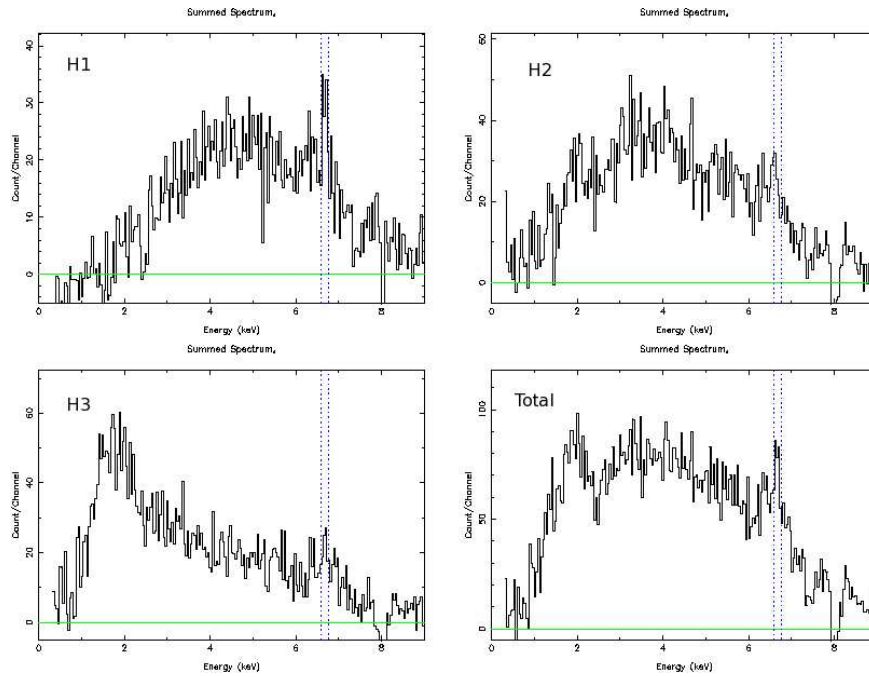
Table 5.2: The source groups with their broad band hardness ratios and number of sources in each group. The groups have been listed according to the spectral hardness: from the hardest (H1) to the softest one (S3).

Group	Hardness ratio	No. of sources
H1	0.9–1.0	14
H2	0.63–0.9	18
H3	0.30–0.63	17
S1	-0.2–0.3	21
S2	-0.8–(-0.2)	19
S3	-1.0–(-0.8)	21

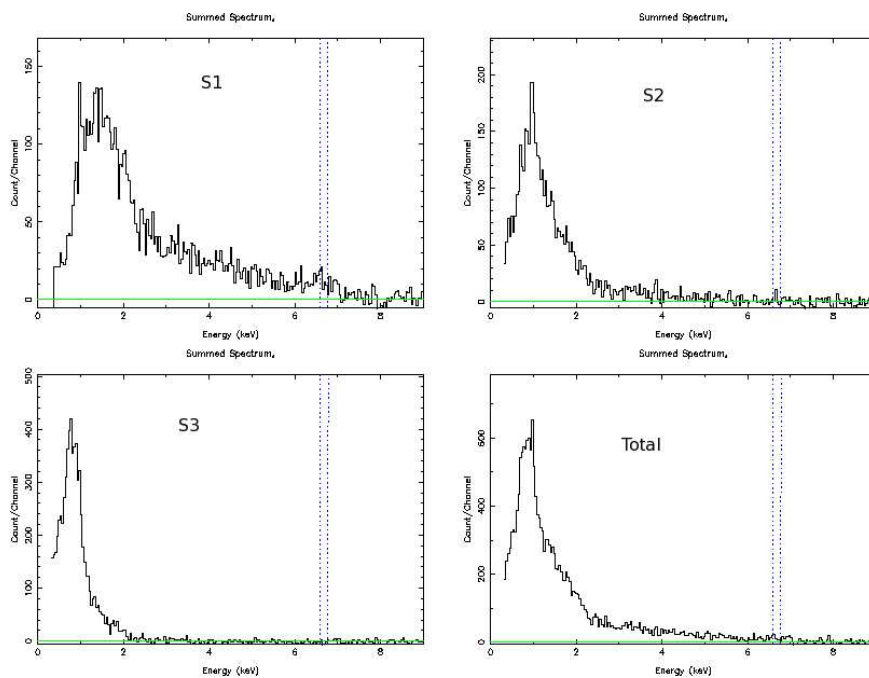
for strong absorption with an evident iron line complex between 6–7 keV is seen in groups H1–H3 (panel (a)), whereas the spectra in panel (b) have clearly become softer and are also affected by absorption. The iron line complex between 6–7 keV is just visible in group S1, but not in S2 and S3.

5.4.1 Spectral fitting

The last two steps before spectral analysis was to create "combined" response files (.rsp) for the summed spectra and to bin the spectra. Thus, the RMFs and ARFs of each individual source spectrum were combined by using the FTOOL MARFRMF v.2.2.0 to create a .rsp file for each source. After this, the individual source response files were combined in ADDRMF v.1.21 in order to create a total summed response file for each source group. MARFRMF is used for multiplying or dividing RMF files by ARF datasets or by a scalar, whereas ADDRMF adds together RMF (or combined RMF+ARF files) by using a weighting factor. In this case, the weighting factor for each source was the net source counts divided by the sum of the net



(a) H1 (top left), H2, H3 and total (lower right corner)



(b) S1 (top left), S2, S3 and total (lower right corner)

Figure 5.5: The background-subtracted spectra for source groups (a) H1, H2, H3, and (b) S1, S2 and S3. The y-axis shows Counts/Channel and the x-axis the energy in keV. The vertical dashed lines identify the region of the spectra around 6.7 keV. The green line on the bottom corresponds to zero counts per channel.

source counts of the group. For the binning of the spectra, the following methods were used: for the harder spectra, i.e. groups H1-H3, PHA channels between 0 and 4095 were grouped in the FTOOL GRPPHA by 8 bins, whereas for the softer spectra (S1, S2, and S3), the PHA channels 0–511 were binned up by 4 and channels 512–4095 by 8 bins.

The spectral analysis of the total, summed source spectra of the 6 groups was carried out in XSPEC11. When looking more closely at the X-ray spectra, it was found that all the X-ray spectra had residual nickel (Ni) $K\alpha$, copper (Cu) $K\alpha$, and zinc (Zn) $K\alpha$ fluorescence lines between ~ 7.2 –9 keV. These lines are present in the detector background as a result of fluorescence in the detector itself and the structure surrounding it. Also, the data were noisy above 9 keV, and thus all the data above 7.2 keV were excluded. In the low energy end, noisy data below 1.0 keV were excluded for H1-S1, and below 0.5 keV for the S2 and S3.

Astronomical objects, such as cataclysmic variables (CVs), are known to show iron lines between 6–7 keV (see e.g. Mukai & Shiokawa, 1993), and spectrally CVs are relatively hard with a typical plasma temperature of ~ 5 –10 keV (e.g. Mukai & Shiokawa, 1993). Thus, the finding of the iron lines at these energies in the harder groups (H1, H2, H3 and S1) together with a hard continuum would imply that at least a subset of the objects studied could possibly be CVs. The softer sources in groups S2 and S3 do not share these characteristics. The X-ray spectra of CVs have traditionally been modelled using thermal plasma models, as the processes producing X-ray emission in these systems are thought to be thermal. As was discussed in Chapter 4, single temperature models can be unphysical since, according to accretion theory, the gas settling onto the white dwarf surface is cooling. Thus, the gas is not expected to be at one temperature, but consists of a range of temperatures varying from the hot shock temperature to the cooler post-shock gas reaching down to the white dwarf surface. But, since the objects in the *XMM-Newton* source sample are not a homogeneous set, I chose to use the simplest possible models to investigate the underlying source spectra. These models are discussed below.

The X-ray spectra of different source groups were investigated by using thermal and non-thermal spectral models. A thermal spectrum, whose shape depends only on the temperature of the emitting material, is produced in collisionally ionised plasmas, whereas a non-thermal spectrum is produced when electrons are accelerated by some other mechanisms than collisions between the particles. The emitted non-thermal spectrum can typically be approximated such that the spectral energy distribution follows powerlaw form with energy. These emission mechanisms were discussed in Chapter 1.

The effect of fitting both types of models were investigated for all source groups. These models were 1) a powerlaw model with photoelectric absorption (`wabs`) and a Gaussian line at 6.7 keV (the intrinsic width of this line was fixed at $\sigma = 10$ eV), and 2) an optically thin thermal plasma model (`mekal`) with photoelectric absorption. I measured the spectral fit parameters and also the EW of the 6.7 keV Gaussian line in the power law fit. The EW in units of eV can be calculated as

$$EW = \frac{\text{Gaussian line normalisation}}{A(E)}, \quad (5.2)$$

where $A(E)$ is the level of the underlying continuum at the line energy E for a simple photon powerlaw

$$A(E) = K \times \left(\frac{E}{1\text{keV}} \right)^{-\Gamma}, \quad (5.3)$$

where K is the normalisation of the continuum in units of photons $\text{keV}^{-1} \text{cm}^{-2} \text{s}^{-1}$ at 1 keV, and Γ the photon index. In addition to the 6.7 keV line, I also measured the EW of the 6.4 keV iron line (also with the intrinsic line width set at 10 eV) by adding an additional Gaussian line as a separate component to the best-fit absorbed powerlaw model, at 6.4 keV.

The results of the spectral fits are given in Tables 5.3, 5.4 and 5.5. When fitting the spectra,

Table 5.3: The results of the X-ray spectral fitting when using the absorbed powerlaw model with an added Gaussian line at 6.7 keV for groups H1–S1. The table also reports the EWs for the 6.4 keV line for the H1–S1 spectra when it was added to the powerlaw model.

Group	n_H $\times 10^{22} \text{ cm}^{-2}$	Γ	EW(6.7 keV) eV	EW(6.4 keV) eV	χ^2_ν/ν	P_0
H1	$7.29^{+2.45}_{-1.17}$	$0.65^{+0.28}_{-0.19}$	173^{+73}_{-64}	59^{+41}_{-47}	1.00/150	0.493
H2	$3.26^{+0.56}_{-0.50}$	$0.99^{+0.09}_{-0.13}$	93^{+54}_{-54}	< 92	1.16/150	0.084
H3	$1.09^{+0.17}_{-0.20}$	$1.12^{+0.09}_{-0.10}$	249^{+83}_{-82}	69^{+53}_{-50}	0.92/150	0.743
S1	$0.53^{+0.05}_{-0.05}$	$1.60^{+0.08}_{-0.08}$	152^{+78}_{-115}	< 109	1.17/215	0.041
S2	$0.34^{+0.03}_{-0.03}$	$2.87^{+0.15}_{-0.13}$	–	–	1.40/215	8.58×10^{-5}
S3	$0.71^{+0.07}_{-0.06}$	$6.85^{+0.48}_{-0.41}$	–	–	1.94/214	5.73×10^{-15}

Table 5.4: The results of the X-ray spectral fitting when using an absorbed optically thin thermal plasma model. The abundance given is the overall abundance relative to the Sun.

Group	n_H $\times 10^{22} \text{ cm}^{-2}$	kT keV	abundance	χ^2_ν/ν	P_0
H1	$13.14^{+1.52}_{-1.30}$	$7.91^{+2.05}_{-1.56}$	$0.35^{+0.14}_{-0.11}$	1.17/150	0.072
H2	$4.87^{+0.40}_{-0.29}$	$11.94^{+0.06}_{-2.71}$	$0.35^{+0.15}_{-0.14}$	1.41/150	7.25×10^{-4}
H3	$1.56^{+0.13}_{-0.11}$	> 10.58	$1.29^{+0.33}_{-0.32}$	1.06/150	0.303
S1	$0.47^{+0.04}_{-0.03}$	$10.35^{+2.31}_{-1.69}$	$0.51^{+0.23}_{-0.20}$	1.14/215	0.085
S2	$0.21^{+0.02}_{-0.02}$	$1.32^{+0.08}_{-0.08}$	$0.05^{+0.02}_{-0.02}$	1.49/215	4.53×10^{-6}
S3	$0.09^{+0.02}_{-0.02}$	$0.66^{+0.02}_{-0.03}$	$0.06^{+0.01}_{-0.01}$	1.26/214	6.26×10^{-3}

Table 5.5: The results of the X-ray spectral fitting for the softer source groups S1, S2 and S3 when using photoelectric absorption with two optically thin thermal plasma models. The abundance given is the overall abundance relative to the Sun.

Group	n_H $\times 10^{22} \text{ cm}^{-2}$	kT_1 keV	kT_2 keV	abundance	χ^2_ν	P_0
S1	$0.52^{+0.07}_{-0.05}$	$1.15^{+0.28}_{-0.24}$	$11.50^{+3.51}_{-2.20}$	$0.54^{+0.24}_{-0.21}$	1.10/213	0.149
S2	$0.21^{+0.03}_{-0.03}$	> 6.70	$1.00^{+0.09}_{-0.12}$	$0.06^{+0.03}_{-0.02}$	1.15/213	0.061
S3	$0.07^{+0.04}_{-0.04}$	$0.90^{+0.25}_{-0.14}$	$0.53^{+0.10}_{-0.14}$	$0.09^{+0.04}_{-0.02}$	1.21/212	0.018

all parameters were allowed to vary free except the line energies and intrinsic widths of the 6.4 and 6.7 keV lines, and the switch, the redshift and the hydrogen density parameters of the optically thin thermal plasma model. The abundances given in Tables 5.4 and 5.5 are the overall abundances relative to the Sun. In addition, the plasma temperature kT was not well-constrained for H2 and H3, thus I chose an upper limit of 12 keV for kT for these spectra, and pegged the temperature at 12 keV in XSPEC. In Table 5.3, I have given the best-fit results when using an absorbed powerlaw with an added Gaussian line at 6.7 keV only (i.e. without the 6.4 keV Gaussian line). According to the χ^2_ν values, the fits are acceptable for groups H1–S1, unlike for groups S2 and S3. A common feature for groups H1–H3 is the strong measured EW of the 6.7 keV iron line. This fact is also supported by Fig. 5.5(a). The line is still detectable in S1. The differences between the values of the equivalent widths of the 6.7 keV line in groups H1–S1 is probably explained by the limited sampling (i.e. we are dealing with samples of between 10–20 sources per group, not all of which may be 6.7 keV emitters). Unlike the 6.7 keV line, the 6.4 keV iron line is not detectable in these data.

The results of fitting the second model, i.e. an absorbed optically thin thermal plasma model, are detailed in Table 5.4. Compared to the results in Table 5.3, the χ^2_ν values are worse for groups H1–H3 and S2, but significantly better for S3. The χ^2_ν value of S1 improved only slightly when using the optically thin thermal plasma model. Since the χ^2_ν values for

S2 and S3 were not satisfactory, I added a second optically thin thermal plasma component to the fits. This resulted as a significant improvement for group S2 (see Table 5.5) and a modest improvement for S3. Although the single temperature model was acceptable for S1, I also tested how the fit would improve with a second thermal plasma model. Again, a slight improvement occurred. Based on the comparison between the results in Tables 5.3 and 5.4, we can not strongly distinguish between the two models within the harder groups (H1-H3), but for the softest groups (S1-S3), single or double optically thin thermal plasma model is clearly better than the power law model. Fig. 5.6 shows the *XMM-Newton* source spectra with residuals of the four hardest groups, H1, H2, H3, and S1 (panels (a)–(d)) when fitted with the absorbed power law and an added 6.7 keV Gaussian line, whereas panels (e) and (f) illustrate the two softest (S2 and S3) source spectra fitted with photoelectric absorption and two optically thin thermal plasma models.

As was shown by Table 5.3, there is a clear trend of decreasing absorption and a steepening power law slope as one moves from the hardest to the softest source groups. This is further illustrated by the contour plots in Fig. 5.7 which shows the relation between the power law slope Γ versus absorption column n_H for groups H1-S1 in panel (a). Similarly, the plasma temperature kT versus n_H relation is plotted for the three softest groups (S1, S2 and S3) in panel (b). According to these plots, groups H1–H3 seem to be containing similar hard source types. S1 deviates from these groups with a higher Γ and a lower n_H , whereas in panel (b) it is clear that S2 and S3 are much softer than S1. Based on this analysis, it could be that the spectrum S1 includes both soft and hard source types, with a few of the harder sources showing 6.7 keV iron line emission.

The plasma temperatures kT obtained with the optically thin thermal plasma model for the harder groups (H1–S1) are consistent with those measured in magnetic CVs (Ezuka & Ishida, 1999) and also with those of non-magnetic CVs (Mukai & Shiokawa, 1993). The soft spectral shapes and thus low measured absorption columns of the source groups S2 and S3 indicate that these groups mainly consist of nearby stars. In fact, the spectral shapes of these groups

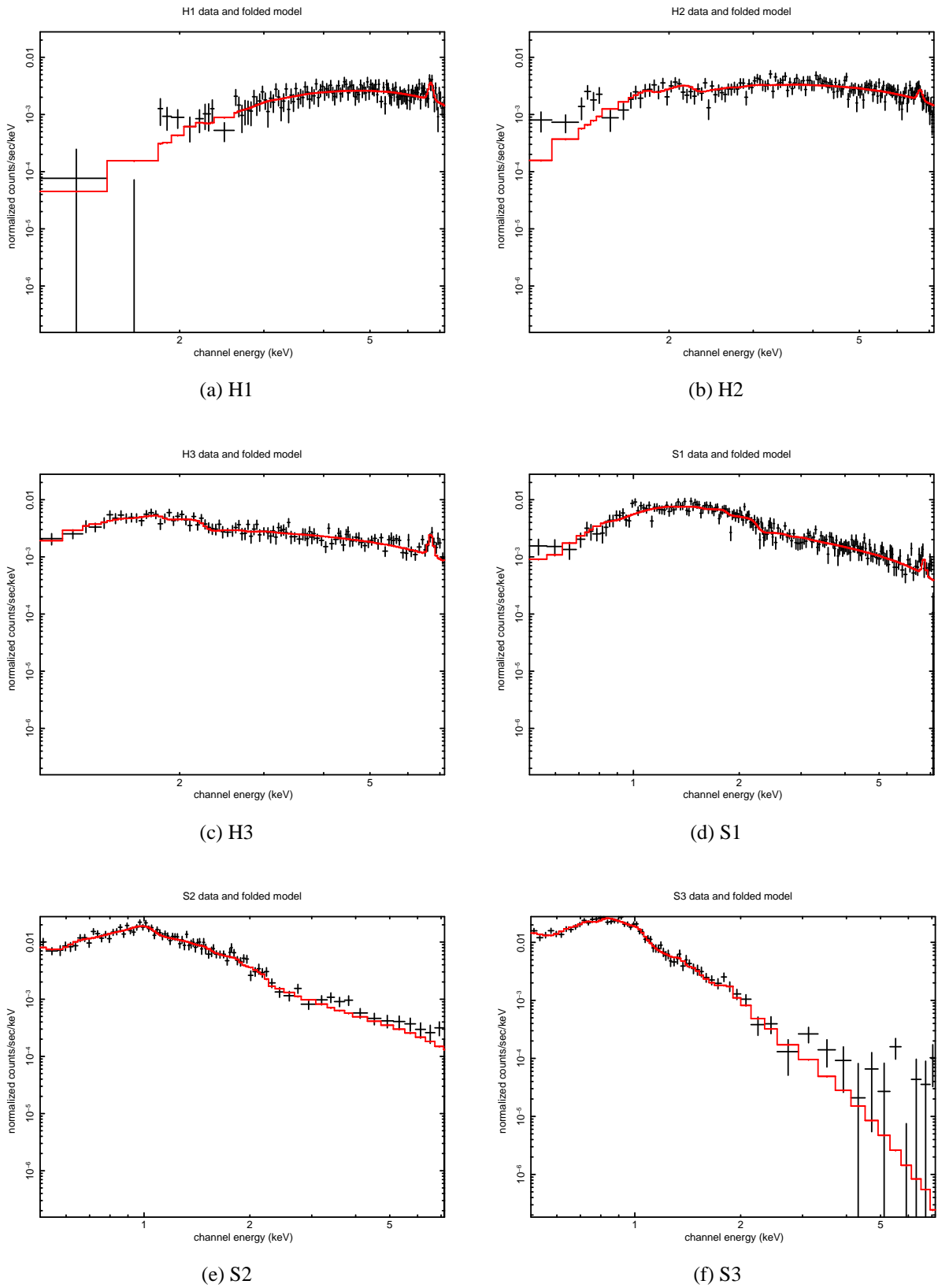
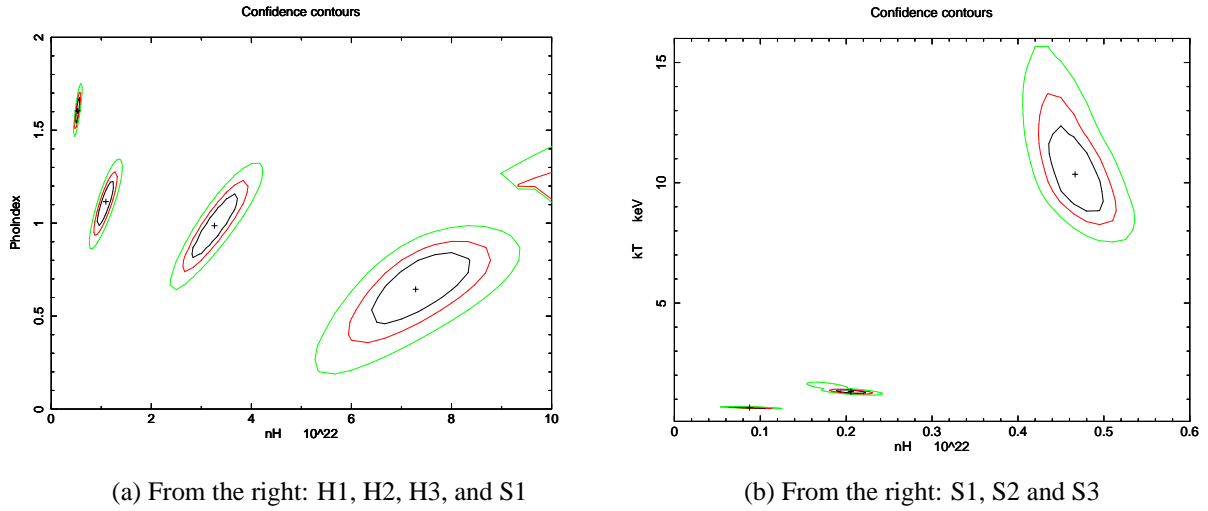


Figure 5.6: The *XMM-Newton* X-ray spectra of the source groups H1–H3 (panels (a)–(c)), and source groups S1–S3 (panels (d)–(f)). Groups H1–S1 have been fitted with an absorbed powerlaw with an added Gaussian line at 6.7 keV, and groups S2 and S3 with photoelectric absorption and two optically thin thermal plasma models.



(a) From the right: H1, H2, H3, and S1

(b) From the right: S1, S2 and S3

Figure 5.7: The contour plots of (a) the four hardest groups H1, H2, H3, and S1 (from H1 on the right) fitted with an absorbed power law and a Gaussian line at 6.7 keV, and (b) the three softest groups S1, S2 and S3 (from S1 on the right) fitted with an absorbed optically thin thermal plasma model.

are similar to the *ASCA* X-ray spectra of the late-type stars Speedy Mic and Gliese 890 (Singh et al., 1999). In addition, the measured plasma temperatures and abundances of groups S2 and S3 obtained with the optically thin thermal plasma model are similar to those measured for Gliese 890 and Speedy Mic by Singh et al. (e.g. with a 1-temperature model $kT \sim 0.80$ keV and the corresponding abundance is $\sim 0.07 Z_{\odot}$ for Gliese 890).

5.4.2 Near-infrared counterparts of the source sample

In order to better understand their nature, I also investigated how many of the X-ray sources in the sample have near-infrared (NIR) counterparts. This was done by looking at the cross-matched 2XMM and the *Two Micron All Sky Survey* (2MASS) catalogues. 2MASS⁵ is a project which has provided all-sky maps in near-infrared (NIR) bands (*J*, *H*, and *K*). It contains accurate positions and fluxes for ~ 300 million stars and for some unresolved objects. One of the scientific benefits of the 2MASS is that the effect of interstellar absorption is much reduced compared to optical wavebands.

In Table 5.6, I have listed all the NIR counterparts which were found as a result of cross-matching the 2XMM and 2MASS catalogues: out of 110 sources, 37 have NIR counterparts. This includes all those sources for which the probability of identification (Rutledge et al., 2000) was > 90 per cent.

Most of the sources, for which counterparts were found, belong to the softest groups S1, S2 and S3. Only three sources in the hardest groups (H1 and H2) have potential NIR counterparts. This result is due to the fact that the softest sources, which are not strongly absorbed in X-rays, are probably nearby stars as was already discussed in Section 5.4.1. Conversely, the strong absorption seen in the hardest X-ray spectra and their lack of optical counterparts suggest these represent a more distant population of objects subject to significant interstellar absorption. What about the soft sources for which no counterparts were found in 2MASS, in particular in S2 and S3? From a sample of faint *Chandra* X-ray sources in the Galactic Plane, Ebisawa et al. (2005) found that for those soft sources with no NIR counterparts, the average X-ray energy flux was ~ 40 per cent smaller than for the soft sources with NIR counterparts. They suggested that the soft X-ray sources without NIR counterparts are farther away and/or intrinsically fainter than the soft sources with counterparts. This could be the case also in my sample, although this work has not involved measuring the average X-ray flux, which will be

⁵<http://www.ipac.caltech.edu/2mass/>

the subject of future work.

The last three columns in Table 5.6 give the J (1.24 μm), H (1.66 μm) and K (2.16 μm) NIR magnitudes, where the numbers in brackets are the central wavelengths in each band. Some magnitudes do not have errors which means that the given magnitude is the 95 per cent confidence upper limit. Using these magnitudes, I created a $J - H$ versus $H - K$ colour-colour diagram (Fig. 5.8) for the identified sources. In Fig. 5.8, the softest sources belonging to groups S1-S3 are plotted in black, and the hardest sources belonging to groups H1 and H2 in red. For comparison, a plot of the $J - H$ versus $H - K$ colour-colour diagram of the Galactic Plane using the 2MASS Point Source Catalogue (PSC)⁶ is shown in Fig. 5.9. The colour bar on the right represents source densities from the highest (red) to the lowest (blue) density. The black solid and dashed curves describe the expected evolutionary tracks for dwarf and giant stars (Koornneef, 1983; Bessell & Brett, 1988), respectively. As described by Bessell & Brett, these curves correspond to dwarfs and giants of spectral classes between G5 and M6. Metal poor M-dwarfs would lie below the solid dwarf line according to Bessell & Brett. The softest sources in Fig. 5.8 seem to be following the shape of the dwarf and giant tracks shown in Fig. 5.9.

The reddening effect is seen in both figures: the source groups extend from the lower left towards the upper right corner (towards the direction of the arrow shown in Fig. 5.8) in the infrared two colour space, i.e. towards higher $J - H$ and $H - K$ values where sources are more reddened. Reddening is caused by *extinction* of interstellar dust, and by the fact that interstellar extinction A_V is a function of wavelength: extinction increases proportional to $1/\lambda$ when moving from longer wavelengths (infrared) to shorter wavelengths (ultraviolet). Thus, the light seen from distant stars is redder (and dimmer) than what it would be if the extinction was zero. The extinction originates from absorption and scattering of photons by interstellar dust. The photons absorbed by dust are thermalised and emitted at infrared wavelengths corresponding to the temperature of the dust, whereas in scattering, photons are scattered out

⁶<http://www.ipac.caltech.edu/2mass/releases/allsky/doc/explsup.html>

Table 5.6: The 2MASS NIR counterparts for which the probability of identification is > 90 per cent. The last three columns give the 2MASS J (1.24 μm), H (1.66 μm) and K (2.16 μm) magnitudes with errors (the numbers in brackets are the central wavelengths in each band). The Group column gives the group ID where the source belongs to.

Source	Group	ObsID	IAU name 2XMM	2MASS	J mag	H mag	K mag
142052	S1	0402910101	J154951.7-541630	15495168-5416297	14.953 \pm 0.054	14.289 \pm 0.113	13.348
142126	S1	0203910101	J155037.5-540722	15503759-5407217	11.019 \pm 0.026	10.132 \pm 0.047	9.824 \pm 0.060
142126	S1	0402910101	J155037.5-540722	15503759-5407217	11.019 \pm 0.026	10.132 \pm 0.047	9.824 \pm 0.060
142126	S1	0410581901	J155037.5-540722	15503759-5407217	11.019 \pm 0.026	10.132 \pm 0.047	9.824 \pm 0.060
148350	S3	0307170201	J163737.0-472951	16373693-4729515	10.391 \pm 0.024	10.018 \pm 0.026	9.935 \pm 0.026
148388	S3	0307170201	J163756.4-471949	16375648-4719500	12.231 \pm 0.036	11.763 \pm 0.044	11.647 \pm 0.039
148509	S2	0307170201	J163840.9-471952	16384096-4719527	14.036 \pm 0.059	13.446 \pm 0.068	13.339 \pm 0.044
148620	S2	0303100101	J163914.5-470020	16391447-4700210	12.624 \pm 0.024	12.018 \pm 0.022	11.903 \pm 0.027
148624	S3	0307170201	J163915.1-472310	16391515-4723101	11.300 \pm 0.022	10.803 \pm 0.021	10.753 \pm 0.019
148790	S3	0303100101	J164004.1-470419	16400422-4704189	11.678 \pm 0.023	11.054 \pm 0.021	10.896 \pm 0.019
155792	S2	0112971201	J174351.2-284638	17435129-2846380	8.535 \pm 0.024	7.858 \pm 0.055	7.681 \pm 0.027
155792	S2	0112971901	J174351.2-284638	17435129-2846380	8.535 \pm 0.024	7.858 \pm 0.055	7.681 \pm 0.027
155792	S2	0302882801	J174351.2-284638	17435129-2846380	8.535 \pm 0.024	7.858 \pm 0.055	7.681 \pm 0.027

Table 5.6: The 2MASS NIR counterparts (contd.).

Source	Group	ObsID	IAU name 2XMM	2MASS	J mag	H mag	K mag
155792	S2	0302884301	J174351.2-284638	17435129-2846380	8.535 ± 0.024	7.858 ± 0.055	7.681 ± 0.027
157004	H1	0112970201	J174645.2-281547	17464524-2815476	15.390	9.960 ± 0.025	7.184
157004	H1	0112971501	J174645.2-281547	17464524-2815476	15.390	9.960 ± 0.025	7.184
157004	H1	0144220101	J174645.2-281547	17464524-2815476	15.390	9.960 ± 0.025	7.184
157045	S2	0112970201	J174654.6-281658	17465462-2816580	11.936 ± 0.024	11.315 ± 0.048	11.081 ± 0.040
157045	S2	0112971501	J174654.6-281658	17465462-2816580	11.936 ± 0.024	11.315 ± 0.048	11.081 ± 0.040
157045	S2	0144220101	J174654.6-281658	17465462-2816580	11.936 ± 0.024	11.315 ± 0.048	11.081 ± 0.040
157045	S2	0203930101	J174654.6-281658	17465462-2816580	11.936 ± 0.024	11.315 ± 0.048	11.081 ± 0.040
157247	S2	0144220101	J174730.8-281347	17473085-2813473	13.350 ± 0.027	12.410 ± 0.040	11.362
157532	H2	0205240101	J174841.1-280136	17484101-2801349	13.772 ± 0.032	11.469 ± 0.041	10.195 ± 0.04
157544	S1	0112970101	J174848.0-281240	17484803-2812400	12.942	11.315	11.287 ± 0.092
157544	S1	0205240101	J174848.0-281240	17484803-2812400	12.942	11.315	11.287 ± 0.092
158008	S2	0206990101	J175035.2-311825	17503526-3118256	12.415 ± 0.032	11.721 ± 0.035	11.488 ± 0.032
158373	S2	0307110101	J175155.9-295113	17515599-2951142	9.616 ± 0.024	8.911 ± 0.028	8.661 ± 0.025
159099	S3	0099760201	J175741.1-214309	17574096-2143106	7.434 ± 0.023	6.867 ± 0.042	6.685 ± 0.021
160502	S3	0135742801	J180154.4-224647	18015438-2246490	5.754 ± 0.019	5.754 ± 0.038	5.756 ± 0.034

Table 5.6: The 2MASS NIR counterparts (contd.).

Source	Group	ObsID	IAU name 2XMM	2MASS	J mag	H mag	K mag
162701	S3	0024940201	J180706.8-192559	18070680-1926006	11.091 ± 0.023	10.402 ± 0.022	10.200 ± 0.019
162701	S3	0212080501	J180706.8-192559	18070680-1926006	11.091 ± 0.023	10.402 ± 0.022	10.200 ± 0.019
162842	S1	0024940201	J180736.4-192658	18073644-1926581	11.408 ± 0.024	10.463 ± 0.024	10.071 ± 0.023
162991	S2	0024940201	J180802.0-191505	18080208-1915048	11.006 ± 0.027	10.322 ± 0.044	9.784 ± 0.032
162991	S2	0152833401	J180802.0-191505	18080208-1915048	11.006 ± 0.027	10.322 ± 0.044	9.784 ± 0.032
163107	S2	0024940201	J180822.4-191813	18082246-1918128	12.138 ± 0.024	11.430 ± 0.029	11.236 ± 0.026
163107	S2	0152833401	J180822.4-191813	18082246-1918128	12.138 ± 0.024	11.430 ± 0.029	11.236 ± 0.026
165111	S3	0152834901	J181848.0-152753	18184806-1527541	9.551 ± 0.026	9.179 ± 0.022	9.073 ± 0.021
165873	S2	0040140201	J182342.7-134947	18234289-1349469	10.803 ± 0.029	10.099 ± 0.047	9.613 ± 0.034
165958	S3	0104460701	J182533.6-121452	18253369-1214505	11.266 ± 0.023	10.762 ± 0.023	10.591 ± 0.023
166459	S3	0051940601	J182845.5-111710	18284546-1117112	9.797 ± 0.022	9.138 ± 0.022	8.957 ± 0.019
166459	S3	0135747001	J182845.5-111710	18284546-1117112	9.797 ± 0.022	9.138 ± 0.022	8.957 ± 0.019
166461	S3	0135741201	J182847.6-101337	18284771-1013354	7.483 ± 0.023	7.219 ± 0.047	7.127 ± 0.026
166461	S3	0135745701	J182847.6-101337	18284771-1013354	7.483 ± 0.023	7.219 ± 0.047	7.127 ± 0.026
167248	S1	0302560301	J183514.6-083740	18351465-0837405	14.713 ± 0.040	11.763 ± 0.026	10.424 ± 0.027
167528	S3	0301880901	J183947.4-024504	18394750-0245056	11.580 ± 0.027	11.079 ± 0.033	10.904 ± 0.034

Table 5.6: The 2MASS NIR counterparts (contd.).

Source	Group	ObsID	IAU name 2XMM	2MASS	J mag	H mag	K mag
168039	S3	0017740201	J184447.7+0111131	18444773+0111320	11.080 ± 0.026	10.658 ± 0.044	10.491 ± 0.034
168039	S3	0017740601	J184447.7+0111131	18444773+0111320	11.080 ± 0.026	10.658 ± 0.044	10.491 ± 0.034
168039	S3	0017740701	J184447.7+0111131	18444773+0111320	11.080 ± 0.026	10.658 ± 0.044	10.491 ± 0.034
168249	S2	0136030101	J184953.6-003007	18495357-0030075	11.521	10.836 ± 0.060	10.586 ± 0.065
168272	S3	0136030101	J185020.0-001313	18502003-0013142	10.584 ± 0.026	10.045 ± 0.023	9.868 ± 0.019
168311	S3	0017740501	J185125.1+000742	18512525+0007422	9.988	9.180 ± 0.047	8.735 ± 0.031
168323	S1	0017740501	J185139.1+001635	18513925+0016350	9.784 ± 0.025	8.757 ± 0.028	8.370 ± 0.028
168324	S3	0017740401	J185139.9+001308	18514005+0013084	9.546	9.272 ± 0.029	9.224 ± 0.037
168324	S3	0017740501	J185139.9+001308	18514005+0013084	9.546	9.272 ± 0.029	9.224 ± 0.037
169247	H2	0136030201	J190144.5+045915	19014457+0459147	11.148 ± 0.022	9.763 ± 0.021	8.841 ± 0.021
169470	S2	0305580201	J190712.7+091109	19071266+0911091	12.849 ± 0.029	12.279 ± 0.033	12.099 ± 0.030
169470	S2	0410580101	J190712.7+091109	19071266+0911091	12.849 ± 0.029	12.279 ± 0.033	12.099 ± 0.030

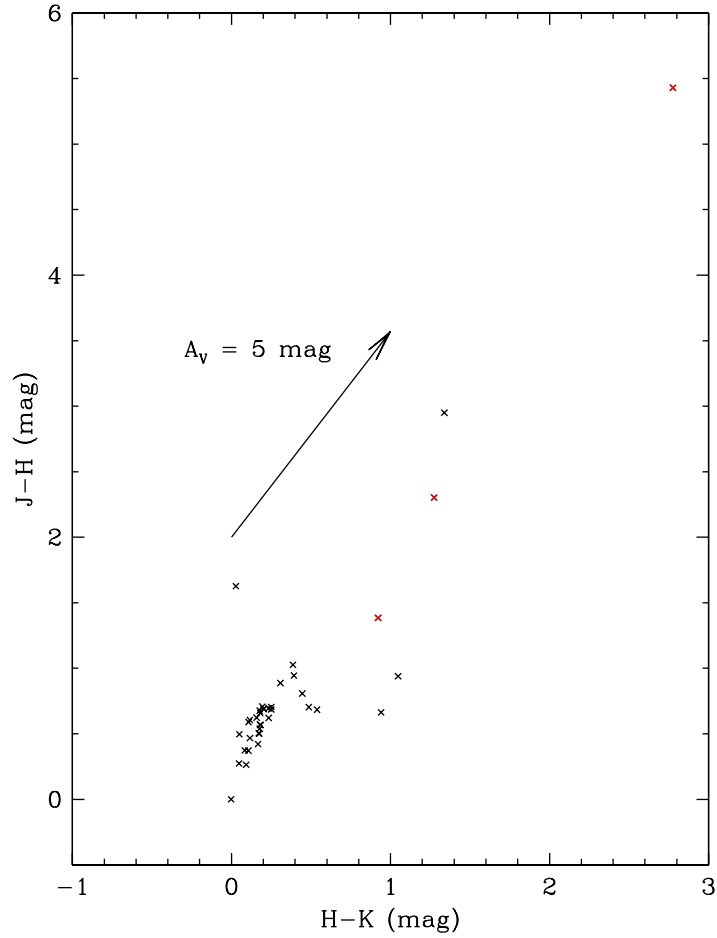


Figure 5.8: The $J - H$ versus $H - K$ colour-colour diagram of this work where the black dots represent the softest sources (groups S1-S3) and the red dots the hardest groups (H1-H2). The arrow with a slope of 1.57 indicates the direction of interstellar reddening and the value of extinction (5 mag) in the V band.

of the line of sight to the object. In both cases, the intensity of light observed from distant sources is reduced. The extinction cross-section C_{ext} of a dust particle is different from the geometric cross-section, πr^2 , where r is the radius of the dust particle. Thus, the extinction cross-section can be calculated from

$$C_{ext} = Q_{ext}\pi r^2, \quad (5.4)$$

where Q_{ext} is extinction efficiency factor.

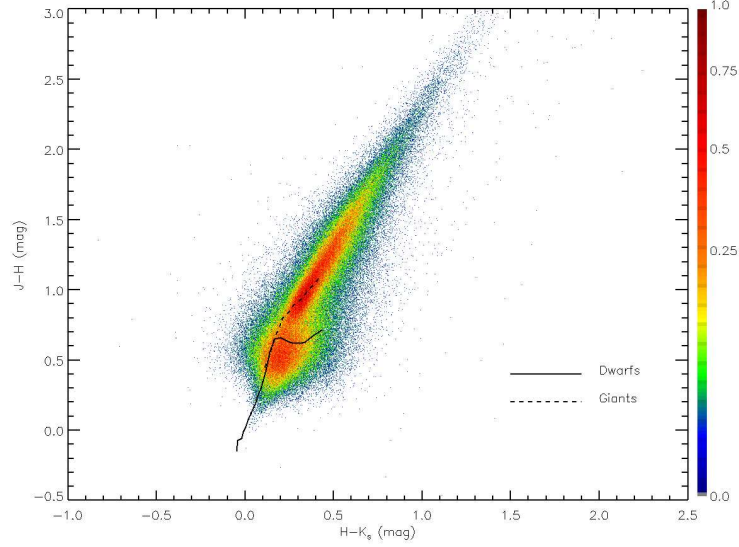


Figure 5.9: The $J - H$ versus $H - K$ colour-colour diagram of the 2MASS Point Source Catalogue (PSC) from the Galactic Plane. The solid and dashed lines describe the expected evolutionary tracks for dwarfs and giants as given by Koornneef (1983) and Bessell & Brett (1988). The colours indicate the highest source density (red) and the lowest source density (blue).

To calculate the slope of the arrow indicating the direction of interstellar reddening in Fig. 5.8, a value of $A_V = 5$ mag was used for the Galactic interstellar extinction in the V band. This value can be used to give the corresponding NIR extinction via the following equations (Chen, Yang, & Zhang, 2007)

$$A_J = 0.272A_V, \quad A_H = 0.173A_V, \quad A_K = 0.110A_V, \quad (5.5)$$

where A_J , A_H and A_K are the Galactic interstellar extinction coefficients in the J , H , and K bands. The observed magnitude m_V of a star at a distance d in units of parsecs in the V band can be calculated from (e.g. Hilditch, 2001)

$$m_V = M_V + 5 \log_{10}\left(\frac{d}{10pc}\right) + A_V, \quad (5.6)$$

where M_V is the absolute magnitude (i.e. the apparent magnitude of a star at a distance of 10

pc from the source) and A_V interstellar extinction in the V band. In a similar manner, this equation can be applied to give the observed magnitude in a different band, e.g., for J band we obtain:

$$m_J = M_J + 5 \log_{10}\left(\frac{d}{10pc}\right) + A_J \quad (5.7)$$

and similarly to H and K bands. Thus, when subtracting m_H from m_J , we obtain

$$m_J - m_H = M_J - M_H + A_J - A_H. \quad (5.8)$$

When re-arranging this by moving $(M_J - M_H)$ to the left side of the equation, we obtain the colour excess

$$E(J - H) = (m_J - m_H) - (M_J - M_H) = A_J - A_H, \quad (5.9)$$

where $(m_J - m_H) = (J - H)$ is the observed colour and $(M_J - M_H) = (J - H)_0$ the intrinsic colour of a source. Similarly, colour excess $E(H - K)$ can be calculated for H and K bands. Finally, the slope of the arrow is given as the ratio of

$$\frac{E(J - H)}{E(H - K)} = \frac{A_J - A_H}{A_H - A_K} = \frac{0.495}{0.315} = 1.57. \quad (5.10)$$

5.5 Discussion

The spectral characteristics of the source groups H1–S1 have provided strong evidence that these source groups contain CVs. As was shown by the measured EWs, the He-like 6.7 keV

iron line, which is produced in a collisionally excited plasma between 5–10 keV, is evident in the hardest source groups H1–S1. This line is known to be characteristic for CV spectra, such as for dwarf novae (e.g. Mukai & Shiokawa, 1993). Thus, the presence of the 6.7 keV line with significant EWs in these four source groups indicates that a significant fraction of the studied sources may well be CVs. Some fraction of the sources probably are background AGNs, however, the non-detection of the 6.4 keV line suggests that background contamination from AGNs is not strong. The 6.4 keV line is known to be seen in AGN X-ray spectra arising from reflection of cold material which is illuminated by an X-ray source, with an EW up to ~ 150 eV (see George & Fabian (1991) and references therein, and Chapter 4, Spectral analysis).

The measured EWs of the 6.7 keV iron lines are consistent with those measured from dwarf novae by Mukai & Shiokawa (1993) and from magnetic CVs (mCVs) by Hellier, Mukai & Osborne (1998). The upper panel in Fig. 5.10 illustrates the measured 6.7 keV line EWs of groups H1–S1 (Table 5.3) from this work with error bars, the middle panel the measured 6.7 keV line EWs of 14 mCVs from the sample of Hellier, Mukai & Osborne (1998), and the bottom panel the EW measurements from the Galactic Ridge regions of R2–R8 by Yamauchi et al. (2009). The obtained mean EW of the 6.7 keV lines of the H1–S1 groups from this work is 167 ± 28 eV, and is shown as a long-dashed line in the upper and bottom panels in Fig. 5.10 (the weighted mean is 150 ± 35 eV, short-dashed line in the upper panel). The typical upper limit of the 6.4 keV line EW in groups H1–S1 is 105 eV. Thus, the lower limit for the EW line ratio (6.7 keV/6.4 keV) is > 1.6 (with the weighted mean > 1.4).

For comparison, the average EW of the 6.7 keV lines in the Hellier et al. sample of mCVs is 178 ± 28 eV (the middle and bottom panels in Fig. 5.10). This was measured from 14 sources out of 15 since one source had a non-detection for the 6.7 keV line. The average 6.4 keV line EW of the mCV sample, measured from 12 sources (excluding 3 non-detections), is ~ 95 eV. Thus, using these values, the 6.7 keV/6.4 keV ratio of the Hellier et al. sample is ~ 1.9 . The lower limit of the line ratio measured in groups H1–S1 (1.6) is close to this

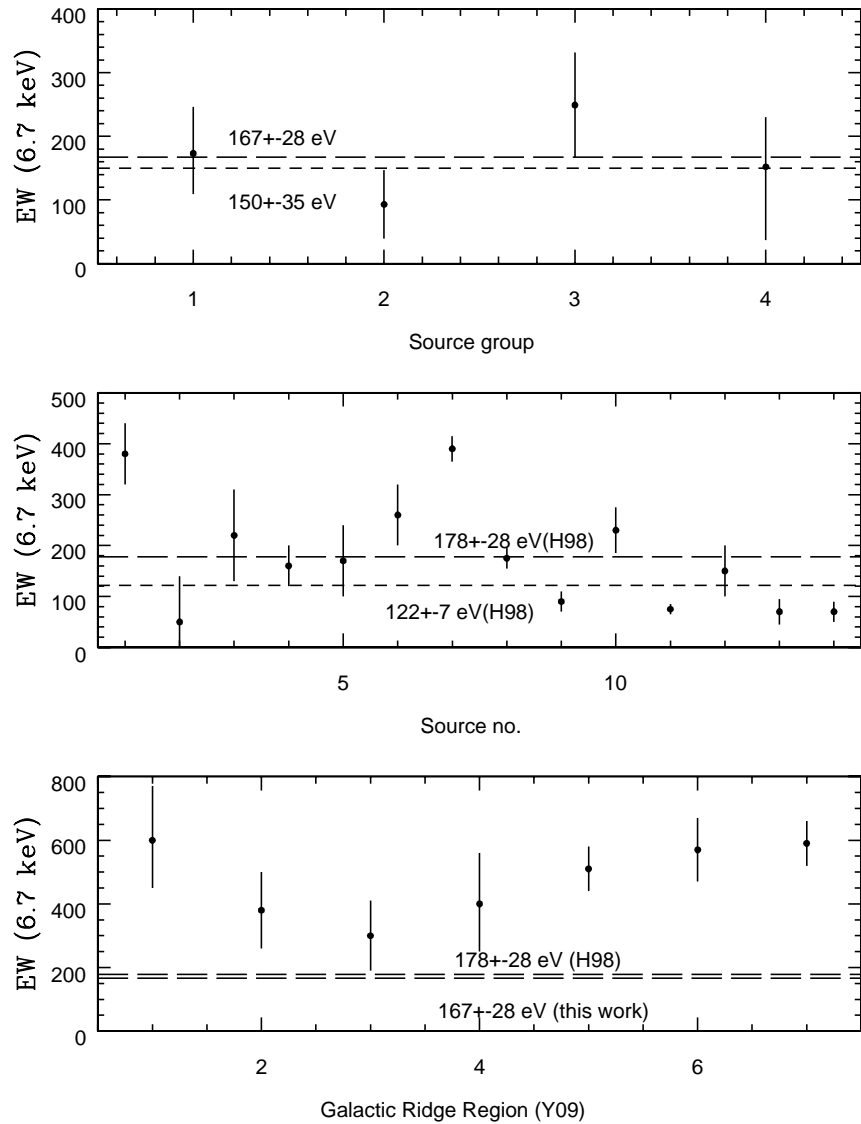


Figure 5.10: Upper panel: the EWs of the 6.7 keV lines with error bars from this work. Middle panel: the EWs of the 6.7 keV lines with error bars of 14 magnetic CVs (H98, Hel-lier, Mukai & Osborne, 1998). The long-dashed lines indicate the straight averages, and the shorter dashed lines the weighted averages of the 6.7 keV line EWs. For the source groups H1–S1, these values are 167 ± 28 eV (average) and 150 ± 35 eV (weighted), and for the H98 sample, 178 ± 28 eV (average) and 122 ± 7 eV (weighted). In the upper panel, the x-axis indicates the source group numbering corresponding to: 1 = H1, 2 = H2, 3 = H3, and 4 = S1, and in the middle panel, the number of the 14 individual magnetic CVs. The bottom panel shows the 6.7 keV line EW measurements (~ 300 – 600 eV) from the Galactic Ridge regions between R2 (corresponds to $x=1$ in the figure) and R8 (corresponds to $x=7$), obtained by Yamauchi et al. (2009) (Y09), compared with the average 6.7 keV line EWs of the H1–S1 groups and the H98 sample.

value, and thus supports the view that the source groups H1–S1 contain 6.7 keV line emitting CVs. Also, the ratio of the average 6.7 keV line EWs of the two samples (167 eV/178 eV) implies that 94_{-23}^{+6} per cent of the sources in groups H1–S1 could be associated with CVs. In the future, deep follow-up near-infrared and optical observations could solve the nature of the harder sources.

If the GRXE mostly has a point source origin, a faint CV-like source population, with prominent 6.7 keV line emission, must contribute a significant flux (i.e. the number of contributing sources must increase towards fainter fluxes below $< 10^{-14}$ erg cm $^{-2}$ s $^{-1}$). This view is supported by previous studies, such as Ebisawa et al. (2001), who found that the number of sources above the flux level of 3×10^{-15} erg cm $^{-2}$ s $^{-1}$ (equivalent to $\sim 2.3 \times 10^{31}$ erg s $^{-1}$ at the distance of 8 kpc from the Galactic Centre, see Chapter 4) is not sufficient to be a major contributor to the GRXE. See also Revnivtsev et al. (2006) and references therein, who noted that sources in the flux range of $\sim 10^{-13}$ – $10^{-10.5}$ erg cm $^{-2}$ s $^{-1}$ do not contribute more than < 10 per cent to the GRXE. However, as is shown by the bottom panel in Fig. 5.10, the 6.7 keV line EW measurements from the Galactic Ridge by Yamauchi et al. (~ 300 – 600 eV), are a factor of 2–4 times higher than what has been measured for intermediate flux CVs and for the source groups H1–S1 in this work. Therefore, in order to produce a 6.7 keV iron line EW consistent with the values measured from the Galactic Ridge, the faint CV-like source population mostly contributing to the GRXE must have a factor of 2–4 higher EW than the values measured from CVs in general. A possible explanation could be higher metallicity due to close proximity to the central regions of the Galaxy. The EW measurements of the 6.4 keV lines obtained by Yamauchi et al. were ~ 90 – 190 eV between the R2 and R8 regions, and thus are not inconsistent with the upper limit measurement of the 6.4 keV line in this work, or with the average 6.4 keV line EW in the sample of Hellier et al.

In order to investigate the effect of abundance (in this case, the abundance is the total abundance of all elements) on the 6.7 keV line EW, I have illustrated a situation in Fig. 5.11, in which the 6.7 keV line EWs have been measured from an optically thin thermal plasma

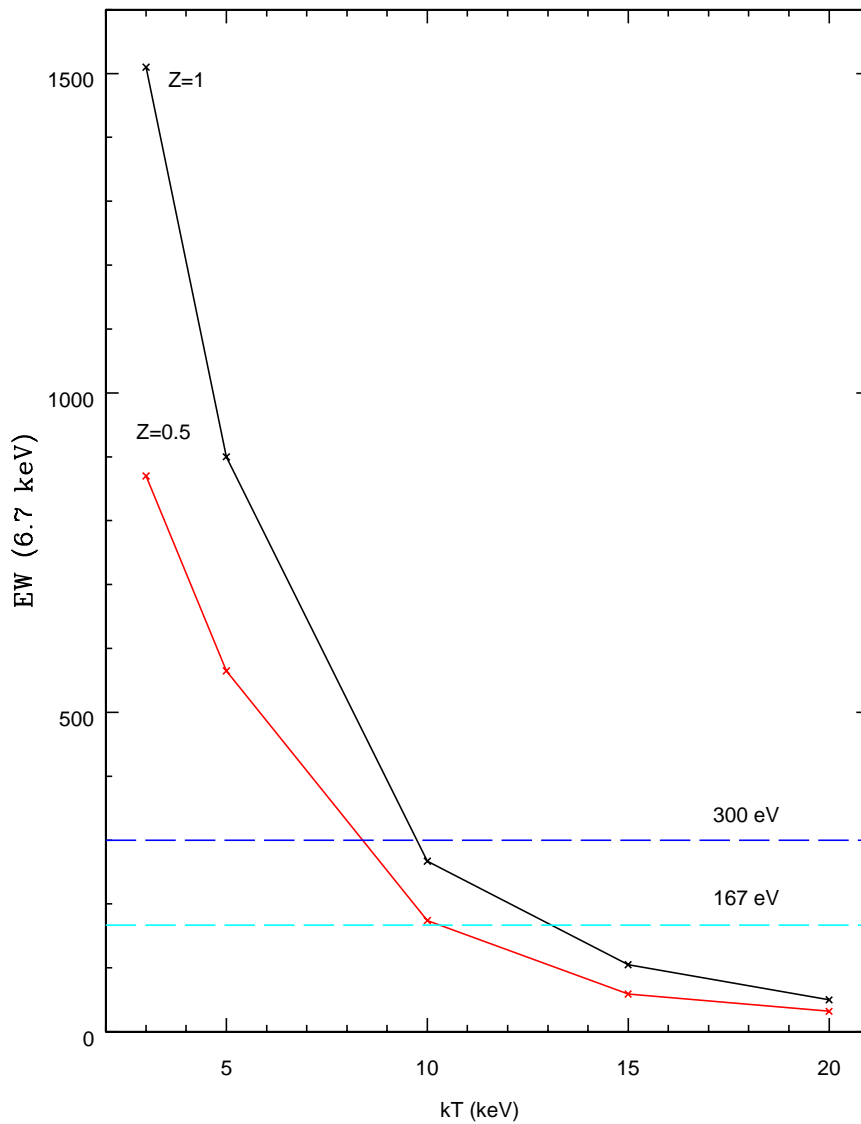


Figure 5.11: The 6.7 keV iron line EW measurements as a function of plasma temperature kT assuming an optically thin thermal plasma spectrum as the underlying spectrum. The black curve illustrates EW measurements for a solar abundance spectrum, and the red curve for a spectrum with $Z = 0.5 Z_0$. The blue and cyan dashed lines indicate the lowest Galactic Ridge EW measurement (300 eV) by Yamauchi et al. (2009), and the average EW measurement (167 eV) of groups H1–S1 for the 6.7 keV iron line, respectively.

spectrum (simulated in XSPEC) at plasma temperatures kT between 3–20 keV and for two different abundances: the red curve in Fig. 5.11 represents EW measurements for spectra with an abundance of $Z = 0.5 Z_0$ which is a typical value measured from CVs (see e.g. Chapter 4 or Ezuka & Ishida, 1999), whereas the black curve represents EW measurements for solar abundance spectra. It is clear from Fig. 5.11 that for sources with plasma temperatures of ~ 10 keV (the temperatures measured for the H1–S1 groups, and also for CVs), higher EW values can be achieved by raising the abundance, i.e. in this case from $Z = 0.5 Z_0$ to solar value in order to reach the EW of 300 eV. Another interpretation of Fig. 5.11 is that, without raising the abundance, a factor of 2 higher EW values for the 6.7 keV line could be obtained with sources which have lower continuum temperatures (in this example, EW = 300 eV could be reached with the lower abundance of $0.5 Z_\odot$ at the temperature of ~ 8.5 keV).

5.6 Conclusions

In this chapter, I have presented a study of serendipitous X-ray point sources which were observed by *XMM-Newton* along the Galactic Plane ($|l| < 45$ degrees, $|b| < 2.5$ degrees). The main emphasis in this chapter has been analysing X-ray spectral characteristics of the source sample. By studying the X-ray spectra, the goal has been to gain some insight into the nature of the underlying source populations.

In a summary, the essential results and conclusions are:

1. The X-ray spectra in groups H1–S1 have strongly absorbed hard continua with an evident He-like iron line at 6.7 keV indicating that a significant fraction (~ 90 per cent) of the sources in these groups may be CVs. The lack of 6.4 keV line emission suggests that contamination by background AGN emission is not strong.
2. The average EW of the 6.7 keV line of the source groups H1–S1 is 167 ± 28 eV, and

the typical upper limit for the 6.4 keV line is 105 eV. The lower limit of the EW line ratio ($6.7 \text{ keV}/6.4 \text{ keV} > 1.6$) is close to the line ratio measured in magnetic CVs (1.9), thus supporting CV origin for these emission lines.

3. Assuming a point source origin, the source population mostly contributing to the GRXE must consist of faint, CV-like sources below the flux limit of $< 10^{-15} - 10^{-14} \text{ erg cm}^{-2} \text{ s}^{-1}$. In order to account for the measured EWs in the Galactic Ridge ($\sim 300 - 600 \text{ eV}$), this faint source population must have 6.7 keV line EWs a factor of 2–4 times higher than measured in intermediate flux CVs in general. Higher EW could be explained by a source population having higher metallicities due to close proximity to the central regions of the Galaxy. Alternatively, a source population with lower continuum temperatures, but with typical CV abundances, could produce equal EWs to the values measured from the Galactic Ridge.
4. Softer sources in groups S2 and S3 are very likely nearby main sequence stars based on the detection of optical counterparts, the derived $J - H$ versus $H - K$ colour-colour diagram and the soft spectral shape similar to late-type stars with a small absorption column.

Chapter 6

Summary and future work

The focus of this thesis has been multiwavelength studies of cataclysmic variables (CVs), with the aim of enhancing the understanding of accretion disc physics in CVs, and the X-ray emission mechanisms in accreting binaries in general. Studying CVs is important for the following reasons:

- CVs are laboratories for studying accretion disc physics and luminous phenomena, i.e. outbursts and eruptions. Understanding the accretion disc physics in CVs helps to understand disc physics in other accreting objects, such as X-ray binaries and Active Galactic Nuclei.
- CVs are strong candidates for progenitors of Type Ia SNe which are used as cosmological distance estimators.
- Direct measurements of the system parameters, such as the binary component masses, the radii and the orbital period of a system, are possible. Also, luminosities can be measured when the distance to the object and the flux of the object are known, in which case it is possible to derive luminosity functions for further studies in order to understand Galactic source populations. In addition, CVs could be responsible for a

large fraction of the Galactic Ridge X-ray Emission (GRXE), and in this view, it is important to understand their properties.

In the following, I will summarise the main results and conclusions of this thesis, and briefly discuss possible future work in these areas.

6.1 The XMM-Newton observations of the polar candidate 2XMM J131223.4+173659

In Chapter 2, I studied the serendipitously discovered polar candidate 2XMM J131223.4 + 173659 (J1312) by carrying out X-ray timing and spectral analysis using *XMM* X-ray data, and derived the system parameters.

Folding the X-ray light curves over the orbital period (~ 92 min, determined from these data) revealed that J1312 is an eclipsing polar. The light curves showed two excursions to zero intensity: 1) a longer one thought to be due to the white dwarf self-occultation and 2) a short and deep eclipse due to the secondary star passing in front of the primary and thus covering the emission region on the primary surface. In addition, the X-ray light curve is characterised by dips, in particular the soft X-ray light curve, suggesting the presence of an accretion stream crossing the line of sight absorbing softer X-rays. Similar characteristics have been seen in the X-ray light curves of other, known eclipsing polars, such as HU Aqr (Schwope et al., 2001) and UZ For (Osborne et al., 1988).

One of the main results of this study is that the X-ray spectra do not show a soft X-ray component, which has previously been considered to be a typical characteristic of polars. According to the accretion theory of polars, the soft X-ray component arises from the surface of the white dwarf which is irradiated by the hard X-rays from the post-shock column: some fraction of the hard X-rays are absorbed and re-emitted as black body emission, which is seen

in the soft X-ray and EUV bands. However, J1312 is not the only polar without a soft X-ray component since e.g. Ramsay & Cropper (2007) and Ramsay et al. (2009) showed that in fact, several polars without the soft component exist. The absence of a soft X-ray component has been explained by too low a temperature of the soft component to be seen in X-rays, but would be seen at lower temperatures in the EUV. One explanation for a low temperature is that the fractional area over which the accretion occurs over the white dwarf surface is large which leads to a lower temperature accretion region on the white dwarf surface. This is due to the inverse proportionality between the effective temperature T_{eff} and the fractional area f : $T_{eff} \propto (\dot{M}/f)^{1/4}$.

The derived system parameters showed that J1312 is a high-inclination system with an inclination of $i > 72^\circ$. The lowest limit to the white dwarf mass fulfilling the stable mass accretion criterion ($q < 5/6$) is $M_1 > 0.14 M_\odot$. Finally, the co-latitude δ of the emission region, corresponding to $i > 72^\circ$, is $\delta < 42^\circ$.

A clear goal of future work would be to confirm the polar-like nature of J1312. Since polars are known to emit strongly polarised optical and infrared light, the polar-like nature could be revealed categorically via ground-based optical and infrared polarimetric observations. A suitable observatory for this kind of observation could be, e.g., the Nordic Optical Telescope (NOT) on La Palma.

6.2 **Swift observations of GW Lib: a unique insight into a rare outburst**

In Chapter 3, I presented multiwavelength light curves (X-ray, UV and optical) of the 2007 outburst of GW Lib which is a WZ Sge-type dwarf nova (DN). In addition, I carried out spectral analysis of the outburst X-ray data. Following the 2007 outburst, two *Swift* follow-

up observations of GW Lib were obtained in 2008 and 2009 in order to compare the X-ray luminosity and spectral parameters post-outburst with those obtained in the outburst state. This is the first multiwavelength study of GW Lib in outburst, and thus provides a unique opportunity of obtaining an insight into the accretion disc physics of a WZ Sge-type DN. In general, the recurrence times of WZ Sge stars are decades, and thus the opportunities to study these outbursts are scarce. The reasons for the long recurrence times are not well-understood, although various theoretical models have been put forward.

The *Swift* X-ray light curve of GW Lib showed that the hard X-rays (0.3–10 keV) are not suppressed during the outburst. This is also seen in U Gem, although U Gem is not a WZ Sge type star. By contrast, in many other DNe, such as in YZ Cnc and WZ Sge, the suppression of X-rays during an outburst has been observed. Thus, GW Lib and U Gem are the only two DNe known where hard X-rays are seen during an outburst. The suppression of hard X-rays during a DN outburst has been explained by the boundary layer turning from an optically thin to an optically thick state, and thus, soft X-ray and EUV emission would replace the hard X-ray emission from an optically thin boundary layer. In fact, a soft X-ray/EUV component is detected in the first outburst spectrum of GW Lib, which could arise from an optically thick boundary layer, assuming that the boundary layer switches from an optically thin to an optically thick state. This component is not seen in the later outburst spectra.

At the start of the outburst of GW Lib, the X-rays decline steeply over 10 days by a factor of 30, and it is not clear whether this kind of steep decline is typical for other systems. A decline in X-rays is also seen in WZ Sge, but only by a factor of 3 over 10 days. This is another difference, in addition to the suppressed hard X-rays, between these two systems. These differences are puzzling since WZ Sge and GW Lib belong to the same CV subclass and thus should share common features. Towards the end of the outburst X-ray light curve, GW Lib shows a bump (a rise in emission) and hardening of X-rays; these features were also seen in SS Cyg in which they were interpreted as the boundary layer changing from an optically thick state back to an optically thin state at the end of the disc outburst.

GW Lib does not stand out as a high luminosity DN during an outburst, however, it is clearly a low luminosity DN in quiescence (Hilton et al., 2007) compared to other systems. The later *Swift* observations obtained in 2008 and 2009 showed that GW Lib was still about an order of a magnitude brighter (1×10^{30} erg s⁻¹ in 0.3–10 keV) than in the quiescent observation obtained in 2005 by Hilton et al. (9×10^{28} erg s⁻¹ in 0.2–10 keV). The peak X-ray luminosity of the outburst is 2×10^{32} erg s⁻¹ in the 0.3–10 keV band, but not well-constrained in the bolometric band 0.0001–100 keV: the lower limit for the peak luminosity in this band is $\sim 2.6 \times 10^{33}$ erg s⁻¹. Since the rise in the X-rays is not seen, it is not clear whether this is the maximum luminosity of the outburst, or whether a stronger luminosity peak existed.

The accretion disc structure in WZ Sge type systems could be explained by a low viscosity or a truncated disc model which both favour extremely long recurrence times compared to other DNe. However, assuming that the outbursts of WZ Sge and GW Lib are driven by a similar mechanism, the observed differences during their outbursts are puzzling. Thus, more observations of WZ Sge type systems are needed in order to test the disc models, and thus to constrain the accretion disc physics in these systems, although, the long recurrence times of the outbursts in these systems do not provide many opportunities for regular monitoring. In particular, more observations would be needed in hard X-rays and in the EUV to properly test the traditional optically thin/optically thick boundary layer model for these objects.

6.3 Deriving an X-ray luminosity function of dwarf novae based on parallax measurements

In Chapter 4, I derived an X-ray luminosity function (XLF) in the 2–10 keV range for a set of 12 DNe in their quiescent states using pointed imaging X-ray observations obtained with *XMM-Newton*, *Suzaku*, and *ASCA*. The aim was to build up the most accurate luminosity function to date using a "fair sample" representation of DNe within 200 pc from the Sun, for

which parallax-based distance estimates exist.

The derived luminosities in the sample are lower than measured from CVs, e.g., by Baskill, Wheatley, & Osborne (2005). In my sample, the luminosities peak at $\sim 10^{30}$ erg s $^{-1}$ and range between 10^{28} – 10^{32} erg s $^{-1}$, whereas the luminosities derived by, e.g. Baskill et al. were mostly biased towards high X-ray flux CVs and concentrated between $\sim 10^{31}$ – 10^{32} erg s $^{-1}$. The shape of the derived DN XLF shows that either 1) the XLF of DNe can be described by a power law with a single slope (the obtained power law slope is $\alpha = -0.64$), but that the sample becomes incomplete below $\sim 3 \times 10^{30}$ erg s $^{-1}$, or 2) the shape of the real XLF of DNe is a broken power law with a break at $\sim 3 \times 10^{30}$ erg s $^{-1}$.

Within 200 pc, the X-ray emissivity of the DN sample is 1.81×10^{26} erg s $^{-1}$ M $_{\odot}^{-1}$ (2–10 keV) which accounts for ~ 16 per cent of the total CV X-ray emissivity as derived by Sazonov et al. (2006) and ~ 5 per cent of the Galactic Ridge X-ray emissivity as derived by Revnivtsev et al. (2006). The total integrated luminosities are 1.48×10^{32} erg s $^{-1}$ (between 1×10^{28} and the maximum luminosity of the sample, 1.50×10^{32} erg s $^{-1}$), and 1.15×10^{32} erg s $^{-1}$ (between 3×10^{30} – 1.50×10^{32} erg s $^{-1}$). These integrated luminosities have large uncertainties due to the small number of sources in the sample. Therefore, to obtain a more accurate value for the integrated luminosity, the power law slope needs to be better established by adding more DNe to the sample. Currently, the integrated luminosity is dominated by the higher luminosity DNe, based on the obtained power law slope. If this slope is not far from the true slope of DNe in the solar neighbourhood, then we need to include more brighter DNe ($\sim 10^{32}$ erg s $^{-1}$) to the sample in order to find a statistically significant constraint on these objects. In order to do this, we would need to survey within a larger volume of space $\sim 10^9$ pc 3 , corresponding to a distance of 620 pc, to find ~ 30 SS Cyg-like objects, and thus a statistically significant constraint for the higher luminosity end.

In addition to deriving the XLF, I tested possible correlations between the X-ray luminosity and the system parameters. For example, the X-ray luminosity and orbital periods are

strongly correlated. On the contrary to earlier correlation measurements of X-ray luminosities and system inclinations in CVs (e.g. van Teeseling, Beuermann, & Verbunt, 1996), these data do not show a correlation between the X-ray luminosities and the inclinations. But, evidence for a correlation between the white dwarf masses and the measured shock temperatures exists. To confirm these results and obtain better statistics, a larger DN sample is needed.

The shape of the current DN XLF below $\sim 10^{30}$ erg s $^{-1}$ needs to be derived more reliably to understand the completeness of the sample. Thus, the interest is in the less famous and fainter DNe with X-ray luminosities of $\sim 10^{29}$ – 10^{30} erg s $^{-1}$. Recent surveys, such as the SDSS survey by Gänsicke et al. (2009), have shown that more intrinsically fainter CVs are being found, and these fainter CVs could represent the true majority of the DN population in the solar neighbourhood. To improve the current XLF, observations of \sim a few dozen fainter DNe would be needed, and could be obtained, e.g., with *Swift*. These DN observations would then be added to the current sample, and this way we would obtain a more reliable picture of the faint CV population, and the shape of the DN XLF. This kind of study would also have an importance for CV population models, which have predicted that ~ 70 per cent of all Galactic CVs have reached the period minimum and thus would have very low mass accretion rates ($\dot{M} \lesssim 10^{-11} M_{\odot} \text{ yr}^{-1}$, Howell, Rappaport & Politano, 1997) and luminosities (Kolb, 1993).

6.4 Surveying the Galactic Plane with XMM-Newton

The final chapter (Chapter 5) focused on serendipitous X-ray sources in the direction of the Galactic Plane by utilising *XMM-Newton* archival observations. The aim was to derive a source sample with sufficient counts for meaningful spectral analysis, and then study their spectral characteristics in order to understand the underlying source population.

The sources were divided into six groups according to their broad band hardness ratios, and a total, summed X-ray spectrum was derived for each source group. The sources in the softest

groups (S2 and S3) are very likely nearby main sequence stars: they show a soft spectrum similar to late-type stars, have optical counterparts in the 2MASS catalogue, and mainly follow the main sequence track in the derived $J - H$ versus $H - K$ colour-colour diagram.

The hardest X-ray spectra (source groups H1–S1) show hard continua with an evident He-like iron line at 6.7 keV. The average equivalent width (EW) of the 6.7 keV iron line in these source groups is 167 ± 28 eV. A comparison of this value with the average EW value (178 eV) found for a magnetic CV (mCV) sample indicates that a significant fraction (~ 90 per cent) of the sources in groups H1–S1 could well be associated with CVs. The 6.4 keV $K\alpha$ fluorescence line is not detected with an upper limit of $EW < 105$ eV, and thus contamination from background AGNs is not strong.

The main result of this work is that the average 6.7 keV line EW values measured for the source groups H1–S1 and for the mCV sample, are a factor of 2–4 lower than the 6.7 keV line EW values measured along the Galactic Ridge (~ 300 – 600 eV) by Yamauchi et al. (2009). The number of point sources mostly contributing to the GRXE must increase towards fainter fluxes below the flux limit of 10^{-15} – 10^{-14} erg cm $^{-2}$ s $^{-1}$, since, as has been shown by previous studies (e.g. Ebisawa et al., 2001), the number of sources above this flux limit is not sufficient to be a major contributor, assuming a point source origin for the GRXE. Therefore, in order to account for the measured EWs from the Galactic Ridge, this faint source population mostly contributing to the GRXE, must have 6.7 keV line EWs a factor of 2–4 times higher than that measured for intermediate flux CVs in general. Higher EW values could be explained by a source population having higher metallicities due to their close proximity to the central regions of the Galaxy. Alternatively, a source population with typical CV abundances, but with lower continuum temperatures, could produce EWs consistent with the values measured from the Galactic Ridge.

In future, deep optical and infrared follow-up of the harder sources in groups H1–S1 could confirm their nature. If these sources, or a significant fraction of them, turned out to be CVs,

further investigation might include follow-up observations in order to identify their CV type. In addition, if these sources are mainly CVs, they would be important in log N-log S and space density studies of CVs, and thus in further GRXE studies.

BIBLIOGRAPHY

Allen D. A., Ward M. J., Wright A. E., 1981, MNRAS, 195, 155

Anders E., Grevesse N., 1989, Geochim. Cosmochim. Acta, 53, 197

Arnaud K.A., 1996, ASP Conf. Ser. Vol. 101, Astronomical Data Analysis Software and Systems V. Astron. Soc. Pac., San Francisco, p. 17

Balbus S. A., Hawley J. F., 1991, ApJ, 376, 214

Barthelmy S.D., 2004, Proc. SPIE, 5165, 175

Baskill D., Wheatley P.J., Osborne J.P. 2001, MNRAS, 328, 71

Baskill D., Wheatley P.J., Osborne J.P. 2005, MNRAS, 357, 626

Bergeron P., Fontaine G., Billères M., Boudreault S, Green E.M., 2004, ApJ, 600, 404

Bessell M. S., Brett J. M., 1988, PASP, 100, 1134

Beuermann K., Thomas H.-C., Reinsch K., Schwope A. D., Trumper J., Voges W., 1999, A&A, 347, 47

Beuermann K., Baraffe I., Kolb U., Weichhold M., 1998, A&A, 339, 518

- Beuermann K., Burwitz V., 1995, in Buckley D. A. H., Warner B., eds., ASP Conf. Ser., Vol. 85, Cape Workshop on Magnetic Cataclysmic Variables, Astron. Soc. Pac., San Francisco, p. 99
- Biermann P., Schmidt G. D., Liebert J. et al., 1985, ApJ, 293, 303
- Bleach R. D., Boldt E. A., Holt S. S., Schwartz D. A., Serlemitsos P. J., 1972, ApJ, 174, 101
- Bowyer S., Malina R. F., 1991, The *EUVE* Mission in Extreme Ultraviolet Astronomy, ed. R. F. Malina & S. Bowyer (New York: Pergamon), 391
- Bowyer S., Lieu R., Lampton M. et al., 1994, ApJS, 93, 569
- Burrows D. N., Hill J. E., Nousek J. A. et al., 2005, SSRv, 120, 165
- Byckling, K., Osborne J. P., Wheatley P. J., Wynn G. A., Beardmore A., Braito V., Mukai K., West R., 2009, MNRAS, 399, 1576
- Capalbi M., Perri M., Saija B., Tamburelli F., Angelini L., 2005, The Swift XRT Data Reduction Guide, v. 1.2
- Cash W., 1979, ApJ, 228, 939
- Cash W., 1976, A&A, 52, 307
- Chan K. L., Chau W. Y., 1979, ApJ, 233, 950
- Chanmugam G., Ray A., 1984, ApJ, 285, 282
- Charles P. A., Seward F. D., 1995, Exploring the X-ray Universe, Cambridge University Press
- Chen P.-E., Yang X.-H., Zhang P., 2007, AJ, 134, 214
- Cochran W. G., 1952, Ann. Math. Statistics, 23, 315
- Cooke B. A., Griffiths R. E., Pounds K. A., 1970, IAUS, 37, 280
- Copperwheat C. M., Marsh T. R., Dhillon V. S. et al., 2009, MNRAS, 393, 157

- Córdova F.A., Mason K.O., 1984, MNRAS, 206, 879
- Crawford D. F., Jauncey D. L., Murdoch H. S., 1970, ApJ, 162, 405
- Cropper M., 1990, SSRv, 54, 195
- den Herder J. W., Brinkman A. C., Kahn S. M. et al., 2001, A&A, 365, L7
- Done C., Osborne J.P., 1997, MNRAS, 288, 649
- Duerbeck H. W., Seitter W. C., 1987, Ap&SS, 131, 467
- Ebeling H., Voges W., Böhringer H., Edge A.C., Huchra J.P., Briel U.G., 1996, MNRAS, 281, 799
- Ebisawa K., Maeda Y., Kaneda H., Yamauchi S., 2001, Science, 293, 1633
- Ebisawa K., Tsujimoto M., Paizis A. et al., 2005, ApJ, 635, 214
- Ebisawa K., Yamauchi S., Tanaka Y. et al., 2008, PASJ, 60, S223
- Eggleton P. P., 1976, in *Structure and Evolution of Close Binary Systems*, IAU Symp., No. 73, eds. P. Eggleton, S. Mitton, J. Whelan, D. Reidel, Dordrecht, p. 209
- Eisberg R., Resnick R., 1985, *Quantum Physics of Atoms, Molecules, Solids, Nuclei and Particles*, John, Wiley & Sons, 2nd ed.
- Eracleous M., Halpern J. P., Patterson J., 1991a, ApJ, 382, 290
- Eracleous M., Halpern J. P., Patterson J., 1991b, ApJ, 370, 330
- Evans P. A., Beardmore A. P., Page K. L. et al., 2009, MNRAS, 397, 1177
- Ezuka H., Ishida M., 1999, ApJS, 120, 277
- Faulkner J., 1971, *ApJ*, 170, L99
- Faulkner J., 1976, in *Structure and Evolution of Close Binary Systems*, IAU Symp. No. 73, eds. P. Eggleton, S. Mitton, J. Whelan, D. Reidel, Dordrecht, p. 193

Forman W., Jones C., Cominsky L., Julien P., Murray S., Peters G., Tananbaum H., Giacconi R., 1978, *ApJS*, 38, 357

Frank J., King A. R., Lasota J.-P., 1988, *A&A*, 193, 113

Frank J., King A., Raine D., 2002, *Accretion Power in Astrophysics*, Cambridge University Press, 3rd ed.

Friedman H., Lichtman S. W., Byram E. T., 1951, *PhRv*, 83, 1025

Friend M. T., Martin J. S., Connon-Smith R., Jones D.H.P., 1990, *MNRAS*, 246, 654

Gehrels N., Chincarini G., Giommi P. et al., 2004, *ApJ*, 611, 1005

George I. M., Fabian A. C., 1991, *MNRAS*, 249, 352

Giacconi R., Gursky H., Paolini F. R., 1962, *PhRvL*, 9, 439

Giacconi R., Kellogg E., Gorenstein P., Gursky H., Tananbaum H., 1971, *ApJ*, 165, L27

Giacconi R., Branduardi G., Briel U. et al., 1979, *ApJ*, 230, 540

Gilfanov M., Grimm H.-J., Sunyaev R., 2004, *MNRAS*, 351, 1365

Greenstein J. L., Matthews M. S., 1957, *ApJ*, 126, 14

Gänsicke B.T., Dillon M., Southworth J. et al., 2009, *MNRAS*, 397, 2170

Hands A. D. P., Warwick R. S., Watson M. G., Helfand D. J., 2004, *MNRAS*, 351, 31

Hameury J. M., King A. R., Lasota J. P., Ritter H., 1988, *MNRAS*, 231, 535

Hameury J. M., King A. R., 1988, *MNRAS*, 235, 433

Harrison T. E., McNamara B. J., Szkody P., McArthur B. E., Benedict G. F., Klemola A. R., Gilliland R. L., 1999, *ApJ*, 515, 93

Harrison T. E., Johnson J. J., McArthur B. E., Benedict G. F., Szkody P., Howell S. B., Gelino D. M., 2004, 127, 460

- Hassall B. J. M., Pringle J. E., Schwarzenberg-Czerny A., Wade R. A., Whelan J. A. J., Hill P. W., 1983, *MNRAS*, 203, 865
- Hellier C., Mukai K., Osborne J. P., 1998, *MNRAS*, 297, 526
- Hellier C., 2001, *Cataclysmic variable stars: how and why they vary*, Springer
- Hertz P., Grindlay J. E., 1984, *ApJ*, 278, 137
- Hessman F. V., Koester D., Schoembs R., Barwig H., 1989, *A&A*, 213, 167
- Hilditch R.W., 2001, *An introduction to close binary stars*, Cambridge University Press
- Hilton E.J., Szkody P., Mukadam A., Mukai K., Hellier C., van Zyl L., Homer L., 2007, *AJ*, 134, 1503
- Horne K., 1986, *PASP*, 98, 609
- Horne K., Wood J.H., Stiening R.F., 1991, *ApJ*, 378, 271
- Hoshi R., 1979, *Prog. Theor. Phys.*, 61, 1307
- Howell S. B., Szkody P., Cannizzo J. K., 1995, *ApJ*, 439, 337
- Howell S.B., Rappaport S., Politano M., 1997, *MNRAS*, 287, 929
- Howell S. B., 2006, *Handbook of CCD Astronomy*, Cambridge University Press, 2nd ed.
- Immler S., Still M., Boyd P. et al., 2006, v.2.0, *The SWIFT UVOT Software Guide*, NASA/GSFC
- Ishida M., Okada S., Hayashi T., Nakamura R., Terada Y., Mukai K., Hamaguchi K., 2009, *PASJ*, 61, S77
- Israel G.-L., Panzera M. R., Campana S., Lazzati D., Covino S., Tagliaferri G., 1999, *A&A*, 349, L1
- Jahreiß H., Wielen R., 1997, *ESA SP-402: Hipparcos - Venice '97*, 675

Jansen F., Lumb D., Altieri B. et al., 2001, A&A, 365, 1

Jauncey D. L., 1967, Nature, 216, 877

Jones M. H., Watson M. G., 1992, MNRAS, 257, 633

Kaneda H., Makishima K., Yamauchi S., Koyama K., Matsuzaki K., Yamasaki N. Y., 1997, ApJ, 491, 638

Kelley R. L., Mitsuda K., Allen C. A. et al., 2007, PASJ, 59, S77

King A. R., Lasota J. P., 1980, MNRAS, 191, 721

King A. R., Lasota J. P., 1990, MNRAS, 247, 214

King A. R., Schenker K., Hameury J. M., 2002, MNRAS, 335, 513

Knigge C., 2006, MNRAS, 373, 484

Koester D., Chanmugam G., 1990, RPPh, 53, 837

Kolb U., 1993, A&A, 271, 149

Kolb U., Baraffe I., 1999, MNRAS, 309, 1034

Kolb U., 2002, in Gänsicke B. T., Beuermann K., Reinsch K., eds., ASP Conf. Ser. Vol. 261, The Physics of Cataclysmic Variables and Related Objects. Astron. Soc. Pac., San Francisco, P. 180

Koornneef J., 1983, A&A, 128, 84

Koyama K., Makishima K., Tanaka Y., Tsunemi H., 1986, PASJ, 38, 121

Koyama K., Inui T., Hyodo Y. et al., 2007, 59, 23

Krautter J., Ögelman H., Starrfield S., Wichmann R., Pfeffermann E., 1996, ApJ, 456, 788

Kuijpers J., Pringle J. E., 1982, A&A, 114, L4

Kuulkers E., Knigge C., Steeghs D., Wheatley P. J., Long K. S., 2002, ASP Conf. Series, Vol. 261

Lamb D. Q., Masters A. R., 1979, ApJ, 234, L117

Lasota J.-P., 2001, NewAR, 45, 449

Leahy D. A., Darbro W., Elsner R. F., Weisskopf M. C., Kahn S., Sutherland P. G., 1983, ApJ, 266, 160

Lemm K., Patterson J., Thomas G., Skillman D.R., 1993, PASP, 105, 1120

Lewin W. H. G., van Paradijs J., van der Klis M., 1988, SSR, 46, 273

Liedahl D. A., Osterheld A. L., Goldstein W. H., 1995, ApJ, 438, L115

Lomb N.R., 1976, Ap. Space Sci., 39, 447

Lombard F., 1998, MNRAS, 294, 657

Longair M. S., 1992, High Energy Astrophysics, Cambridge University Press, Vol. 1, 2nd ed.

MacDonald J., 1984, ApJ, 283, 241

Makishima K., 1986, The Physics of Accretion onto Compact Objects, Vol.266, ed. K. P. Mason, M. G. Watson, N. E. White, Springer-Verlag, Berlin, Heidelberg, New York, 249

Mason K. O., Breeveld A., Much R. et al., 2001a, A&A, 365, 36

Mason E., Skidmore W., Howell S. B., Mennickent R. E., 2001b, ApJ, 563, 351

Mattei J. A., Mauche C., Wheatley P. J., 2000, JAVSO, Vol. 28, 160

Matthews O. M., Speith R., Wynn G. A., West R. G., 2007, MNRAS, 375, 105

Mauche C. W., Raymond J. C., 2000, AJ, 541, 924

Maza J., Gonzalez L.E., 1983, IAU Circ., 3854, 2

- McGowan K.E., Priedhorsky W.C., Trudolyubov S.P., 2004, ApJ, 601, 1100
- Mewe R., Lemen J.R., van den Oord G.H.J., 1986, A&A, 65, 511
- Mitsuda K., Bautz M., Inoue H. et al., 2007, PASJ, 59, 1
- Monet D. G., Levine S. E., Canzian B. et al., 2003, AJ, 125, 984
- Motch C., Guillout P., Haberl F., Pakull M., Pietsch W., Reinsch K., 1997, A&A, 318, 111
- Motch C., Herent O., Guillout P., 2003, AN, 324, 61
- Motch C., 2006, ESA Special Publication, Vol. 604, The X-ray Universe 2005, ed. A. Wilson, 383
- Moretti A., Campana S., Mineo T. et al., SPIE, 2005, 5898, 360
- Morrison R., McCammon D., 1983, ApJ, 270, 119
- Mukai K., Shiokawa K., 1993, ApJ, 418, 863
- Mukai K., Wood J. H., Naylor T., Schlegel E. M., Swank J. H., 1997, ApJ, 475, 812
- Mukai K., Kinkhabwala A., Peterson J. R., Kahn S. M., Paerels F., 2003, ApJ, 586, L77
- Mukai K., Zietsman E., Still M., 2009, ApJ, 707, 652
- Mushotzky R. F., Szymkowiak A. E., 1988, in Cooling Flows in Clusters and Galaxies, ed. A.C. Fabian, (Dordrecht:Kluwer), 53
- Nauenberg M., 1972, ApJ, 175, 417
- Nelemans G., Yungelson L. R., van der Sluys M. V., Tout C. A., 2010, MNRAS, 401, 1347
- Nevalainen J., Lumb D., dos Santos S., Siddiqui H., Stewart G., Parmar A. N., 2001, A&A, 374, 66
- Norton A. J., Watson M. G., 1989, MNRAS, 237, 853

Osborne J. P., Beuermann K., Charles P., Maraschi L., Mukai K., Treves A., 1987, *ApJ*, 315, L123

Osborne J. P., Giommi, P., Angelini, L., Tagliaferri, G., Stella, L., 1988, *ApJ*, 328, L45

Paczyński B., 1971, *ARA&A*, 9, 183

Paczyński B., 1976, *IAUS*, 73, 75

Paczyński B., Sienkiewicz R., 1981, *ApJ*, 248, L27

Pandel D., Córdova F. A., Mason K. O., Priedhorsky W. C., 2005, *ApJ*, 626, 396

Pandel D., Córdova F. A., Howell S. B., 2003, *MNRAS*, 346, 1231

Patterson J., Williams G., Hiltner W. A., 1981, *ApJ*, 245, 618

Patterson J., 1984, *ApJS*, 54, 443

Patterson J., Beuermann K., Lamb D. Q., Fabbiano G., Raymond J. C., 1984, *ApJ*, 279, 785

Patterson J., Raymond J. C., 1985, *ApJ*, 292, 535

Patterson J., Richman H., Kemp J., Mukai K., 1998, *PASP*, 110, 403

Patterson J. Kemp J., Harvey D. A. et al., 2005, *PASP*, 117, 1204

Pearson K., 1900, *Phil. Mag. Series 5*, 50, 157

Pollacco D. L., Skillen I., Cameron A. et al., 2006, *PASP*, 118, 1407

Poole T. S., Breeveld A. A., Page M. J. et al., 2008, *MNRAS*, 383, 627

Press W. H., Vetterling W. T., Flannery B. P., Teukolsky W. H., 1992, *Numerical Recipes in Fortran 77*, Cambridge University Press, 2nd ed.

Pretorius M. L., Knigge C., Kolb U., 2007, *MNRAS*, 374, 1495

Pringle, J. E., Webbink, R. F., 1975, *MNRAS*, 172, 493

Pringle J. E., 1977, MNRAS, 178, 195

Pringle J. E., Savonije G. J., 1979, MNRAS, 187, 777

Pringle J. E., Bateson F. M., Hassall B. J. M. et al., 1987, MNRAS, 225, 73

Protassov R., van Dyk D. A., Connors A., Kashyap V. L., Siemiginowska A., 2002, ApJ, 571, 545

Ramsay G., Mason K. O., Cropper M., Watson M. G., Clayton K. L., 1994, MNRAS, 270, 692

Ramsay G., Cropper, M., 2004, MNRAS, 347, 497

Ramsay G., Cropper M., 2007, MNRAS, 379, 1209

Ramsay G., Wheatley P. J., Norton A. J., Hakala P., Baskill D., 2008, MNRAS, 387, 1157

Ramsay G., Rosen S., Hakala P., Barclay T., 2009, MNRAS, 395, 416

Rappaport S., Joss P., Webbink R. F., 1982, ApJ, 254, 616

Revnivtsev M., Sazonov S., Gilfanov M., Churazov E., Sunyaev R., 2006, A&A, 452, 169

Revnivtsev M., Sazonov S., Krivonos R., Ritter H., Sunyaev R., 2008, A&A, 489, 1121

Revnivtsev M., Sazonov S., Churazov E., Forman W., Vikhlinin A., Sunyaev R., 2009, Nature, 458, 1142

Ricketts M. J., King A. R., Raine D. J., 1979, MNRAS, 186, 233

Ritter H., Kolb U., 2003, A&A, 404, 301 (update RKcat7.12, 2009)

Ritter H., 1990, A&AS, 85, 1179

Roelofs G. H. A., Nelemans G., Groot P. J., 2007, MNRAS, 382, 685

Romano P., Campana S., Chincarini G. et al., 2006, A&A, 456, 917

Roming P. W. A., Kennedy T. E., Mason K. O. et al., 2005, *SSRv*, 120, 95

Rucinski S. M., 1984, *Observatory*, 104, 259

Rutledge R. E., Brunner R. J., Prince T. A., Lonsdale C., 2000, *ApJS*, 131, 335

Sazonov S., Revnivtsev M., Gilfanov M., Churazov E., Sunyaev R., 2006, *A&A*, 450, 117

Scargle J. D., 1982, *ApJ*, 263, 835

Schmidt G. D., Szkody P., Vanlandingham K. M. et al., 2005, *ApJ*, 630, 1037

Schwope A. D., Brunner H., Buckley D. et al., 2002a, *A&A*, 396, 895

Schwope A. D., Brunner H., Hambaryan V., Schwarz R., Staude A., Szokoly G., 2002b, *ASP Conf. Series, The Physics of Cataclysmic Variables and Related Objects*, Vol. 261, 102

Schwope A. D., Schwarz R., Sirk M., Howell S. B., 2001, *A&A*, 375, 419

Serlemitsos P. J., Soong Y., Chan K.-W. et al., 2007, *PASJ*, 59, S9

Shakura N. I., Sunyaev R. A., 1973, *A&A*, 24, 337

Singh K. P., Drake S. A., Gotthelf E. V., White N. E., 1999, *ApJ*, 512, 874

Sion E. M., 1999, *PASP*, 111, 532

Sion E. M., Cheng F., Godon P., Urban J. A., 2004, *AJ*, 128, 1834

Smak J., 1993, *Acta Astron.*, 43, 101

Sokoloski J. L., Luna G. J. M., Mukai K., Kenyon S. J., 2006, *Nature*, 442, 276

Spruit H. C., Ritter H., 1983, *A&A*, 124, 267

Sterken C., 2005, *ASP Conf. Series.*, Ed. C. Sterken, 335

Stauffer J., Spinrad H., Thorstensen J., 1979, *PASP*, 91, 59

Strüder L., Briel U., Dennerl K. et al., 2001, *A&A*, 365, L18

Sugizaki M., Mitsuda K., Kaneda H., Matsuzaki K., Yamauchi S., Koyama K., 2001, *ApJS*, 134, 77

Swank J. H., Boldt E. A., Holt S. S., Rothschild R. E., Serlemitsos P. J., 1978, *ApJ*, 226, L133

Szkody P., Anderson S. F., Agueros M. et al., 2002, *AJ*, 123, 430

Szkody P., Gänsicke B. T., Howell S. B., Sion E. M., 2002, *ApJ*, 575, 79

Szkody P., Anderson S. F., Hayden M. et al., 2009, *AJ*, 137, 4011

Takahashi T., Abe K., Endo M. et al., 2007, *PASJ*, 59, S35

Talavera A., 2009, *Ap&SS*, 320, 177

Tamuz O., Mazeh T., Zucker S., 2005, *MNRAS*, 356, 1466

Tanaka Y., Inoue H., Holt S. S., 1994, *PASJ*, 46, L37

Templeton M. R., Leaman R., Szkody P. et al., 2006, *PASP*, 118, 236

Templeton M., 2007, *AAVSO Alert Notice* 349

Thorstensen J. R., Patterson J., Kemp J., Vennes S., 2002, *PASP*, 114, 1108

Thorstensen J. R., 2003, *AJ*, 126, 3017

Thorstensen J. R., Lépine S., Shara M., 2008, *AJ*, 136, 2107

Townsley D. M., Arras P., Bildsten L., 2004, *ApJ*, 608, L105

Turner M. J. L., Abbey A., Arnaud M. et al., 2001, *A&A*, 365, L27

Urban J. A., Sion M. E., 2006, *ApJ*, 642, 1029

Valinia A., Marshall F. E., 1998, *ApJ*, 505, 134

- van Teeseling A., Beuermann K., Verbunt F., 1996, *A&A*, 315, 467
- van der Woerd H., Heise J., 1987, *MNRAS*, 225, 141
- van Zyl L., Warner B., O'Donoghue D., Sullivan D., Pritchard J., Kemp J., 2000, *Baltic Astronomy*, 9, 231
- van Zyl L., Warner B., O'Donoghue D. et al., 2004, *MNRAS*, 350, 307
- Verbunt F., Zwaan C., 1981, *A&A*, 100, L7
- Verbunt F., Wheatley P. J., Mattei J. A., 1999, *A&A*, 346, 146
- Vogel J., Byckling K., Schwöpe A., Osborne J.P., Schwarz R., Watson M.G., 2008, *A&A*, 485, 787
- Voges W., Aschenbach B., Boller Th. et al., 1999, *A&A*, 349, 389
- Wall J. V., Jenkins C. R., 2003, *Practical Statistics for Astronomers*, Cambridge University Press, 1st ed.
- Warner B., 1995, *Cataclysmic Variable Stars*, Cambridge University Press
- Warner B., Livio M., Tout C. A., 1996, *MNRAS*, 282, 735
- Warner B., van Zyl L., 1998, *IAU Symp. no. 185. New Eyes to See Inside the Sun and Stars*, ed. F.-L. Deubner, J. Christensen-Dalsgaard, & D. Kurtz, 321
- Warwick R. S., Marshall N., Fraser G. W. et al., 1981, *MNRAS*, 197, 865
- Warwick R. S., Turner M. J. L., Watson M. G., Willingale R., 1985, *Nature*, 317, 218
- Watson M. G., Mayo S. K., King A. R., 1980, *MNRAS*, 192, 689
- Watson M. G., Schröder A. C., Fyfe D. et al., 2009, *A&A*, 493, 339
- Wheatley P. J., van Teeseling A., Watson M. G., Verbunt F., Pfeiffermann E., 1996a, *MNRAS*, 283, 101

Wheatley P. J., Verbunt F., Belloni T., Watson M. G., Naylor T., Ishida M., Duck S. R.,
Pfeffermann E., 1996b, A&A, 307, 137

Wheatley P.J., Mauche C.W., Mattei J.A., 2003, MNRAS, 345, 49

Wheatley P. J., Mauche C. W., 2005, ASPC, 330, 257

Wheeler J. C., 1991, ASPC, 20, 483

Whitehurst R., 1988, MNRAS, 232, 35

Wood K. S., Meekins J. F., Yentis D. J. et al., 1984, ApJS, 56, 507

Worrall D. M., Marshall F. E., Boldt E. A., Swank J. H., 1982, ApJ, 255, 111

Worrall D. M., Marshall F. E., 1983, ApJ, 267, 691

Woudt P. A., Warner B., 2002, Ap&SS, 282, 433

Yamauchi S., Koyama K., 1993, ApJ, 404, 620

Yamauchi S., Ebisawa K., Tanaka Y., Koyama K., Matsumoto H., Yamasaki N. Y., Takahashi
H., Ezoe Y., 2009, PASJ, 61, S225

Yamasaki N. Y., Ohashi T., Takahara F. et al., 1997, ApJ, 481, 821

York D. G., Adelman J., Anderson J. E. et al., 2000, AJ, 120, 1579